N72-33564

NASA CR-120937
LMSC-D281476

FIBERGLASS SUPPORTS FOR CRYOGENIC TANKS

Final Report

by

C. W. KELLER

Prepared for

NATIONAL AERONAUTICS AND SPACE ADMINISTRATION
NASA LEWIS RESEARCH CENTER
CONTRACT NAS 3-12037
JAMES R. BARBER, PROJECT MANAGER

LOCKHEED MISSILES & SPACE COMPANY, INC.
A SUBSIDIARY OF LOCKHEED AIRCRAFT CORPORATION
SPACE SYSTEMS DIVISION · SUNNYVALE, CALIFORNIA

NASA CR-120937
LMSC-D281476

FINAL REPORT

FIBERGLASS SUPPORTS FOR CRYOGENIC TANKS

by

C. W. Keller

Lockheed Missiles & Space Company, Inc.
Sunnyvale, California 94088

Prepared for

NATIONAL AERONAUTICS AND SPACE ADMINISTRATION

10 October 1972

CONTRACT NAS 3-12037

NASA Lewis Research Center
Cleveland, Ohio 44135

James R. Barber, Project Manager
PROPULSION SYSTEMS BRANCH

LOCKHEED MISSILES & SPACE COMPANY

FOREWORD

The Lockheed Missiles & Space Company, Inc. is submitting this Final Report in completion of the requirements of Contract NAS 3-12037, "Fiberglass Supports for Cryogenic Tanks", dated 12 May 1969. The total scope of work, data, results, and conclusions pertinent to this program are presented in this volume. The program was conducted under the technical direction of Mr. James R. Barber, Propulsion Systems Branch, Chemical Propulsion Division of the NASA Lewis Research Center.

CONTENTS

Section		Page
	FOREWORD	iii
	ILLUSTRATIONS	vii
	TABLES	xiii
	ABSTRACT	xv
1	SUMMARY	1-1
2	INTRODUCTION	2-1
3	TASK 1 - STRUCTURAL DESIGN	3-1
	3.1 Parametric Structural and Thermal Analysis	3-2
	3.1.1 Design Requirements and Guidelines	3-2
	3.1.2 Monocoque Fiberglass Cylinders	3-8
	3.1.3 Monocoque Fiberglass Ogives	3-20
	3.1.4 Monocoque Fiberglass-Boron Cylinders	3-26
	3.1.5 Stiffened Fiberglass Cylinders	3-28
	3.1.6 Stiffened Fiberglass Ogives	3-37
	3.1.7 Heat Leak Comparison	3-40
	3.1.8 System Weight Comparison	3-48
	3.1.9 Selection of Candidates for Detailed Analysis	3-60
	3.2 Design and Analysis of Selected Candidates	3-62
	3.2.1 End Fittings and Rod Ends	3-62
	3.2.2 Core Insulation Analysis	3-74
	3.2.3 Development of Final Designs	3-77
4	TASK 2 - EXPERIMENTAL CONCEPT SCREENING PROGRAM	4-1
	4.1 Preparation of Test Hardware and Facilities	4-1
	4.1.1 Short-Column Test Specimens	4-1
	4.1.2 Instrumentation for Strain Measurements	4-4
	4.1.3 Test Machine Setup	4-7
	4.2 Short-Column Screening Tests	4-7

CONTENTS (Cont'd)

Section			Page
	4.2.1	Test Operations and Results	4-7
	4.2.2	Data Reduction and Analysis	4-10
5	TASK 3 - STRUT FABRICATION		5-1
	5.1	Material and Fitting Procurement	5-1
	5.1.1	Glass Fibers and Resin-Prepreg	5-1
	5.1.2	Titanium End Fittings and Caps	5-2
	5.1.3	Rod-End Fittings	5-3
	5.2	Tooling and Mandrel Fabrication	5-3
	5.2.1	Metal Masters and Fiberglass Molds	5-4
	5.2.2	Cast Salt Mandrels	5-4
	5.3	Strut Fabrication and Assembly	5-6
	5.3.1	Setup and Filament Winding Operations	5-8
	5.3.2	Debulking and Curing Operations	5-10
	5.3.3	Mandrel Removal and Final Assembly	5-10
6	TASK 4 - TEST PROGRAM		6-1
	6.1	Facility Description	6-1
	6.1.1	Dynamic Test Machine	6-1
	6.1.2	Instrumentation and Data Acquisition Equipment	6-3
	6.2	Structural Testing	6-7
	6.2.1	Static Tension-Compression Tests	6-9
	6.2.2	Cyclic Tests	6-13
	6.2.3	Test Results and Analysis	6-13
7	TASK 5 - POST-TEST INSPECTION AND DATA CORRELATION		7-1
	7.1	Laboratory Analysis and Evaluation	7-2
	7.1.1	Task 2 Test Specimens	7-2
	7.1.2	Task 4 Test Specimens	7-9
	7.2	Review of Fiberglass Strut Technology	7-16
	7.2.1	Thermal and Mechanical Properties	7-16
	7.2.2	Recommended Design Approach	7-16

CONTENTS (Cont'd)

Section			Page
	7.2.3	Evaluation of Other System Concepts	7-18
	7.2.4	Comparison of System Performance for Fiberglass and Metallic Strut Supports	7-20
8	DISCUSSION OF RESULTS		8-1
9	CONCLUSIONS		9-1

Appendix

A	DESCRIPTION OF COMPUTER PROGRAMS FOR STRUCTURAL ANALYSIS	A-1
B	COMPRESSIVE LOAD CAPABILITY FOR LONGERON-STIFFENED FIBERGLASS STRUTS	B-1
C	CALCULATION OF ONE-DIMENSIONAL HEAT LEAKS	C-1
D	CALCULATION OF COMPARATIVE SYSTEM WEIGHTS	D-1
E	PROCESS SPECIFICATION NO. 3060993, FIBERGLASS SUPPORTS FOR CRYOGENIC TANKS	E-1
F	ANALYTICAL METHOD TO DETERMINE WINDING REQUIREMENTS	F-1
G	NOMENCLATURE	G-1
H	REFERENCES	H-1
I	DISTRIBUTION	I-1

ILLUSTRATIONS

Figure		Page
3-1	End View of Integrally-Wound Fiberglass Strut	3-3
3-2	Composite Cross-Section Area as a Function of Thickness and Outside Diameter	3-12
3-3	Composite Radius of Gyration as a Function of Thickness and Outside Diameter	3-13
3-4	Predicted Ultimate Compressive Loads for Monocoque Fiberglass Cylinders with a 12-mil (0.30-mm) Longo Wrap Thickness	3-14
3-5	Predicted Ultimate Compressive Loads for Monocoque Fiberglass Cylinders with an 18-mil (0.46-mm) Longo Wrap Thickness	3-15
3-6	Predicted Ultimate Compressive Loads for Monocoque Fiberglass Cylinders with a 24-mil (0.61-mm) Longo Wrap Thickness	3-16
3-7	Outside Diameter as a Function of Strut Length for Optimum Monocoque Fiberglass Cylinders	3-18
3-8	Predicted Ultimate Compressive Loads as a Function of Outside Diameter for 40-in.-(101.6-cm) Long Monocoque Fiberglass Cylinders	3-19
3-9	Predicted Ultimate Compressive Loads for Monocoque Fiberglass Ogives with a 12-mil (0.30-mm) Longo Wrap Thickness at Midspan	3-22
3-10	Predicted Ultimate Compressive Loads for Monocoque Fiberglass Ogives with an 18-mil (0.46-mm) Longo Wrap Thickness at Midspan	3-23
3-11	Predicted Ultimate Compressive Loads for Monocoque Fiberglass Ogives with a 24-mil (0.61-mm) Longo Wrap Thickness at Midspan	3-24
3-12	Outside Diameter at Midspan as a Function of Strut Length for Optimum Monocoque Fiberglass Ogives	3-25
3-13	Predicted Ultimate Compressive Loads as a Function of Outside Diameter at Midspan for 40-in.-(101.6-cm-) Long Monocoque Fiberglass Ogives	3-27
3-14	Predicted Ultimate Compressive Loads for Monocoque Fiberglass-Boron Cylinders with a 17-mil (0.43-mm) Longo Wrap Thickness	3-29

Figure		Page
3-15	Predicted Ultimate Compressive Loads for Optimally-Stiffened Fiberglass Cylinders with a 12-mil (0.30-mm) Longo Wrap Thickness	3-33
3-16	Optimum Number of Stiffeners Required for Fiberglass Cylinders with a 12-mil (0.30-mm) Longo Wrap Thickness	3-34
3-17	Predicted Ultimate Compressive Loads for 40-in.-(101.6-cm-) Long Fiberglass Cylinders Optimally Stiffened with Boron-Fiber Longerons	3-36
3-18	Predicted Ultimate Compressive Loads for Fiberglass Cylinders with a 12-mil (0.30-mm) Longo Wrap Thickness Stiffened with Boron-Fiber Longerons	3-38
3-19	Predicted Ultimate Compressive Loads for Fiberglass Ogives with a 12-mil (0.30-mm) Longo Wrap Thickness at Midspan Stiffened with Boron-Fiber Longerons	3-39
3-20	Thermal Conductivity Model for Glass Fiber-Epoxy Composites	3-42
3-21	Comparison of Calculated and Test Values of Thermal Conductivity for Glass Fiber-Epoxy Composites	3-44
3-22	Comparison of Calculated and Test Values of Thermal Conductivity for Boron Fiber-Epoxy Composites	3-47
3-23	Predicted Heat Leaks for Monocoque Fiberglass Cylinders with a 12-mil (0.30-mm) Longo Wrap Thickness and Boundary Temperatures of 520°R (289°K) to 37°R (20°K)	3-49
3-24	Predicted Heat Leaks for Monocoque Fiberglass Cylinders with a 12-mil (0.30-mm) Longo Wrap Thickness and Boundary Temperatures of 400°R (222°K) to 140°R (78°K)	3-50
3-25	Comparative Total System Weights for Short, Lightly-Loaded Struts with 520°R (289°K) to 37°R (20°K) Boundary Temperatures	3-54
3-26	Comparative Total System Weights for Short, Lightly-Loaded Struts with 400°R (222°K) to 140°R (78°K) Boundary Temperatures	3-55
3-27	Comparative Total System Weights for Medium-Length, Medium-Load Struts with 520°R (289°K) to 37°R (20°K) Boundary Temperatures	3-56
3-28	Comparative Total System Weights for Medium-Length, Medium Load Struts with 400°R (222°K) to 140°R (78°K) Boundary Temperatures	3-57
3-29	Comparative Total System Weights for Long, Highly-Loaded Struts with 520°R (289°K) to 37°R (20°K) Boundary Temperatures	3-58
3-30	Comparative Total System Weights for Long, Highly-Loaded Struts with 400°R (222°K) to 140°R (78°K) Boundary Temperatures	3-59

ILLUSTRATIONS (Cont'd)

Figure		Page
3-31	Preliminary Design of Monocoque Cylinders	3-63
3-32	Preliminary Design of Stiffened Cylinders	3-64
3-33	Preliminary Design of Monocoque Ogives	3-65
3-34	Strut Fitting Designs with Externally-Threaded Rod-Ends	3-68
3-35	Strut Fitting Designs with Internally-Threaded Rod-Ends	3-72
3-36	Compressive Modulus of Elasticity for Fiberglass Struts as a Function of Cross-Ply Distribution	3-81
3-37	Revised Ultimate Compressive Loads for Monocoque Fiberglass Cylinders with a 12-mil (0.30-mm) Longo Wrap Thickness	3-82
3-38	Revised Ultimate Compressive Loads for Monocoque Fiberglass Cylinders with an 18-mil (0.46-mm) Longo Wrap Thickness	3-83
3-39	Revised Ultimate Compressive Loads for Monocoque Fiberglass Cylinders with a 24-mil (0.61-mm) Longo Wrap Thickness	3-84
3-40	Revised Ultimate Compressive Loads for Monocoque Fiberglass Ogives with a 12-mil (0.30-mm) Longo Wrap Thickness at Midspan	3-86
3-41	Revised Ultimate Compressive Loads for Monocoque Fiberglass Ogives with an 18-mil (0.46-mm) Longo Wrap Thickness at Midspan	3-87
3-42	Revised Ultimate Compressive Loads for Monocoque Fiberglass Ogives with a 24-mil (0.61-mm) Longo Wrap Thickness at Midspan	3-88
3-43	Revised Ultimate Compressive Loads as a Function of Longo Wrap Thickness for a 24-in.-(61-cm-) Long, 1.5-in.-(3.81-cm-) Diameter Monocoque Fiberglass Cylinder	3-89
3-44	Revised Ultimate Compressive Loads as a Function of Longo Wrap Thickness for a 19-in.- (48.3-cm-) Long, 1.5 in.-(3.81-cm-) Diameter Monocoque Fiberglass Cylinder	3-90
3-45	Revised Ultimate Compressive Loads as a Function of Longo Wrap Thickness at Midspan for a 36-in.-(101.6-cm-) long 2.5-in.-(6.35-cm-) Midspan Diameter Monocoque Fiberglass Ogive	3-91
3-46	**Design Assembly Drawing for Strut Configurations II-1 and III-1**	3-93
3-47	**Design Assembly Drawing for Strut Configurations II-2, II-3, and III-2**	3-95
3-48	**Design Assembly Drawing for Strut Configurations II-4 and III-3**	3-97

ILLUSTRATIONS (Cont'd)

Figure		Page
4-1	Configuration II-1 Monocoque Fiberglass Cylinders	4-2
4-2	Configuration II-3 Stiffened Fiberglass Cylinders	4-3
4-3	Setup of Short-Column Test Specimens with Single-Axis Bending Control and Strain Measurements	4-6
4-4	Setup of Short-Column Test Specimens with Two-Axis Bending Control and Strain Measurements	4-8
4-5	Specimens of Configuration II-1 After Compressive Failure	4-11
4-6	Specimens of Configuration II-2 After Compressive Failure	4-12
4-7	Specimen X-17-23-3 After Failure in Compressive Crippling	4-13
4-8	Specimens of Configuration II-3 After Compressive Failure	4-14
4-9	Compressive Stress-Strain Curves for the Configuration II-1 Monocoque Fiberglass Cylinders	4-16
4-10	Compressive Stress-Strain Curves for the Configuration II-2 Monocoque Fiberglass Cylinders	4-17
4-11	Compressive Stress-Strain Curves for the Configuration II-3 Stiffened Fiberglass Cylinders	4-18
4-12	Compressive Stress-Strain Curves for the Configuration II-4 Monocoque Fiberglass Ogives	4-19
5-1	Typical Split Casting Mold Used to Produce Salt Mandrels for Ogive Struts	5-5
5-2	Completed Fiberglass Test Specimens	5-7
5-3	Typical Salt Mandrel, End Fittings, and a Completed III-1 Specimen	5-9
5-4	Typical Winding Operation Near Completion	5-11
6-1	Cryogenic Test Complex	6-2
6-2	Typical Test Setup	6-4
6-3	Schematic of the Dynamic Test System	6-5
6-4	Maximum Displacement-Frequency Characteristics of the MTS Test System	6-6
6-5	Specimen III-1A After Failure in Tension	6-10
6-6	Specimen III-3F After Failure In Tension	6-11
6-7	Specimen III-2B After Failure in Compressive Crushing	6-12
6-8	Specimen III-3D After Failure in Cyclic Loading	6-14
6-9	Specimens of Configuration III-1 After Testing to Failure	6-17

ILLUSTRATIONS (Cont'd)

Figure		Page
6-10	Specimens of Configuration III-2 After Testing to Failure	6-18
6-11	Specimens of Configuration III-3 After Testing to Failure	6-19
6-12	Stress-Strain Curves for Typical Specimens of Strut Configuration III-1	6-20
6-13	Stress-Strain Curves for Typical Specimens of Strut Configuration III-2	6-21
6-14	Stress-Strain Curves for Typical Specimens of Strut Configuration III-3	6-22
7-1	Photomicrograph of a Typical Specimen	7-14
7-2	Typical S-N Fatigue Data for Composite Fiberglass Materials	7-15
7-3	Comparison of Monocoque Fiberglass and Titanium Strut Inert Weights	7-21
7-4	Comparison of Heat Rates for Fiberglass and Titanium Strut Supports	7-23
B-1	Predicted Ultimate Compressive Loads for 18-in.-(45.7-cm-) Long, 1.5-in.-(3.81-cm-) Diameter Stiffened Fiberglass Cylinders with a 12-mil (0.30-mm) Longo Wrap Thickness	B-2
B-2	Predicted Ultimate Compressive Loads for 18-in.-(45.7-cm-) Long, 1.75-in.-(4.45-cm-) Diameter Stiffened Fiberglass Cylinders with a 12-mil (0.30-mm) Longo Wrap Thickness	B-3
B-3	Predicted Ultimate Compressive Loads for 18-in.-(45.7-cm-) Long, 2.0-in.-(5.08-cm-) Diameter Stiffened Fiberglass Cylinders with a 12-mil (0.30-mm) Longo Wrap Thickness	B-4
B-4	Predicted Ultimate Compressive Loads for 18-in.-(45.7-cm-) Long, 2.25-in.-(5.72-cm-) Diameter Stiffened Fiberglass Cylinders with a 12-mil (0.30-mm) Longo Wrap Thickness	B-5
B-5	Predicted Ultimate Compressive Loads for 18-in.-(45.7-cm-) Long, 2.5-in.-(6.35-cm-) Diameter Stiffened Fiberglass Cylinders with a 12-mil (0.30-mm) Longo Wrap Thickness	B-6
B-6	Predicted Ultimate Compressive Loads for 29-in.-(73.7-cm-) Long, 1.75-in.-(4.45-cm-) Diameter Stiffened Fiberglass Cylinders with a 12-mil (0.30-mm) Longo Wrap Thickness	B-7
B-7	Predicted Ultimate Compressive Loads for 29-in.-(73.7-cm-) Long, 2.0-in.-(5.08-cm-) Diameter Stiffened Fiberglass Cylinders with a 12-mil (0.30-mm) Longo Wrap Thickness	B-8
B-8	Predicted Ultimate Compressive Loads for 29-in.-(73.7-cm-) Long, 2.25-in.-(5.72-cm-) Diameter Stiffened Fiberglass Cylinders with a 12-mil (0.30-mm) Longo Wrap Thickness	B-9

ILLUSTRATIONS (Cont'd)

Figure		Page
B-9	Predicted Ultimate Compressive Loads for 29-in.-(73.7-cm-) Long, 2.5-in.-(6.35-cm-) Diameter Stiffened Fiberglass Cylinders with a 12-mil (0.30-mm) Longo Wrap Thickness	B-10
B-10	Predicted Ultimate Compressive Loads for 40-in.-(101.6-cm-) Long, 2.0-in.-(5.08-cm-) Diameter Stiffened Fiberglass Cylinders with a 12-mil (0.30-mm) Longo Wrap Thickness	B-11
B-11	Predicted Ultimate Compressive Loads for 40-in.-(101.6-cm-) 2.25-in.-(5.72-cm-) Diameter Stiffened Fiberglass Cylinders with a 12-mil (0.30-mm) Longo Wrap Thickness	B-12
B-12	Predicted Ultimate Compressive Loads for 40-in.-(101.6-cm-) Long, 2.5-in.-(6.35-cm-) Diameter Stiffened Fiberglass Cylinders with a 12-mil (0.30-mm) Longo Wrap Thickness	B-13
B-13	Predicted Ultimate Compressive Loads for 40-in.-(101.6-cm) Long, 2.75-in.-(6.99-cm-) Diameter Stiffened Fiberglass Cylinders with a 12-mil (0.30-mm) Longo Wrap Thickness	B-14
B-14	Predicted Ultimate Compressive Loads for 40-in.-(101.6-cm-) Long, 3.0-in.-(7.62-cm-) Diameter Stiffened Fiberglass Cylinders with a 12-mil (0.30-mm) Longo Wrap Thickness	B-15
B-15	Predicted Ultimate Compressive Loads for 40-in.-(101.6-cm-) Long, 1.5-in-(3.81-cm-) Diameter Stiffened Fiberglass Cylinders with an 18-mil (0.46-mm) Longo Wrap Thickness	B-16
B-16	Predicted Ultimate Compressive Loads for 40-in-(101.6-cm-) Long, 2.0-in.-(5.08-cm-) Diameter Stiffened Fiberglass Cylinders with an 18-mil (0.46-mm) Longo Wrap Thickness	B-17
B-17	Predicted Ultimate Compressive Loads for 40-in.-(101.6-cm-) Long, 2.5-in.-(6.35-cm-) Diameter, Stiffened Fiberglass Cylinders with an 18-mil (0.46-mm) Longo Wrap Thickness	B-18
B-18	Predicted Ultimate Compressive Loads for 40-in.-(101.6-cm-) Long, 3.0-in.-(7.62-cm-) Diameter Stiffened Fiberglass Cylinders with an 18-mil (0.46-mm) Longo Wrap Thickness	B-19
F-1	**Idealized Strut Cross-Section Geometry**	**F-3**

TABLES

Table		Page
3-1	Summary of Design Parameters	3-6
3-2	Summary of Parametric Analysis Cases	3-7
3-3	Preliminary Estimates of End-Fitting Weights	3-52
3-4	Characteristics of Struts Selected for Detailed Studies	3-61
3-5	Comparison of Physical-Thermal Properties of Candidate End-Fitting Materials with those of Fiberglass	3-66
3-6	Summary of Strut and Fitting Design Ultimate Loads	3-69
3-7	Ultimate Static Load Capability for SWRM- and DREM-Series Rod-Ends	3-70
3-8	Summary of Static and Cyclic Load Capability for SWRF and 2BREF Series Rod-Ends	3-73
3-9	Required Radiation Shield Spacing Density, n/L_c	3-76
3-10	Comparison of System Heat Transfer and Weight Data for Strut Configuration 1 with Three Candidate Radiation Barriers	3-78
3-11	Summary of Design Requirements for Selected Task 2 Struts	3-79
3-12	Summary of Design Requirements for Selected Task 3 Struts	3-92
4-1	Summary of Winding Requirements for Task 2 Struts	4-5
4-2	Summary of Task 2 Test Results	4-9
5-1	Property Data for Paraplast 36 Salt	5-6
6-1	Summary of Measured Eccentricities and Predicted Ultimate Compression Loads for Task 4 Strut Specimens	6-8
6-2	Summary of Task 4 Fiberglass Strut Test Results	6-15
7-1	Results of Laboratory Analysis for Configuration II-1 Test Specimens	7-4
7-2	Results of Laboratory Analysis for Configuration II-2 Test Specimens	7-5
7-3	Results of Laboratory Analysis for Configuration II-3 Test Specimens	7-6
7-4	Results of Laboratory Analysis for Configuration II-4 Test Specimens	7-7
7-5	Summary of Compressive Stress, Elastic Modulus, and Crippling Coefficient Values from Task 2 Short-Column Tests	7-8
7-6	Results of Laboratory Analysis for Configuration III-1 Test Specimens	7-10

TABLES (Cont'd)

Table		Page
7-7	Results of Laboratory Analysis for Configuration III-2 Test Specimens	7-11
7-8	Results of Laboratory Analysis for Configuration III-3 Test Specimens	7-12
7-9	Thermal and Mechanical Properties of Tubular Fiberglass Support Structures	7-17
7-10	Comparison of Effective System Weights for Fiberglass and Titanium Strut Supports	7-24
C-1	Summary of Heat Leaks for Monocoque Fiberglass Cylinders with a 12-mil (0.30-mm) Longo Wrap Thickness	C-2
C-2	Summary of Heat Leaks for Monocoque Fiberglass Cylinders with an 18-mil (0.46-mm) Longo Wrap Thickness	C-3
C-3	Summary of Heat Leaks for Monocoque Fiberglass Cylinders with a 24-mil (0.61-mm) Longo Wrap Thickness	C-4
C-4	Summary of Heat Leaks for Monocoque Fiberglass Ogives with a 12-mil (0.30-mm) Longo Wrap Thickness at Midspan	C-5
C-5	Summary of Heat Leaks for Monocoque Fiberglass Ogives with an 18-mil (0.46-mm) Longo Wrap Thickness at Midspan	C-6
C-6	Summary of Heat Leaks for Monocoque Fiberglass Ogives with a 24-mil (0.61-mm) Longo Wrap Thickness at Midspan	C-7
C-7	Summary of Heat Leaks for Monocoque Fiberglass-Boron Cylinders	C-8
C-8	Summary of Heat Leaks for Glass-Stiffened Fiberglass Cylinders	C-9
C-9	Summary of Heat Leaks for Boron-Stiffened Fiberglass Cylinders	C-10
C-10	Summary of Heat Leaks for Boron-Stiffened Fiberglass Ogives	C-11
D-1	Summary of Comparative System Weights for Analysis Cases 1 Through 6	D-2
D-2	Summary of Comparative System Weights for Analysis Cases 7 Through 10 and 12 Through 16	D-3
E-1	Summary of Dimensions and Winding Requirements	E-10
E-2	Summary of Maximum Allowable Manufacturing Tolerances	E-11

ABSTRACT

A comprehensive 5-task program of analysis, design, fabrication, and test activities was conducted under Contract NAS 3-12037 to develop additional technology needed for application of filament-wound fiberglass struts to cryogenic flight tankage. It was conclusively verified during the program that monocoque cylinder or ogive struts are optimum or near-optimum for the range of lengths and loads studied, that a higher strength-to-weight ratio can be achieved for fiberglass struts than for any metallic struts, and that integrally-wrapped metallic end fittings can be used to achieve axial load transfer without reliance on bond strength or mechanical fasteners. In addition, design predictability within approximately ± 15 percent and manufacturing reproducibility within approximately ± 10 were demonstrated.

Section 1

SUMMARY

The primary objective of the NAS 3-12037 contract program was to develop a low heat leak, filament-wound fiberglass strut with integral end fittings that has a strength-to-weight ratio in tension and compression exceeding that for any metallic strut of equal length and load capability. This objective was achieved with a comprehensive program of analysis, design, fabrication, and test activities conducted under five related tasks.

It was found in the Task 1 studies that monocoque cylinders are optimum for short, lightly-loaded struts. For this application, inert weights vary insignificantly, whereas system weight* variations are substantial, for different candidate designs. For example, for 18-in.-(45.7-cm-) long LF_2 tank supports designed for an ultimate compressive load of 980 lbf (4360 N), it was found that the inert weight per strut varied less than 0.06 lbm (0.027 kg), while the maximum scatter in system weight per strut including boiloff for 200 days of storage was 3.62 lbm (1.64 kg). The average inert and system weights per strut computed for all candidate designs in this example were 1.13 lbm (0.51 kg) and 6.07 lbm (2.75 kg), respectively.

For 40-in.-(101.6-cm-) long LH_2 and LF_2 tank support strut candidates designed for an ultimate compressive load of 8400 lbf (37,360 N), stiffened cylinder and monocoque ogive designs were found to be optimum. In this case, maximum variations of 0.34 lbm (0.15 kg) for an average inert weight of 3.36 lbm (1.52 kg), and 0.66 lbm (0.30 kg) for an average system weight of 6.75 lbm (3.06 kg), were determined from the analysis.

Experimental values of compressive modulus of elasticity determined from short-column compression tests conducted in Task 2 ranged from 6.47×10^6 psi (4.46×10^{10} N/m^2) to 7.64×10^6 psi (5.27×10^{10} N/m^2) for ratios of longo-to-circ glass area of 1.0 and 2.0, respectively. Results of these tests also showed that isotropic crippling coefficients ranging from 0.242 to 0.299 were achieved.

* as used herein, system weight is defined as the sum of the inert and boiloff weights per strut

Design data, analysis procedures, and fabrication processes developed in Tasks 1, 2, and 3 were verified conclusively by the results of tension, compression, and cyclic-load tests conducted in Task 4. In general, failure loads achieved were within ± 15 percent of those predicted by analysis for tension and compression test specimens. Typical failures occurred in tensile fracture of the longo rovings near midspan or at the warm-end fitting for tension specimens, and in crushing of the strut body wall near midspan for the compression specimens. In the cyclic load tests, from 207 to 5761 cycles of near-limit loading were achieved prior to tensile fracture of the longo rovings near the warm-end fitting. No failures were encountered in the fittings or in the fiberglass near the cold end of any of the specimens during any of the tests.

Results of extensive pre-test and post-test analysis conducted under Task 5 showed that significant manufacturing parameters could be controlled within approximately ± 10 percent with existing equipment and procedures. This task was concluded by compiling thermal and mechanical design properties for general use, and by showing the advantages in system weight and other important characteristics for fiberglass struts compared to fiberglass tension straps or titanium struts. For example, the total system weight computed for six 36-in.-(91.4-cm-) long fiberglass struts, each designed for an ultimate compressive load of 8400 lbf (37,360 N) to support a LH_2 tank for a 220-day mission, was 33.9 lbm (15.4 kg) compared to 120 lbm (54.2 kg) for six titanium struts of the same length and load capability.

It was concluded from results of the analysis and test activities conducted during this program that monocoque cylinder or ogive strut designs are either optimum or can be used with negligible weight penalties compared to other designs for the entire spectrum of lengths and loads investigated. In addition, it was shown that fiberglass struts offer strength-to-weight ratios superior to those which can be achieved for any metallic struts. Also, it was demonstrated that ultimate axial load capabilities for fiberglass struts can be predicted within approximately ± 15 percent, and that manufacturing parameters

can be controlled within approximately ± 10 percent. Finally, the concept of using integrally-wrapped metallic end fittings rather than bonded joints or mechanical fasteners to achieve axial load transfer was verified by test, and it was shown that the fatigue-life of titanium end fittings can be extended by using rolled external threads. The technology developed to date can readily be applied to the design of high-strength, low heat leak fiberglass struts for any future flight hardware applications. However, additional cyclic-load testing is needed to completely characterize the fatigue-life capability of particular designs.

Section 2

INTRODUCTION

Heretofore, much of the potential advantage offered by fiberglass tank supports due to the high tensile strength, low density, and low thermal conductivity of the material has not been realized because of grossly inefficient glass-to-metal joint designs and non-optimum winding patterns. Previous designs achieved load transfer from metallic end fittings into the fiberglass strut body through either bonded joints or mechanical fasteners. Also, some previous designs relied on helic rather than polar windings in the longitudinal direction to react primary axial loads. Since the helic windings intercept the longitudinal axis of the strut at a significant angle (e.g., 25 to 35 degrees for typical designs), a thicker wall is required for given material properties. This does not necessarily result in a significant increase in composite inert weight, but does result in a significantly higher heat leak and boiloff weight for long-duration missions.

The most significant feature of the designs investigated during this contract program is that polar-oriented longo rovings are wound continuously over captured internal metallic fittings, thus providing a continuous, efficient, tension load path. In addition, metallic caps are then installed over the longo rovings at each end to provide a direct compression load path in bearing. The compression caps are secured to the internal fittings with lock nuts and safety wire. Reaction of axial loads in either direction is, therefore, optimum as well as completely independent of the bond shear strength of the resultant joint, and mechanical fasteners are not required between the metal and fiberglass components.

Initially, the basic concept of a tubular, filament-wound fiberglass support strut with integral metallic end fittings was evolved under Contract NAS 3-7979, "Cryogenic Tank Support Evaluation." The manufacturing

feasibility was demonstrated under a concurrent Lockheed Independent Research and Development program wherein three prototype struts were fabricated. One of these was thermally tested under the NAS 3-7979 contract. Based on the promising results obtained from that previous work, the present program under Contract NAS 3-12037, "Fiberglass Supports for Cryogenic Tanks," was undertaken. In this program, structural design data were developed and the structural integrity of the basic design concept was successfully demonstrated. Additional data on manufacturing alternatives and the reproducibility achieved have also been provided under a Lockheed Manufacturing Research Investigation, MRI 615.00, conducted concurrently with the present contract program.

The primary goal of the NAS 3-12037 contract program was to develop a low heat leak, filament-wound fiberglass strut with integral end fittings that has a strength-to-weight ratio in tension and compression exceeding that for any metallic strut of equal length and load capability. To achieve this goal, the program was conducted under five related tasks which are:

Task 1 - Structural Design
Task 2 - Experimental Concept Screening Program
Task 3 - Strut Fabrication
Task 4 - Test Program
Task 5 - Post-Test Inspection and Data Correlation

In Task 1, parametric structural and thermal analyses were conducted on sixteen selected design configurations which offered five different types of wall construction. These included both cylindrical and ogive shells of revolution, and both monocoque and longeron-stiffened wall designs. Each of the selected configurations was investigated for a wide range of specified design loads and strut lengths. Many of the guidelines and design values used were derived from previous work performed by the Boeing Company under Contract NAS 8-18037. Based on the results of the parametric analysis, six configurations were selected and used as the basis for

detailed design and analysis of internal end fittings, rod-end fittings, and core insulation. Four of these designs were then selected for further investigation.

A screening program was conducted under Task 2 to obtain experimental values of compressive modulus of elasticity and crippling coefficient. Three specimens each of the four selected designs were fabricated, and short column specimens cut from each were tested to failure in compression at room temperature. Results of these tests were used to revise and update the parametric structural analysis and to finalize the design of three selected configurations under Task 1.

Subsequently, eight specimens each of the three final designs were fabricated under Task 3. Mandrel tooling, water-soluble mandrels, internal end fittings, rod-end fittings, and attachment hardware for all struts fabricated during the program were either procured or manufactured under this task.

Full-scale tension, compression, and cyclic loading structural tests were performed on the final design hardware in Task 4. Two or more specimens of each design were tested to failure in each of the three loading modes. All of these specimens were tested with one end of the strut completely submerged in liquid nitrogen to simulate design environment temperatures.

Extensive pre-test and post-test laboratory analyses of the Task 2 and Task 4 strut specimens were conducted under Task 5. In addition, a review of current technology was conducted with regard to the design, analysis, and fabrication of fiberglass struts. A compilation of thermal and mechanical properties, and a comparison of system performance for fiberglass and titanium struts with equal structural capabilities, were included in this review.

Section 3

TASK 1 - STRUCTURAL DESIGN

Early in Task 1, a parametric analysis was conducted to assess structural and thermal capabilities of filament-wound fiberglass struts for a wide range of specified lengths and loads. Design guidelines and constraints, established at the beginning of the analysis, were based on the results of previous contract studies. Parameters selected for investigation included strut wall configuration, stiffener material and configuration, composite thickness, column length, and outside diameter. Initially, only compressive load capabilities were determined for the selected analysis cases since, in general, struts optimized for compressive loads were not found to be critical in tension. For stiffened configurations, the effect of varying the number and spacing of the stiffeners was also investigated. A one-dimensional thermal analysis was performed for each candidate design to determine longitudinal heat leak due to conduction and radiation heat transfer mechanisms. Strut component inert weights and propellant boiloff weights resulting from the heat leak for representative mission durations were computed and compared.

Results of the parametric analysis were evaluated to select six promising candidate strut designs for more detailed study. Preliminary design drawings were prepared for each of these candidates. Basic configuration details, alternate end fitting designs, and approximate dimensions were established in these drawings. Detailed tradeoff studies of the end fitting designs and internal radiation barrier concepts were conducted. Based on an evaluation of the resulting data, four of the six candidate designs were selected for fabrication and test during the Task 2 experimental screening program.

Subsequently in Task 1, detailed design drawings were prepared for each of the four selected candidates. Hardware dimensions and manufacturing tolerances were established in these drawings for the basic strut body, end

fittings, compression caps, and mandrels. Other design characteristics such as resin content, winding pattern, and end fitting surface treatment were also established.

Following completion of the Task 2 experimental screening program, three of the four design candidates were selected for fabrication in Task 3 and full-scale testing in Task 4. The final effort in Task 1 consisted of revising the design drawings and parametric design curves previously developed for these three candidates. Experimentally-derived values of elastic modulus, which were obtained during the Task 2 test program, were used in the revision.

Details of the work performed in Task 1, together with the drawings and the parametric data which resulted from it, are presented in this section.

3.1 PARAMETRIC STRUCTURAL AND THERMAL ANALYSIS

3.1.1 Design Requirements and Guidelines

Basic requirements for all strut design candidates were specified in the contract. These requirements can be summarized as follows:

- The main column structures shall be of a tubular configuration, and shall be fabricated from S-901 glass-fiber filaments embedded in an E-787 epoxy resin matrix

- The glass-fiber filaments shall be oriented in the two principal directions of the strut (i.e., approximately parallel to the longitudinal axis and circumferential)

- The longo (i.e., longitudinal) wraps shall be wound continuously over the end fittings in order to provide an integral structure

- The end fittings shall be of a metallic material that will provide a minimum overall strut weight consistent with optimum structural and thermal performance

- An internal radiation barrier or low-emittance thermal coating shall be provided to reduce heat transfer by radiation through the strut core cavity

It was determined early in the Task 1 analysis that for integrally-wound struts the longo rovings must be applied in double-thickness wraps (i.e., two complete longo wraps for each complete rotation of the mandrel about the longitudinal axis). As shown in Fig. 3-1, a complete rotation of the mandrel is required in order to provide continuous wraps, since the longo rovings must clear the threaded portion of the end fittings. Consequently,

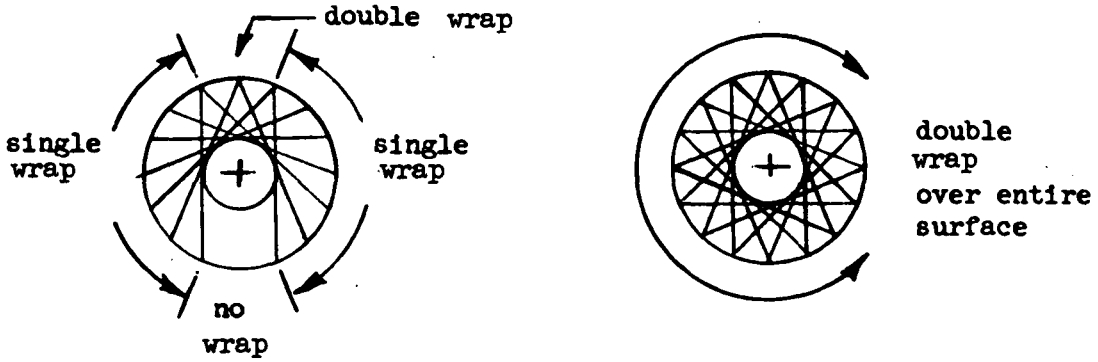

(a) Winding pattern after 180° of mandrel rotation

(b) Winding pattern after 360° of mandrel rotation

Fig. 3-1 End View of Integrally-Wound Fiberglass Strut

only struts with two, four, or some other even number of longo wraps can be fabricated by this technique. However, the thickness of each pair of longo

wraps (and, therefore, total longo thickness) can be varied to achieve optimum designs by adjusting the spacing between successive longo rovings.*

During the selection of candidate configurations for the parametric analysis, results of two previous contract studies (Refs 1 and 2) were evaluated. It was found from the evaluation of NAS 8-18037 contract results that minimum scatter for compressive load capability was achieved with winding patterns where the longo rovings were sandwiched between inner and outer circ (i.e., circumferential) wraps. It was also found for these winding patterns that stress values at failure varied only slightly with resin content where the latter was kept within the approximate range of 18 to 23 percent by weight (31.3 to 38 percent by volume) (Ref 1, Figs. 6-77 and 6-83). The optimum resin content was found to be approximately 20.8 percent by weight (35 percent by volume). This value was selected as the nominal target for all designs which were investigated during this contract program.

It was found during fabrication of prototype strut hardware, which was later thermally tested in the NAS 3-7979 contract study, that the minimum practical diameter for integrally-wound struts is approximately 1.5 in. (3.8 cm). This limitation results from the thread size of suitable rod-end hardware and from the necessity to maintain the ratio of end fitting outside diameter to threaded section outside diameter sufficiently high so that the longo rovings will not slip off of the fitting shoulders during winding.

Based on these previous study results, and on preliminary design work conducted under this program, the following design guidelines were established for the Task 1 analysis:

---

* This was demonstrated later in Tasks 2 and 3 where it was shown that the thickness of a double longo wrap could be varied within the approximate range of 8 to 24 mils (0.20 to 0.61 mm) using 8-end roving yarn without introducing significant thickness irregularities or excessive voids

- Investigate both cylindrical and ogive* column shapes

- Consider only winding patterns which consist of inner and outer circ wraps with longo wraps sandwiched in between

- Assume a nominal thickness of 6 mil (0.15 mm) each for the inner and outer circ wraps, and vary the thickness of the longo wraps to achieve an optimum design (i.e., one where failures in column buckling and local crippling will occur at approximately the same compressive load)

- Assume a minimum practical strut diameter of 1.5 in. (3.8 cm)

- Consider both monocoque designs and those stiffened with longerons, rings, or a combination of these

- Evaluate chopped Dexiglas+, spaced aluminized Mylar discs (radiation shields), and gold coating of the internal surfaces of the strut in order to determine the relative effectiveness of these methods for reducing radiative heat transfer

- Evaluate the use of a rigid open-cell polyurethane foam core material as a combined structural stiffener (to resist local crippling of the tube wall) and as an internal radiation barrier

- Evaluate the use of laid-up boron fiber longos and longerons as a means of providing additional stiffness and strength to the basic fiberglass-epoxy structures

---

* a surface of revolution formed by rotating a circular arc of large radius about the longitudinal axis

\+ C. H. Dexter and Sons Paper Company

The ranges of design loads, strut lengths, and end temperatures which were considered in the parametric analysis were specified in the contract. These are summarized in Table 3-1. An ultimate factor of safety of 1.4, applied to the design limit loads in order to obtain ultimate loads, was also specified.

Table 3-1

SUMMARY OF DESIGN PARAMETERS

Design Parameter	Minimum	Maximum
Design Limit Load, lbf (N):		
• Compression	700 (3110)	6000 (26,700)
• Tension	1750 (7780)	15000 (66,700)
Design Ultimate Load, lbf (N):		
• Compression	980 (4360)	8400 (37,400)
• Tension	2450 (10,900)	21000 (93,400)
Strut Length, in. (cm)	18.0 (45.7)	40.0 (101.6)
End Temperature, °R (°K)		
• Warm End	400 (222)	520 (289)
• Cold End	37 (21)	140 (78)

A total of 16 different basic strut configurations were selected for the parametric analysis. Characteristics of these configurations are summarized in Table 3-2. They reflect the design guidelines discussed earlier and span the ranges of loads and lengths specified in Table 3-1. As shown, longo wrap thicknesses were varied from 12 to 24 mil (0.30 to 0.61 mm), strut lengths

Table 3-2

SUMMARY OF PARAMETRIC ANALYSIS CASES

Analysis Case No.	Strut Wall Configuration[1]	Stiffener Configuration	Longo Wrap Thickness, mil (mm)	Strut Length, in. (cm)	Outside Diameter, in. (cm)
1	Monocoque Fiberglass Cylinders[2]	N.A.	12 (0.30)	18 to 40 (45.7 to 101.6)	1.5, 1.75, 2.0, 2.25, 2.5, 2.75, 3.0, 3.25 (3.81, 4.45, 5.08, 5.72, 6.35, 6.99, 7.62, 8.26)
2	↓	↓	18 (0.46)	18 to 40 (45.7 to 101.6)	1.5, 1.75, 2.0, 2.25, 2.5, 2.75 (3.81, 4.45, 5.08, 5.72, 6.35, 6.99)
3	↓	↓	24 (0.61)	18 to 40 (45.7 to 101.6)	1.5, 1.75, 2.0, 2.25, 2.5, 2.75 (3.81, 4.45, 5.08, 5.72, 6.35, 6.99)
4	Monocoque Fiberglass Ogives[2]	N.A.	12 (0.30)	18 to 40 (45.7 to 101.6)	1.5, 1.75, 2.0, 2.25, 2.5, 2.75, 3.0, 3.25, 3.5 (3.81, 4.45, 5.08, 5.72, 6.35, 6.99, 7.62, 8.26, 8.89)
5	↓	↓	18 (0.46)	18 to 40 (45.7 to 101.6)	1.5, 1.75, 2.0, 2.25, 2.5, 2.75, 3.0 (3.81, 4.45, 5.08, 5.72, 6.35, 6.99, 7.62)
6	↓	↓	24 (0.61)	18 to 40 (45.7 to 101.6)	1.5, 1.75, 2.0, 2.25, 2.5, 2.75 (3.81, 4.45, 5.08, 5.72, 6.35, 6.99)
7	Monocoque Fiberglass-Boron Cylinders[3]	N.A. ↓	17[3] (0.43)	18 to 40 (45.7 to 101.6)	1.5, 1.75, 2.0, 2.25 (3.81, 4.45, 5.08, 5.72)
8	Stiffened Fiberglass Cylinders	Semi-Circular Fiberglass Longerons[4]	12 (0.30)	18, 29 (45.7, 73.7)	1.5, 1.75, 2.0, 2.25, 2.5 (3.81, 4.45, 5.08, 5.72, 6.35)
9	↓	↓	12 (0.30)	40 (101.6)	1.5, 2.0, 2.5, 3.0, 3.5 (3.81, 5.08, 6.35, 7.62, 8.89)
10	↓	↓	18 (0.46)	40 (101.6)	1.5, 2.0, 2.5, 3.0 (3.81, 5.08, 6.35, 7.62)
11	↓	Flat Boron Tape Longerons[5]	12 (0.30)	40 (101.6)	2.0, 2.25, 2.5, 2.75, 3.0 (5.08, 5.72, 6.35, 6.99, 7.62)
12	↓	↓	12 (0.30)	18 (45.7)	1.5 (3.81)
13	↓	↓	12 (0.30)	29 (73.7)	1.94 (4.93)
14	↓	↓	12 (0.30)	40 (101.6)	2.40 (6.10)
15	Stiffened Fiberglass Ogives	Flat Boron Tape Longerons[5]	12 (0.30)	29 (73.7)	1.96 (4.98)
16	↓	↓	12 (0.30)	40 (101.6)	2.46 (6.25)

NOTES:

(1) Basic wall construction for all designs consists of integrally-wound longo wraps sandwiched between 6-mil- (0.15-mm-) thick inner and outer circ wraps.
(2) Analysis performed for both non-structural radiation barriers and polyurethane foam core material.
(3) Longo layer consists of 5 mil (0.13 mm) of boron fiber composite laid up over 12 mil (0.30 mm) of integrally-wound fiberglass rovings.
(4) Each longeron consists of half-round cross-section 0.080 in. (0.203 cm) in diameter and 0.0025 in.^{2} (0.016 cm^2) in area.
(5) Each longeron consists of a rectangular cross-section 0.32 in. (0.82 cm) wide, 5 mil (0.13 mm) thick, and 0.0016 in.^{2} (0.0103 cm^2) in area.

were varied from 18 to 40 in. (45.7 to 101.6 cm), and strut diameters were varied from 1.5 to 3.5 in. (3.81 to 8.89 cm).

3.1.2 Monocoque Fiberglass Cylinders

Initially in the analysis, monocoque fiberglass cylinders were investigated since this configuration is the simplest of those selected in terms of both the analysis and fabrication requirements. The struts previously investigated in the NAS 8-18037 and NAS 3-7979 contract studies were of this general type.

For this configuration, ultimate compressive load capabilities for general instability failures were predicted by hand analysis using the classic Euler column buckling equation given by

$$P_c = \pi^2 E_c A_c \Big/ (L'/\rho_c)^2 \qquad (3\text{-}1)$$

Values of E_c, A_c, and ρ_c which correspond to the total composite cross-section (i.e., longo wraps plus circ wraps) were used. The effective column length, L', was taken as the actual strut length from center to center of the rod-end pins, since only pin-ended columns were considered.

Prior to beginning the analysis, it was recognized that, for composite struts, compressive load capabilities for local instability (crippling) failures are more difficult to predict (i.e., the scatter of predicted and actual values is greater) than for general instability failures, since they are dependent upon axial, circumferential, and shear stiffness properties. Consequently, they are much more sensitive to fabrication imperfections and dimensional tolerances than are the column buckling capabilities. In the analysis, crippling load capabilities were predicted in two different ways and the results were compared.

Initially, the classic isotropic crippling equation for thin-wall tubes was

used. This is given by

$$P_{CRP} = KE_c A_c (t_c/R_c) \qquad (3\text{-}2)$$

where the tube radius, R_c, was evaluated at the center of the total composite cross-section thickness, t_c. Values of the isotropic crippling coefficient, K, were taken from the previous experimental work (Ref 1, Fig. 6-78).

However, past experience with large filament-wound composite structures (i.e., rocket motor cases) has shown that a better correlation can be obtained between predicted and actual crippling load values for structures of this type using orthotropic properties and a more general solution of the form

$$P_{CRP} = f\left[E, I, G, J, \mu, A, L, t_c/R_c\right] \qquad (3\text{-}3)$$

In this functional expression, the modulus, stiffness, and geometry variables indicated are selected to precisely define both the longitudinal and transverse characteristics of the stiffeners and the structural core material (where applicable) as well as those of the basic orthotropic shell. Because of the complex interaction of these variables, a computer solution is required. In the Task 1 analysis, the final predictions of crippling capability shown on each design curve were obtained using a solution of this form and the BARSIN computer program which is described briefly in Appendix A.

Test results from the NAS 8-18037 contract program (Ref 1, Table 6-10) were compared with analytical predictions of crippling capabilities obtained using the BARSIN computer program. No "knockdown factor" to account for fabrication imperfections was used initially in this analysis. It was found that the analytical results were consistently double the test results for the configurations of interest (i.e., configurations 4, 5, and 6 from Ref 1, Fig. 6-70). Since no other test data were available at that time, it was assumed that the reduced experimental failure loads resulted from

inherent fabrication imperfections and tolerances. Consequently, in the subsequent parametric analysis of Task 1, a knockdown factor of 0.5 was used.

Later, when results of the Task 2 short-column tests from this program were compared with the predicted values, it was found that the original predictions (which did not include the knockdown factor) correlated very well with the test values. It was concluded that the knockdown factor was not required.

It was also found in the Task 2 work that the experimental failure load obtained for a particular specimen, for which bending was measured and controlled about only one transverse axis, was approximately half that for a similar specimen of the same design for which bending was measured and controlled about both transverse axes. It was concluded that bending effects can be extremely significant for this type of structure, and that measurement and control about both axes was mandatory for all subsequent specimen tests (see discussion in Section 4.2.1).
Since the NAS 8-18037 contract tests were performed in a standard test machine (Ref 1, Fig. 6-71) without measurement or control of inherent bending effects, it can only be assumed that such effects may have decreased the true crippling capability. No other explanation can be found for the apparent discrepancy between the test results obtained in the two programs.

During the Task 1 parametric analysis, no attempt was made to predict compressive load capabilities for bond shear (local crushing) failures. Later, this mode of failure was encountered during Task 2 testing, and the analysis was expanded to include prediction techniques and results (see Section 4.2.1).

In the analysis, composite elastic modulus values were computed using known values of the elastic modulii for glass fibers and epoxy resin and the "law of mixtures" given by

$$E_c = \frac{A_{\ell g} E_g + A_r E_r}{A_c} \qquad (3\text{-}4)$$

It was shown in the NAS 8-18037 contract work (Ref 1, page 140) that elastic modulus values computed in this manner correlated well with those obtained experimentally. Using this equation, the circ wraps are treated as though they are composed entirely of resin, since the glass fibers are not continuous in the longitudinal direction. Values of E_g and E_r from the literature (Ref 1, page 145) are 12.5×10^6 and 5.28×10^5 psi (8.62×10^{10} and 3.64×10^9 N/m^2), respectively. Substituting these values into equation (3-4), longitudinal modulus values computed for the total composite cross-section were 4.42×10^6, 5.20×10^6, and 5.72×10^6 psi (3.05×10^{10}, 3.59×10^{10}, and 3.94×10^{10} N/m^2), respectively, for monocoque cylindrical struts composed of 12-, 18-, and 24- mil (0.30-, 0.46-, and 0.61- mm) longo wraps sandwiched between 6-mil (0.15- mm) inner and outer circ wraps.

Composite cross-section area, A_c, and radius of gyration, ρ_c, values are presented in Figs. 3-2 and 3-3, respectively, as a function of composite thickness, t_c, and outside diameter, D_o, for monocoque fiberglass cylinders. These data were taken from standard tube tables, and are included herein only for convenience in performing hand calculations.

Plots of predicted ultimate compressive load capability as a function of column length and strut diameter, which were developed during the parametric analysis, are presented in Figs. 3-4, 3-5, and 3-6, respectively, for monocoque fiberglass cylinders with longo wrap thicknesses of 12, 18 and 24 mil (0.30, 0.46, and 0.61 mm). In developing these plots, predicted ultimate compressive load capabilities for general instability failures were computed by hand using equation (3-1). The capabilities for local crippling failures, both for struts with foam-core radiation barriers and for those with nonstructural cores, were computed using the BARSIN computer program.

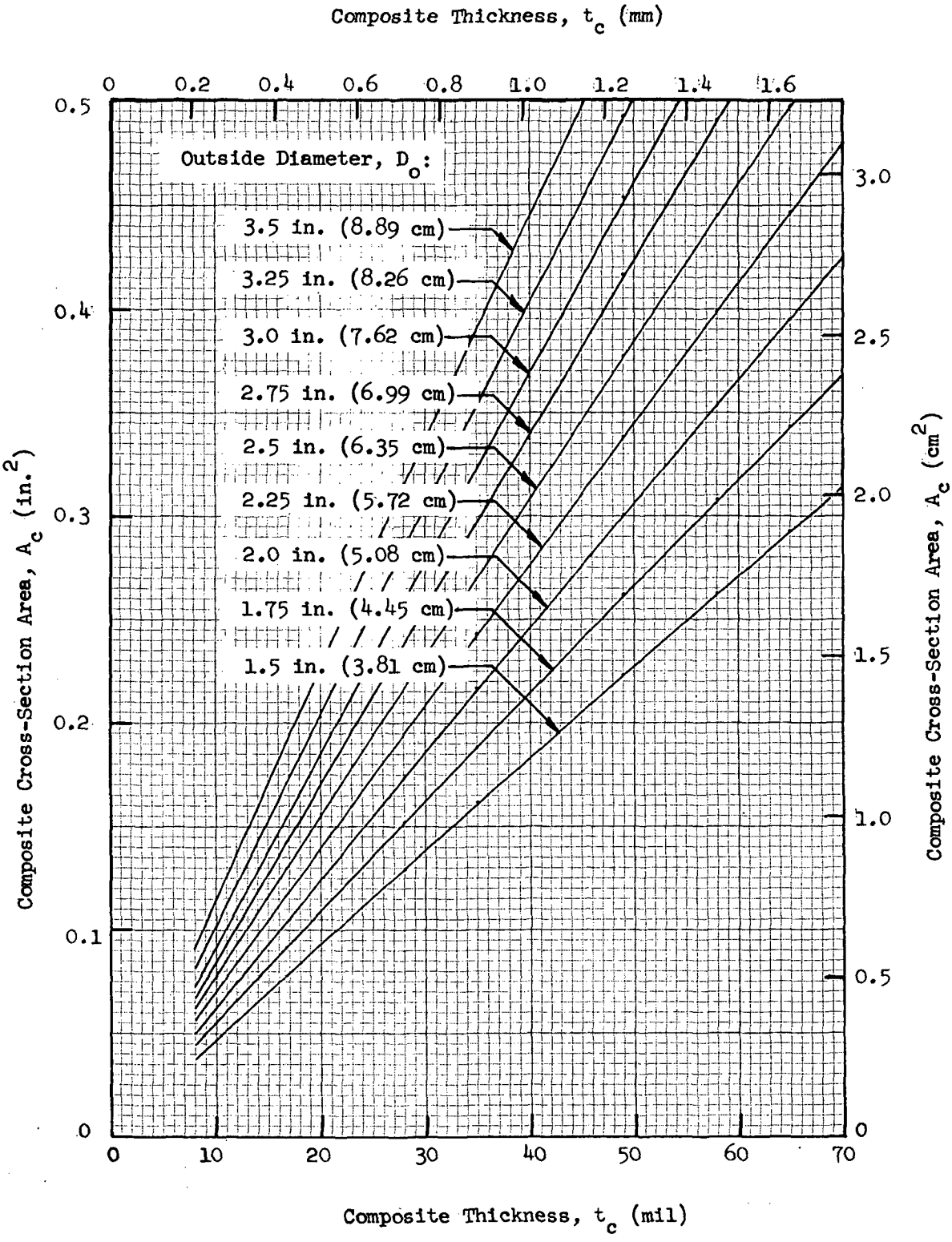

Fig. 3-2 Composite Cross-Section Area as a Function of Thickness and Outside Diameter

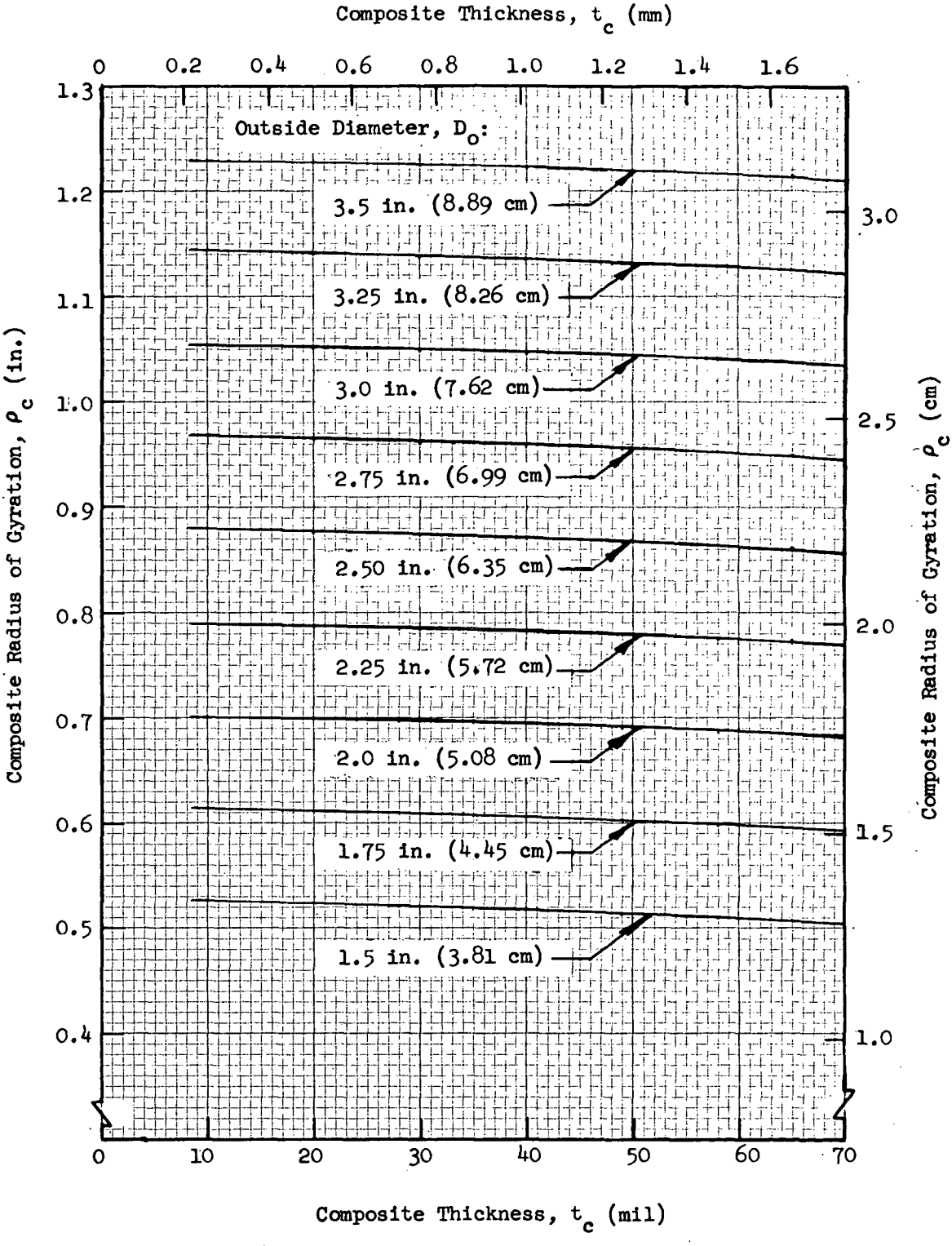

Fig. 3-3 Composite Radius of Gyration as a Function of Thickness and Outside Diameter

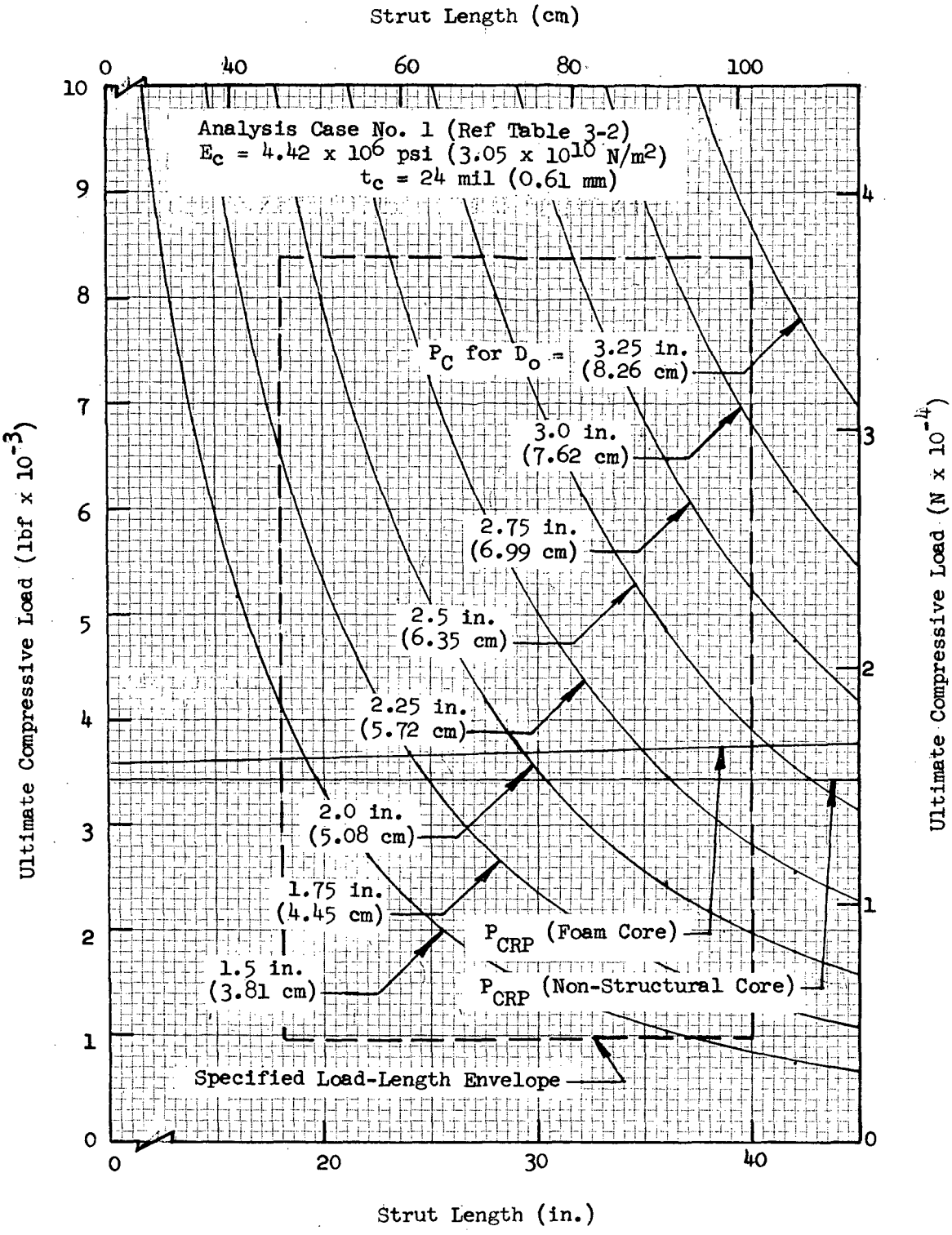

Fig. 3-4 Predicted Ultimate Compressive Loads for Monocoque Fiberglass Cylinders with a 12-mil (0.30-mm) Longo Wrap Thickness

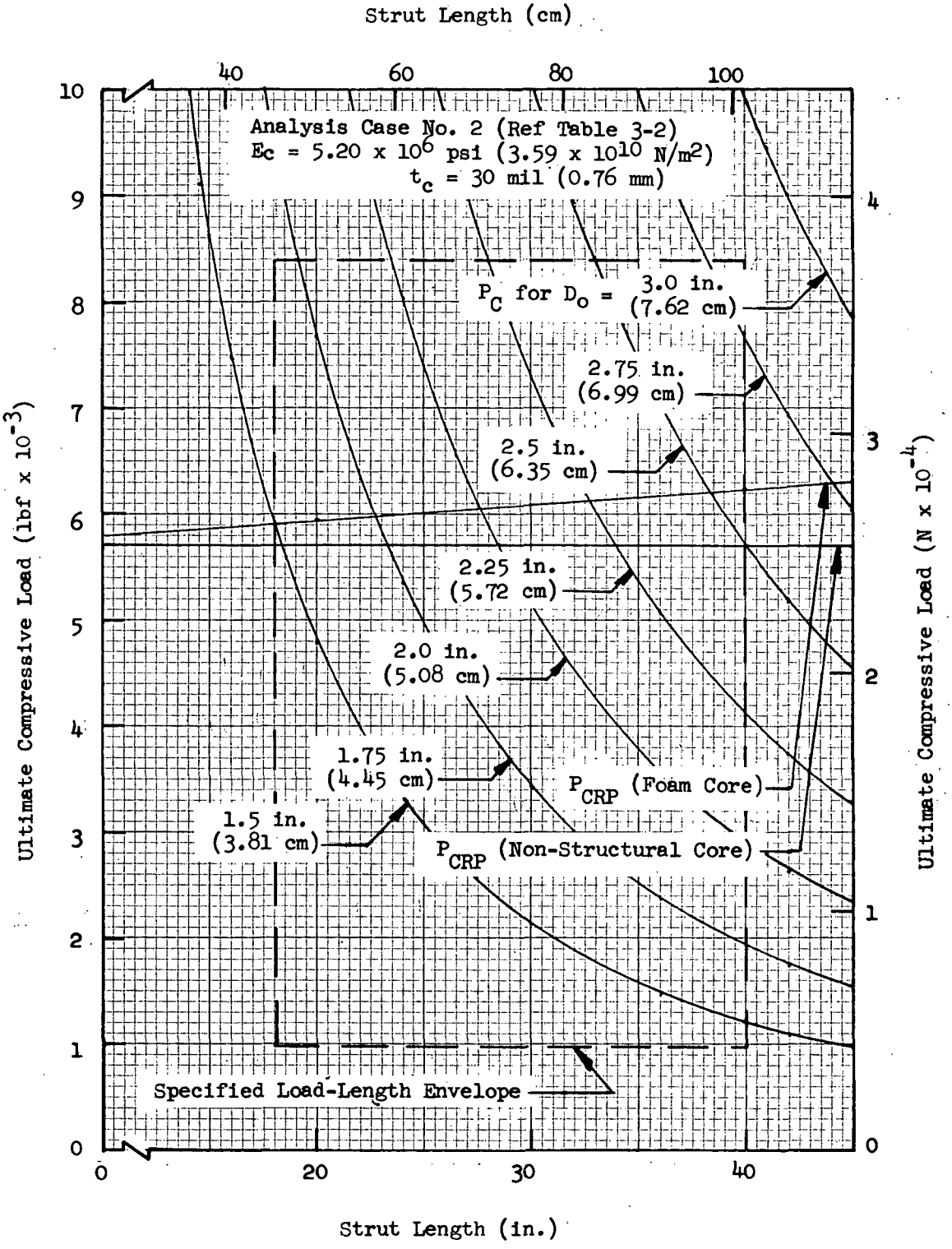

Fig. 3-5 Predicted Ultimate Compressive Loads for Monocoque Fiberglass Cylinders With an 18-mil (0.46-mm) Longo Wrap Thickness

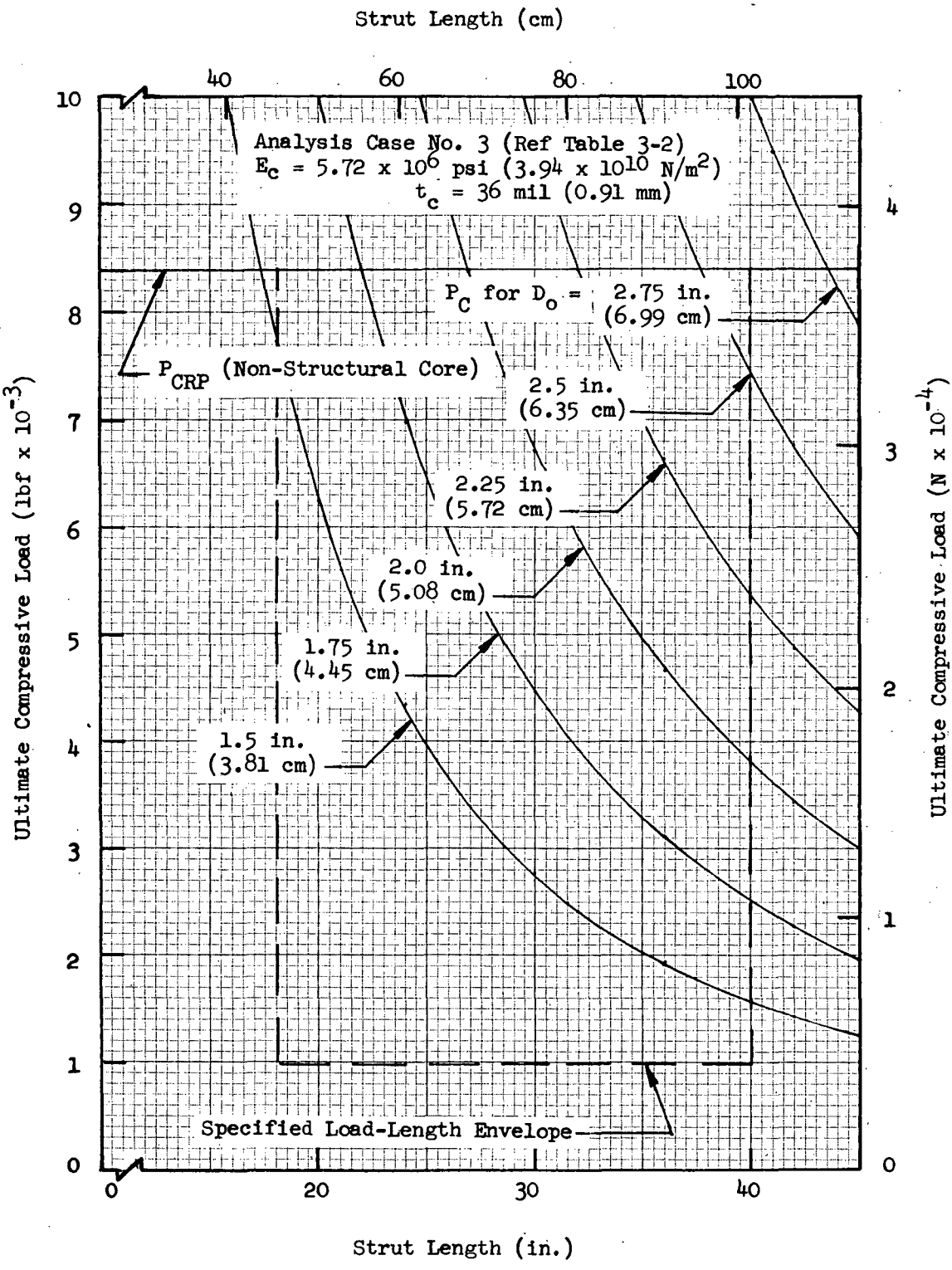

Fig. 3-6 Predicted Ultimate Compressive Loads for Monocoque Fiberglass Cylinders with a 24-mil (0.61-mm) Longo Wrap Thickness

Structural properties of the rigid, open-cell polyurethane foam assumed in the analysis were obtained from a previous study of foam insulations (Ref 3, pages 39 and 40). The elastic modulus value used was 1050 psi (7.24×10^6 N/m^2), and a value of 0.3 was used for Poisson's ratio.

As shown in Figs. 3-4 and 3-5 for monocoque cylinders with 12- and 18-mil (0.30- and 0.46-mm) longo wrap thicknesses, respectively, the foam core material provides additional crippling load capability, but does not appreciably increase the general column buckling capability. For example, for a 2.5-in.-(6.35-cm-) diameter strut with a 12-mil (0.30-mm) longo wrap thickness, the addition of a foam core results in an increase in ultimate crippling load capability from 3460 lbf (15,390 N) to 3780 lbf (16,810 N), or approximately 9 percent. However, for this example case, the general column buckling capability (proportional to the EI product) increases only approximately 0.3 percent. Consequently, the effect of the foam core on column buckling capability was neglected in the data presented. Note that the increase of crippling strength for struts with foam cores is slightly dependent on diameter, whereas that for struts with non-structural cores is not. The crippling load capability of foam-core struts with a 24-mil (0.61-mm) longo wrap thickness (Fig. 3-6) is not shown since it is greater than the maximum load value requirement specified in Table 3-1.

The relationship of strut outside diameter with length required for optimum monocoque fiberglass cylinders (i.e., those with equal column buckling and local crippling capabilities) was determined by cross-plotting the data given in Figs. 3-4, 3-5, and 3-6. Results are presented in Fig. 3-7 for longo wrap thicknesses of 12, 18, and 24 mil (0.30, 0.46, and 0.61 mm).

Predicted ultimate compressive loads as a function of strut outside diameter can also be determined by cross-plotting the data given in Figs. 3-4, 3-5, and 3-6 for struts of any particular length. Fig. 3-8 shows a plot of this type for struts 40 in. (101.6 cm) long.

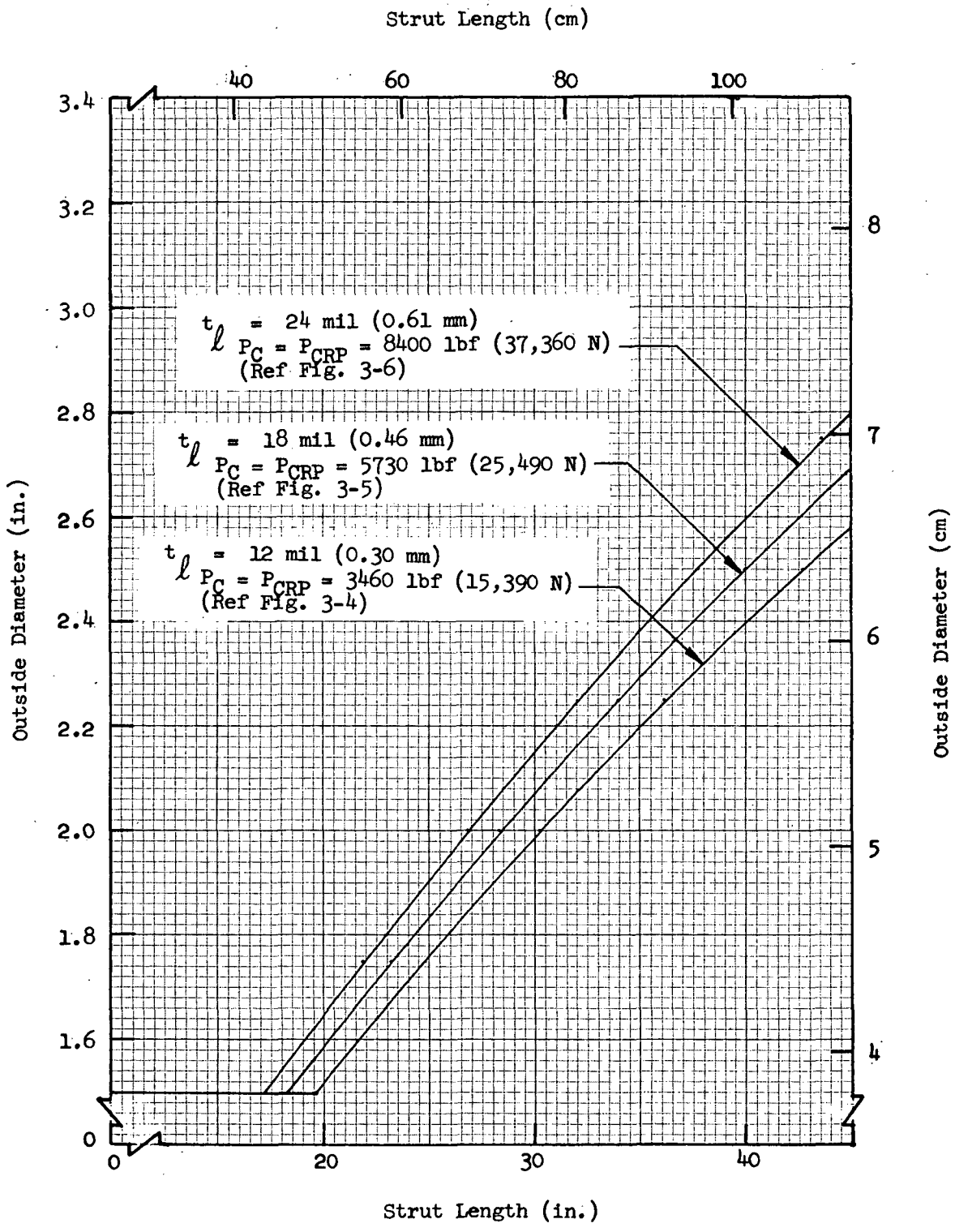

Fig. 3-7 Outside Diameter as a Function of Strut Length for Optimum Monocoque Fiberglass Cylinders

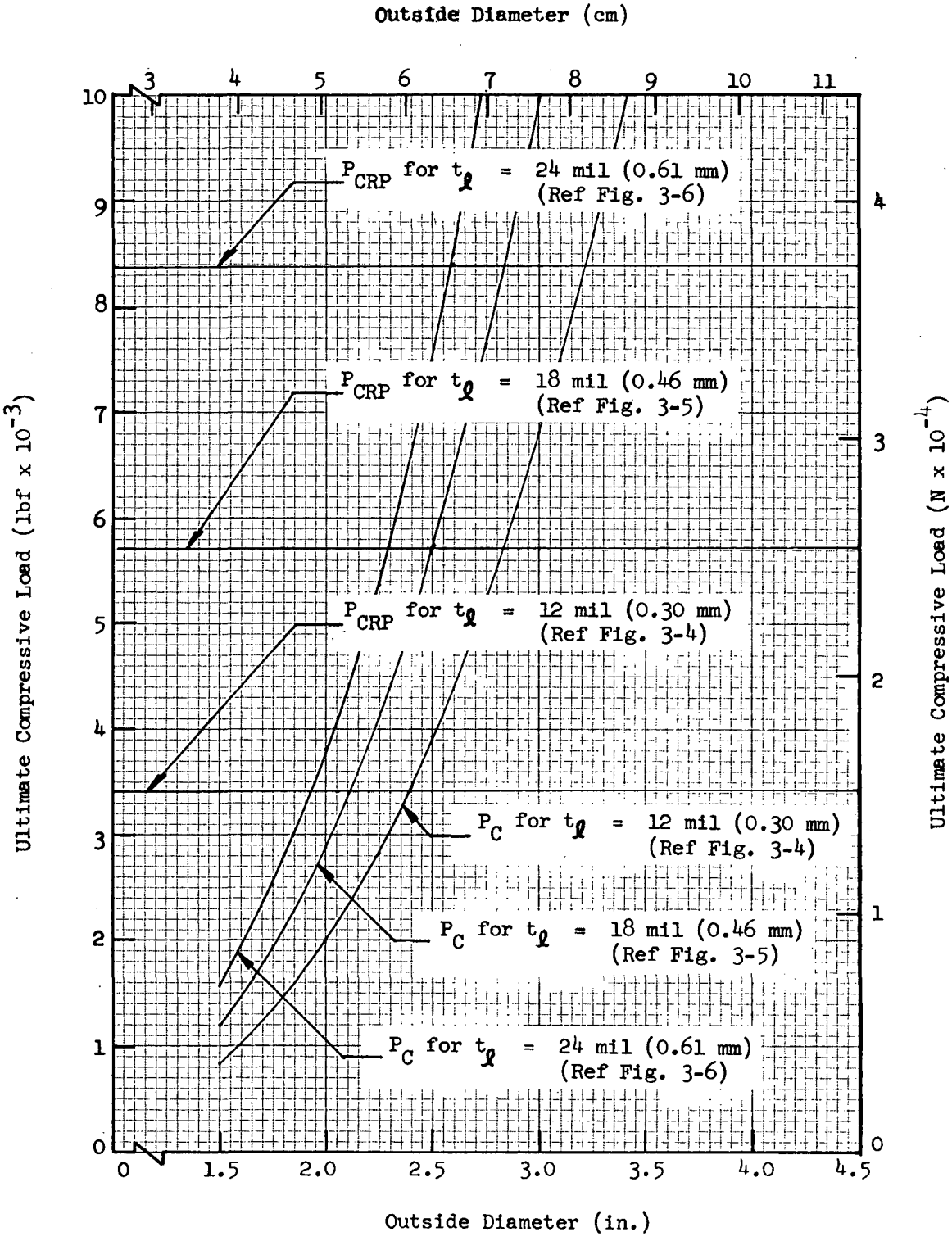

Fig. 3-8 Predicted Ultimate Compressive Loads as a Function of Outside Diameter for 40-in.-(101.6-cm-) Long Monocoque Fiberglass Cylinders

3.1.3 Monocoque Fiberglass Ogives

The shape of the exterior wall of this strut configuration is a surface of revolution formed by rotating a circular arc of large radius about the longitudinal axis. Since the resulting cross-section geometry, ratio of longo glass to circ glass, and elastic modulus values all vary along the length, it is somewhat more complex to analyze than the monocoque cylinder. However, in terms of fabrication requirements, it is quite similar to the monocoque cylinder. The primary advantage of the ogive shape is that the maximum cross-section radius of gyration is at the midspan where it provides maximum column buckling capability with minimum diameter (and weight) end fittings. A secondary advantage is that during winding of the longos, a component of the tension maintained in the roving is directed inward toward the center of the mandrel arc. This inward component of force aids in achieving a compact composite cross-section with minimum voids.

Since the number of longo rovings (and, therefore, total longo composite area) is constant over the length of an ogive strut, the thickness of the longo wrap varies inversely with cross-section radius, R_c. The thickness of the circ wrap, on the other hand, remains constant over the length, thus providing a total circ composite area directly proportional to the cross-section radius. As a consequence, the ratio of longo-to-circ glass area, $A_{\ell g}/A_{cg}$, and the elastic modulus of the composite cross-section, E_c, vary over the length of the strut. In addition, since the cross-section radius, R_c, varies along the length, values of total composite thickness, t_c, total composite cross-section area, A_c, and cross-section radius of gyration, ρ_c, also vary with longitudinal position along the strut.

Compressive load capabilities for monocoque fiberglass ogives can be predicted using the same general analytical approach described earlier for cylinders. However, since the cross-section properties vary along the length, a computer solution was used in the parametric analysis to determine values of predicted ultimate column buckling capability. The COLUMN computer program (Ref Appendix A) was used for this purpose.

Local crippling failures will always occur at midspan for the monocoque ogive configuration, since this is where the critical crippling parameter, t_c/R_c, is always minimum. In the initial analysis, an allowable orthotropic crippling load value was computed using equation (3-3) for an equivalent cylindrical strut where the value of t_c/R_c was taken as that at midspan for the ogive strut. This provided an approximate solution only, since it neglects the additional capability afforded by the double curvature of the ogive wall. Later, an exact crippling analysis was performed for a few selected cases using the BOSOR 2 computer program (Ref Appendix A). However, it was found that the additional crippling capability due to the double curvature for monocoque ogive struts is negligible.

Bond shear (local crushing) compressive load capabilities for monoque fiberglass ogives were not computed in the Task 1 parametric analysis. As in the case of monocoque cylinders, however, this capability was investigated later (Ref Section 3.2.3).

Predicted ultimate compressive load capabilities for column buckling and local crippling failures, as a function of column length and midspan diameter, are presented in Figs. 3-9, 3-10, and 3-11, respectively, for monocoque fiberglass ogives with longo wrap thicknesses at midspan of 12, 18, and 24 mil (0.30, 0.46, and 0.61 mm). As shown, crippling values were computed for ogive struts with rigid, open-cell polyurethane foam cores as well as for those with non-structural radiation barriers. However, the crippling capability of foam-core ogives with 24-mil (0.61-mm) longo wrap thicknesses at midspan is not shown since it is greater than the maximum load requirement specified in Table 3-1. As in the case of monocoque fiberglass cylinders, the foam core material provides a modest increase in crippling capability, which varies slightly with diameter, but adds negligibly to the column buckling capability.

A cross-plot of strut outside diameter at midspan as a function of length is presented in Fig. 3-12 for optimum monocoque fiberglass ogives with longo

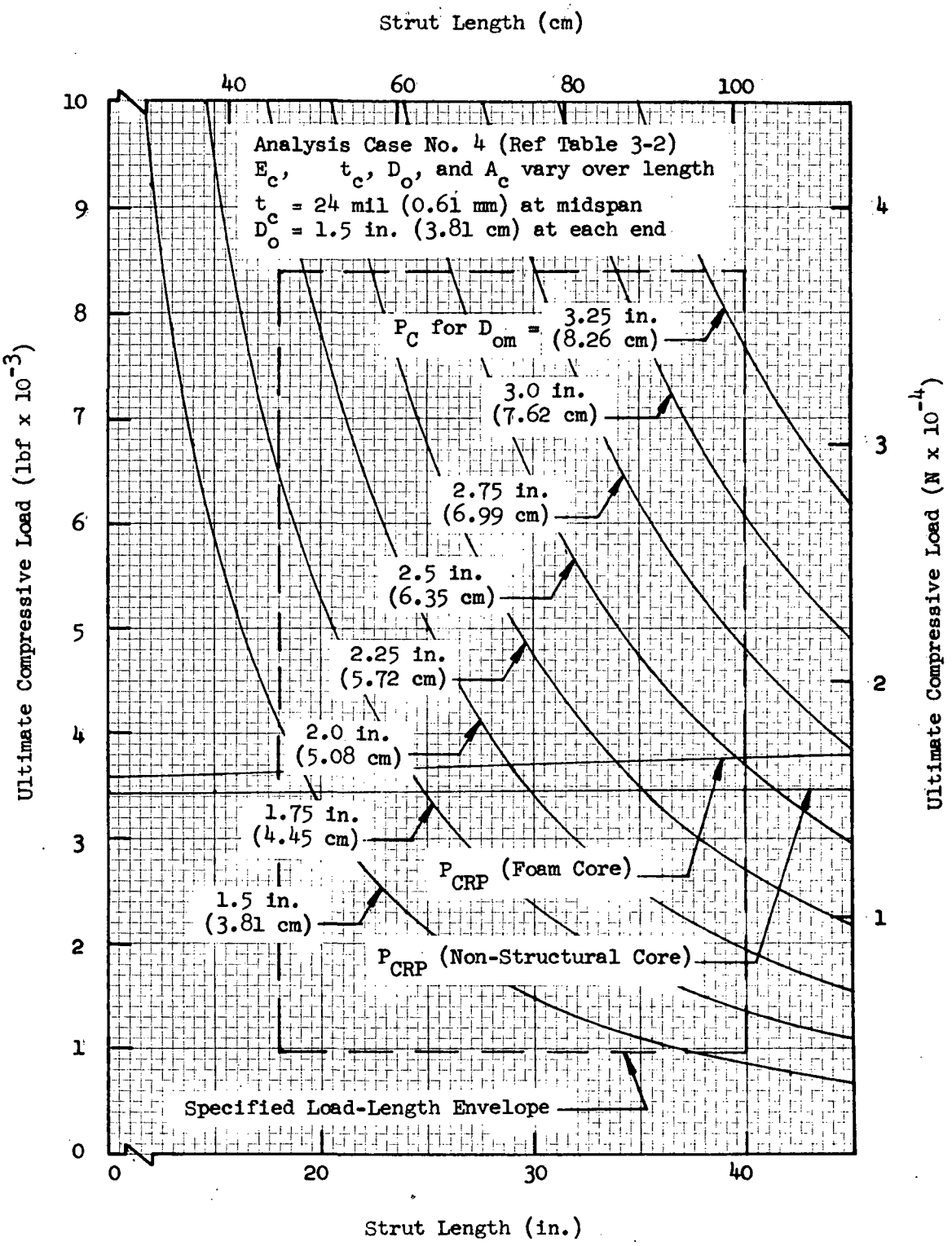

Fig. 3-9 Predicted Ultimate Compressive Loads for Monocoque Fiberglass Ogives with a 12-mil (0.30-mm) Longo Wrap Thickness at Midspan

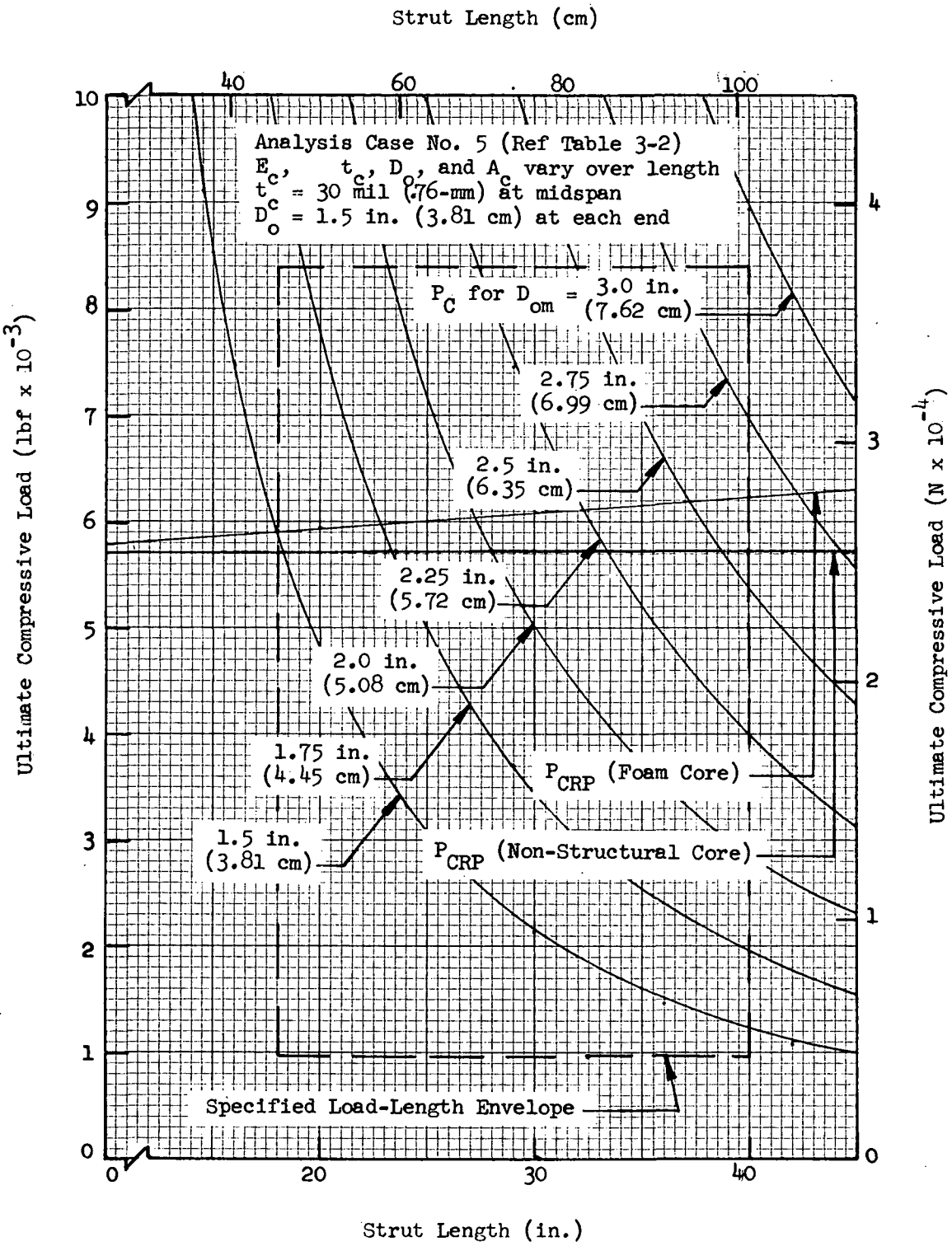

Fig. 3-10 Predicted Ultimate Compressive Loads for Monocoque Fiberglass Ogives with an 18-mil (0.46-mm) Longo Wrap Thickness at Midspan

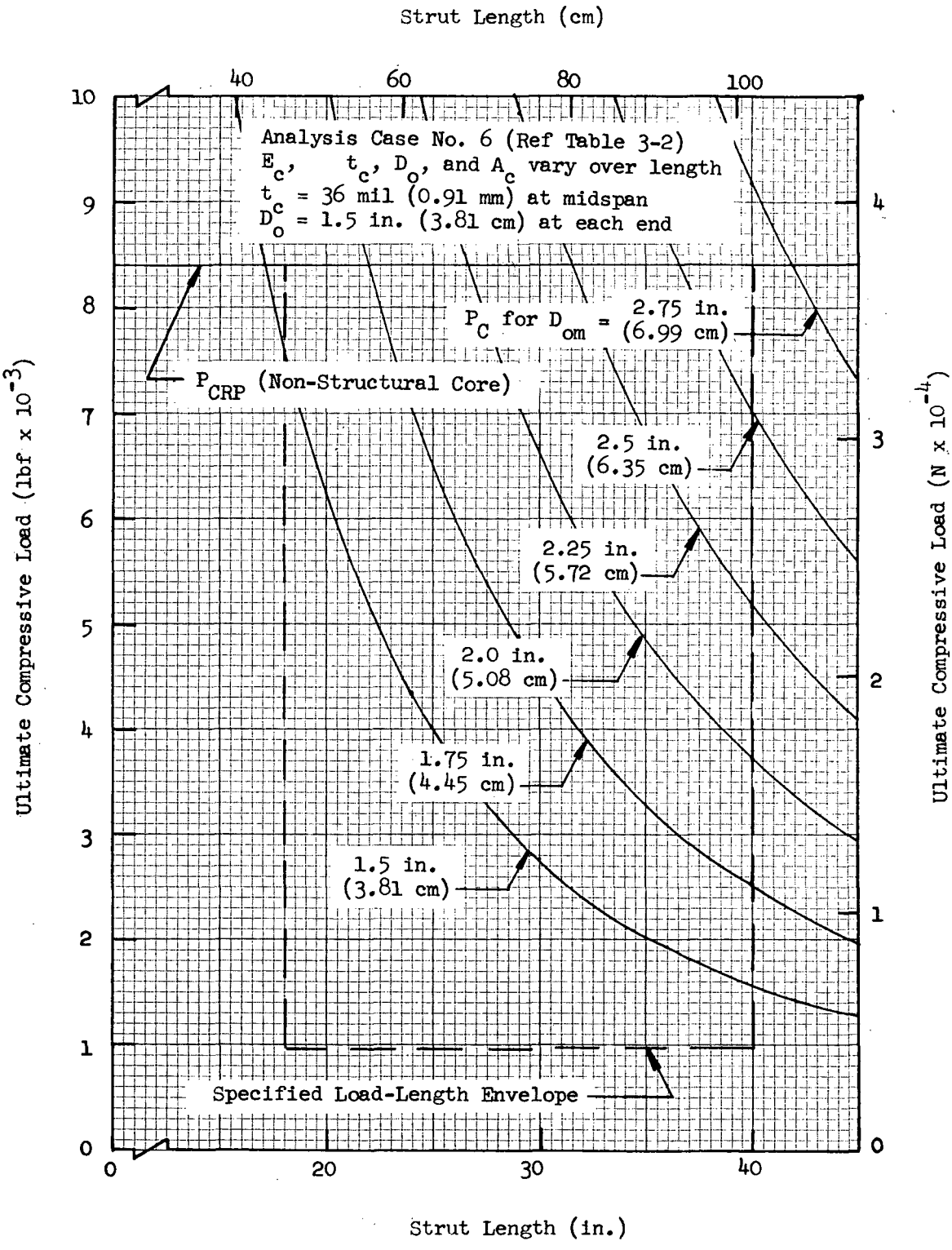

Fig. 3-11 Predicted Ultimate Compressive Loads for Monocoque Fiberglass Ogives with a 24-mil (0.61-mm) Longo Wrap Thickness at Midspan

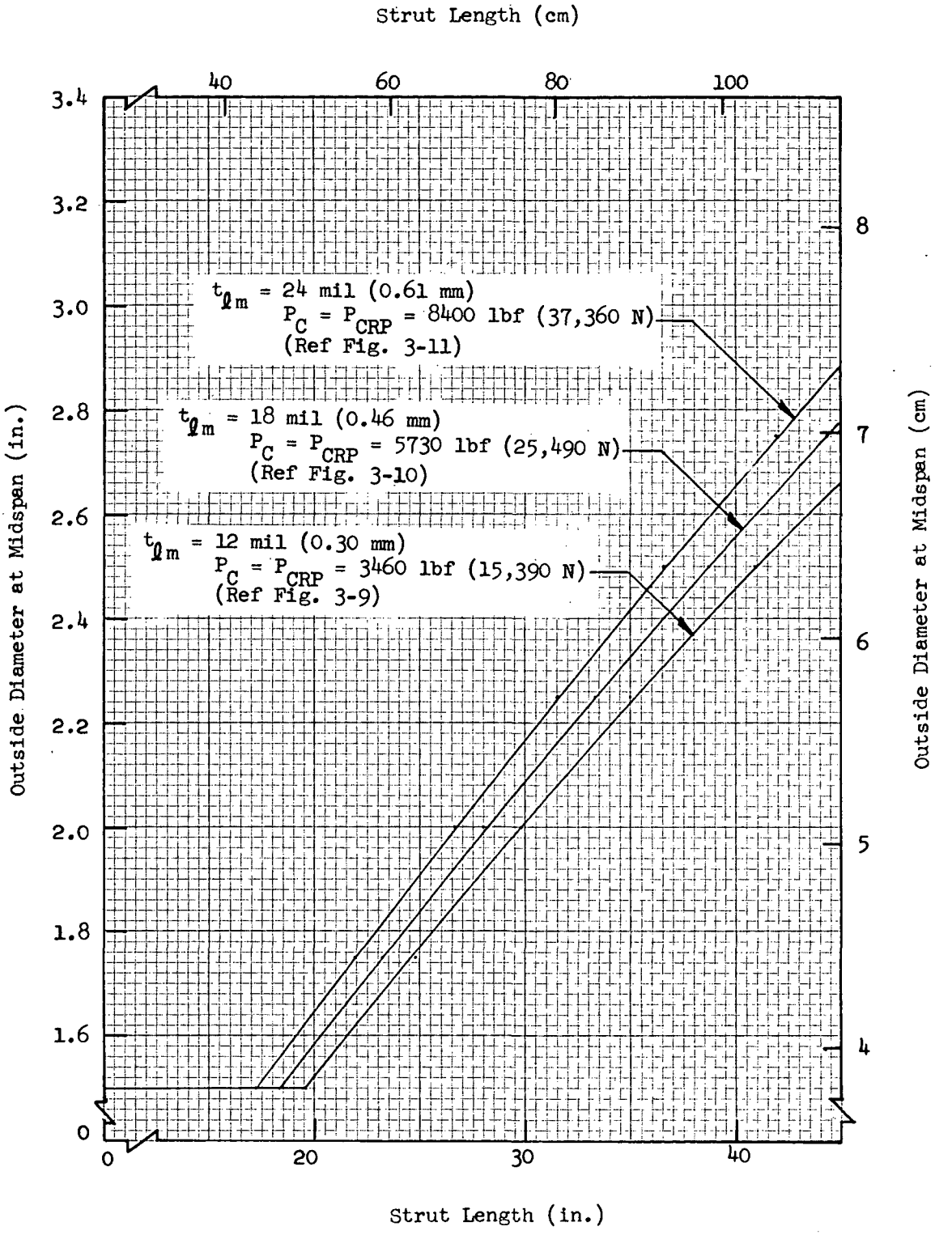

Fig. 3-12 Outside Diameter at Midspan as a Function of Strut Length for Optimum Monocoque Fiberglass Ogives

wrap thicknesses at midspan of 12, 18, and 24 mil (0.30, 0.46, and 0.61 mm). An additional cross-plot showing predicted ultimate compressive loads as a function of strut outside diameter at midspan is given in Fig. 3-13 for 40-in.-(101.6-cm-) long ogive struts.

It can be seen by comparison of the data presented in Figs. 3-8 and 3-13 that the midspan diameter of an ogive strut must be somewhat greater than that of a cylindrical strut of equal length and composite thickness at midspan in order to achieve equal column buckling capability. For example, a monocoque ogive strut 2.56 in. (6.50 cm) in diameter and 40 in. (101.6 cm) long with a 24-mil (0.61-mm) longo wrap thickness has the same column buckling capability, 7490 lbf (33,320 N), as a 2.5-in.-(6.35-cm-) diameter monocoque cylindrical strut of the same length and longo wrap thickness. The total composite weight of the longo and circ wraps for the ogive strut is approximately 96 percent of that for the cylindrical strut in this example. However, an additional (and more significant) weight savings would also be realized since the outside diameter of the end fittings for the ogive could be as low as 1.5 in. (3.81 cm) compared to 2.5 in. (6.35 cm) for the cylinder. For struts of shorter length and/or smaller diameter, the differences in midspan diameter and in weight are less for ogives and cylinders of equal column buckling capability.

3.1.4 Monocoque Fiberglass-Boron Cylinders

A variation of the monocoque fiberglass cylinder configuration, also investigated during the Task 1 parametric study, utilizes a constant-thickness layer of boron fiber longos sandwiched between the integrally-wrapped fiberglass longos and the outer fiberglass circ wrap. Since the boron fibers are too brittle to be wrapped continuously around the end fittings, they are laid up within an epoxy resin matrix and depend on lap shear load transfer through the resin bond in order to distribute axial loads. The potential advantage of this configuration lies in the increased composite stiffness provided by the high-modulus boron fibers. However, these fibers also

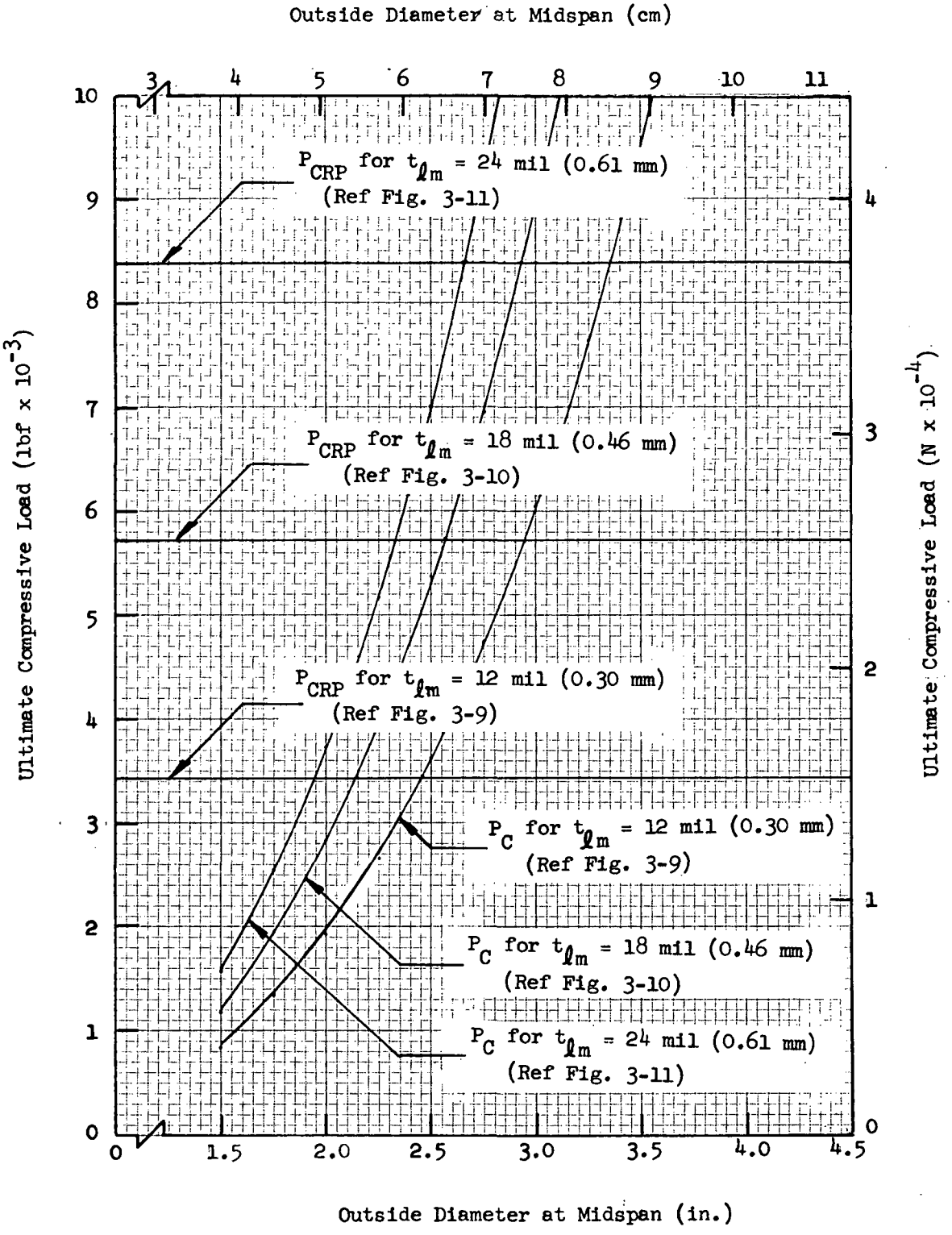

Fig. 3-13 Predicted Ultimate Compressive Loads as a Function of Outside Diameter at Midspan for 40-in.-(101.6-cm-) Long Monocoque Fiberglass Ogives

introduce significantly greater thermal conductivity in the longitudinal direction. This increase in axial heat transfer must be traded off against the improved structural capability.

In the structural analysis, an equivalent all-fiberglass composite cross-section was determined based on the ratio of the elastic modulii. An elastic modulus value of 58×10^6 psi (4.0×10^{11} N/m^2) for the boron fibers (Ref 4, Section 2.2, page 1) and a resin content of 50 percent by volume for this longo layer were used, together with the values presented previously for the glass fibers and the epoxy resin. Predicted ultimate compressive load capabilities for the resultant equivalent all-fiberglass cross-section were then computed in the same manner as that described in Section 3.1.2. The results are presented in Fig. 3-14 for composite struts with a 12-mil (0.30-mm) fiberglass longo wrap thickness combined with a 5-mil (0.13-mm) boron layer thickness. The local crippling load capability is not shown in the figure since it exceeds the maximum load requirement specified in Table 3-1.

It can be seen by comparison of Fig. 3-14 with Fig. 3-5 that the substitution of a 5-mil (0.13-mm) thickness of boron fiber longos for a 6-mil (0.15-mm) thickness of fiberglass longos results in a significant increase in column buckling capability. For example, for a 40-in.-(101.6-cm-) long, 2.0-in.-(5.08-cm-) diameter monocoque fiberglass cylinder with an 18-mil (0.46-mm) longo wrap thickness, the ultimate column buckling capability is approximately 2900 lbf (12,900 N). For the same size strut with fiberglass-boron longos, the ultimate column buckling capability increases to approximately 4660 lbf (20,730 N), a gain of approximately 61 percent.

3.1.5 Stiffened Fiberglass Cylinders

The use of stiffeners to improve the structural efficiency of monocoque fiberglass cylinders was also investigated in the parametric analysis. Initially, the addition of circumferential ring stiffeners only was investigated since it was obvious that the ring material would not contribute

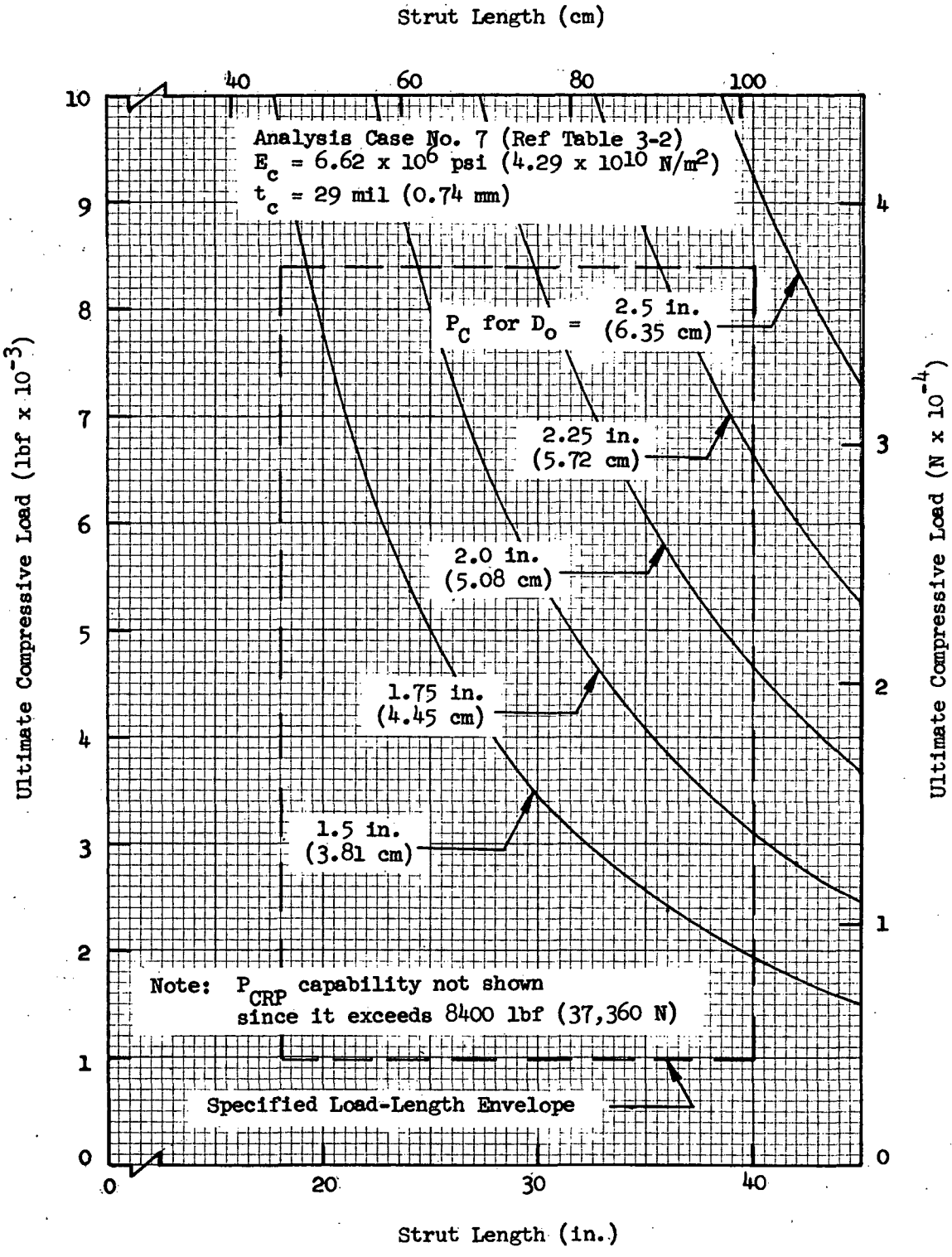

Fig. 3-14 Predicted Ultimate Compressive Loads for Monocoque Fiberglass-Boron Cylinders with a 17-mil (0.43-mm) Longo Wrap Thickness

significantly to the longitudinal heat leak. However, this stiffener arrangement was found to be impractical as the required ring spacing for the range of R_c/t_c values analyzed is on the order of 0.375 to 0.75 in. (0.953 to 1.91 cm) resulting in an excessive number of rings. Subsequently, configurations with longeron stiffeners and those with a combination of both rings and longerons were considered. The configuration finally selected for the parametric analysis consists of prefabricated longerons bonded to the exterior surface of integrally-wrapped cylinders. Both glass-fiber (laid up section) and boron-fiber (pretrimmed tape section) longerons were evaluated.

Ultimate compressive load capabilities for general instability (column buckling) failures of this configuration were predicted by hand analysis. The Euler column buckling criteria described earlier for monocoque cylinders (Equation 3-1) was used. Modulus of elasticity values were determined using the law of mixtures (Equation 3-4) where the longerons were treated in the same manner as were the longo wraps for the monocoque cylinders. In the case of the boron-fiber longerons, the analysis was based on an all-fiber-glass cross-section of equivalent elastic modulus **(i.e., increased area).**

As expected, prediction of ultimate compressive load capabilities for local instability (crippling) failures of longeron-stiffened tubular cylinders was found to be considerably more complex than for monocoque cylinders. In the analysis, it was desired to determine both the optimum stiffener spacing and the minimum stiffener area required to force crippling of the wall panels between stiffeners (i.e., to preclude stiffener crippling). Since there was no existing computer program that could be used to determine these values directly, a combination of computer and hand analysis was used.

When a thin-wall monocoque cylinder is loaded to failure in a crippling mode, the number of natural waves (local diamond buckles), n, which form around the circumference is that requiring minimum deformation energy and resulting in some minimum compressive allowable load. At selected cross-sections, each resulting wave has two points of inflection (sine wave form), and the

wave length, by definition, is equal to the circumference divided by n. If stiffeners of sufficient cross-sectional area are then added, with a uniform spacing less than one-half of this natural wave length, the actual number of waves (with a stiffener located at each point of inflection) can be forced to increase. Each of these shorter waves requires a higher deformation energy, resulting in an increase in the allowable load. The optimum number of waves is that which results in equal total compressive load capabilities, for the wall panels alone, in the general instability (column buckling) and local (crippling) failure modes.

In the parametric analysis, the BARSIN computer program was used to compute values of allowable panel crippling load as a function of the number of waves, n. These values were then plotted along with the hand-computed values of allowable column buckling loads for general instability of the wall panels alone and for the combination of wall panels and stiffeners together. In computing the latter values, the axial strain incurred in the stiffeners was assumed to equal that in the wall panels so that the total allowable column buckling load was directly proportional to the number of stiffeners.

Initially in the analysis of cylinders stiffened with glass-fiber longerons, a stiffener cross-section 0.100 in. (0.254 cm) square with an area of 0.010 $in.^2$ (0.0645 cm^2) was assumed. Later it was found that this could be reduced to a half-round section 0.080 in. (0.203 cm) in diameter with an area of 0.0025 $in.^2$ (0.0161 cm^2). The half-round cross-section was found to be sufficient to preclude crippling of the stiffeners, and this shape also provided a maximum bond area to reduce shear stress in the resin. For the boron-fiber longerons, a flat rectangular tape cross-section 0.32 in. (0.81 cm) wide by 5 mil (0.13 mm) thick with a cross-sectional area of 0.0016 $in.^2$ (0.0103 cm^2) was selected. In this case the flat shape was found to be necessary to reduce the bond area shear stress to an acceptable value.

Plots of predicted ultimate compressive loads as a function of the number of waves formed around the circumference during crippling of longeron-stiffened

fiberglass cylinders are presented in Appendix B. These data were computed for strut lengths of 18, 29, and 40 in. (45.7, 73.7, and 101.6 cm), for strut diameters ranging from 1.5 to 3.0 in. (3.81 to 7.62 cm), and for longo wrap thicknesses of 12 and 18 mil (0.30 and 0.46 mm). As shown, the data for 40-in.-(101.6-cm-) long struts include allowables for both glass-fiber and boron-fiber longerons, and for both 12- and 18-mil (0.30- and 0.46-mm) longo wrap thicknesses. The conditions required for optimally-stiffened designs (i.e., those where column buckling and local crippling capabilities of the panels are equal) are indicated in each figure.

Evaluation of the data presented in Appendix B for 40-in.-(101.6-cm-) long stiffened cylinders with 12- and 18-mil (0.30- and 0.46-mm) longo wrap thicknesses (Figs. B-10 through B-18) shows that, for any given compressive loading, the stiffened struts with 12-mil (0.30-mm) longo wrap thicknesses are always more efficient than those with 18-mil (0.46-mm) thicknesses. Consequently, only struts with 12-mil (0.30-mm) longo wrap thicknesses were investigated for the 18- and 29-in. (45.7- and 73.7-cm) lengths.

Summary plots of the data presented in Appendix B for fiberglass cylinders with 12-mil (0.30-mm) longo wrap thicknesses which are optimally-stiffened with glass-fiber longerons are presented in Figs. 3-15 and 3-16. These figures show predicted ultimate compressive loads and the optimum number of stiffeners, respectively, as a function of strut length and diameter. In Fig. 3-15, reference data are also shown for monocoque cylinders (these data were presented earlier in Fig. 3-4). It can be seen that, for compressive loads below approximately 3460 lbf (15,400 N), the monocoque designs are optimum. For loads above this value, the optimally-stiffened designs provide significantly higher capabilities and are much more efficient. For example, for a 2.5-in.-(6.35-cm-) diameter optimally-stiffened cylinder 35 in. (88.9 cm) long, 23 stiffeners are required and the predicted load capability is 8080 lbf (35,940 N) compared to 5120 lbf (22,770 N) for a monocoque design of the same diameter and length. This is a 58 percent increase in load capability, but requires only a 31 percent increase in total cross-sectional area.

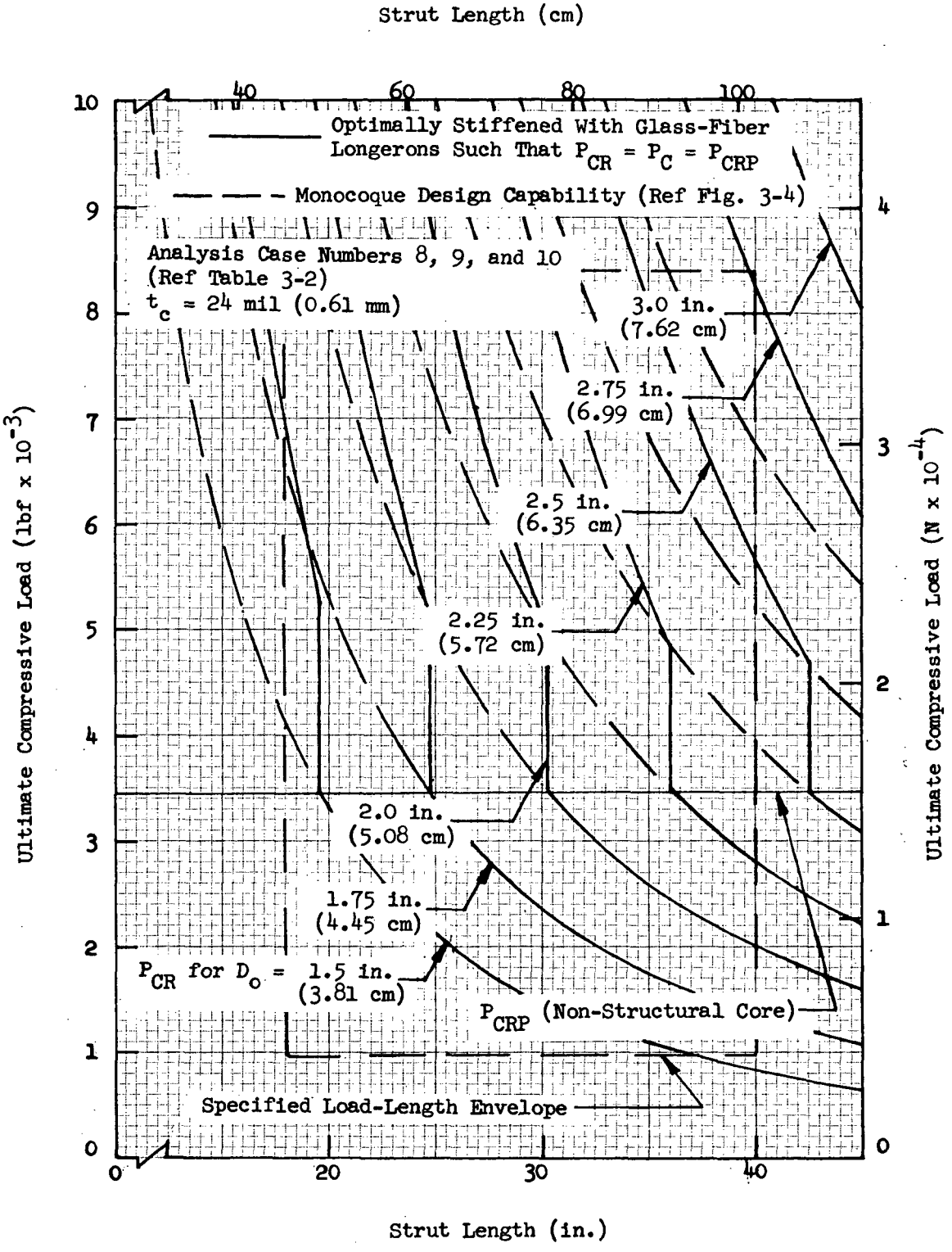

Fig. 3-15 Predicted Ultimate Compressive Loads for Optimally-Stiffened Fiberglass Cylinders with a 12-mil (0.30-mm) Longo Wrap Thickness

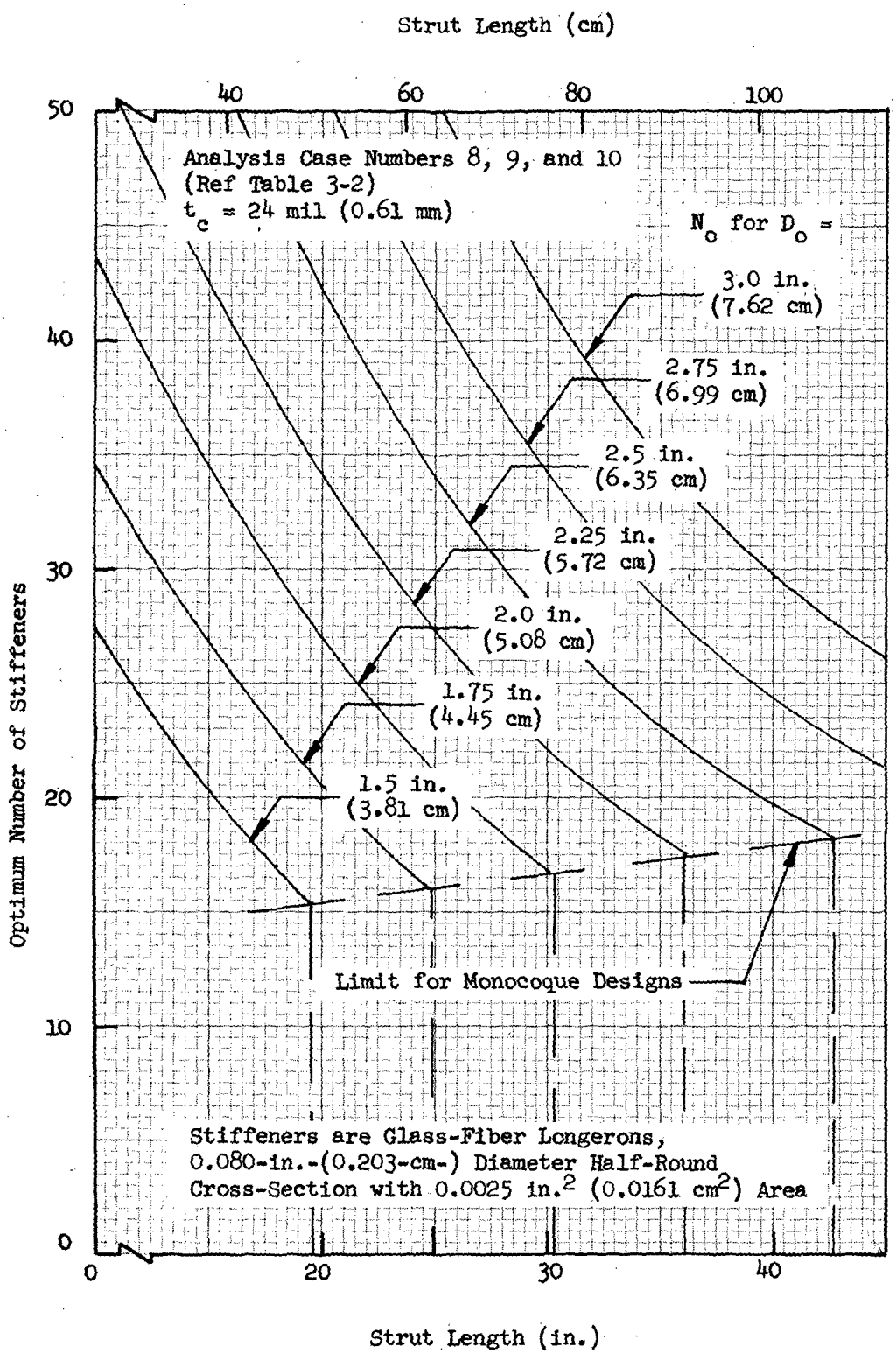

Fig. 3-16 Optimum Number of Stiffeners Required for Fiberglass Cylinders With a 12-mil (0.30-mm) Longo Wrap Thickness

In the analysis of cylindrical fiberglass struts stiffened with the flat boron-fiber longerons, two different design approaches were investigated in order to determine the most advantageous configurations for the load range of interest. Initially, values of the total column buckling allowables (i.e., for wall panels plus stiffeners) were computed as a function of the number of stiffeners (two stiffeners per wave) for 40-in.-(101.6-cm-) long struts. The resulting values are superimposed on the plots of predicted ultimate compressive loads for cylinders stiffened with glass-fiber longerons (Figs. B-10 through B-14), and a summary plot is presented in Fig. 3-17. Inspection of these plots shows that optimum designs can provide load capabilities significantly above the maximum value of interest as specified in Table 3-1. For example, the ultimate compressive load capability for a 3.0-in.-(7.62-cm-) diameter cylinder, optimally stiffened with 30 **boron-fiber longerons, is 18,900 lbf (84,070 N) which is more than twice the specified maximum value. In addition to the high-load capability, it** also becomes apparent that such a design is impractical since the width of 30 stiffeners is greater than the circumference of the cylinder. Consequently, a more practical design, which provides load capabilities suitable for this study, is one where fewer than the optimum number of stiffeners is used.

For this latter design case, allowable column buckling and local crippling stress levels for a monocoque design must be used to determine the total compressive load capability of the wall panels alone. Additional load capability can then be added in proportion to the number of stiffeners, where the allowable axial strain in the stiffeners is matched to that in the panels. For monocoque cylinders with a 12-mil (0.30-mm) longo wrap thickness, the ultimate compressive load capability was shown in Fig. 3-7 to be 3460 lbf (15,390 N). From this figure, it can be seen that the strut diameters for which the column buckling and local crippling load capabilities are equal are 1.5, 1.94, and 2.40 in. (3.81, 4.93, and 6.10 cm) for column lengths of 18, 29, and 40 in. (45.7, 73.7, and 101.6 cm), respectively. The total column allowables for wall panels plus stiffeners were determined

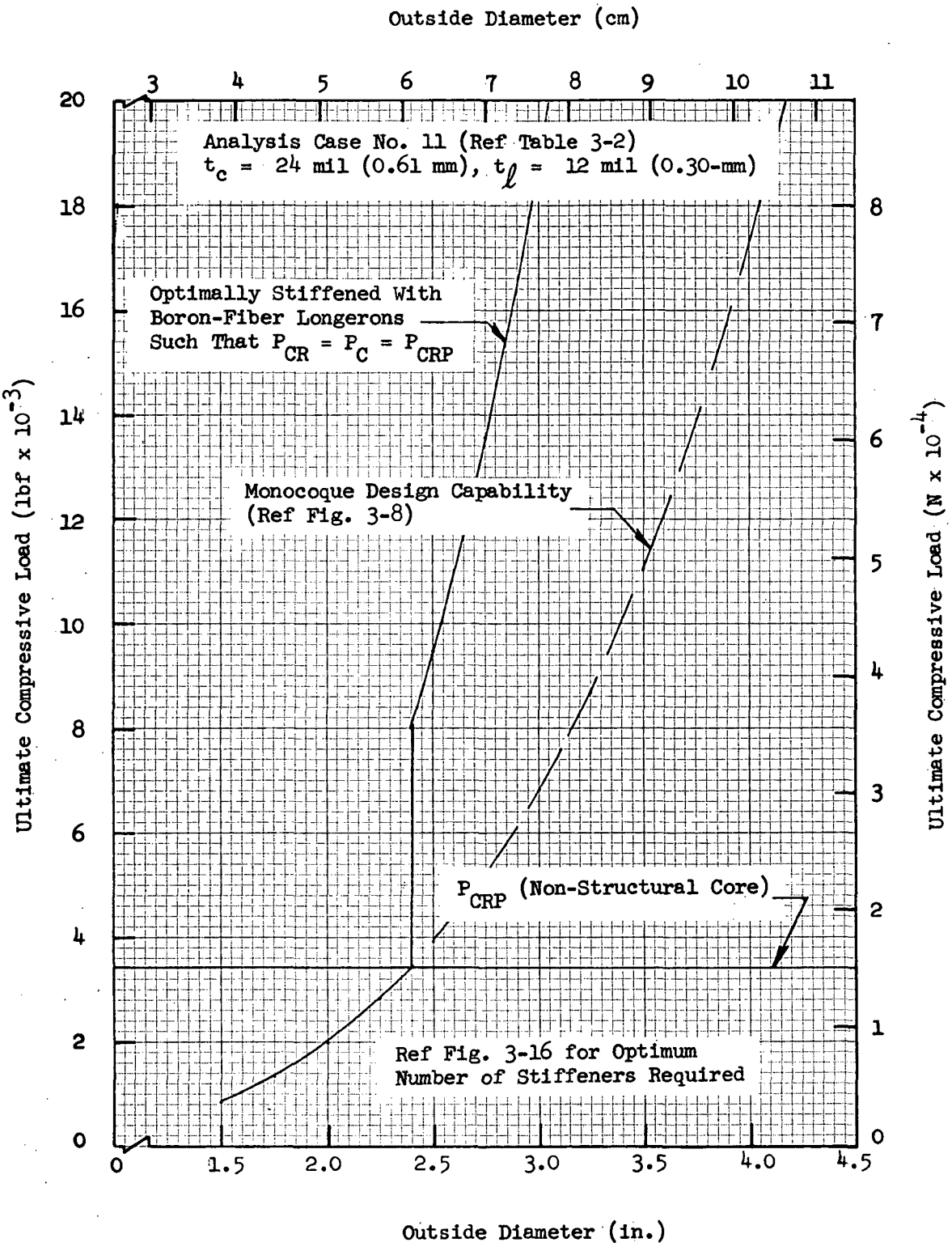

Fig. 3-17 Predicted Ultimate Compressive Loads for 40-in.-(101.6-cm-) Long Fiberglass Cylinders Optimally Stiffened With Boron-Fiber Longerons

by adding the column load capabilities provided by the stiffeners to the 3460 lbf (15,390 N) capability of the panels. Results are presented in Fig. 3-18 for the 18-, 29-, and 40-in.-(45.7-, 73.7-, and 101.6-cm-) long struts, respectively.

3.1.6 Stiffened Fiberglass Ogives

The final configuration that was investigated in the parametric analysis was stiffened fiberglass ogives. In this work, only flat boron-fiber tape longerons were considered since these were previously shown to be the most efficient for cylindrical struts (Ref Section 3.1.5).

It was found in the analysis that fiberglass ogives optimally-stiffened (i.e., stiffeners spaced such that compressive load capabilities are equal for general instability and local crippling failure modes) with boron-fiber longerons provide significantly higher column allowables than are required for the load range specified in Table 3-1. This is consistent with the results of the analysis for fiberglass cylinders optimally-stiffened with the boron-fiber longerons, as discussed earlier in Section 3.1.5. Consequently, only designs with fewer than the optimum number of stiffeners were analyzed using the same approach that was used previously for the cylinders. Also, only ogive struts with a longo wrap thickness of 12 mil (0.30 mm) at midspan were analyzed.

Based on the data presented in Fig. 3-12 for monocoque ogives of this longo wrap thickness, the midspan diameters for which general column buckling and local crippling capabilities are equal are 1.96 in. (4.98 cm) and 2.46 in. (6.25 cm) for 29-in.-(73.7-cm-) long and 40-in.-(101.6-cm-) long struts, respectively.* Predicted ultimate compressive loads for these same respective configurations are presented in Fig. 3-19 as a function of the number of equally-spaced stiffeners used. Note that the additional load capability afforded by the stiffeners is proportional to the number of stiffeners since the axial strain in the stiffeners was assumed to equal that in the wall panels.

* The 18-in.-(45.7-cm-) long ogive designs are not discussed since the corresponding diameter is 1.5 in. (3.81 cm) which defines a cylindrical configuration.

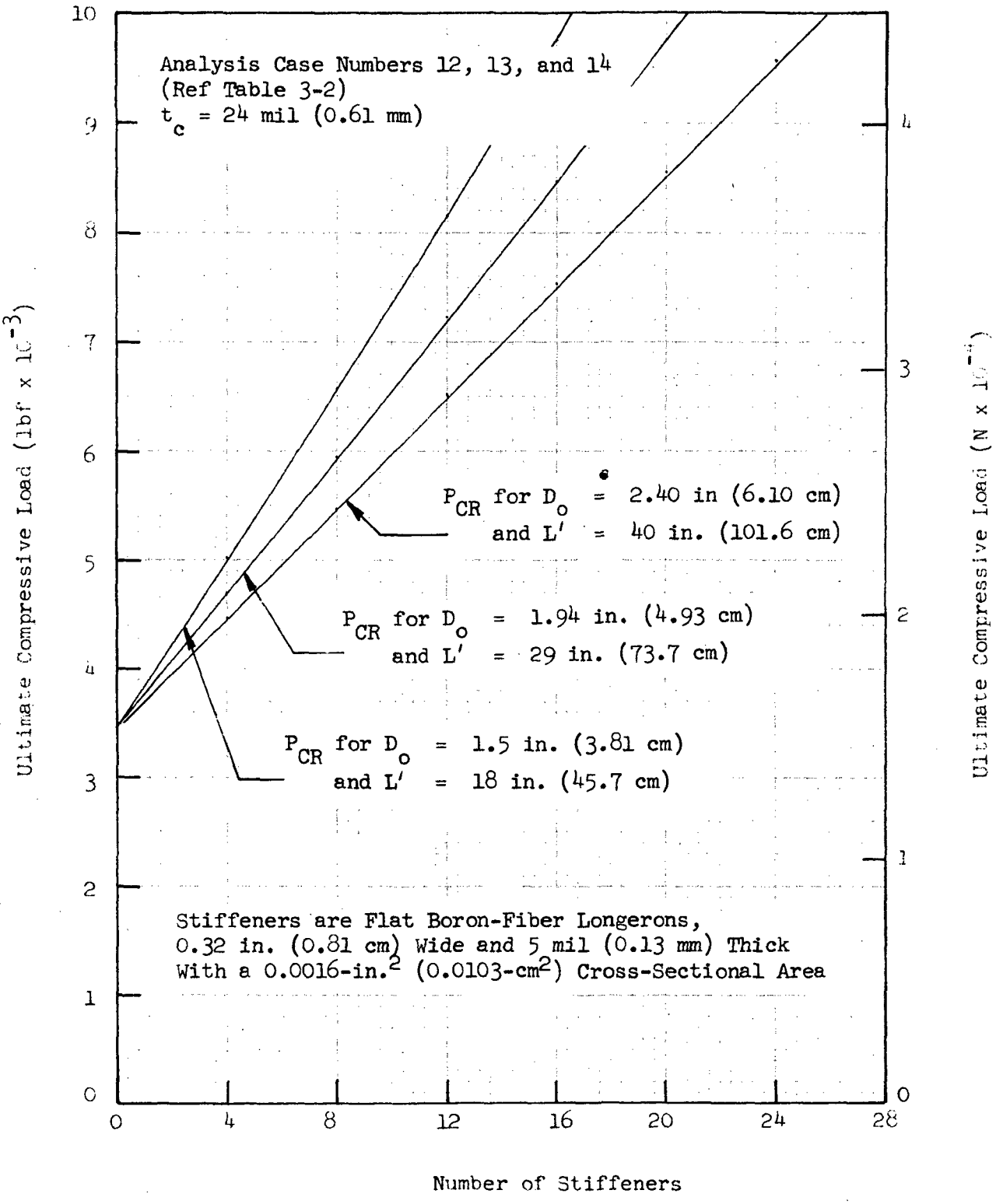

Fig. 3-18 Predicted Ultimate Compressive Loads for Fiberglass Cylinders With a 12-mil (0.30-mm) Longo Wrap Thickness Stiffened With Boron-Fiber Longerons

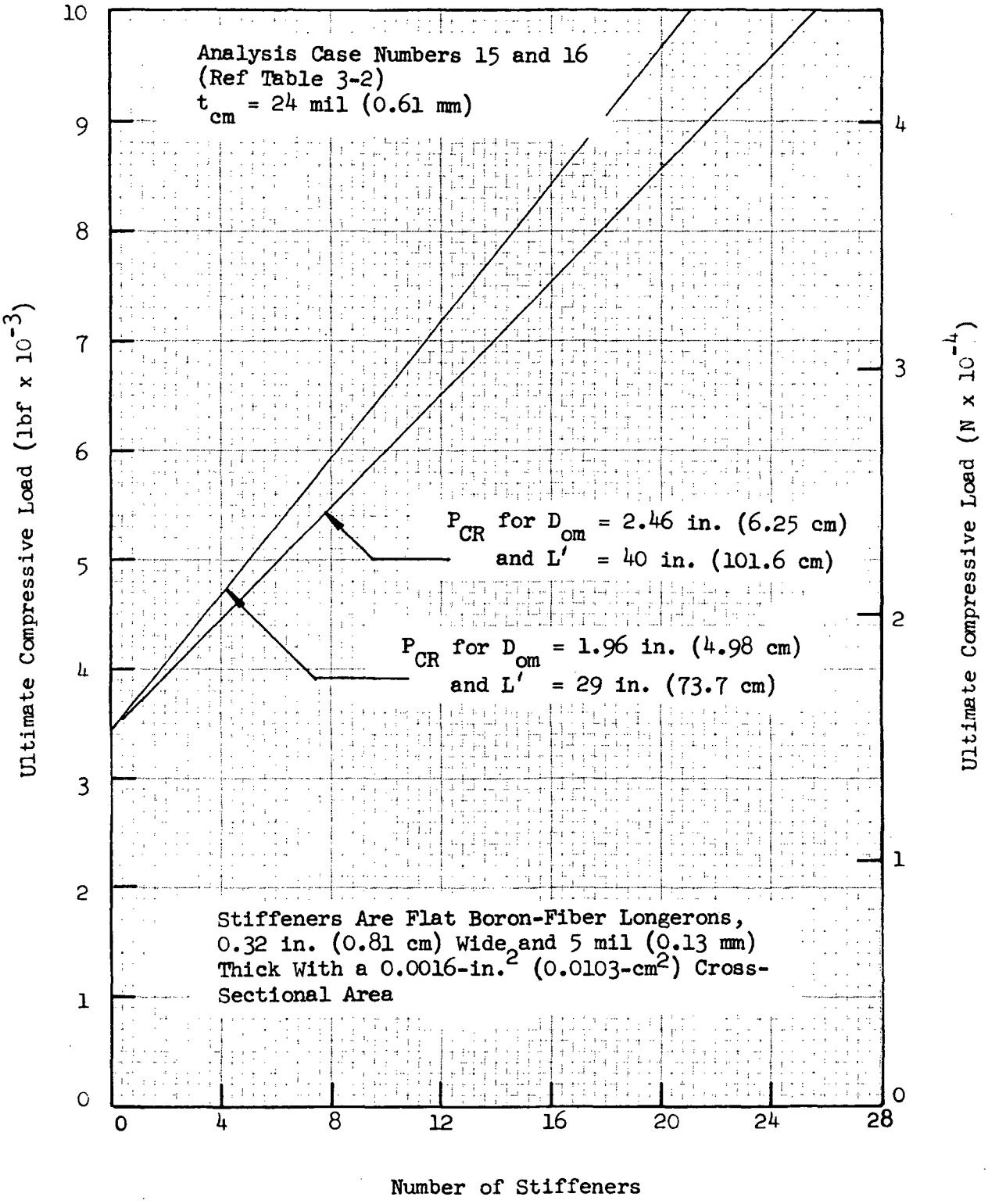

Fig. 3-19 Predicted Ultimate Compressive Loads for Fiberglass Ogives With a 12-mil (0.30-mm) Longo Wrap Thickness at Midspan Stiffened With Boron-Fiber Longerons

3.1.7 Heat Leak Comparison

At the conclusion of the parametric structural analysis, a one-dimensional heat leak study was conducted for each of the 16 analysis cases defined in Table 3-2. In this study, values of conductive heat transfer through the strut body wall were computed and compared. Radiative and/or conductive heat transfer through the strut core insulation was neglected (temporarily), since it was shown in preliminary studies that the core heat leak is nominally less than 10 percent of that conducted through the wall when properly insulated. Consequently, selection of the core insulation does not significantly affect optimization of the strut body wall design. A detail analysis was conducted later in Task 1 to select the most suitable core insulation system for selected strut body designs (Ref Section 3.2.2).

Assuming that all candidate strut designs would be perfectly insulated over the exterior surface, one-dimensional heat leak values were computed using the equation

$$Q_c = \frac{k_c A_c (T_H - T_C)}{L_c} \qquad (3\text{-}5)$$

In this equation, the thermal conductivity of the composite wall, k_c, was evaluated for the mean temperature, T_m, of the hot and cold end boundaries, T_H and T_C, respectively. Heat leak values were computed for boundary temperature combinations of 520°R (289°K) to 37°R (20°K) and 400°R (222°K) to 140°R (78°K) for each candidate design. The composite strut length, L_c, was considered to be the total strut length less 6 in. (15.2 cm). A section 3 in. (7.6 cm) long at each end of each strut was assumed to provide negligible thermal resistance in order to account for the relatively high thermal conductivity of the metallic end fittings compared to that of the composite strut body wall.*

---

* The thermal conductivity of 6 Al-4V titanium at a mean temperature of 278°R (154.7°K) is 2.94 Btu/hr ft°R (5.09 x 10^{-2} W/cm°K) (Ref 5, Fig. 3-2) compared to 0.227 Btu/hr ft°R (3.93 x 10^{-3} W/cm°K) for glass fiber-epoxy at the same temperature (Ref 2, Fig. 23).

Springer and Tsai (Ref 6) have shown that the thermal conductivities in the longitudinal direction of composite structures with unidirectional filaments which are oriented in the parallel (longo) and normal (circ) directions can be approximated closely by the relationships for parallel and series interdependence which are given, respectively, by

$$k_{\ell} = v_f k_f + v_r k_r \qquad \text{(longo)} \qquad (3\text{-}6)$$

and

$$k_{cr} = \frac{k_r}{(v_f k_r / k_f) + v_r} \qquad \text{(circ)} \qquad (3\text{-}7)$$

In each of these expressions v_f and v_r correspond to the fiber and resin volume fractions, respectively, while k_f and k_r correspond to the thermal conductivities of the fiber and resin components, respectively.

Combining these values of k_{ℓ} and k_{cr} in parallel, the average conductivity of a filament-wound composite strut, in a direction parallel to the longitudinal axis, can then be determined using the relationship

$$k_c = \frac{k_{\ell} A_{\ell} + k_{cr} A_{cr}}{A_{\ell} + A_{cr}} \qquad (3\text{-}8)$$

Values of thermal conductivity for typical glass fiber materials, $k_f = k_g$, epoxy resin, k_r, and composite fiberglass struts, k_{cg}, based on this analytical model, are presented in Fig. 3-20 as a function of mean temperature T_m. As shown, conductivity data for glass fibers from three sources were averaged in this analysis. However, conductivity values actually used in the heat leak study were based on less precise glass and resin conductivity data (not shown) obtained at that time from Ref 5. The resulting composite values used are shown in the figure for a T_m of 278.5°R (154.7°K), which corresponds to the 520°R (289°K) to 37°R (20°K) boundary temperature combination. Comparison of the composite values used in the study with those derived from the glass and resin data presented in the figure shows maximum deviations of approximately ±6 percent for the all-circ ($A_{\ell}/A_{cr} = 0$) and the all-longo

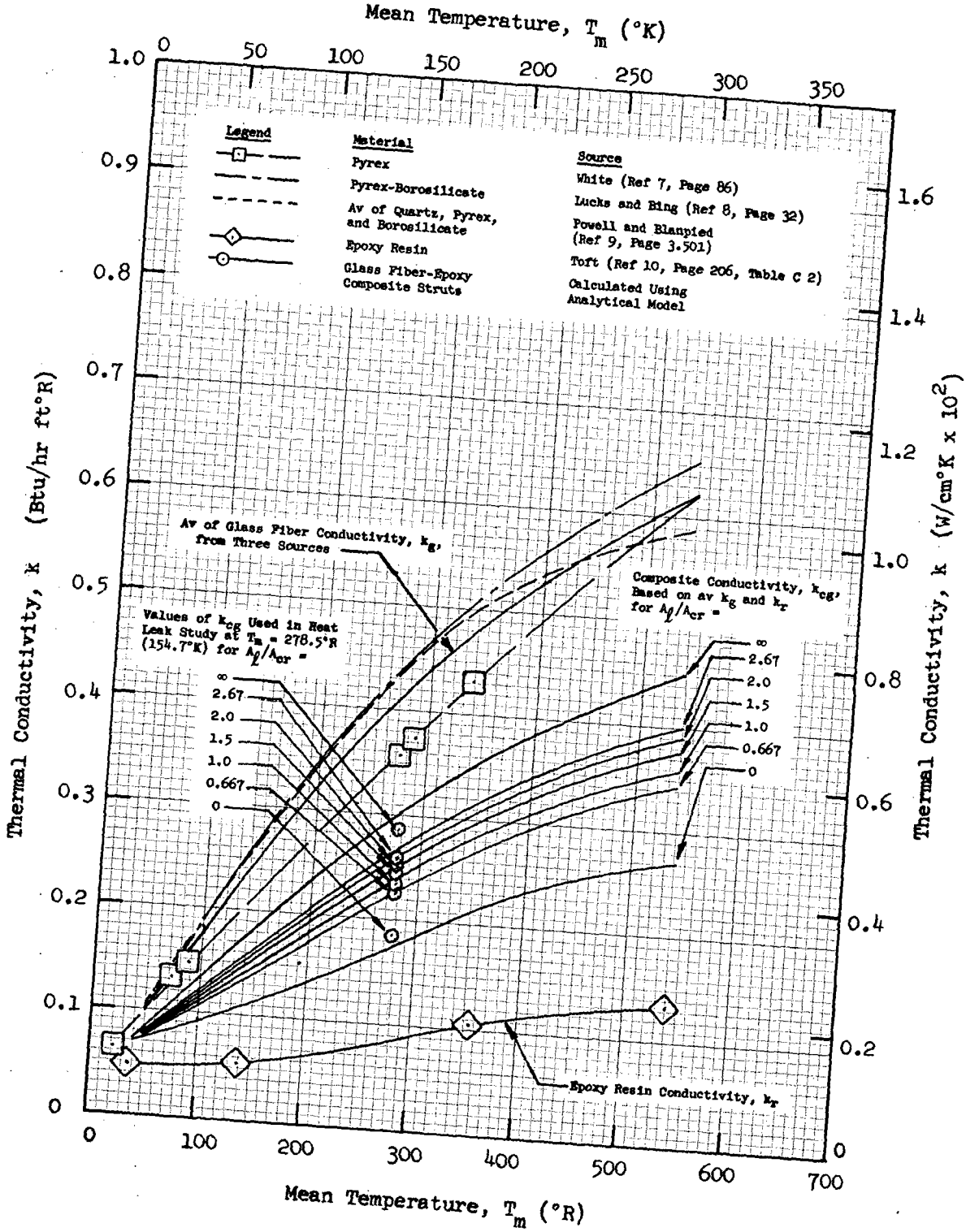

Fig. 3-20 Thermal Conductivity Model for Glass Fiber-Epoxy Composites

($A\ell/A_{cr} = \infty$) configurations, respectively. However, for the analysis cases defined in Table 3-2, the ratio $A\ell/A_{cr}$ varies from 1.0 to 2.0, and the maximum deviation reduces to approximately -2.3 percent. The comparison of model values of thermal conductivity with those used in the study for the 400°R (222°K) to 140°R (78°K) temperature combination (not shown in the figure) is similar.

A comparison of composite fiberglass conductivity values, calculated using the model described above, with conductivity values obtained by test from three sources is presented in Fig. 3-21. Additional data from General Dynamics/Convair (Ref 11, Figs. 50 and 51, and Ref 12, Figs. 19 and 20), North American Rockwell (Ref 13, Fig. 1), and Arthur D. Little (Ref 14, Page 29) were excluded from this comparison, either because they represented test data obtained with the specimens exposed to 1 atmosphere of nitrogen or helium gas, or because their source and the environmental conditions were not clearly specified. Inspection of the later GD/C data (Ref 11, Figs. 50 and 51), however, shows conclusively that thermal conductivity data obtained with the specimens exposed to 1 atmosphere of nitrogen or helium gas are up to 3 times greater than those obtained in a vacuum environment. It was concluded that gas-environment conductivity data were invalid for use in this study, and as a consequence only vacuum-environment data are shown in Fig. 3-21.

Inspection of Fig. 3-21 shows generally good correlation between the analytical model and the Ref 2 test data. The model values, compared to the best fit of these test values, range from 1.7 percent low at 50°R (27.8°K) to 17.9 percent high at 300°R (167°K), and finally to 5.5 percent high at 500°R (278°K). Correlation of model values with test values from other sources is generally less satisfactory; however, the model values are nearly always greater (conservative). The poorest correlation is exhibited for a mean temperature of 355°R (197°K), where the model value is 300 percent greater than the Goodyear test value for a resin content of 18 percent and $A\ell/A_{cr} = \infty$. It should be noted that the GD/C and the Goodyear test data

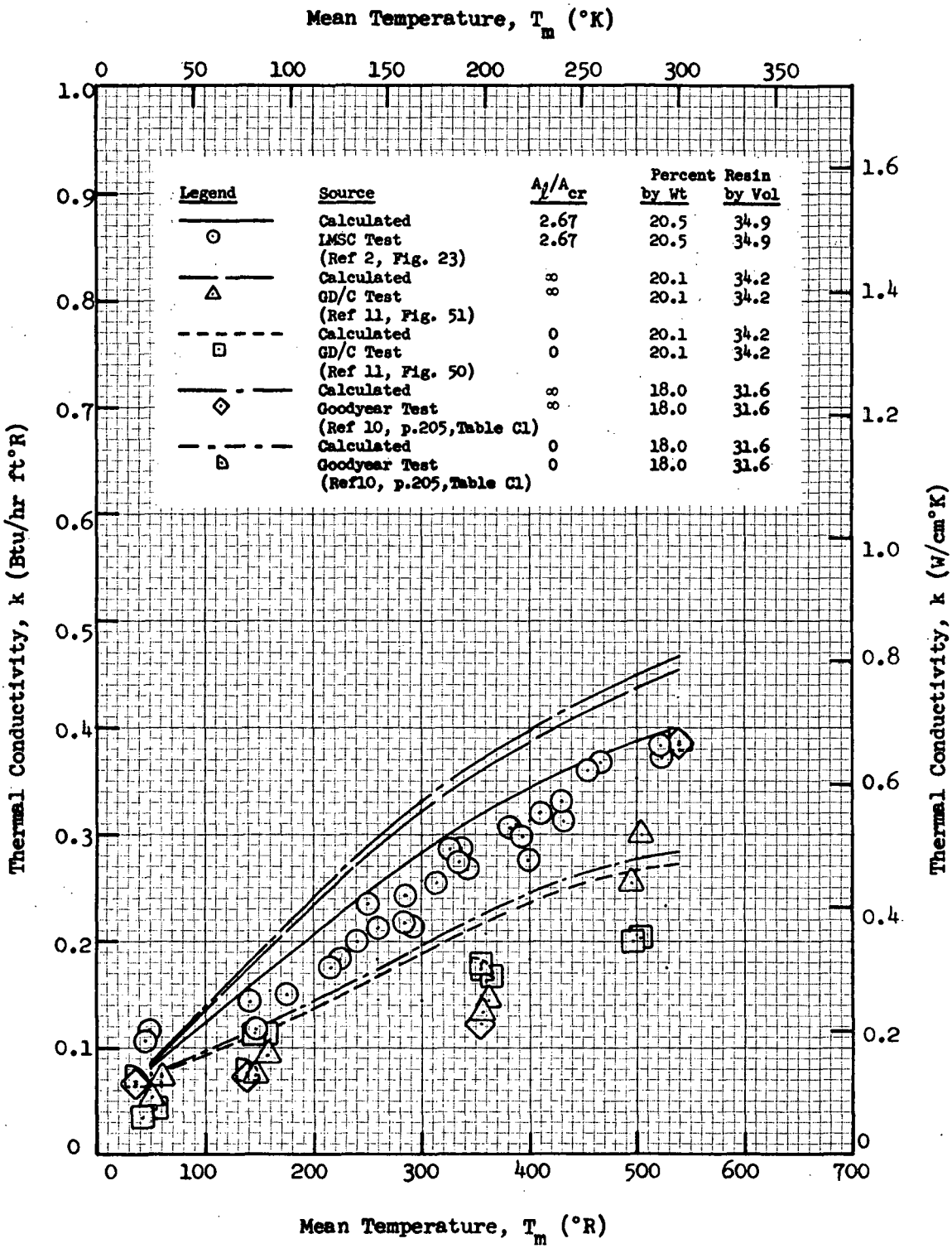

Fig. 3-21 Comparison of Calculated and Test Values of Thermal Conductivity for Glass Fiber-Epoxy Composites

were obtained from relatively few small-panel specimens, generally tested using a guarded hot plate method, whereas the Ref 2 data are much more extensive, and were obtained using a full-scale strut specimen and a calorimetric test apparatus constructed specifically for this purpose.

In applying the analytical thermal conductivity model, given by Equations 3-6, 3-7, and 3-8, to compute strut heat leaks using Equation 3-5, several differences were noted for the various candidate strut designs. For cylindrical struts, values of the total composite cross-sectional area, $A_c = A_\ell + A_{cr}$, as well as values of the ratio of longo-to-circ composite area, A_ℓ/A_{cr}, are constant over the entire composite length, L_c. For ogive struts, however, the value of A_{cr} decreases from a maximum at midspan to a minimum at the ends by the ratio of the end diameter to the midspan diameter. The longo composite area remains constant over the length, since this depends solely on the number of longo rovings. Because the ratio of longo-to-circ composite area, A_ℓ/A_{cr}, varies over the length of an ogive strut, the conductivity value also varies over the length, even neglecting the variation due to changing temperature from T_H to T_C. In addition, the total composite area, A_c, varies over the length, and the true heat leak through the ogive strut is proportional to the product of $k_c A_c$ integrated over the composite length. In the analysis, it was found that heat leak values based on average values of k_c and A_c, for section properties at midspan and at the ends, were within approximately 1.6 percent of those obtained by integration of the $k_c A_c$ product. Consequently, the average value method was used in the heat leak study.

In the analysis of fiberglass struts with boron fiber longos (analysis case number 7) or longeron stiffeners (analysis case numbers 11 through 16), experimental values of thermal conductivity for the boron fiber-epoxy composite from two different sources were compared with a single calculated value. These data are presented as a function of mean temperature for an all-longo fiber orientation ($A_\ell/A_{cr} = \infty$) in Fig. 3-22. The calculated value is based on the parallel interdependence model (Equation 3-6) extended to include the effects of the tungsten core. The resulting

expression is

$$k_\ell = v_b k_b + v_t k_t + v_r k_r \qquad (3\text{-}9)$$

In evaluating this equation, values of 0.492, 0.008, and 0.50 were used for v_b, v_t, and v_r, respectively. These values correspond to a resin content of 32.7 percent by weight (the same as for the experimental data), and diameters of 4 mil (0.10 mm) and 0.5 mil (0.013 mm) for the boron fibers and the tungsten wire cores, respectively). Component thermal conductivity values of 1.845 Btu/hr ft°R* (3.193×10^{-2} W/cm°K) (Ref 17, pages 94-104), 97.6 Btu/hr ft°R (1.69 W/cm°K) (Ref 9, page 3.161), and 0.133 Btu/hr ft°R (2.302×10^{-3} W/cm°K) (Ref Fig. 3-20) were used for boron, tungsten, and epoxy resin, respectively. The resulting calculated value is 1.74 Btu/hr ft°R (3.01×10^{-2} W/cm°K) for a mean temperature of 549.2°R (305.1°K or 31.8°C , the measured boron conductivity specimen temperature). Although conductivity values as a function of temperature are available from these references for the tungsten and epoxy resin components, no applicable data could be found for the conductivity of boron at other temperatures.

In conducting the heat leak analysis, the Ref 15(Martin) experimental conductivity data were used. As shown in Fig. 3-22, these data show reasonable agreement (± 30 percent) with the calculated value and the Nadler (NA/SD) experimental data, and they also span the entire temperature range of interest.

Incremental heat leaks for the basic fiberglass strut bodies, boron-fiber longo wraps, and glass-fiber or boron-fiber longeron stiffeners were calculated independently and then summed to obtain total predicted heat leak values for each analysis case. Results of the detailed calculations are

---

* Ref 17 gives k = 1.863 Btu/hr ft°R (3.225×10^{-2} W/cm°K) for a 73.2-mil-(1.86-mm-) diameter boron rod with a 0.984-mil-(0.025-mm-) diameter tungsten core; the value given above was calculated using the parallel conductivity model.

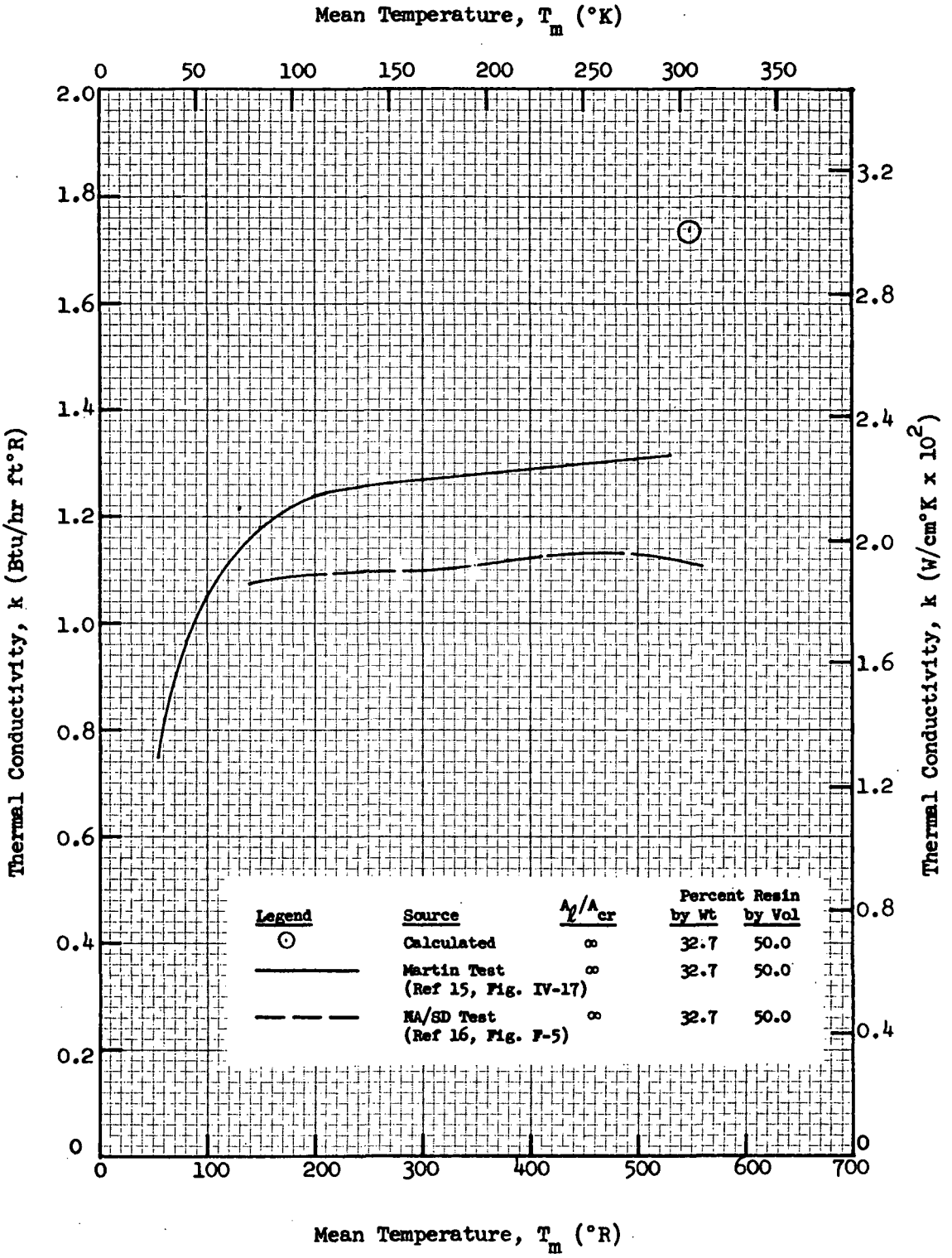

Fig. 3-22 Comparison of Calculated and Test Values of Thermal Conductivity for Boron Fiber-Epoxy Composites

summarized in Appendix C. Figs. 3-23 and 3-24 show the calculated heat leaks plotted as a function of strut length and outside diameter for one typical analysis case, monocoque fiberglass cylinders, for boundary temperatures of 520°R (289°K) to 37°R (20°K) and 400°R (222°K) to 140°R (78°K), respectively.

3.1.8 System Weight* Comparison

The broad parametric structural and thermal analysis conducted in Task 1 was culminated in a system weight tradeoff study. In this study, the sum of component weights for the basic strut body including stiffeners, the end fittings, core insulation, external insulation, and propellant boiloff were computed and compared as a function of mission duration (storage time) for nine selected design points within the specified load-length envelope (Ref Table 3-1). System weights for fifteen of the sixteen basic analysis cases (Ref Table 3-2) were evaluated and compared for each of the nine design points to which they were applicable and for which the system weights appeared to be competitive. Weights were not computed for analysis case No. 11, since this design configuration had already been eliminated in the structural analysis (Ref Section 3.1.5). Liquid hydrogen boiloff weights were computed for the 520°R (289°K) to 37°R (20°K) boundary temperature combination, and boiloff weights assuming liquid fluorine as the stored propellant were computed for the 400°R (222°K) to 140°R (78°K) boundary temperature case.

In the calculation of strut body weights, the density values used for glass fiber-epoxy and boron fiber-epoxy, respectively, were 0.0736 lbm/in.^{3} (2.04 gm/cm^3) and 0.0669 lbm/in.^{3} (1.85 gm/cm^3). These values were based on a glass fiber density of 0.0897 lbm/in.^{3} (2.48 gm/cm^3) (Ref 1, Fig. 6-83), a boron fiber density of 0.0849 lbm/in.^{3} (2.35 gm/cm^3) (Ref 17), and an epoxy resin density of 0.0437 lbm/in.^{3} (1.21 gm/cm^3) (Ref 1, Fig. 6-83). The glass fiber-epoxy composite density was evaluated for a resin content

* i.e., total inert plus boiloff weight per strut

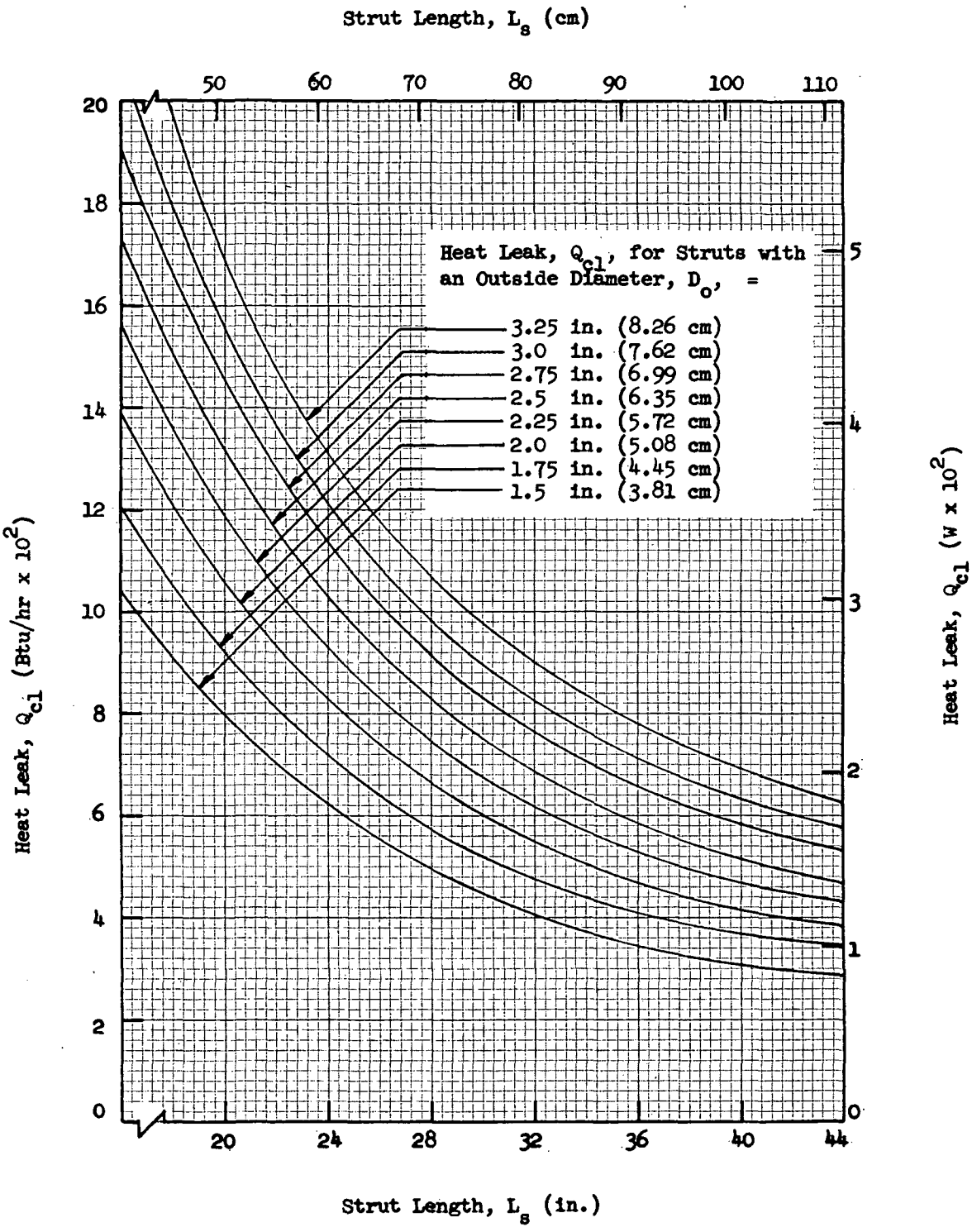

Fig. 3-23 Predicted Heat Leaks for Monocoque Fiberglass Cylinders with a 12-mil (0.30-mm) Longo Wrap Thickness and Boundary Temperatures of 520°R (289°K) to 37°R (20°K)

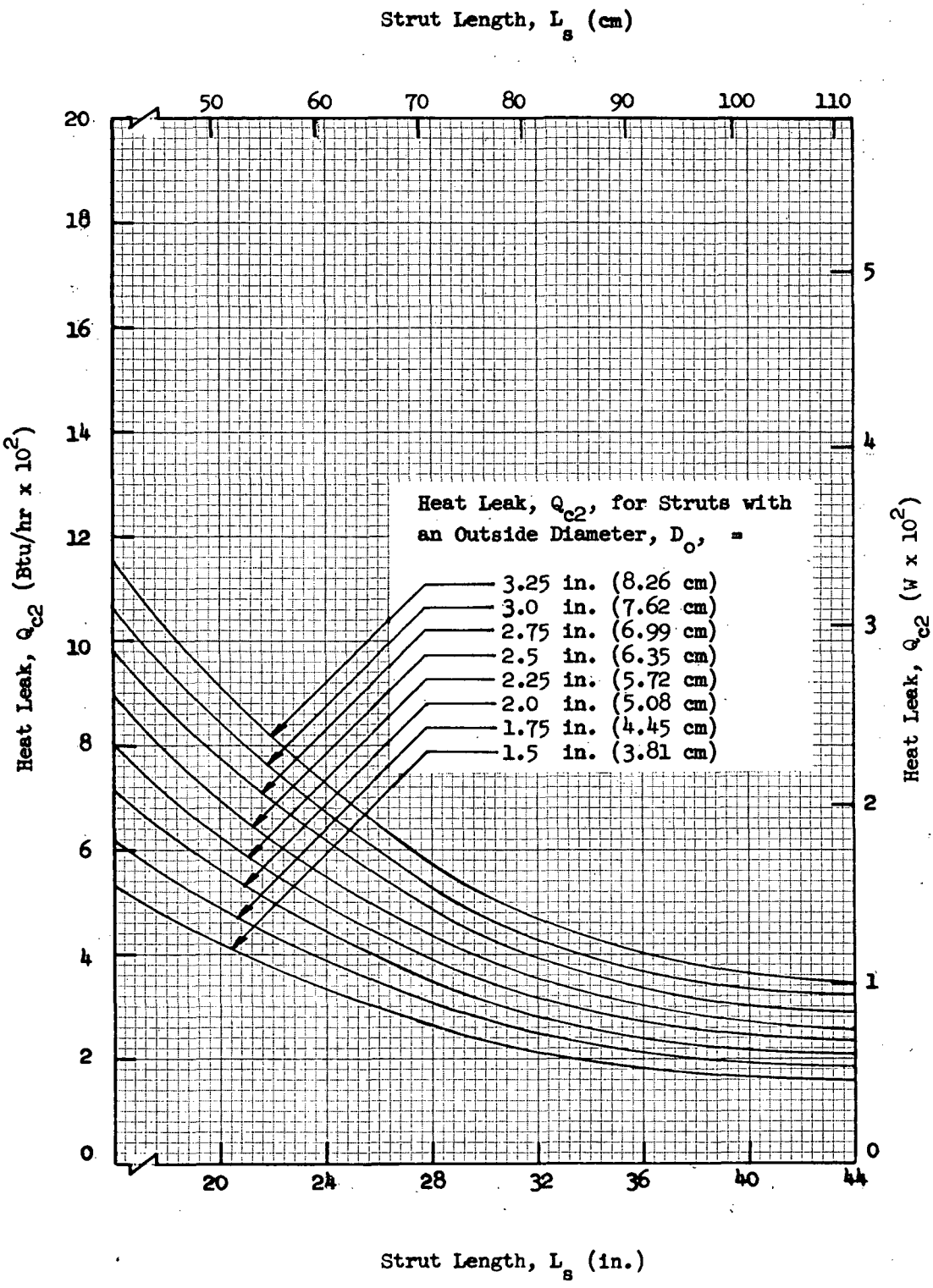

Fig. 3-24 Predicted Heat Leaks for Monocoque Fiberglass Cylinders with a 12-mil (0.30-mm) Longo Wrap Thickness and Boundary Temperatures of 400°R (222°K) to 140°R (78°K)

of 35 percent by volume, whereas that used for the boron fiber-epoxy composite corresponds to a resin content of 50 percent by volume.

The length of the composite strut body, and that of any longeron stiffeners required, was assumed to be the total strut length, L_s, less 3 in. (7.6 cm) for all candidate designs. This provides an allowance for the longo material wrapped around the end fittings as well as circ fillet material, but does not reflect the increased length of rod-end fittings required for high-load designs. This simplifying assumption was made to expedite the analysis considering the relatively large number of cases to be evaluated. The resulting error in absolute weight is small, and the difference in relative system weights for competing designs at any given length and load is negligible.

A preliminary analysis of the strut end fittings was performed to determine approximate weights for representative rod-ends, internal fittings, compression caps, and the corresponding attachment hardware. This analysis showed that the end fitting weights are essentially independent of strut length, somewhat dependent on strut end diameter, and very strongly dependent on design loads. Unlike the basic strut body, the end fittings are critical for design ultimate tension loads, since these are significantly greater than the corresponding compression loads (Ref Table 3-1). A summary of the component fitting weights which resulted from the preliminary analysis is presented in Table 3-3 as a function of design ultimate loading.

For any given load-length design point, the variation in the required strut diameter for various competing design configurations (analysis cases) is typically less than ± 10 percent of the mean diameter required. Consequently, this same variation applies generally to the required end fitting diameters, since these correspond to the required strut diameters for all designs other than ogives. Since the end fitting weights are dependent primarily on ultimate design loads anyway, the effect of diameter on these fitting weights was neglected in the system weight comparison. This, in effect, penalizes

Table 3-3

PRELIMINARY ESTIMATES OF END-FITTING WEIGHTS

Design Ult Compression Load, lbf (N)	980 (4360)	4690 (20,860)	8400 (37,360)
Design Ult Tension Load, lbf (N)	2450 (10,900)	11,725 (52,150)	21,000 (93,400)
Selected Rod-End Fittings: (Ref 18, pages 49 and 50)			
Warm End	DREMHD-4	DREMHD-7	DREMHD-10
Cold End	SWRM-4-100	SWRM-4-100	SWRM-4-100
Estimated Weights, lbm (kg):			
Rod-End Fittings(1)	0.18 (0.082)	0.35 (0.159)	0.61 (0.276)
Internal Fittings(2)	0.40 (0.181)	0.65 (0.295)	1.00 (0.454)
End Caps(2)	0.20 (0.091)	0.25 (0.113)	0.35 (0.159)
Attachment Hardware(3)	0.14 (0.063)	0.25 (0.113)	0.38 (0.172)
Total (Each Strut)	0.92 (0.417)	1.50 (0.680)	2.34 (1.061)

(1) Actual weights supplied by Southwest Products Company, Inc., Monrovia, California.
(2) Estimates for titanium parts based on preliminary design.
(3) Estimates for CRES lock nuts and washers.

the ogive designs for long, heavily-loaded struts since the end fittings for these cases could in fact be significantly smaller in diameter. However, the error in total comparative system weights is relatively small, even for ogive designs, and is negligible for all other configurations. The error in absolute fitting weights, for the range of strut lengths and design loads investigated, may be significant.

For the system weight comparison, the core insulation was assumed to be identical for all designs. Weight values were computed by multiplying the strut

core volume by a constant density of 2.0 lbm/ft^3 (32.0 kg/m^3).* Optimization of the core insulation system for selected designs is discussed in Section 3.2.2.

In calculating external insulation weights, it was assumed that each strut design would be insulated over its full length with approximately a 0.5-in.-(1.27-cm-) thickness of crinkled, single-aluminized Mylar at a layer density of approximately 55 layers/in. (21.7 layers/cm). The bulk density for such an insulation is 1.2 lbm/ft^3 (19.2 kg/m^3) (Ref 19, Fig. 5-3).

Boiloff weights were added directly to the strut inert weights to compute the total weight values per strut. For liquid hydrogen, a heat of vaporization of 187 Btu/lbm (435 joules/gm) was used, assuming venting of saturated vapor at 25 psia (1.72x10^5 N/m^2) (Ref 20, Unit 6, Fig. 8). The corresponding value for liquid fluorine, vented at the same pressure, is 69.1 Btu/lbm (161 joules/gm) (Ref 20, Unit 14, Fig. 7).

Other details and summaries of the system weights calculated during the study are presented in Appendix D. Plots of the resulting total system weights are presented in Figs. 3-25 through 3-30 for three selected points within the load-length design envelope. In these figures, weight values are shown as a function of mission duration and boundary temperatures.

It can be seen by inspection of the data presented in these figures, and in Appendix D for other load-length design points, that inert weights per strut for any given design point do not vary significantly for the configurations studied. For example, weights for 18-in.-(45.7-cm-) long struts with a design ultimate compressive load of 980 lbf (4360 N) vary less than 0.1 lbm (0.045 kg). For 40-in.-(101.6-cm-) long struts with a design ultimate

---

* A core insulation density of approximately 4 to 6 lbm/ft^3 (64.1 to 96.1 kg/m^3) was selected during final design; however, since the core insulation weight is typically 6 to 8 percent of the inert weight and 3 to 5 percent of the total system weights, this had no significant effect on the selection of optimum designs.

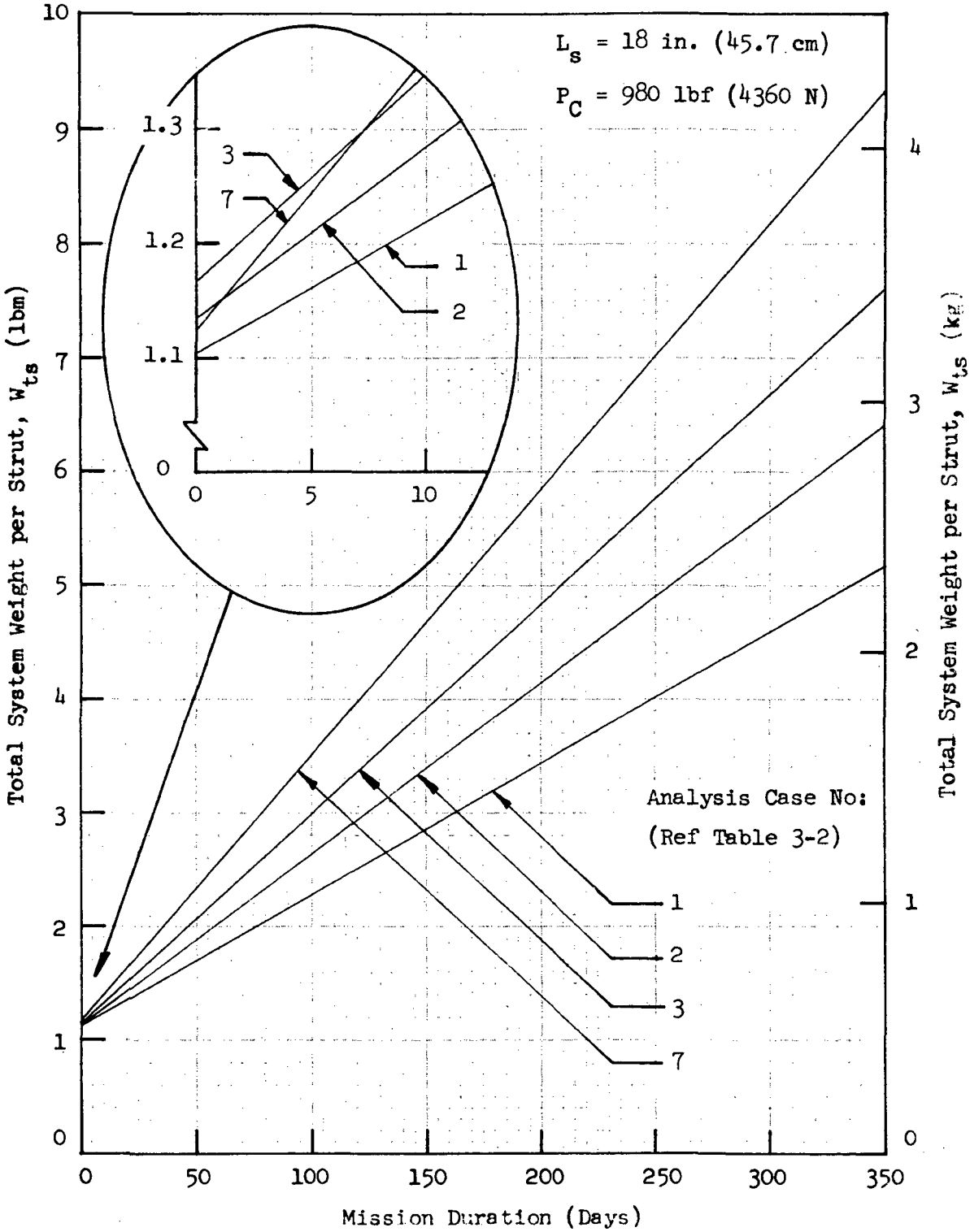

Fig. 3-25 Comparative Total System Weights for Short, Lightly-Loaded Struts with 520°R (289°K) to 37°R (20°K) Boundary Temperatures

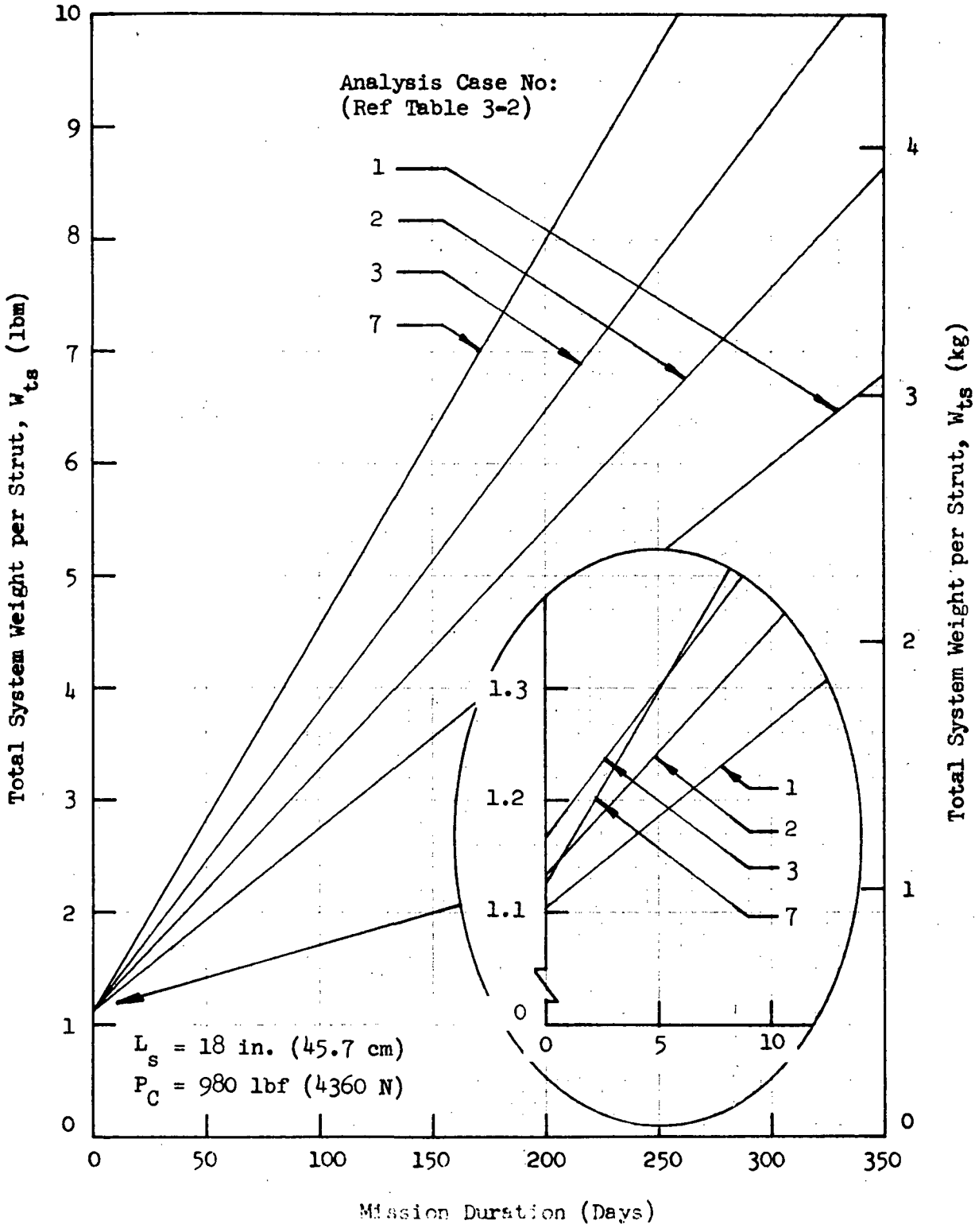

Fig. 3-26 Comparative Total System Weights for Short, Lightly-Loaded Struts with 400°R (222°K) to 140°R (78°K) Boundary Temperatures

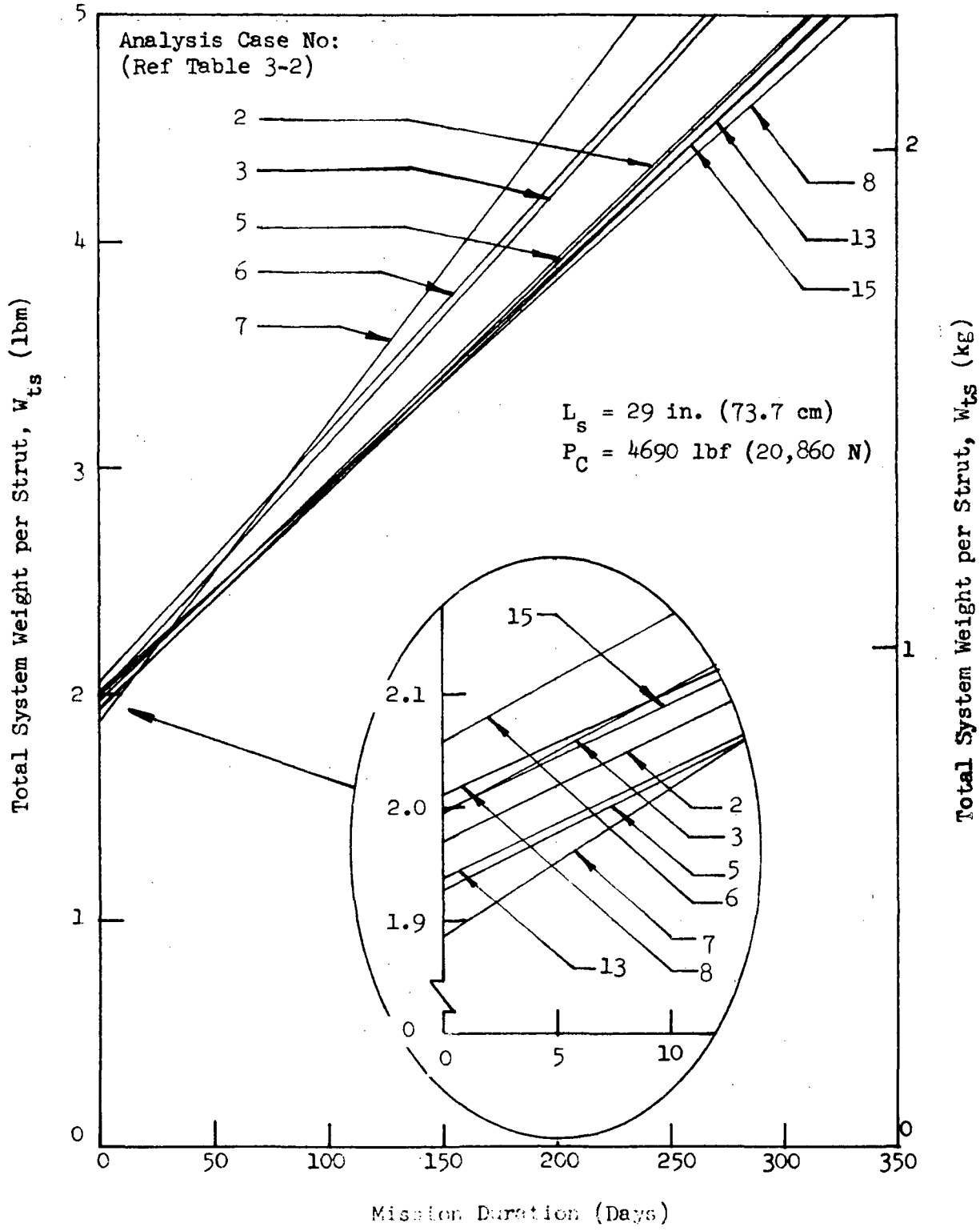

Fig. 3-27 Comparative Total System Weights for Medium-Length, Medium-Load Struts with 520°R (289°K) to 37°R (20°K) Boundary Temperatures

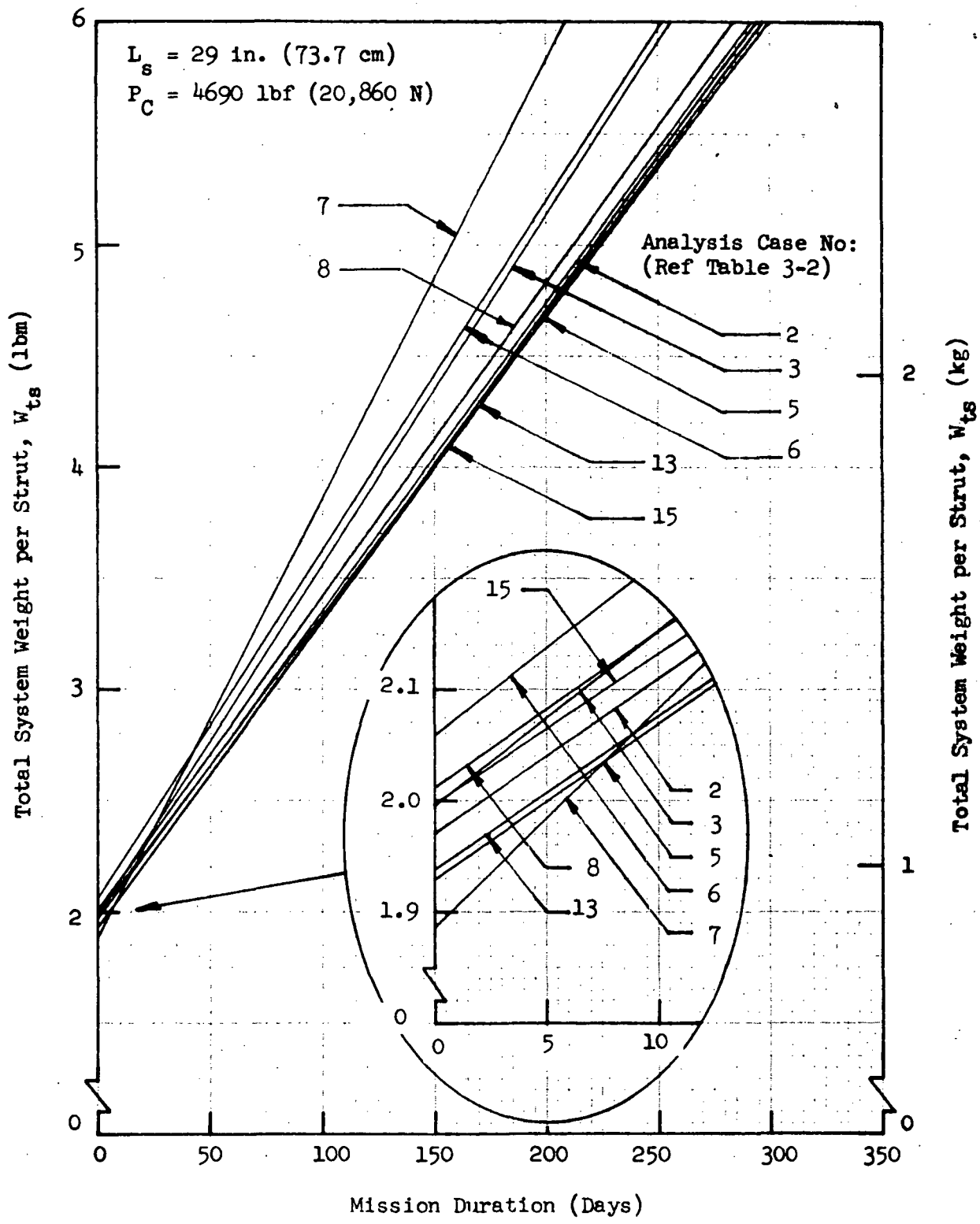

Fig. 3-28 Comparative Total System Weights for Medium-Length, Medium-Load Struts with 400°R (222°K) to 140°R (78°K) Boundary Temperatures

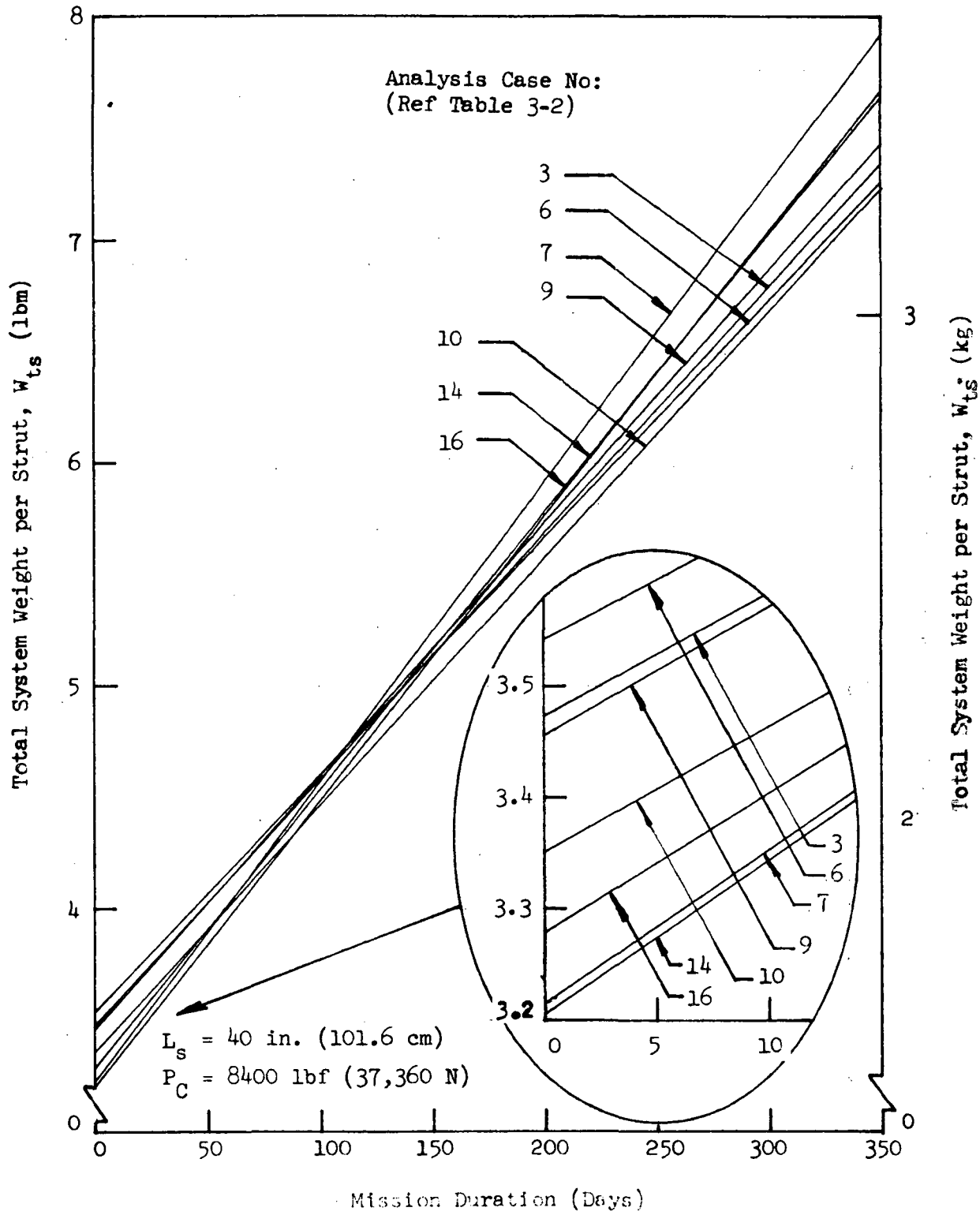

Fig. 3-29 Comparative Total System Weights for Long, Highly-Loaded Struts with 520°R (289°K) to 37°R (20°K) Boundary Temperatures

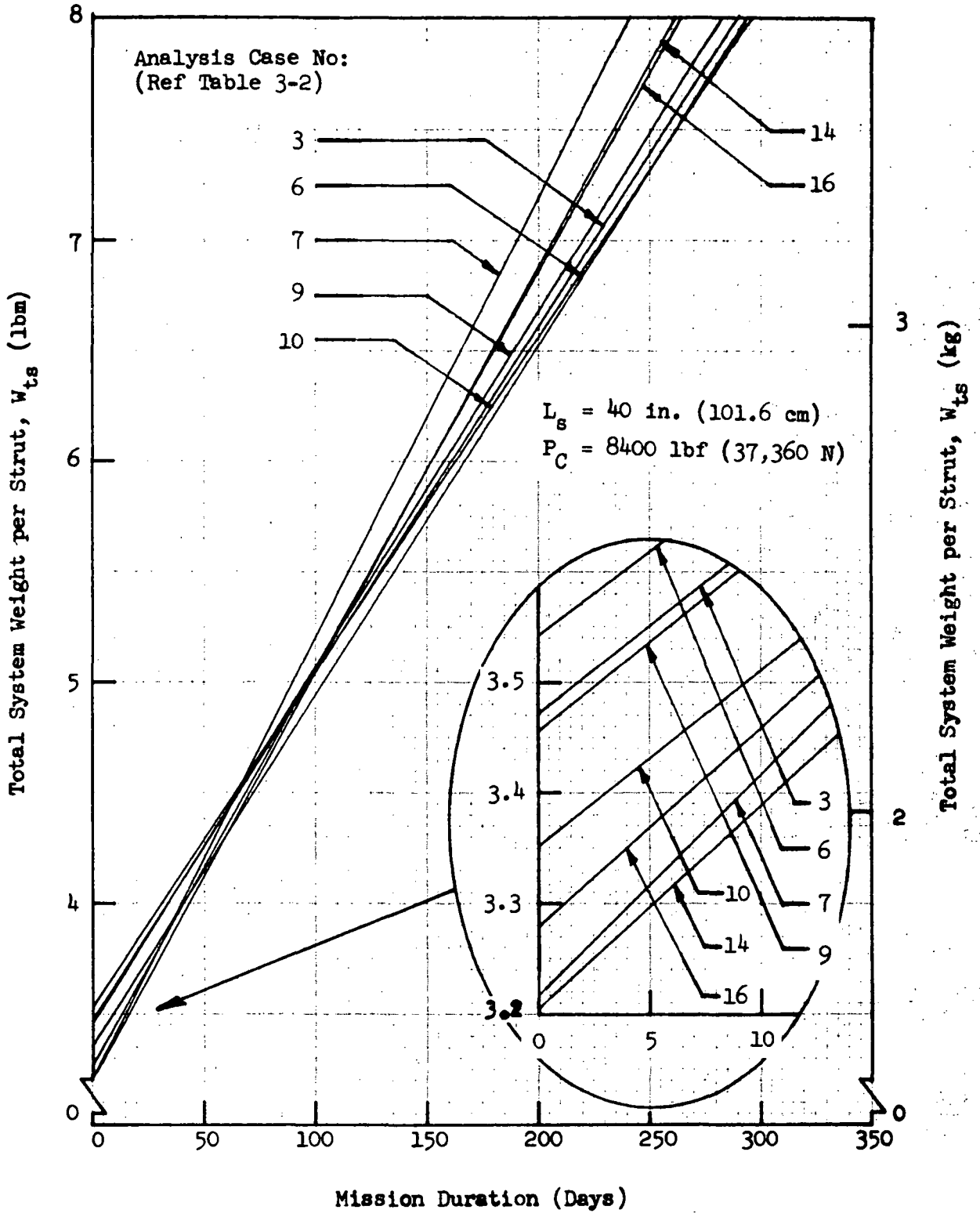

Fig. 3-30 Comparative Total System Weights for Long, Highly-Loaded Struts with 400°R (222°K) to 140°R (78°K) Boundary Temperatures

compressive load of 8400 lbf (37,360 N), the inert weights vary by a maximum of approximately 0.35 lbm (0.16 kg) for the seven applicable design configurations studied.

Variations in total strut system weights including boiloff for particular design points were found to be significantly greater in terms of the percent of total system weight. Maximum variations were found for the 400°R (222°K) to 140°R (78°K) boundary temperature case where liquid fluorine was assumed to be the stored cryogen. Significant but smaller variations were determined for the other boundary temperature case with liquid hydrogen as the cryogen. In the case of an 18-in.-(45.7-cm-) long strut support for a liquid fluorine tank, designed for an ultimate compressive load of 980 lbf (4360 N), the maximum variation in comparative system weight for 350 days of storage time was found to be approximately 6.3 lbm (2.8 kg). However, a major part of this variation results from the over-design of particular candidates due to the 1.5-in. (3.81-cm) minimum diameter and 24-mil (0.61-mm) minimum wall thickness requirements imposed in the study. For a 40-in.-(101.6-cm-) long strut, with the same application and storage time, designed for an ultimate compressive load of 8400 lbf (37,360 N), the maximum variation in total system weight was only approximately 1.4 lbm (0.64 kg).

3.1.9 Selection of Candidates for Detailed Analysis

Based on results of the parametric structural and thermal analysis conducted in Task 1, six optimum strut configurations were selected for detailed design and analysis studies. Characteristics of these six candidates are summarized in Table 3-4.

Table 3-4

CHARACTERISTICS OF STRUTS SELECTED FOR DETAILED STUDIES

Configuration No.	Configuration Description	Longo Wrap Thickness mil (mm)	Strut Length, L_s in. (cm)	Outside Diameter, D_{om} in. (cm)	No. of Stiffeners, N	Predicted Ult Comp Load, P_c lbf (N)
1	Monocoque Cylinder	12 (0.30)	24.0 (61.0)	1.71 (4.34)	0	3460 (15,390)
2	Monocoque Cylinder	18 (0.46)	19.0 (48.3)	1.54 (3.91)	0	5730 (25,490)
3	Stiffened Cylinder	12 (0.30)	24.8 (63.0)	1.75 (4.45)	16	5100 (22,680)
4	Stiffened Cylinder	12 (0.30)	36.0 (91.4)	2.25 (5.72)	18	4830 (21,480)
5	Monocoque Ogive	24 (0.61)	26.0 (66.0)	1.96 (4.98)	0	8400 (37,360)
6	Monocoque Ogive	24 (0.61)	36.0 (91.4)	2.46 (6.25)	0	8400 (37,360)

The configurations selected incorporate three of the five basic types of wall construction which were investigated in the parametric analysis (Ref Table 3-2). Configurations with the other two types of construction (i.e., those with either boron fiber longos or longerons) were eliminated because the modest inert weight savings offered for some length-load design points by these designs were considered insufficient to justify the additional complexity and cost required to fabricate them. In addition, the relatively high heat leaks attributed to the boron fiber designs in general resulted in total comparative system weights greater than those for the more conventional fiberglass construction for long-duration missions (e.g. $>$ 30 days).

As shown in Table 3-4, the wall thickness, length, diameter, and compressive load capabilities of the six selected strut configurations are representative of the total ranges investigated (Ref Tables 3-1 and 3-2).

3.2 DESIGN AND ANALYSIS OF SELECTED CANDIDATES

After selection of six optimum strut configurations (Ref Section 3.1.9), preliminary design drawings of each were developed. These designs are shown in Figs. 3-31, 3-32, and 3-33, respectively, for the monocoque cylinder, stiffened cylinder, and monocoque ogive configurations. Detailed analysis of the end fittings, rod-ends, and core insulation was then conducted using these typical designs as a basis.

3.2.1 End Fittings and Rod Ends

As specified in the contract, the longo wraps for all design candidate struts are to be wound continuously over the end fittings in order to provide an integral structure (Ref Section 3.1.1). With this concept, tension loads are transferred directly from the metal end fittings to the composite strut body through bearing of the fitting on to the closed-end composite structure. Compression loads also can be transferred in bearing by the addition of metal compression caps over the longo wraps at each end. Consequently, primary loads in either direction can be transferred through the metal-to-glass joints without reliance on lap-shear through the resin bond between the metal and fiberglass parts.

Although preservation of the resin bond is not essential for primary load transfer, close matching of the thermal coefficient of expansion of the metal end fitting to that of the fiberglass is still an important design requirement. If the internal end fitting shrinks significantly more than the fiberglass during chilldown of the cold end, the resulting gap at the bond line will permit some slippage and working of the fiberglass material when cyclic loads are applied. If this occurs, local failures in inter-fiber shear and bending at points of high stress concentration will result in low fatigue life.

Other properties which are important in the selection of the end fitting

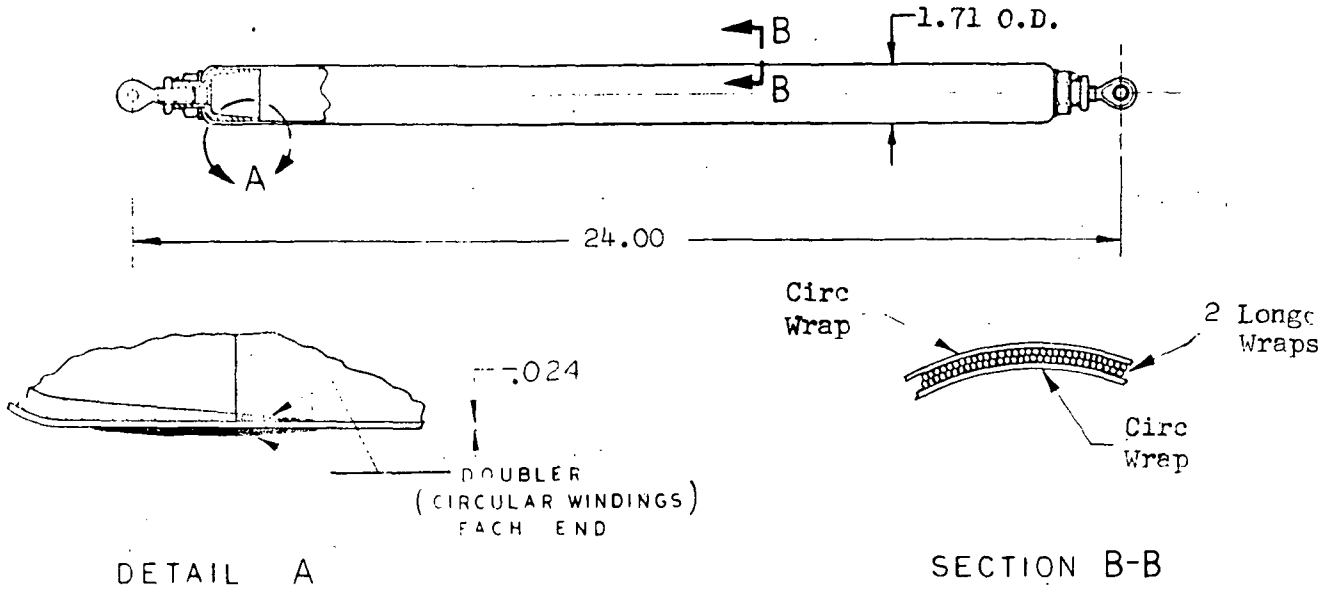

(a) Configuration No. 1

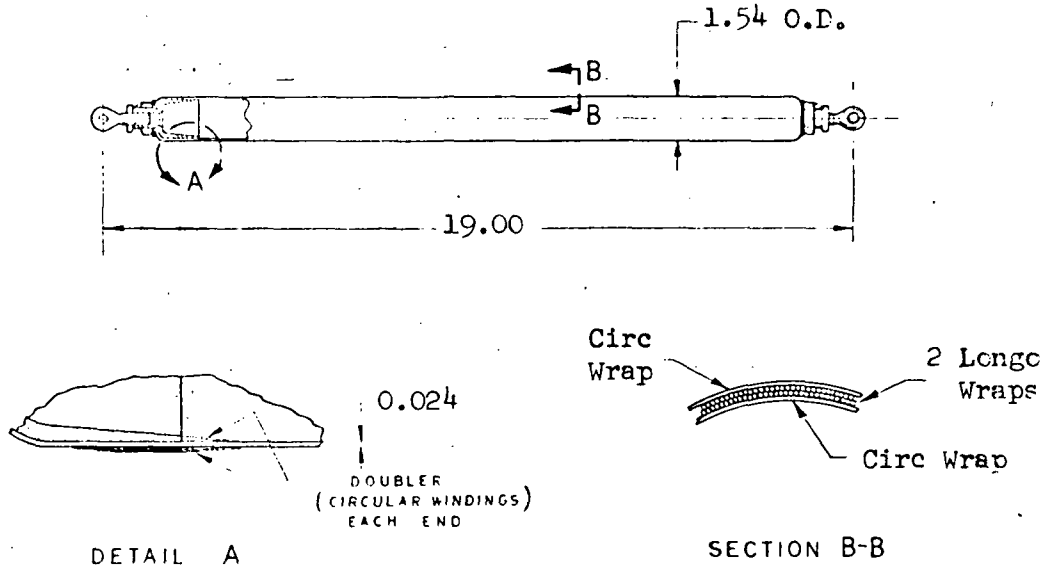

(b) Configuration No. 2

Fig. 3-31 Preliminary Design of Monocoque Cylinders

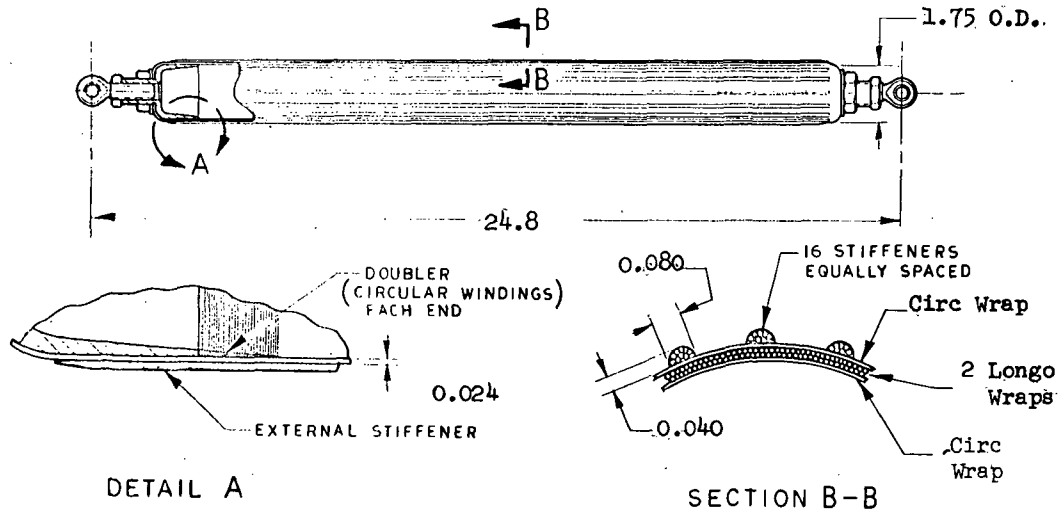

(a) Configuration No. 3

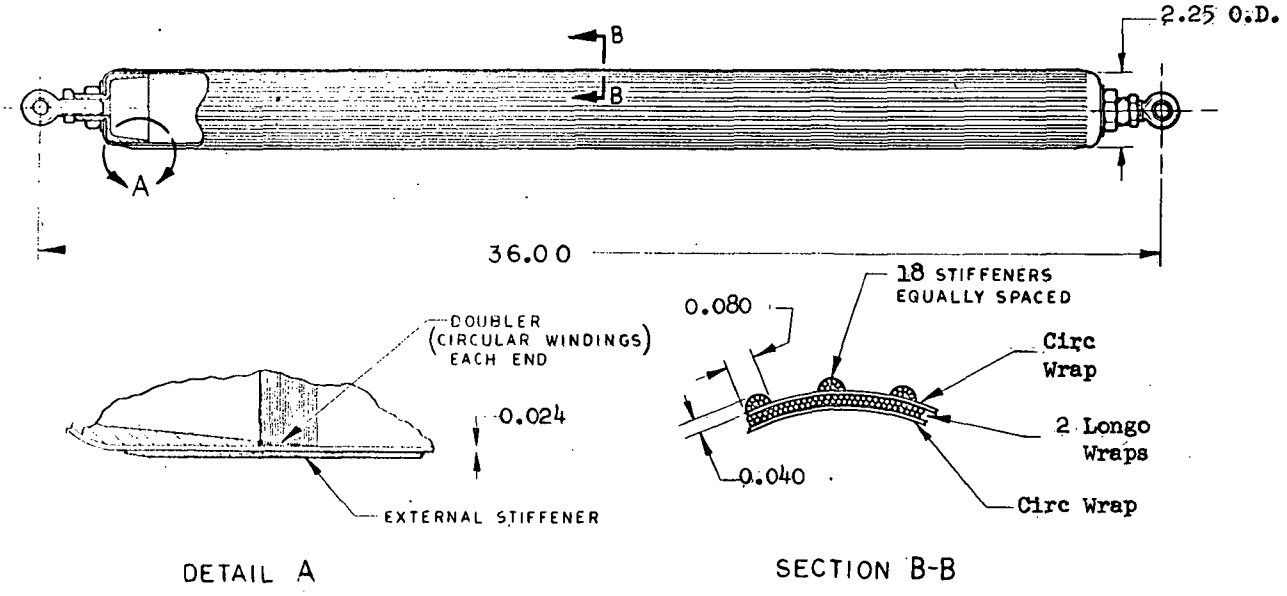

(b) Configuration No. 4

Fig. 3-32 Preliminary Design of Stiffened Cylinders

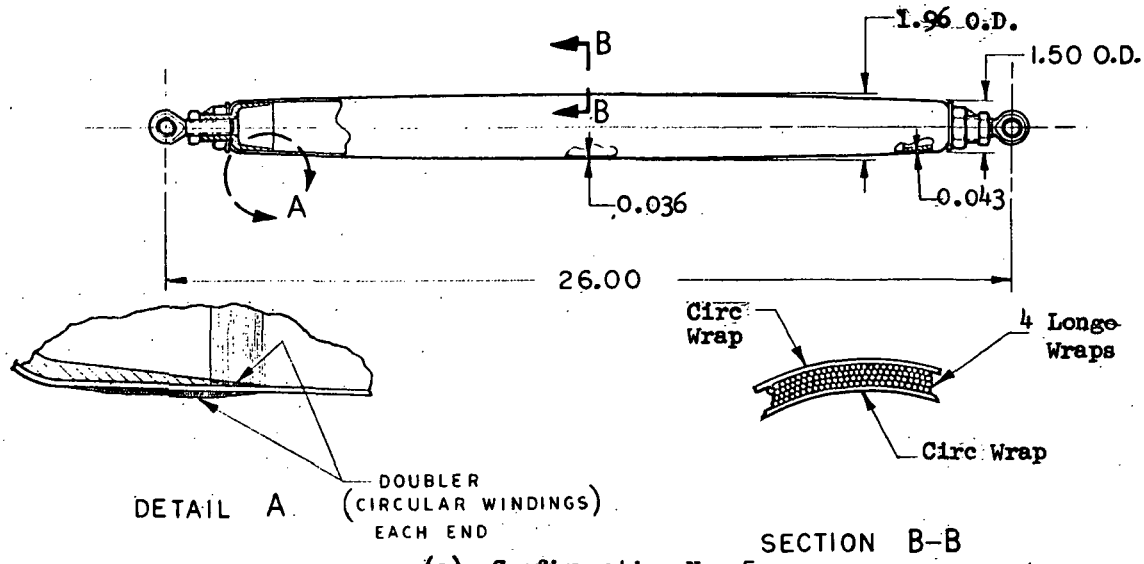

(a) Configuration No. 5

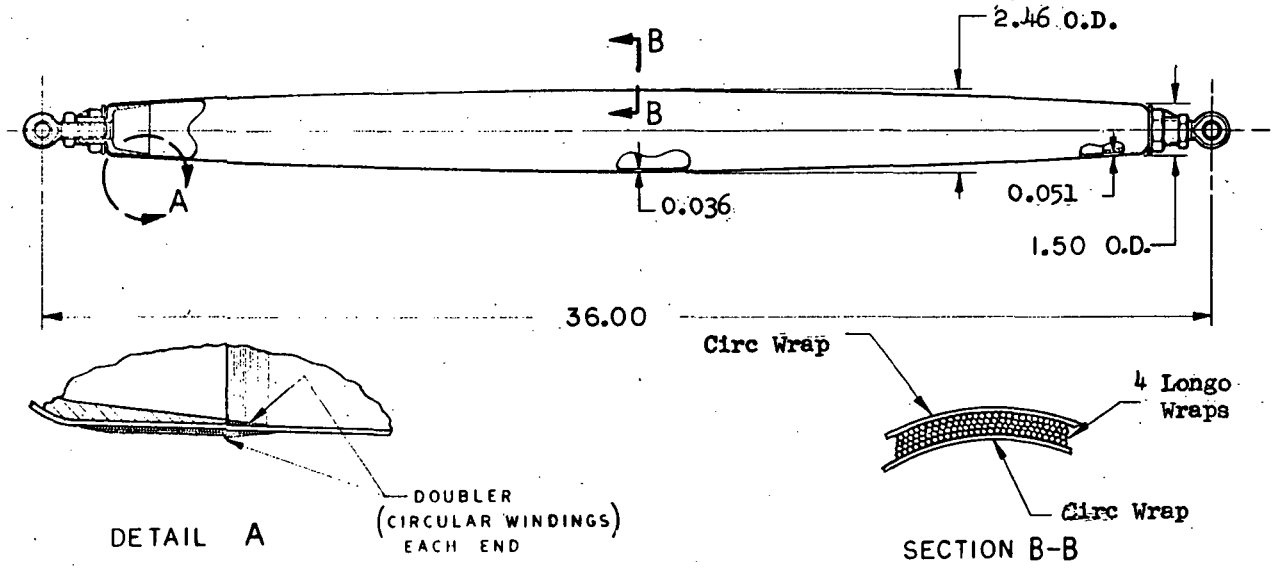

(b) Configuration No. 6

Fig. 3-33 Preliminary Design of Monocoque Ogives

material, in addition to the thermal coefficient of expansion, are density and thermal conductivity. A low density is desirable to minimize end fitting weights, while low thermal conductivity is desirable to minimize heat leaks.

Values of relative thermal expansion, density, and thermal conductivity of three candidate end-fitting and compression cap materials are compared to those of fiberglass in Table 3-5. The thermal expansion values shown were evaluated for chilldown from room temperature to LH_2 temperature and are, therefore, negative. Density values at room temperature are shown, and the thermal conductivity values presented correspond to the mean temperature for boundary temperature case 1, T_{H1} = 520°R (289°K) and T_{C1} = 37°R (20°K).

Table 3-5

COMPARISON OF PHYSICAL-THERMAL PROPERTIES OF CANDIDATE END-FITTING MATERIALS WITH THOSE OF FIBERGLASS

Material	Aluminum (2000 Series)	CRES (301)	Titanium (6 Al4V)	Fiberglass (S-Glass-Epoxy)
Expansion from 535°R (297°K) to 37°R (20°K), Percent	-0.418(Ref 5, Fig. 2-1)	-0.290(Ref 5, Fig. 2-1)	-0.167(Ref 5, Fig. 2-1)	-0.138*(Ref 5, (Fig. 3-1)
Density at 535°R (297°K), lbm/in.^{3} (gm/cm^3)	0.102(2.82) (Ref 5, Table 2-1)	0.286(7.92) (Ref 5, Table 2-1)	0.161(4.46) (Ref 5, Table 2-1)	0.0736(2.04) (Ref Section 3.1.8)
Conductivity at 278.5°R (154.7°K), Btu/hr ft°R (W/cm°K)	49(0.85) (Ref 5, Fig. 2-2)	6.7(0.12) (Ref 5, Fig. 2-3)	2.94(0.0509) (Ref 5, Fig. 2-3)	0.227(0.00393) (Ref 2, Fig. 23)

* Parallel to the glass fiber reinforcement

Titanium was selected as the most suitable material for the internal end fittings and compression caps primarily because its thermal coefficient of

expansion most nearly approaches that of the fiberglass. In chilling from 535°R (297°K) to 37°R (20°K), the titanium will contract approximately 20 percent more than fiberglass, whereas stainless steel will contract approximately 100 percent more and aluminum approximately 200 percent more. In addition, the thermal conductivity of titanium is the lowest of the metals evaluated, but still exceeds that of fiberglass by a factor of approximately 13. The conductivities of stainless steel and aluminum are greater than that of fiberglass by factors of approximately 30 and 216, respectively. Of the three metals investigated, all are more dense than fiberglass by factors of approximately 1.4 for aluminum, approximately 2.2 for titanium, and approximately 3.9 for stainless steel. Although aluminum fittings would be somewhat lighter than those fabricated from titanium, this material was eliminated from consideration on the basis of its poor thermal properties.

An initial layout drawing, showing overall dimensions and a preliminary design of the internal fittings and rod-ends for each of the six selected strut candidates, is presented in Fig. 3-34. As shown, externally-threaded Monoball* rod-ends of the SWRM series were selected for use on the cold end, while those of the DREM series** were selected for the warm end. The SWRM series fittings are recommended by the manufacturer for use with high-impact loads at cryogenic temperatures, whereas those of the DREM series are recommended for application at near room temperature and feature a very low-friction design.

Both the rod-ends and the mating internal titanium fittings were sized for the design ultimate strut loads in tension (Ref Table 3-1) multiplied by a fitting factor of 2.0. A summary of the strut loads and the resulting fitting design loads is presented in Table 3-6. The ultimate static load ratings for several sizes of rod ends in each of these series are presented

---

* Southwest Products Company, Monrovia, California

** Fittings with opposite-hand threads were selected to provide length-adjustment capability.

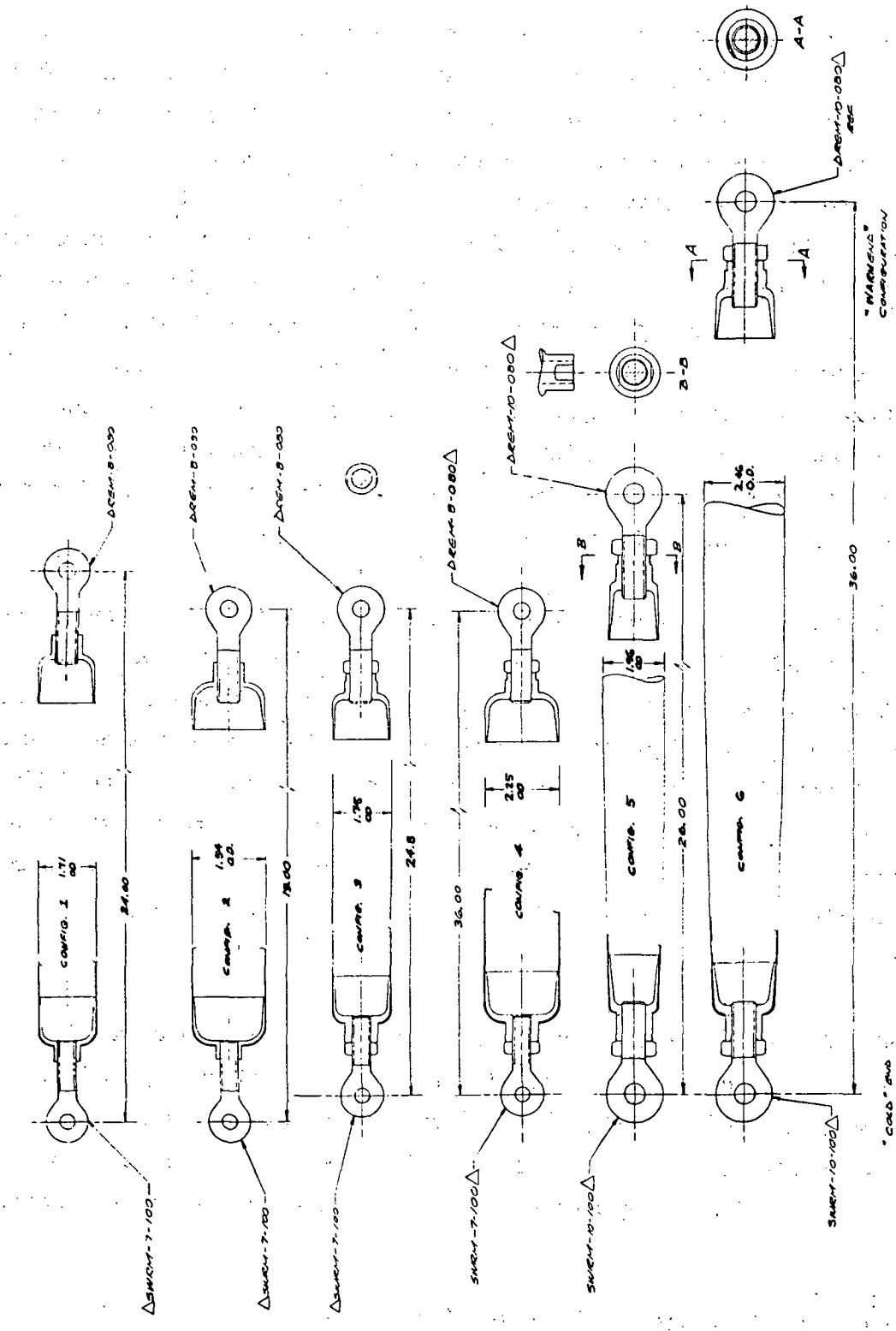

Fig. 3-34 Strut Fitting Designs with Externally-Threaded Rod-Ends

Table 3-6

SUMMARY OF STRUT AND FITTING DESIGN ULTIMATE LOADS

Strut Configuration No.	Ultimate Strut Loads				Ultimate Fitting Loads, Tension	
	Compression		Tension			
	lbf	(N)	lbf	(N)	lbf	(N)
1	3460	(15,390)	8,650	(38,480)	17,300	(76,950)
2	5730	(25,490)	14,330	(63,740)	28,660	(127,500)
3	5100	(22,680)	12,750	(56,710)	25,500	(113,400)
4	4830	(21,480)	12,080	(53,730)	24,160	(107,500)
5	8400	(37,360)	21,000	(93,410)	42,000	(186,800)
6	8400	(37,360)	21,000	(93,410)	42,000	(186,800)

in Table 3-7 (Ref 18). The double-shear ultimate load ratings of the corresponding attachment bolts are also shown. Inspection of the data given in Tables 3-6 and 3-7 shows that the SWRM-6-100 and the DREM-7-080 rod-ends would satisfy the design requirements for strut configuration 1. Similarly, the SWRM-7-100 and DREM-8-080 fittings are suitable for use with configurations 2, 3, and 4, although the 0.4375-in.-(1.111-cm-) diameter bolt for the cold end fitting is marginal in shear capability for configuration 2. Finally, the SWRM-10-100 and DREM-10-080 fittings were selected for strut configurations 5 and 6. For these latter two configurations, the warm-end rod-end load rating is also marginal. In the design study, the SWRM-7-100 and DREM-8-080 rod-end fittings were selected for strut configuration 1, as well as for configurations 2, 3, and 4, to minimize the number of different test machine clevis fittings required.

During the design and stress analysis of the internal end fittings and rod-ends shown in Fig. 3-34, two potential problem areas were encountered. First, an evaluation of the fabricability of each design showed that the ratio of strut end diameter to threaded section diameter was marginal for configurations

Table 3-7

ULTIMATE STATIC LOAD CAPABILITY FOR SWRM- AND DREM-SERIES ROD-ENDS

Part No.	Ultimate Static Load Rating lbf (n)	Attach Bolt Dia in. (cm)	Ultimate Double-Shear Rating lbf (N)
SWRM-4-100	17,200 (76,510)	0.250 (0.635)	8,600 (38,250)
SWRM-5-100	22,700 (101,000)	0.3125 (0.794)	13,500 (60,050)
SWRM-6-100	30,000 (133,400)	0.375 (0.953)	20,400 (90,740)
SWRM-7-100	35,200 (156,600)	0.4375 (1.111)	27,800 (123,700)
SWRM-8-100	53,000 (235,700)	0.500 (1.270)	34,600 (153,900)
SWRM-10-100	64,500 (286,900)	0.625 (1.588)	54,000 (240,200)
DREM-4-080	6,100 (27,130)	0.250 (0.635)	8,600 (38,250)
DREM-5-080	12,900 (57,380)	0.3125 (0.794)	13,500 (60,050)
DREM-6-080	15,200 (67,610)	0.375 (0.953)	20,400 (90,740)
DREM-7-080	19,200 (85,400)	0.4375 (1.111)	27,800 (123,700)
DREM-8-080	29,000 (129,000)	0.500 (1.270)	34,600 (153,900)
DREM-10-080	41,200 (183,300)	0.625 (1.588)	54,000 (240,200)

1 and 3, and was very likely below the minimum practical limit for satisfactory placement and stability of the polar-wound longo rovings for configuration 5. Although the actual minimum limit for this ratio has not been determined experimentally, it was found during fabrication of prototype strut hardware for Contract NAS 3-7979 that the tendency for yarn slippage increases significantly as this ratio is reduced. This characteristic prompted the selection of a 1.5-in. (3.81-cm) minimum diameter for the struts of this study (Ref Section 3.1.1).

The other potential problem area encountered in the design study was that of establishing an adequate design criteria and determining suitable allowables for the internally-threaded titanium end fittings. No data could be found in the literature regarding the notch fatigue strength of either titanium or stainless steel bar stock at cryogenic temperatures. Available data on annealed sheet stock from Ref 21 show generally high notch fatigue strengths for Ti-6Al-4V-ELI, Ti-5Al-2.5 Sn-ELI, and AISI-301 stainless steel. In addition, MIL-HDBK-5B (Ref 22) indicates generally good toughness characteristics down to LH_2 temperature for both of these titanium alloys in the ELI

grade. Since the struts designed and fabricated in this program were to be subjected to cyclic loads at full design limit stress values, the fatigue life capability of the end fittings was an important consideration.

As a possible solution to both of these problems, strut designs with externally-threaded internal end fittings (and mating internally-threaded rod-ends) were evaluated. A layout drawing of the six selected strut configurations with fittings of this type is presented in Fig. 3-35. These designs provide somewhat higher strut end diameter to threaded section diameter ratios, with improved longo winding characteristics. In addition, rolled threads can now be used to enhance the fatigue life capability of the internal titanium end fittings. Lacking specific design allowable data, a conservative working stress level of 50,000 psi in net section tension was assumed for application of the ultimate design fitting loads (Ref Table 3-6). Data obtained from the rod-end manufacturer* indicated that the internally-threaded stainless steel rod ends could provide adequate cycle life capability for selected series fittings.

Initially, for the designs shown in Fig. 3-35, SWRF series fittings were selected for the cold end with DREF series fittings (not shown) for the warm end. However, the data obtained showed extremely poor fatigue life capability at high load levels for the SWRF series, and indicated that the Dyflon® bearing material used to obtain low friction for the DREM and DREF series fittings was also not suitable for high-level cyclic load applications. Based on the manufacturer's recommendations, the 2BREF series fittings shown in Fig. 3-35 were finally selected for use on both the cold and warm ends of the strut. These fittings are of all stainless-steel construction, employ a molybdenum film lubricant on both ball and race, and offer excellent fatigue life capability for cyclic load applications. A summary of the data obtained on static and cyclic load capabilities of the SWRF and 2BREF series rod-ends is presented in Table 3-8 for comparison. It can be seen from inspection of these data

* Southwest Products Company, Monrovia, California

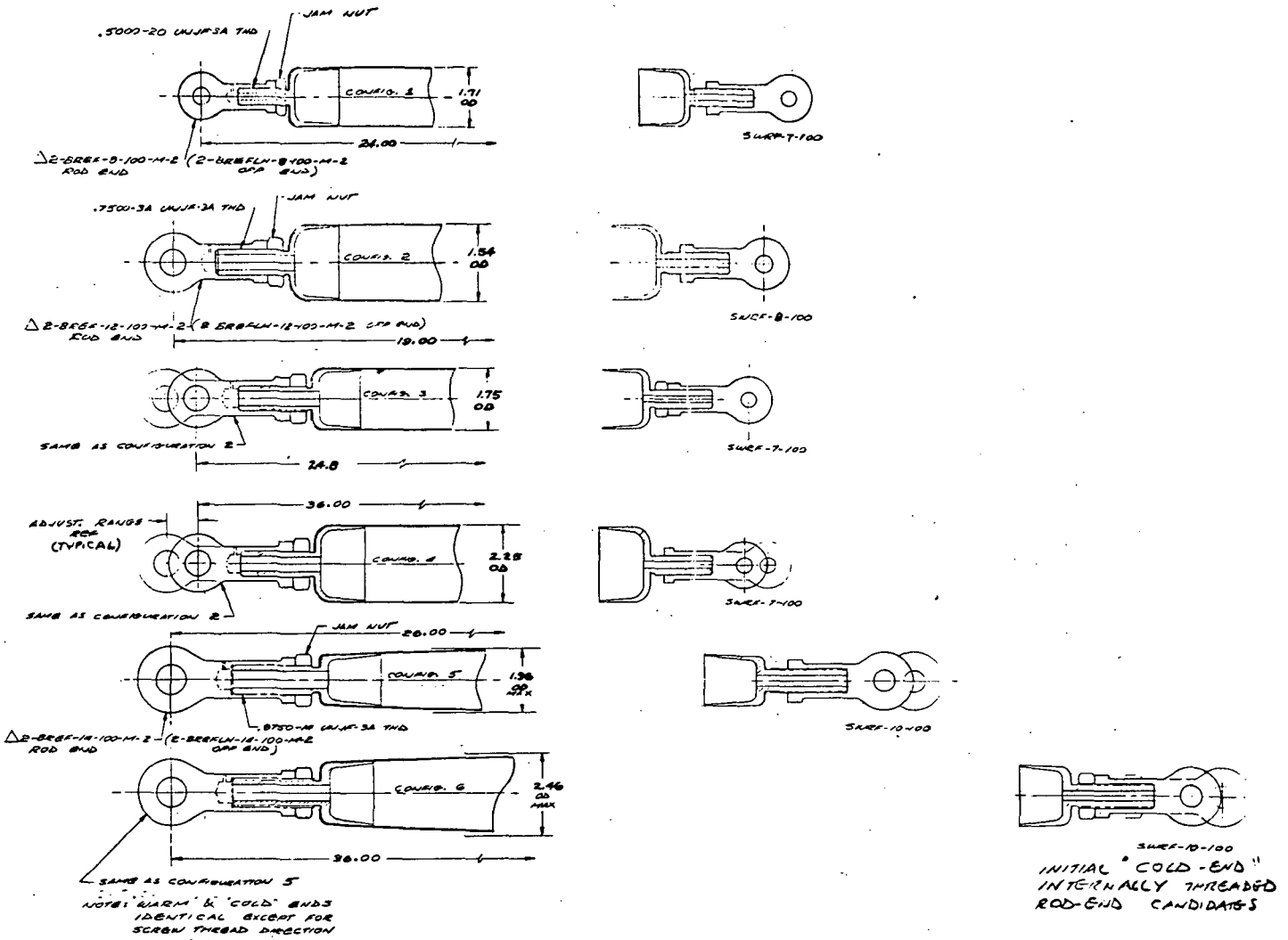

Fig. 3-35 Strut Fitting Designs with Internally-Threaded Rod-Ends

Table 3-8

SUMMARY OF STATIC AND CYCLIC LOAD CAPABILITY FOR SWRF AND 2BREF SERIES ROD-ENDS

Strut Configuration No.	Rod-End Part No.	Static Load Capability lbf (N)	Cyclic Load Capability lbf (N)	No. of Cycles to Failure
1	SWRF-7-100	35,200 (156,600)	6,175[1] (27,470)	80,000
2	SWRF-8-100	53,000 (235,700)	10,240[1] (45,550)	57,000[2]
3	SWRF-7-100	35,200 (156,600)	9,110[1] (40,520)	12,800[2]
4	SWRF-7-100	35,200 (156,600)	8,630[1] (38,390)	14,300[2]
5	SWRF-10-100	64,500 (286,900)	15,000[1] (66,720)	24,000[2]
6	SWRF-10-100	64,500 (286,900)	15,000[1] (66,720)	24,000[2]
1	2BREF-8-100	22,400 (99,640)	14,500 (64,500)	25,000
			7,200 (32,030)	100,000
			6,100 (27,130)	200,000
			5,600 (24,910)	400,000
			4,950 (22,020)	800,000
	2BREF-10-100	26,000 (115,600)	17,000 (75,620)	25,000
			8,600 (38,250)	100,000
			7,300 (32,470)	200,000
			6,750 (30,020)	400,000
			5,950 (26,470)	800,000
2, 3 and 4	2BREF-12-100	33,300 (148,100)	12,000 (53,380)	100,000
			10,200 (45,370)	200,000
			9,450 (42,030)	400,000
			8,300 (36,920)	800,000
5 & 6	2BREF-14-100	49,200 (218,800)	16,800 (74,730)	100,000
			14,200 (63,160)	200,000
			13,100 (58,270)	400,000
			11,600 (51,600)	800,000

Notes: (1) Values shown correspond to design limit strut loads in tension.
(2) Approximate values based on interpolation of Manufacturer's data.

that the 2BREF series of fittings offers significantly greater cycle life capability than does the SWRF series, ranging from approximately 165,000 cycles at the design limit tension load for strut configurations 5 and 6 to approximately 650,000 cycles at the design limit tension load for configuration 4.

During the study, an additional internal end fitting concept was also evaluated which relies on lap-shear through the resin bond to achieve load transfer from the metal end fitting to the fiberglass strut body. With this design, the external compression caps are not required. Although slightly lighter for some strut configurations, this concept was eliminated primarily because of the poor fatigue life capability of the bonded joint. An internal conical doubler was employed to reduce the shear stress level, but high stress concentrations result none-the-less where the titanium fitting terminates due to the great difference in relative stiffness of the titanium and fiberglass components.

Based on the tradeoff studies described above, titanium end fittings with rolled external threads were selected for all strut configurations. Internally-threaded rod-end fittings of the 2BREF series were also selected for use on both the cold and warm ends of each configuration.

3.2.2 Core Insulation Analysis

A hollow support strut provides a path for radiation tunneling. This can have a profound effect on the temperature distribution in the strut wall and on the net heat transfer into the propellant tank. Parametric data has been developed by Brogan (Ref 23) which accounts for the complex interactions between the parallel radiation and conduction paths in a cryogenic tank penetration. Applying this data to strut configuration 1 (Ref Table 3-4) indicates that the net effect of the radiation tunnel is to increase the heat leak through the support by a factor of 8 over that due to conduction in the fiberglass wall. Therefore, it is necessary to find an effective

method to eliminate the radiation tunnel.

An analysis was conducted to compare the performance of three candidate core insulation concepts. These are (1) closed-cell polyurethane foam (which also would provide some additional crippling capability by supporting the strut wall), (2) chopped Dexiglas, and (3) spaced metallized Mylar radiation shields. System geometry, heat rates, and system inert weights were computed for each of these candidates using strut configuration 1 for the comparison. It was assumed that the strut would be used to support a LH_2 tank in space for a mission duration of 220 days (5280 hours). Boundary temperatures were assumed to be 520°R (289°K) and 37°R (20°K) at the warm and cold ends of the strut, respectively.

For the polyurethane foam and chopped Dexiglas candidates, heat transfer rates for the composite system were computed as the sum of the conduction components through the glass fiber shell and through the core material assuming negligible interaction effects. For evaluating the metallized Mylar radiation shield candidate, it was assumed that the shield spacing would be sufficiently close that the view factor between successive shields would be unity and the radiation would be decoupled from the strut wall. The general equation for net radiation heat transfer through n successive shields is given by

$$Q_R = \frac{\epsilon_{os}\epsilon_{ss}\sigma A_R(T_H^4 - T_C^4)}{(n-1)\epsilon_{os} + 2\epsilon_{ss}} \qquad (3\text{-}10)$$

where

$$\epsilon_{os} = \frac{\epsilon_o \epsilon_s}{\epsilon_s + \epsilon_o - \epsilon_o\epsilon_s} \quad \text{and} \quad \epsilon_{ss} = \frac{\epsilon_s}{2 - \epsilon_s}$$

If the assumptions are made that $n \gg 1$, and $\epsilon_o = \epsilon_s$, Equation (3-10) reduces to

$$Q_R = \frac{\sigma A_R(T_H^4 - T_C^4)}{(2/\epsilon_s - 1)(n-1)} \qquad (3\text{-}11)$$

The ratio of radiant heat transfer to that conducted down the wall can be written as

$$\frac{Q_R}{Q_C} = \frac{A_R \sigma (T_H^4 - T_C^4) L_c}{(n-1)(2/\epsilon_s - 1) A_c k_c (T_H - T_C)} \tag{3-12}$$

The approach used herein was to select acceptable values for Q_R/Q_C and solve for the required number of shields. It is convenient to rearrange Equation (3-12) as follows:

$$\frac{n-1}{L_c} = \frac{(A_R/k_c A_c)(T_H + T_C)(T_H^2 + T_C^2)}{(2/\epsilon_s - 1)(Q_R/Q_C)} \tag{3-13}$$

For strut configuration 1, the quantity $(A_R/k_c A_c)$ is approximately 80 hr ft°R/Btu (4620 cm°K/W). Using this constant, the shield spacing density was computed for values of Q_R/Q_C = 0.10 and 0.02, and shield emmissivities, ϵ_s, of 0.10 and 1.0. The results are presented in Table 3-9. For the higher heat rate ratio and the lower emmissivity, the spacings are sufficiently high

Table 3-9

REQUIRED RADIATION SHIELD SPACING DENSITY, n/L_c, shields/in. (shields/cm)

T_H	T_C	Q_R/Q_C = 0.1		Q_R/Q_C = 0.02	
°R (°K)	°R (°K)	ϵ_s = 0.1	ϵ_s = 1.0	ϵ_s = 0.1	ϵ_s = 1.0
520 (289)	37 (20)	1.0 (0.4)	17 (6.7)	4.5 (1.8)	85 (33)
	140 (78)	1.2 (0.5)	22 (8.7)	6.0 (2.4)	110 (43)
400 (222)	37 (20)	0.5 (0.2)	8 (3.1)	2.0 (0.8)	40 (16)
	140 (78)	0.7 (0.3)	11 (4.3)	3.0 (1.2)	55 (22)

that the view factor is less than unity. Although the direct radiation is

less than that calculated, the reduction is partially offset by increased radiation to the strut wall. The significant conclusion from this simplified radiation model is that it takes relatively few shields to effectively reduce the radiation tunneling.

The comparative evaluation of the three core insulation concepts is presented in Table 3-10, along with the geometry and thermal-physical properties used in the computations. The heat rate for the glass fiber shell includes the total effect of the tunneling and emphasizes the need for the barrier. The chopped Dexiglas is approximately 30 percent more effective than the foam core. The radiation barrier concept was compared by selecting only enough shields to reduce the core heat flux to the same level ($Q_R/Q_C = 0.018$) as for the chopped Dexiglas. The corresponding density is approximately 5 shields/in. (2 shields/cm). The difference in total weight penalty between the Dexiglas core and the Mylar shields is insignificant. Reducing the number of shields below 74 would increase the heat rate with a miniscule reduction in inert weight. Conversely, the core heat rate is less than 2 percent of that conducted down the strut body wall, and a large increase in the number of shields would not materially reduce the total weight penalty.

Although the spaced Mylar shield system is theoretically optimum based on weight, some additional weight penalty would be incurred to install and support the shields. Since the weight penalty associated with the chopped Dexiglas system is insignificant in comparison, and since this system can be installed with relative ease and without regard for surface optical properties, this candidate was selected for use throughout the program.

3.2.3 Development of Final Designs

Four of the six basic strut configurations which were investigated during the Task 1 end fitting and core insulation studies were selected for fabrication and experimental screening tests under Task 2. Some dimensional changes, with respect to those given in Table 3-4, were made to reflect the selection

Table 3-10

COMPARISON OF SYSTEM HEAT TRANSFER AND WEIGHT[1] DATA FOR STRUT CONFIGURATION 1 WITH THREE CANDIDATE RADIATION BARRIERS

Candidate Component	Glass Fiber Shell	Polyurethane Foam Core	Chopped Dexiglass Core	Spaced Mylar Radiation Shield Core
k_c, Btu/hr ft°R at 278°R (W/cm°K at 154.4°K)	0.235[2] (0.00407)	0.006[3] (0.0001)	0.000245 (0.00000424)	N/A
ρ, lbm/ft^3 (kg/m^3)	127.2[5] (2038)	2.5[6] (40)	4.3[4] (69)	N/A[7]
L_c, ft (m)	1.317 (0.401)	1.317 (0.401)	1.317 (0.401)	1.317 (0.401)
A_c, ft^2 (m^2)	0.000916 (0.000085)	0.0158 (0.00147)	0.0158 (0.00147)	N/A
V, ft^3 (m^3)	0.00121 (0.000034)	0.0208 (0.00059)	0.0208 (0.00059)	N/A
n(ϵ_s=0.10)	N/A	N/A	N/A	74
Q_{core}, Btu/hr (W)	0.555 (0.163)	0.0348 (0.0102)	0.00142 (0.00042	0.00142 (0.00042)
Q_{total}, Btu/hr (W)	0.633 (0.185)	0.114 (0.0334)	0.080 (0.023)	0.080 (0.023)
W_{inert}, lbm (kg)	0.153 (0.069)	0.052 (0.024)	0.089 (0.040)	0.002 (0.0009)
$W_{boiloff}$, lbm (kg)	17.85 (8.10)	3.688 (1.673)	2.250 (1.021)	2.250 (1.021)
W_{total}, lbm (kg)	18.00 (8.16)	3.740 (1.696)	2.339 (1.061)	2.252 (1.022)

Notes: (1) System inert weights shown exclude all strut end fitting components since these do not influence the tradeoff of radiation barrier weights.

(2) Ref Fig. 3-20.

(3) Ref 24, Page 20.

(4) Ref 25, Fig. 43

(5) Ref 1, Fig. 6-83.

(6) Ref 3, Pages 39 and 40.

(7) Each shield cut from double-aluminized 1/4-mil Mylar with a surface area of 2.275 in.^{2} (14.7 cm^2) and a unit weight of 3.153×10^{-5} lbm (1.430×10^{-5} kg).

of different load-length design points. A summary of the general design requirements for these configurations is presented in Table 3-11.

Table 3-11

SUMMARY OF DESIGN REQUIREMENTS FOR SELECTED TASK 2 STRUTS

Configuration No.	II-1	II-2	II-3	II-4
Configuration Description	Monocoque Cylinder	Monocoque Cylinder	Stiffened Cylinder	Monocoque Ogive
Longo Wrap Thickness, mil (mm)	12(0.30)	18(0.46)	12(0.30)	24(0.61)
Strut Length, in.(cm)	24.0(61.0)	19.0(48.3)	19.0(48.3)	36.0(91.4)
Midspan Outside Dia, in. (cm)	1.5(3.81)	1.5(3.81)	1.5(3.81)	2.5(6.35)
End Outside Dia.,in(cm)	1.5(3.81)	1.5(3.81)	1.5(3.81)	1.85(4.70)
No. of Glass-Fiber Stiffeners	0	0	16	0
Predicted Ult Comp Load, lbf (N)	2300 (10230	5300 (23570)	5900 (26240)	8400 (37360)
Predicted Ult Tension Load, lbf (N)	5750 (25580)	13250 (58940)	14750 (65610)	21000 (93410)
Design Ult Fitting Load, lbf (N)	11500 (51150	26500 (117900)	29500 (131200)	42000 (186800)
Design Limit Cyclic Load, lbf (N)	4110 (18280)	9460 (42080)	10540 (46880)	15000 (66720)

Based on these requirements design drawings were prepared for each of the selected configurations*. The titanium internal end fittings were designed, and mating rod-end fittings were selected, to satisfy these requirements. The 2BREF-8-100 rod-end selected for configuration II-1 provides approximately double the required ultimate static load rating (Ref Table 3-8) compared to the design ultimate fitting load shown in Table 3-11. Also, at the predicted limit strut tension load (i.e., the design limit cyclic load), the rated

* These drawings were subsequently revised to incorporate requirements for the Task 3 struts. The revised drawings are presented later in this section.

fatigue life for this fitting is in excess of 800,000 cycles. However, selection of the next smaller size (2BREF-7-100) would significantly reduce the static and cycle-life performance with a reduction in weight of only 0.1 lbm (0.045 kg).

The 2BREF-10-100 rod-end selected for configurations II-2 and II-3 is marginal with respect to the ultimate static load rating, but provides an adequate fatigue life capability of approximately 75,000 cycles. For strut configuration II-4, the 2BREF-14-100 rod-end provides approximately 15 percent more than the required ultimate static load rating, with an estimated fatigue life of approximately 150,000 cycles at the predicted limit tension load. The next smaller rod-end (2BREF-12-100) does not provide adequate ultimate static load capability, and is marginal in cycle life as well.

Subsequent to completion of the Task 2 tests, the compressive load design data developed previously in Task 1 were revised and updated to reflect the elastic modulus values obtained from the tests. Detailed discussions of these tests and the results obtained from them are presented in Sections 4 and 7.

Data on the compressive modulus of elasticity for composite fiberglass struts are presented in Fig. 3-36 as a function of the percent of fibers in the longo direction. As shown, values for all-circ and all-longo designs were taken from MIL-HDBK-17A (Ref 26). Values shown for designs with 50-, 60-, and 63.5-percent longos were obtained from the Task 2 tests results. The smooth curve drawn through the data was used for all subsequent analysis conducted during the program.

Revised ultimate compressive loads as a function of strut length and outside diameter are presented in Figs. 3-37, 3-38, and 3-39, respectively, for monocoque fiberglass cylinders with longo wrap thicknesses of 12, 18, and 24 mil (0.30, 0.46, and 0.61 mm). Column buckling allowables, P_C, were computed using equation (3-1) and the elastic modulus data from Fig. 3-36. As in the initial parametric analysis, orthotropic crippling cut-off values, P_{CRP}, were

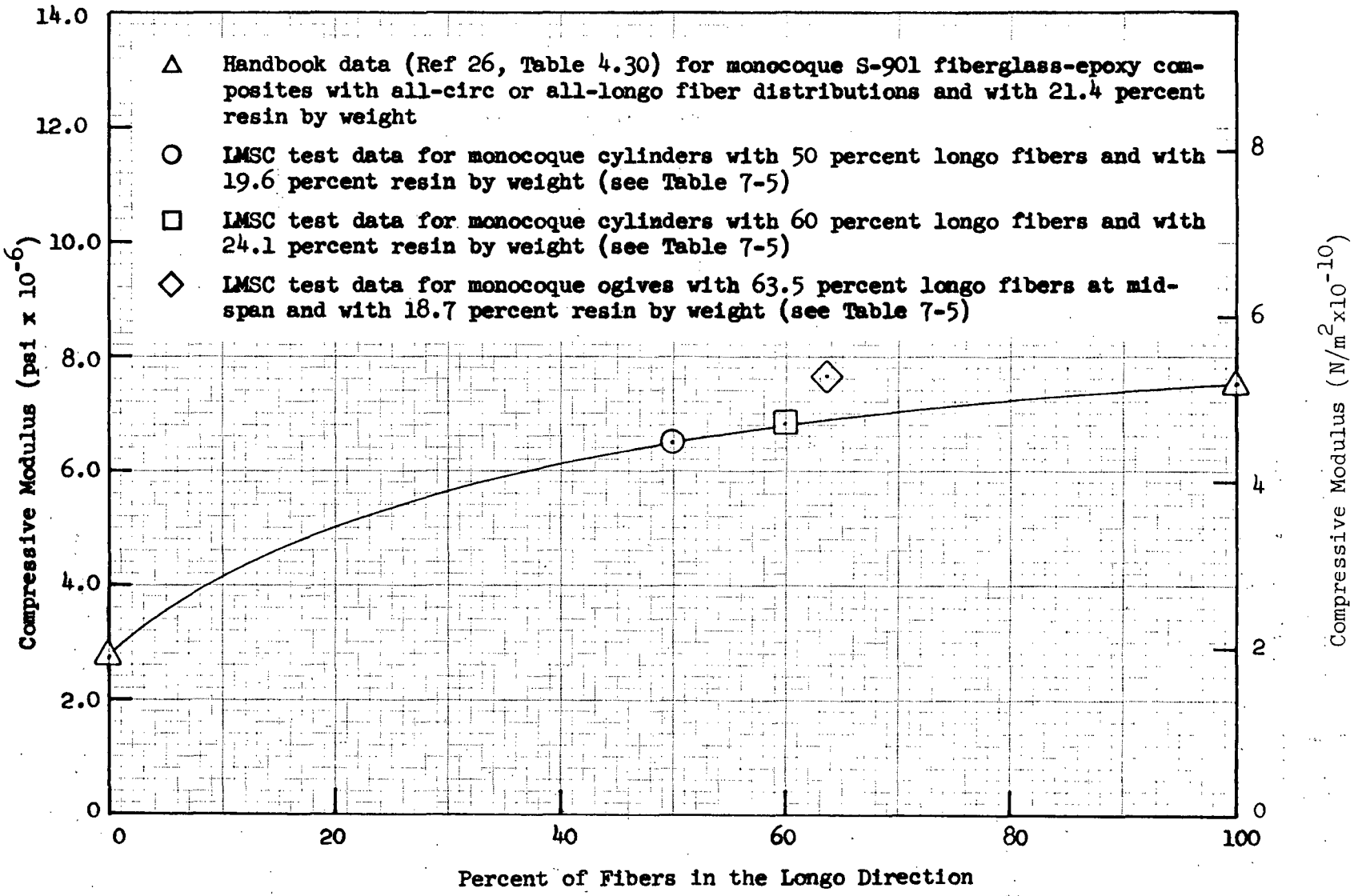

Fig. 3-36 Compressive Modulus of Elasticity for Fiberglass Struts as a Function of Fiber Distribution

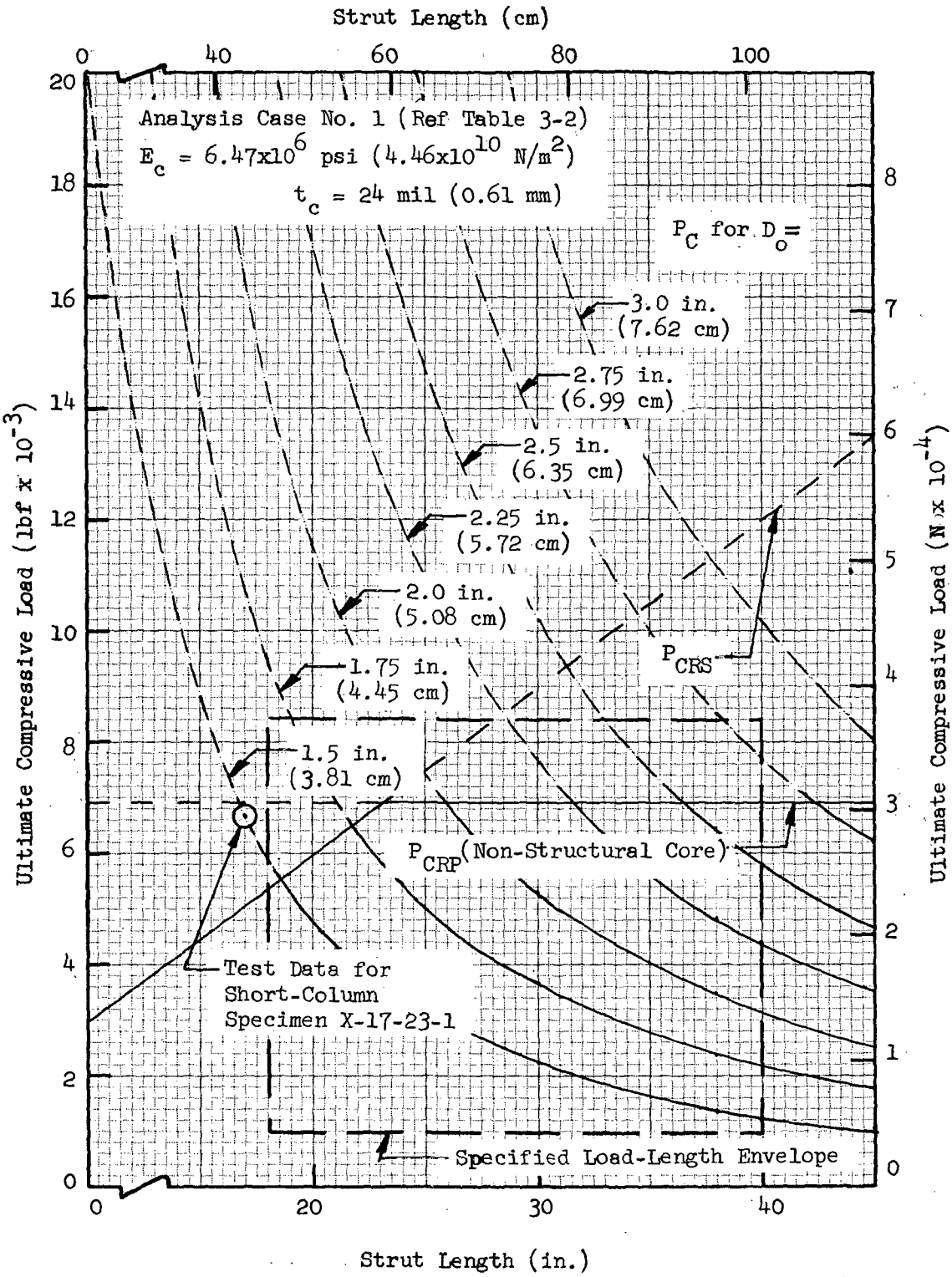

Fig. 3-37 Revised Ultimate Compressive Loads for Monocoque Fiberglass Cylinders with a 12-mil (0.30-mm) Longo Wrap Thickness

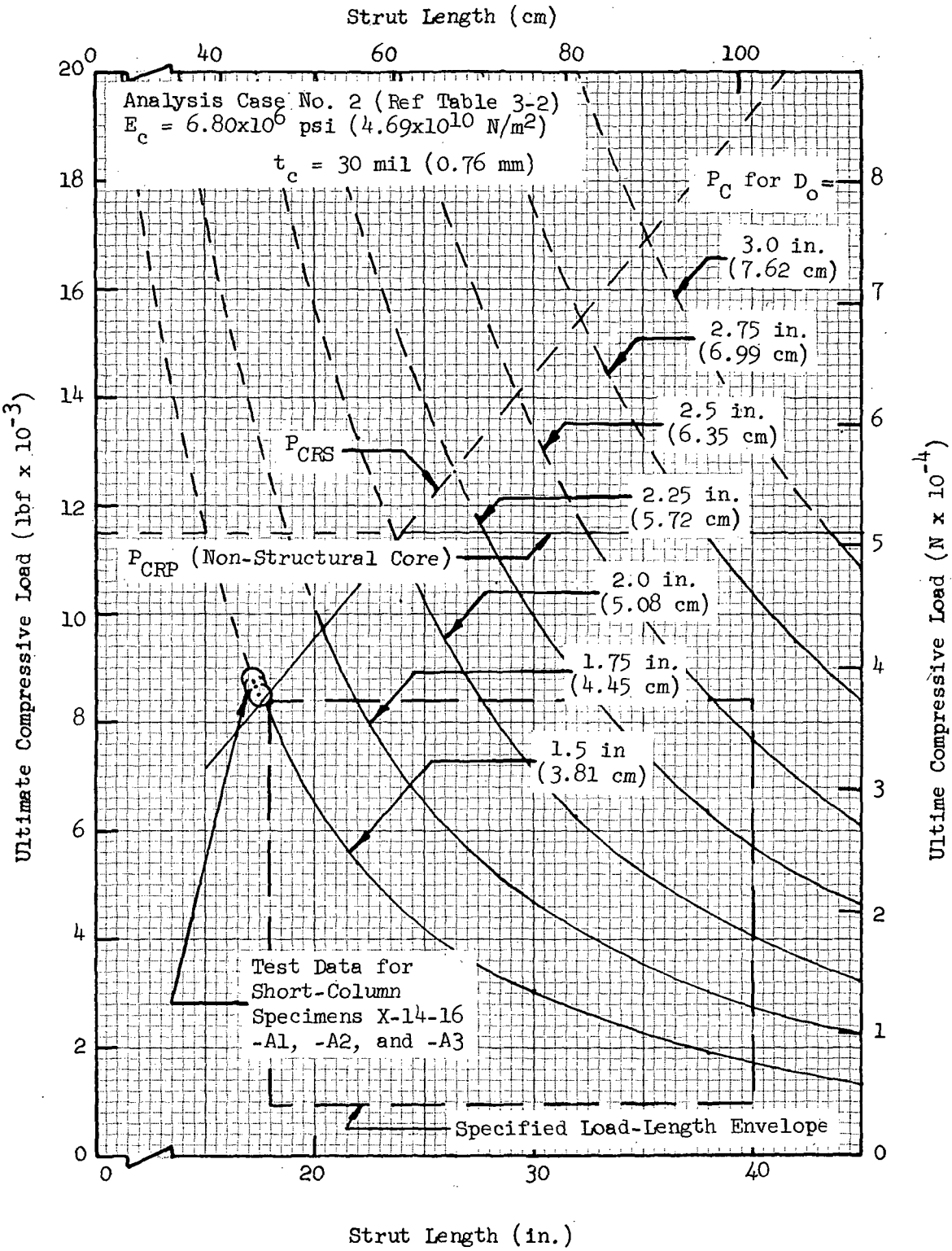

Fig. 3-38 Revised Ultimate Compressive Loads for Monocoque Fiberglass Cylinders with an 18-mil (0.46-mm) Longo Wrap Thickness

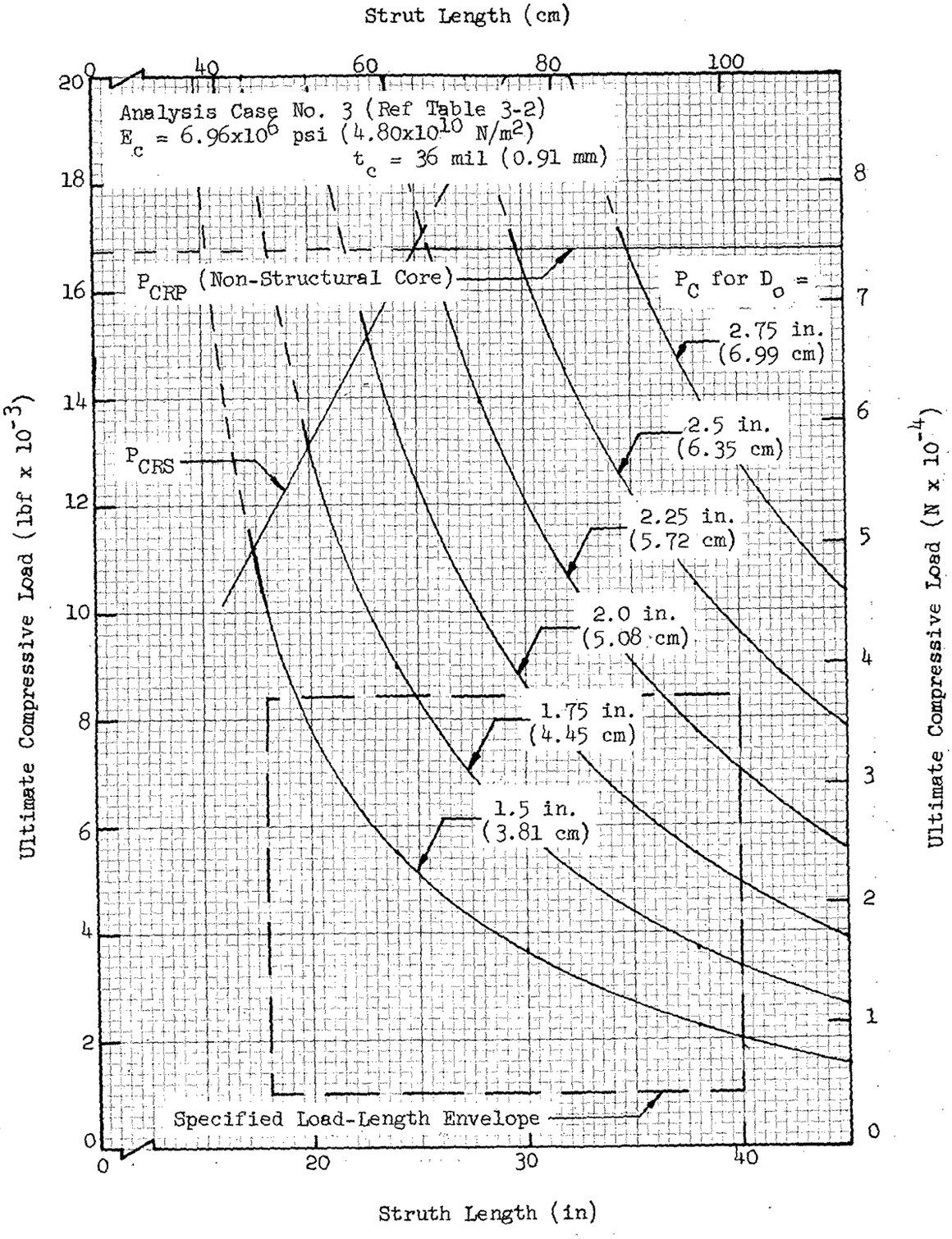

Fig. 3-39 Revised Ultimate Compressive Loads for Monocoque Fiberglass Cylinders with a 24-mil (0.61-mm) Longo Wrap Thickness

computed for struts with non-structural cores only using equation (3-3) and the BARSIN computer program. Also, since some of the specimens tested in Task 2 exhibited failures in compressive crushing of the composite material, cut-off values for allowable crushing loads, P_{CRS}, were included in these figures. These allowables were computed as the product of the longo composite area and an ultimate crushing stress of 100,000 psi (6.9×10^8 N/m^2) (Ref 26, Table 4.30). Note that the crushing cut-off allowables increase with increasing diameter, whereas the crippling cut-off allowables are independent of diameter.

The boundaries of the load-length design envelope specified in the contract (Ref Table 3-1) are superimposed on the data presented in each figure for reference. Also, in those areas of each design map where failures are predicted in any one of the three primary failure modes, the data are shown as broken-line curves. Where solid-line data curves are shown, no failures are predicted.

Similar design maps showing revised ultimate compressive loads as a function of strut length and outside diameter at midspan are presented in Figs. 3-40, 3-41, and 3-42, respectively, for monocoque fiberglass ogives with longo wrap thicknesses at midspan of 12, 18, and 24 mil (0.30, 0.46, and 0.61 mm). As for the cylindrical strut designs, cut-off values of ultimate crippling and crushing loads, together with the boundaries of the specified load-length design envelope, are superimposed on the column buckling curves in each figure.

Cross-plots of the revised ultimate compressive loads (Figs. 3-37 through 3-42) as a function of nominal longo wrap thickness were employed to determine the characteristics of optimum designs (i.e., those where predicted ultimate loads are equal for two of the three primary failure modes, and are either equal or greater for the third mode). These plots are presented in Figs. 3-43, 3-44, and 3-45, respectively, for strut with the same general construction, lengths, and diameters as those specified in Table 3-11 for configurations II-1, II-2, and II-4. Configuration II-3 was not selected for further investigation. It can be seen by inspection of these figures that the designs recommended for further investigation

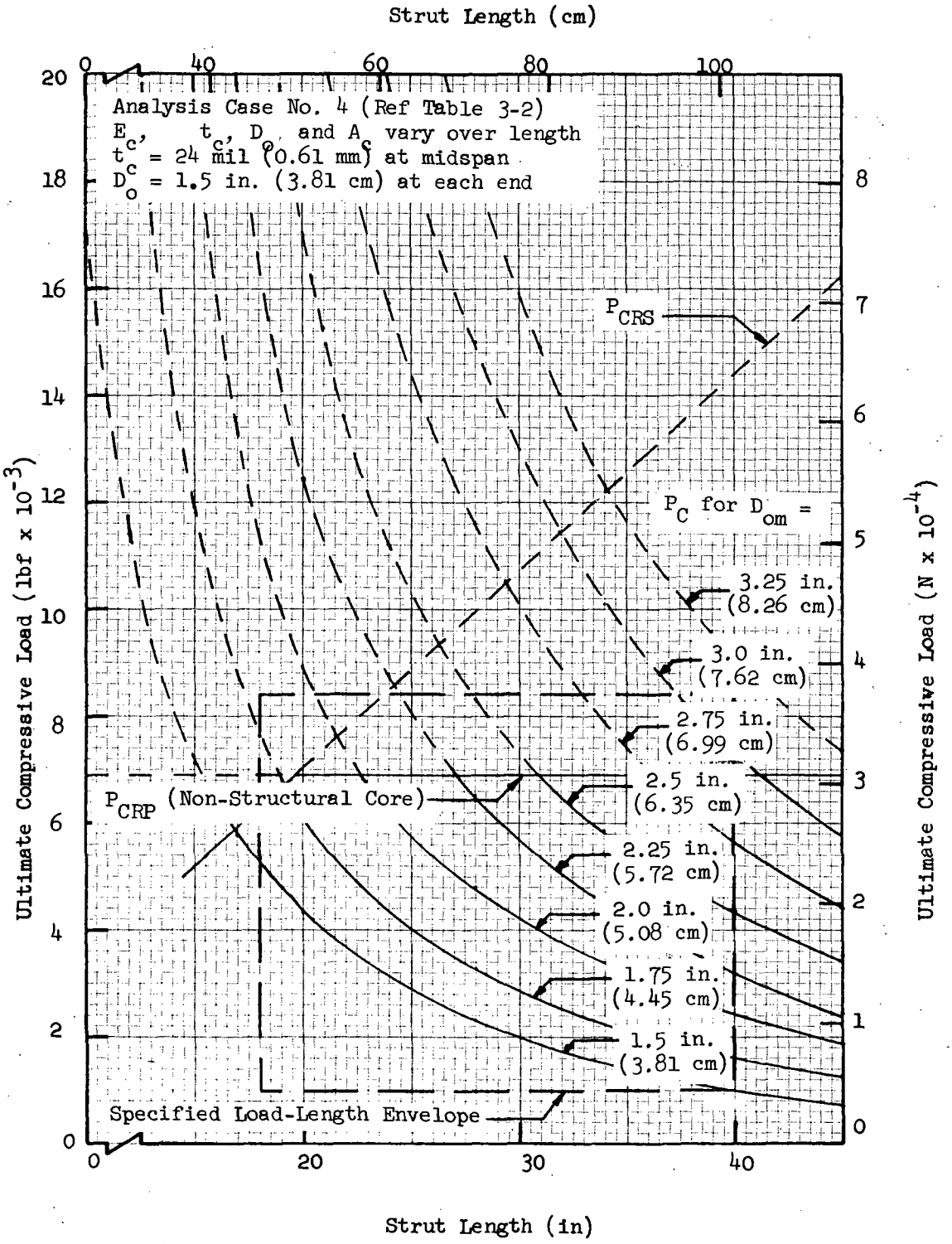

Fig. 3-40 Revised Ultimate Compressive Loads for Monocoque Fiberglass Ogives with a 12-mil (0.30-mm) Longo Wrap Thickness at Midspan

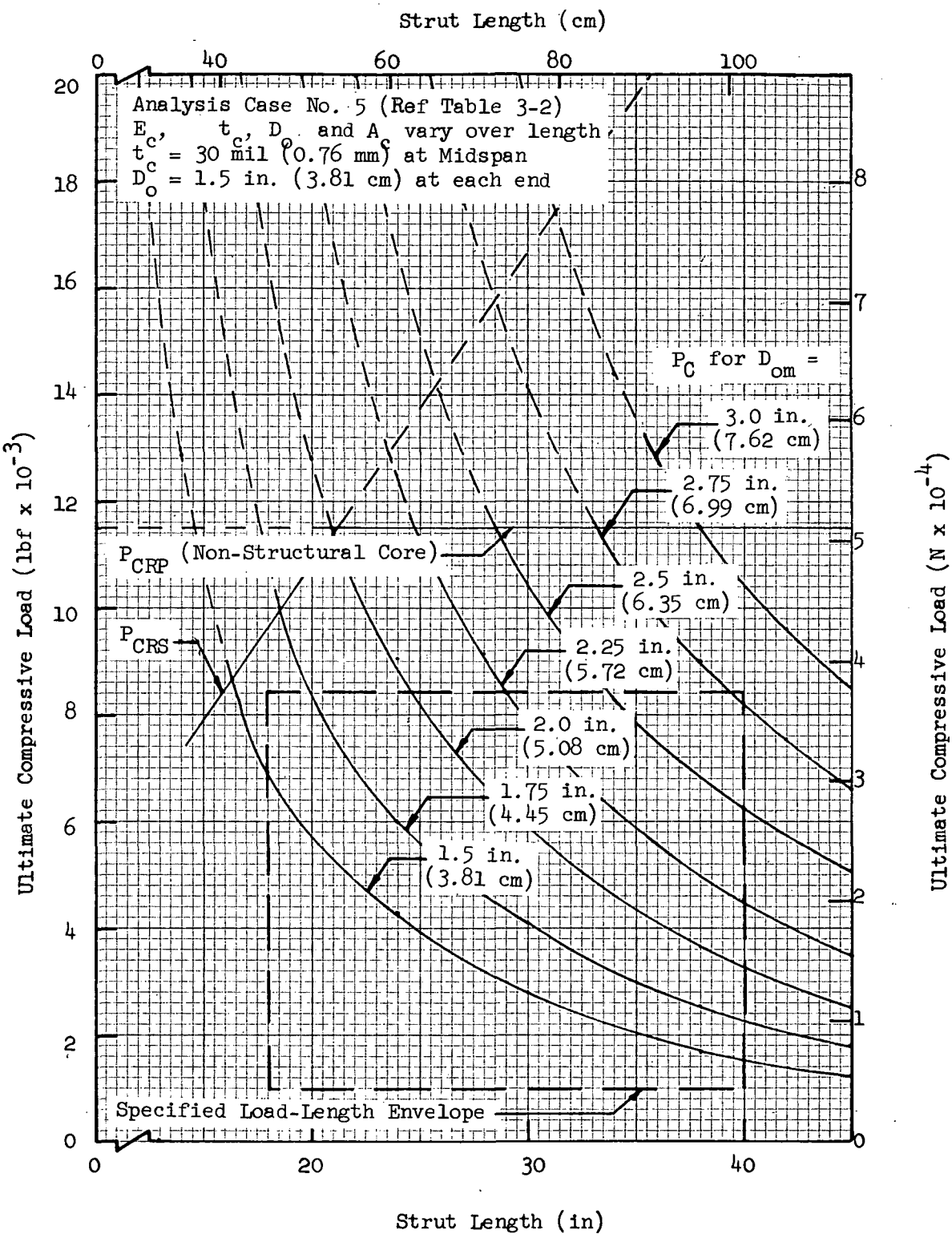

Fig. 3-41 Revised Ultimate Compressive Loads for Monocoque Fiberglass Ogives with an 18-mil (0.46-mm) Longo Wrap Thickness at Midspan

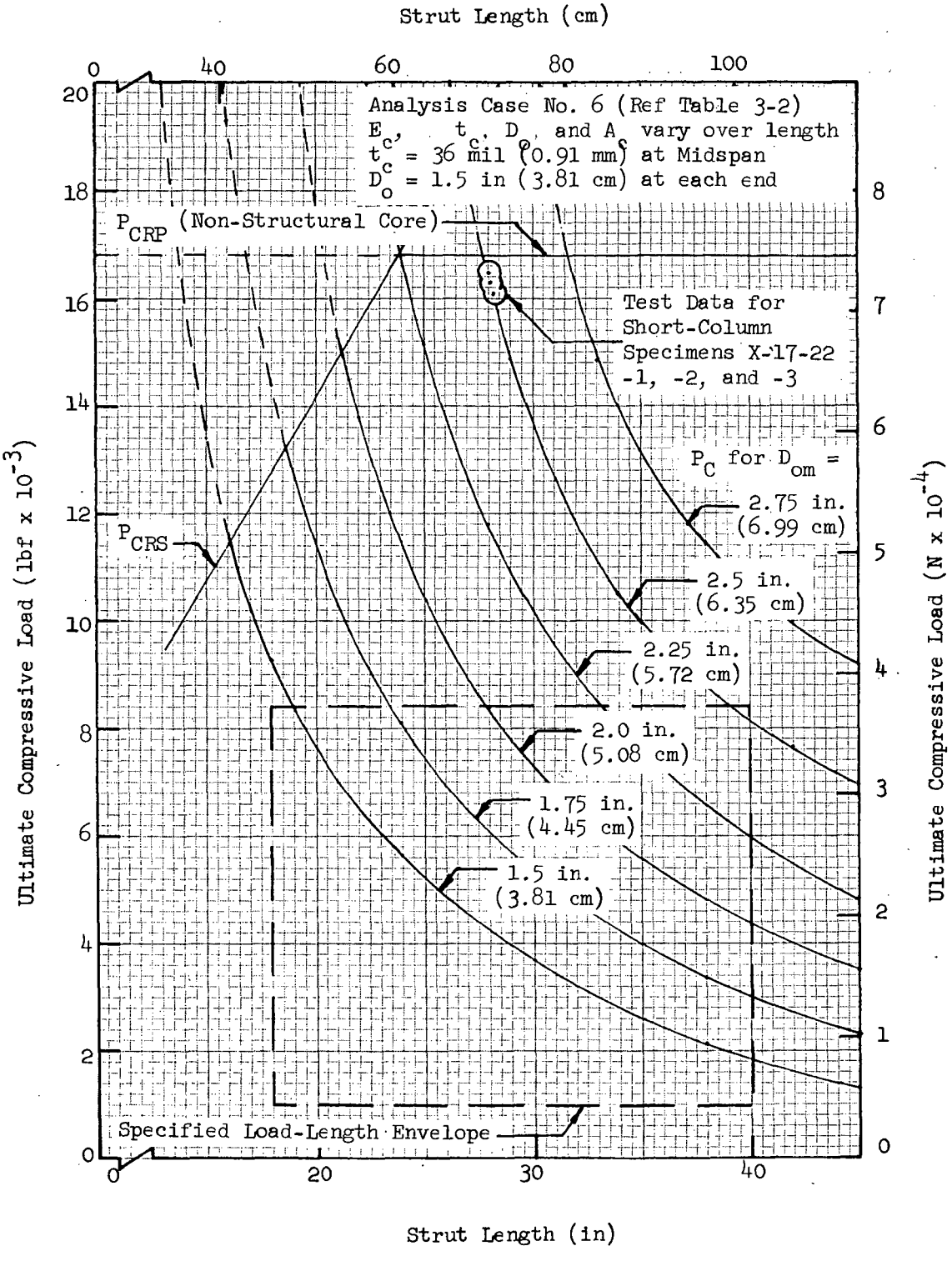

Fig. 3-42 Revised Ultimate Compressive Loads for Monocoque Fiberglass Ogives with a 24-mil (0.61-mm) Longo Wrap Thickness at Midspan

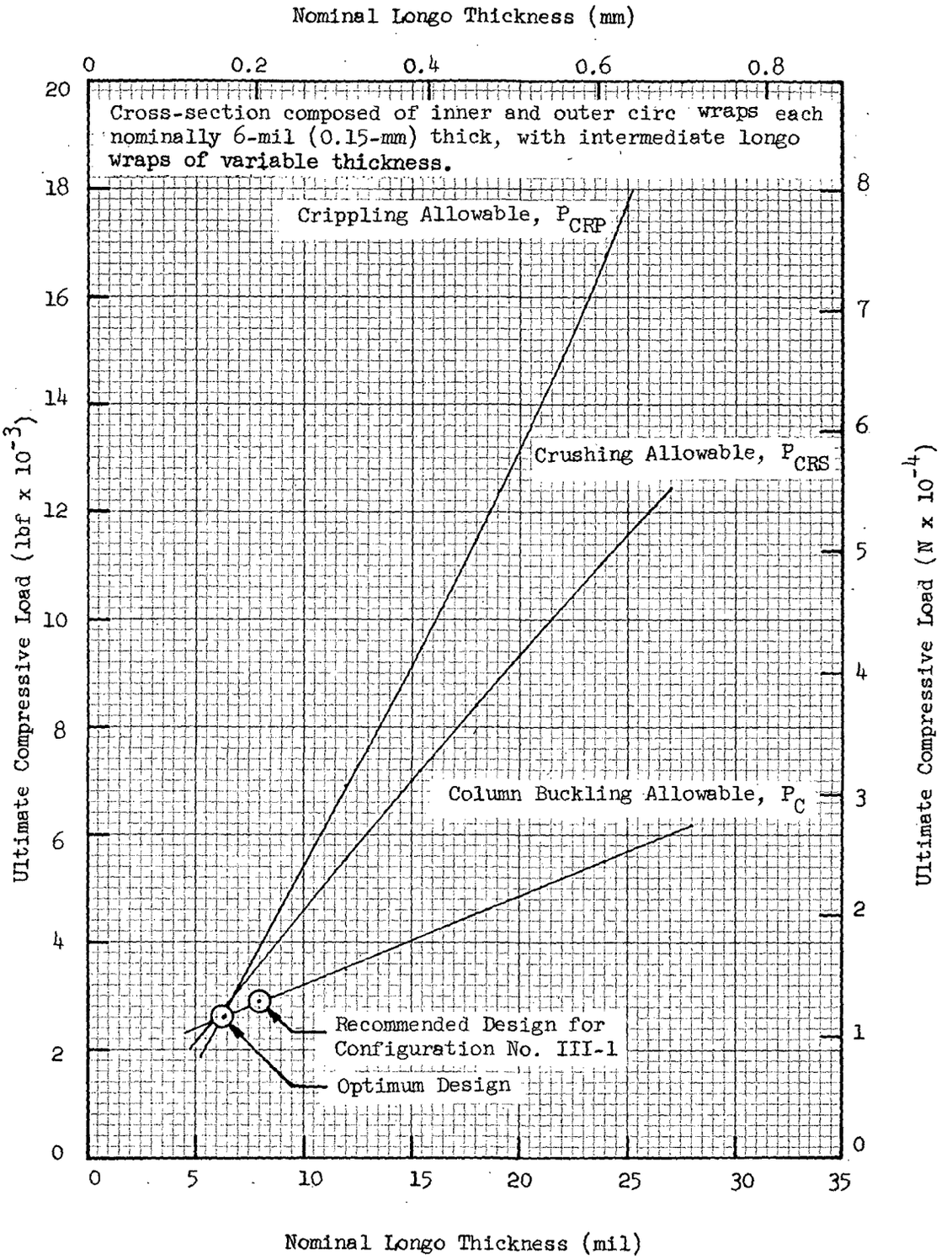

Fig. 3-43 Revised Ultimate Compressive Loads as a Function of Longo Wrap Thickness for a 24-in.-(61-cm-) Long, 1.5-in.-(3.81-cm-) Diameter Monocoque Fiberglass Cylinder

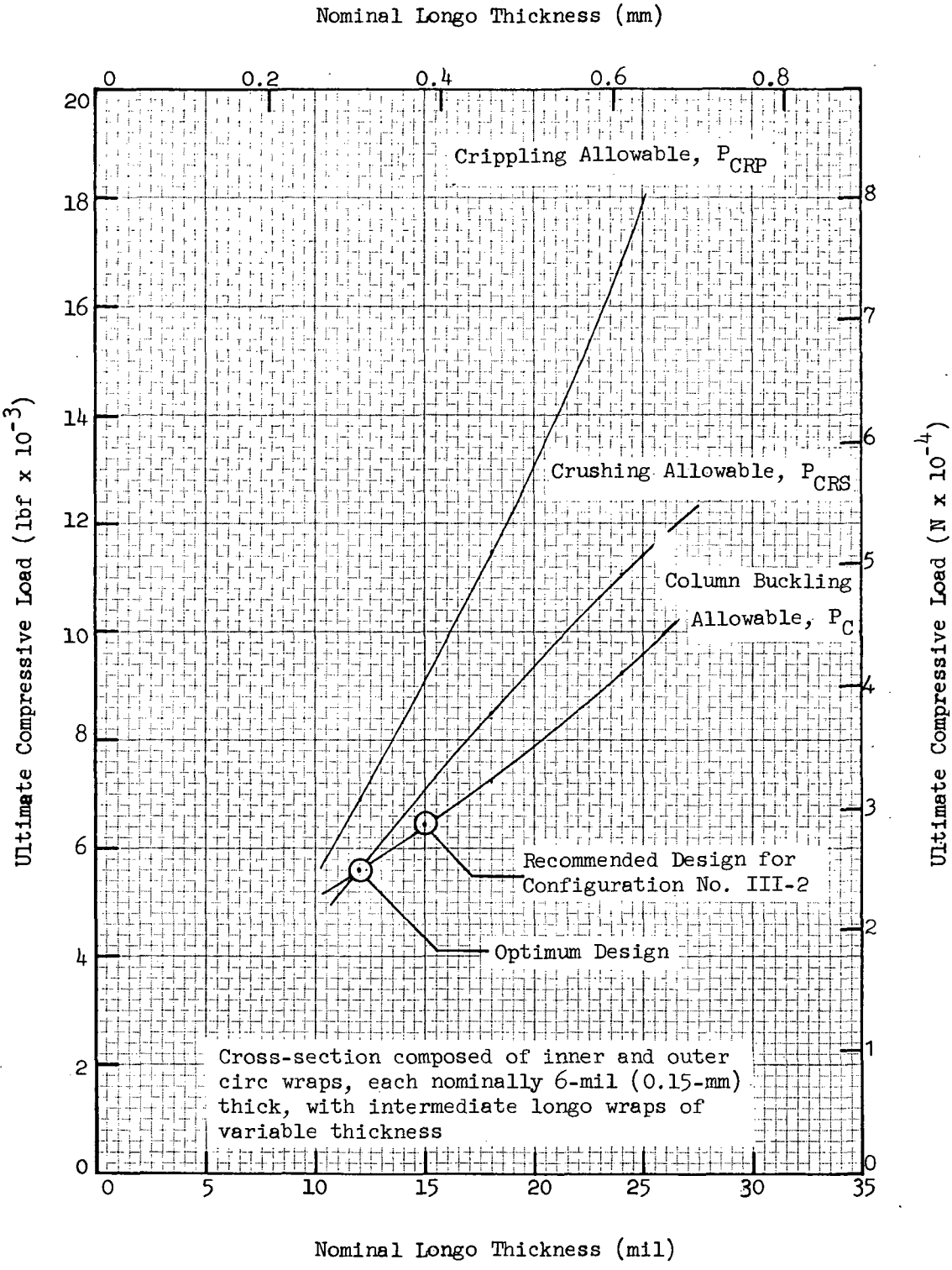

Fig. 3-44 Revised Ultimate Compressive Loads as a Function of Longo Wrap Thickness for a 19-in.-(48.3-cm-) Long, 1.5-in.-(3.81-cm-) Diameter Monocoque Fiberglass Cylinder

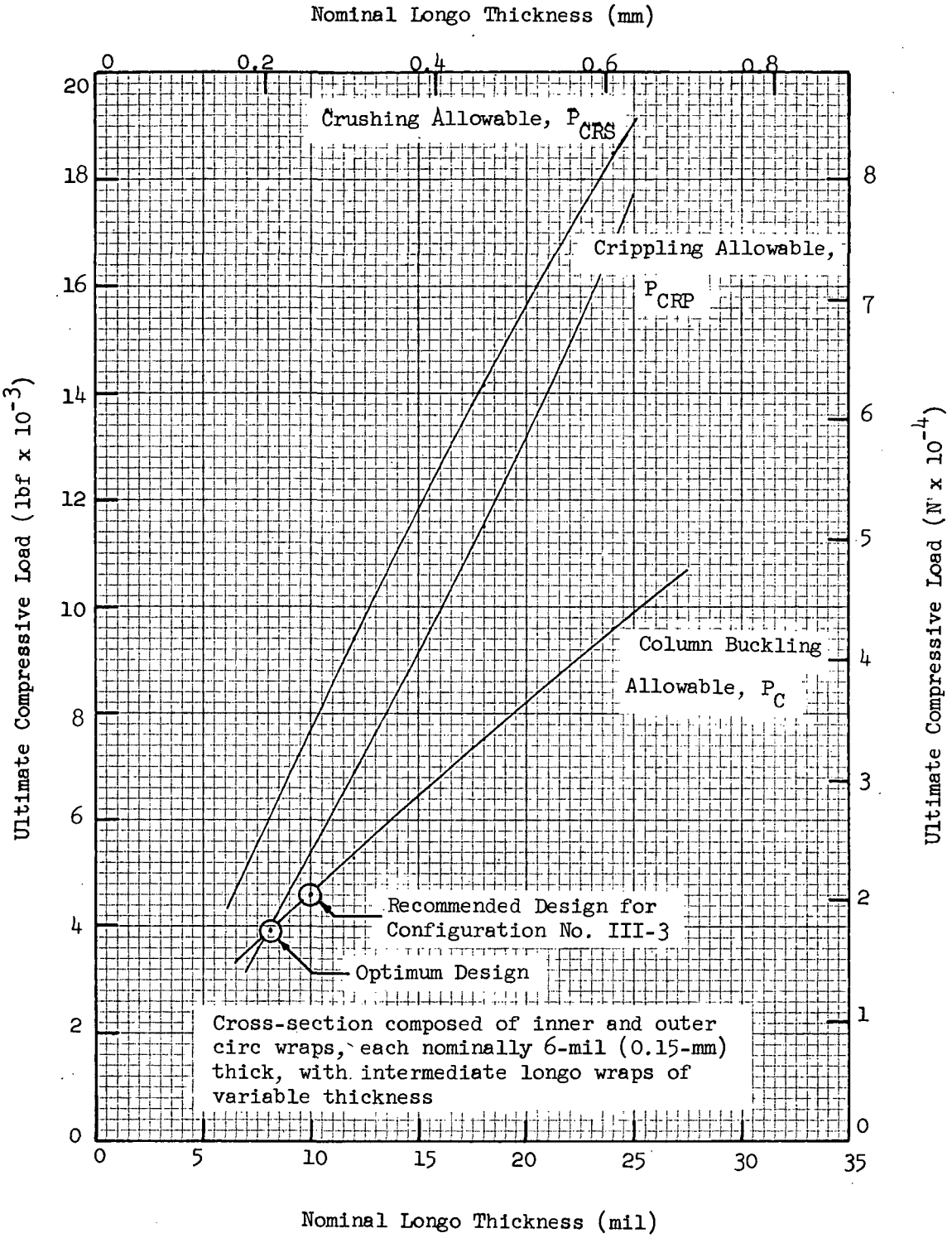

Fig. 3-45 Revised Ultimate Compressive Loads as a Function of Longo Wrap Thickness at Midspan for a 36-in.-(101.6-cm-) Long, 2.5-in.-(6.35-cm-) Midspan Diameter Monoque Fiberglass Ogive

in Tasks 3 and 4 were biased slightly so that each was critical in column buckling rather than either the crippling or the crushing modes of failure. This was done to improve design predictability, since the test data show less scatter for failures in column buckling.

The designs recommended in Figs 3-43, 3-44, and 3-45 were selected for fabrication in Task 3 and for full-scale testing in Task 4. A summary of requirements for these designs, designated as configurations III-1, III-2, and III-3, respectively, is presented in Table 3-12. Detailed requirements are given on the design assembly drawings which are presented in Figs 3-46, 3-47, and 3-48, respectively, for configurations III-1, III-2, and III-3. Note that these drawings also apply in general to the designs fabricated and tested in Task 2. Fig. 3-46 applies to strut configuration II-1, Fig. 3-47 shows strut configurations II-2 and II-3, and Fig. 3-48 corresponds to strut configuration II-4.

Table 3-12

SUMMARY OF DESIGN REQUIREMENTS FOR SELECTED TASK 3 STRUTS

Configuration No.	III-1	III-2	III-3
Configuration Description	Monocoque Cylinder	Monocoque Cylinder	Monocoque Ogive
Longo Wrap Thickness, mil(mm)	8(0.20)	15(0.38)	10(0.25)
Strut Length, in.(cm)	24.0(61.0)	19.0(48.3)	36.0(91.4)
Midspan Outside Dia, in.(cm)	1.5(3.81)	1.5(3.81)	2.5(6.35)
End Outside Dia, in.(cm)	1.5(3.81)	1.5(3.81)	1.85(4.70)
Predicted Ult Comp Load, lbf (N)	2900(12900)	6430(28600)	4600(20460)
Predicted Ult Tension Load, lbf (N)	7660(34070)	14320(63700)	16010(71210)
Design Ult Fitting Load, lbf(N)	15320(68140)	28640(127400)	32020(142400)
Design Limit Cyclic Load, lbf (N)	5470(24330)	10230(45500)	11440(50890)

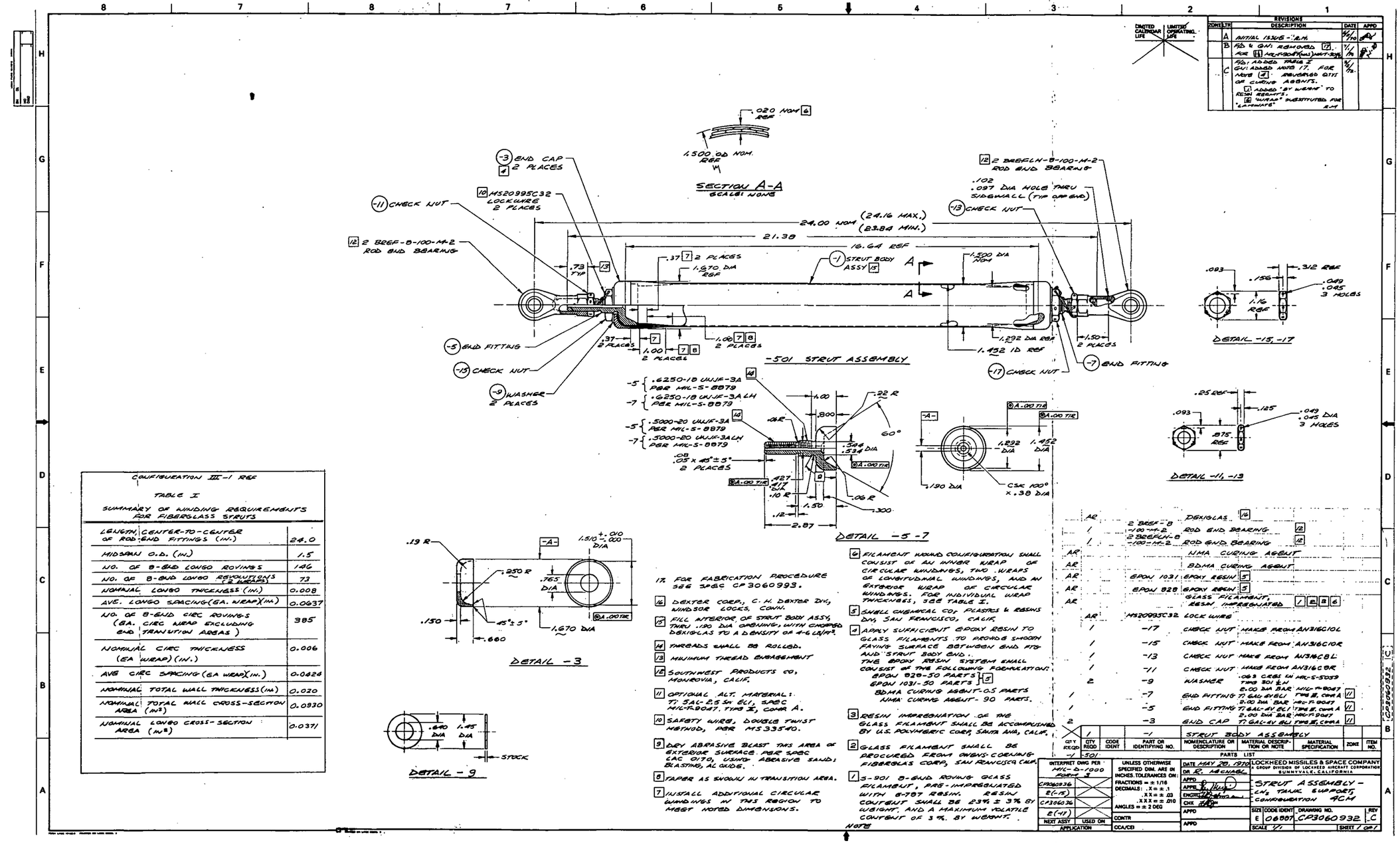

Fig. 3-46 Design Assembly Drawing for Strut
Configurations II-1 and III-1

"Page missing from available version"

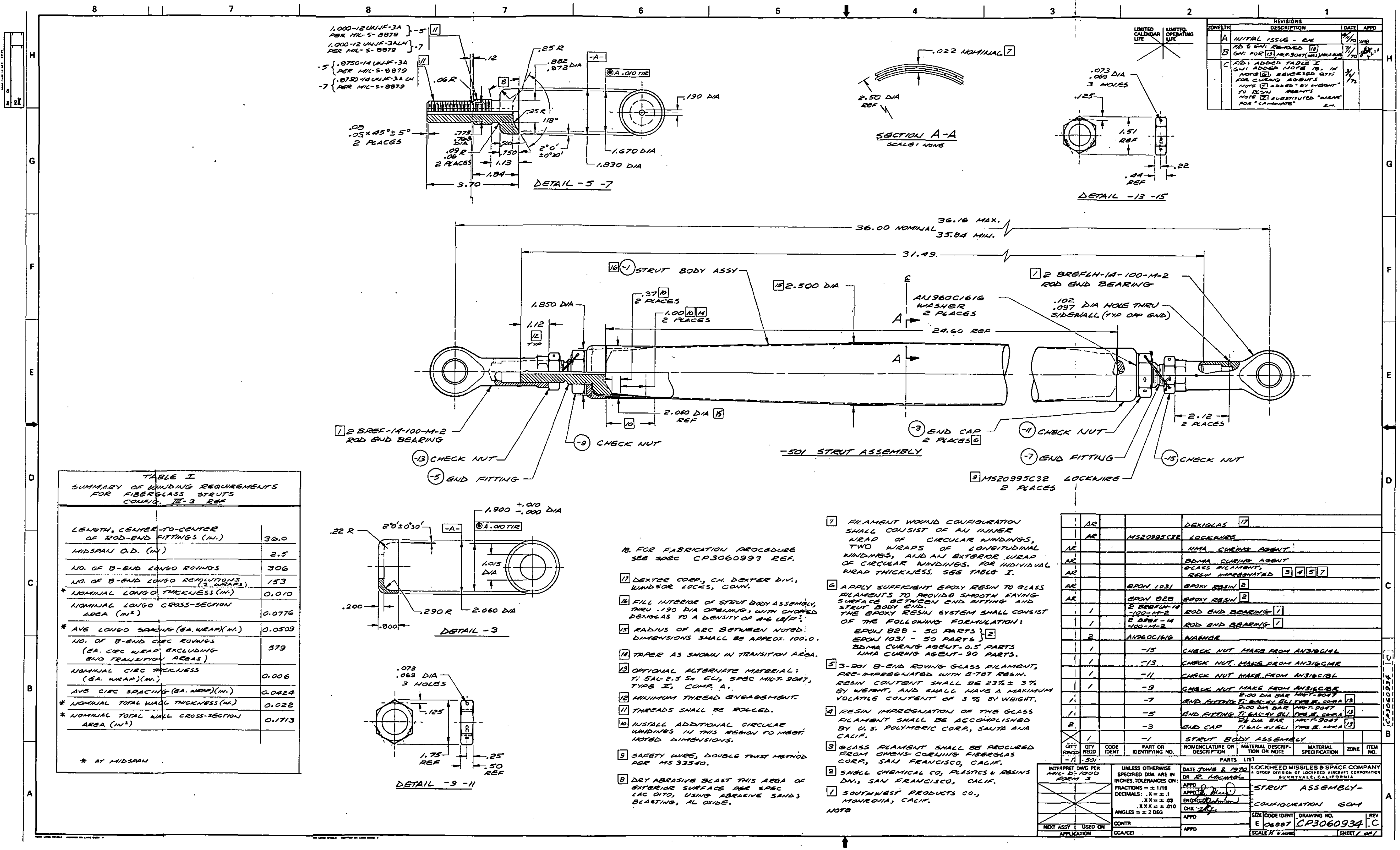

Fig. 3-47 Design Assembly Drawing for **Strut Configurations II-2, II-3, and III-2**

"Page missing from available version"

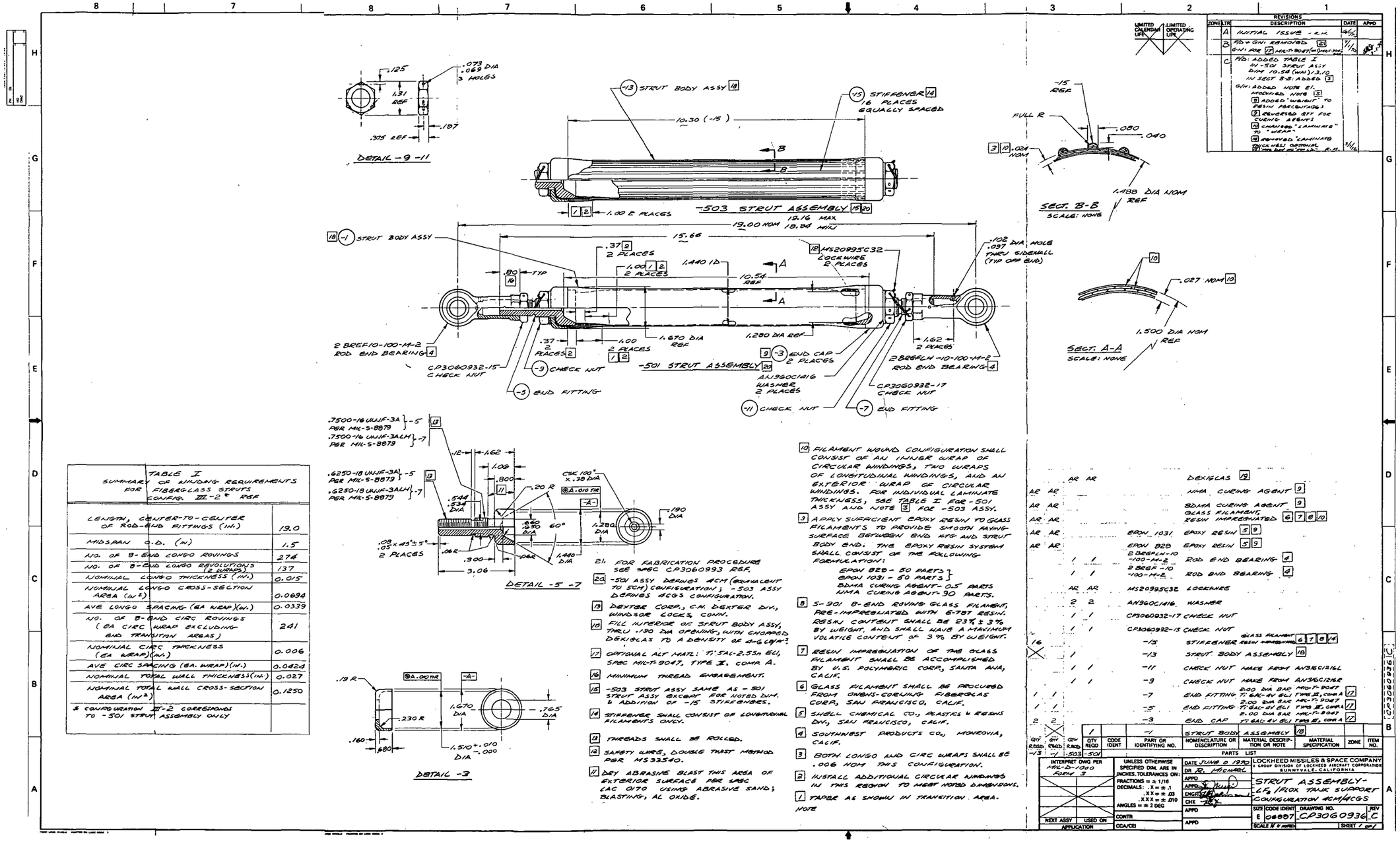

Fig. 3-48 Design Assembly Drawing for **Strut Configurations II-4 and III-3**

"Page missing from available version"

Detailed winding requirements for the Task 2 strut configurations are not shown in these drawings, **but are presented in Section 4.1.1.**

Comparison of the design ultimate fitting loads and the design limit cyclic loads for Task 2 and Task 3 struts (Tables 3-11 and 3-12, respectively) with the rated ultimate static and cycle-life capabilities of the selected 2BREF series rod-end fittings (Ref Table 3-8) shows that a 2BREF-12-100 rod-end would satisfy the requirements of the III-3 strut. The difference in weight between the -14 and the -12 rod-ends is approximately 0.5 lbm (0.23 kg) each, **or** a reduction in weight of approximately 1.0 lbm (0.45 kg) per strut. However, the -14 rod-end was retained **for the III-3 strut design, since both** the rod-ends and the mating titanium fittings had already been obtained on the basis of the Task 2 design, and a substitution was impractical in terms of program cost and schedule. A similar comparison shows that the rod-ends selected for the III-1 and III-2 strut designs are suitably matched to the design requirements.

Section 4

TASK 2 - EXPERIMENTAL CONCEPT SCREENING PROGRAM

In Task 2, three struts each of four selected designs (Ref Table 3-11) were fabricated to verify that all design and manufacturing requirements could be achieved, and to provide short-column specimens for test. These specimens were potted at each end with epoxy, instrumented with strain-measurement transducers, and tested to failure in compression at room temperature. The data obtained were used to derive experimental values of compressive modulus of elasticity which were in turn used to revise and update the parametric structural design curves developed in Task 1. The failed specimens were subjected to a laboratory analysis to determine resin content, composite thickness and density, void volume fraction, and other critical manufacturing parameters. Details of the work conducted in Task 2 are presented in this section.

4.1 PREPARATION OF TEST HARDWARE AND FACILITIES

4.1.1 Short-Column Test Specimens

The short-column specimens required for Task 2 tests were cut from the mid-span section of full-scale struts. These struts were fabricated using the same internal titanium end fittings manufactured in Task 3 for later use to produce the Task 4 test specimens. Also, the cast salt mandrels used to wind the Task 2 struts were produced using the mandrel tooling provided under Task 3. Fabrication of both the titanium end fittings and the cast salt mandrels is discussed in Section 5.

Typical struts fabricated in Task 2 are shown in the photographs of Figs 4-1 and 4-2, respectively, for configurations II-1 and II-3. General design requirements for each of the four selected configurations were presented previously (Ref Table 3-11). Details of each design, excluding specific

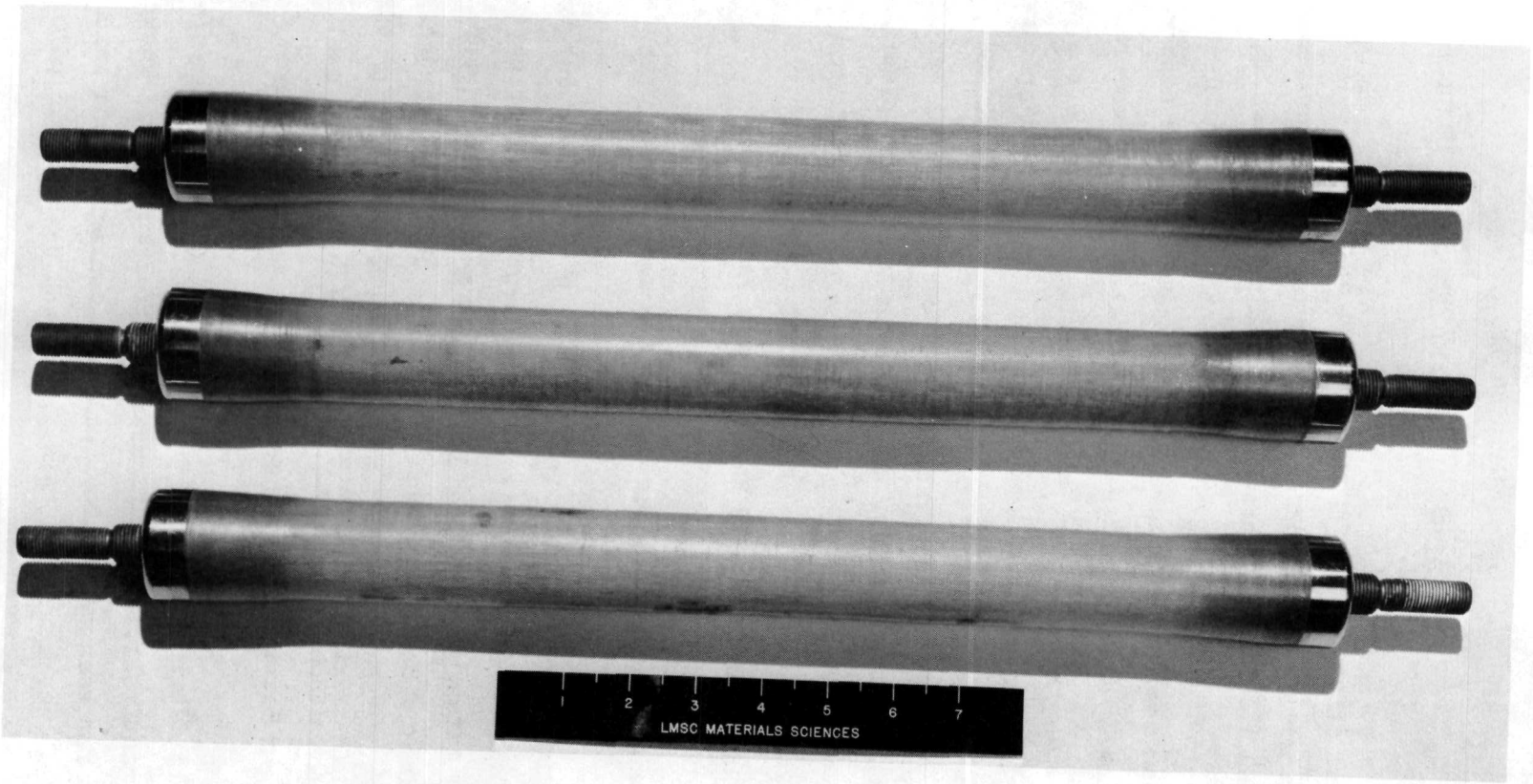

Fig. 4-1 Configuration II-1 Monocoque Fiberglass Cylinders

Fig. 4-2 Configuration II-3 Stiffened Fiberglass Cylinders

winding requirements, were also presented in the design drawings (Ref Figs. 3-46, 3-47, and 3-48). Winding, curing, and final assembly operations for these struts were conducted according to the procedures presented and discussed in Section 5 and Appendix E. The number and spacing of the longo and circ rovings required for each design are summarized in Table 4-1 below. These values were determined using the method described in Appendix F.

For configuration II-3 (Fig. 4-2), the half-round fiberglass stiffeners were fabricated independently by hand layup of all-longo rovings over a metal mandrel plate which contained machined grooves of the required radius. The stiffeners were then cured, cut to the proper length, and secondary-bonded to the strut body cylinder using epoxy resin.

After winding, curing, and mandrel removal operations had been completed, the struts were set up one at a time in a lathe and the short-column specimens were cut from the midspan section of each. Initially, each specimen was cut approximately 1 in. (2.54 cm) longer than the desired 8-in. (20.3-cm) final length. Subsequently, wooden mandrel plugs were installed into each end of each specimen to support the wall during the final cutting operations. These cuts were also performed on a lathe using an abrasive cutting tool. Extreme care was exercised in the preparation of these specimens to ensure that the ends were flat and parallel within ±0.001 in. (±0.00254 cm), and were perpendicular to the longitudinal axis within ±0.005 in.(±0.0127 cm). When cut to the final length, each end of each specimen was then potted with epoxy to complete the preparation.

4.1.2 Instrumentation for Strain Measurements

Linear variable differential transformers (LVDTs), nominally accurate to ±0.1 mil (±0.00254 mm), were used to measure specimen deflections under load. Special clamps were used to position these transducers over a 3.5-in. (8.89-cm) gage length centered about the midspan of each specimen. Initially,

Table 4-1

SUMMARY OF WINDING REQUIREMENTS FOR TASK 2 STRUTS

Configuration	II-1	II-2	II-3	II-4
Configuration Description	Monocoque Cylinder	Monocoque Cylinder	Stiffened Cylinder	Monocoque Ogive
Drawing No.	CP3060932	CP3060936	CP3060936	CP3060934
No. of 8-End Longo Rovings	220	328	220	730
No. of 8-End Longo Revolutions	110	164	110	635
No. of Longo Wraps	2	2	2	4
Av. Longo Spacing, Ea. Wrap, in. (cm)	0.0424 (0.1077)	0.0282 (0.0716)	0.0424 (0.1077)	0.0424 (0.1077)
No. of 8-End Circ Rovings (Ea. Circ Wrap Excluding End Transition Fillets)	385	241	241	579
Av. Circ Spacing, Ea. Wrap, in. (cm)	0.0424 (0.1077)	0.0424 (0.1077)	0.0424 (0.1077)	0.0424 (0.1077)

two transducers were used as shown in Fig. 4-3. These transducers were oriented to coincide with one principal axis of the support system, about which spurious bending moments were minimized. This was achieved by loading the specimen through a tilting base plate mounted on coupled hydraulic cylinders.

It was found, after conducting the initial series of tests on specimens of the II-1 configuration, that additional hydraulic cylinder supports to control tilting of the base plate about both principal axes were required to truly minimize bending moments and reduce the scatter of the data obtained. Control about both axes was required because the bending stiffness of these relatively small-diameter tubular specimens was insufficient to equalize the hydraulic oil pressure between the coupled cylinders. With the two-axis control system, four equally-spaced LVDTs were required and hydraulic pressure was equalized manually using the output signals from each opposed pair

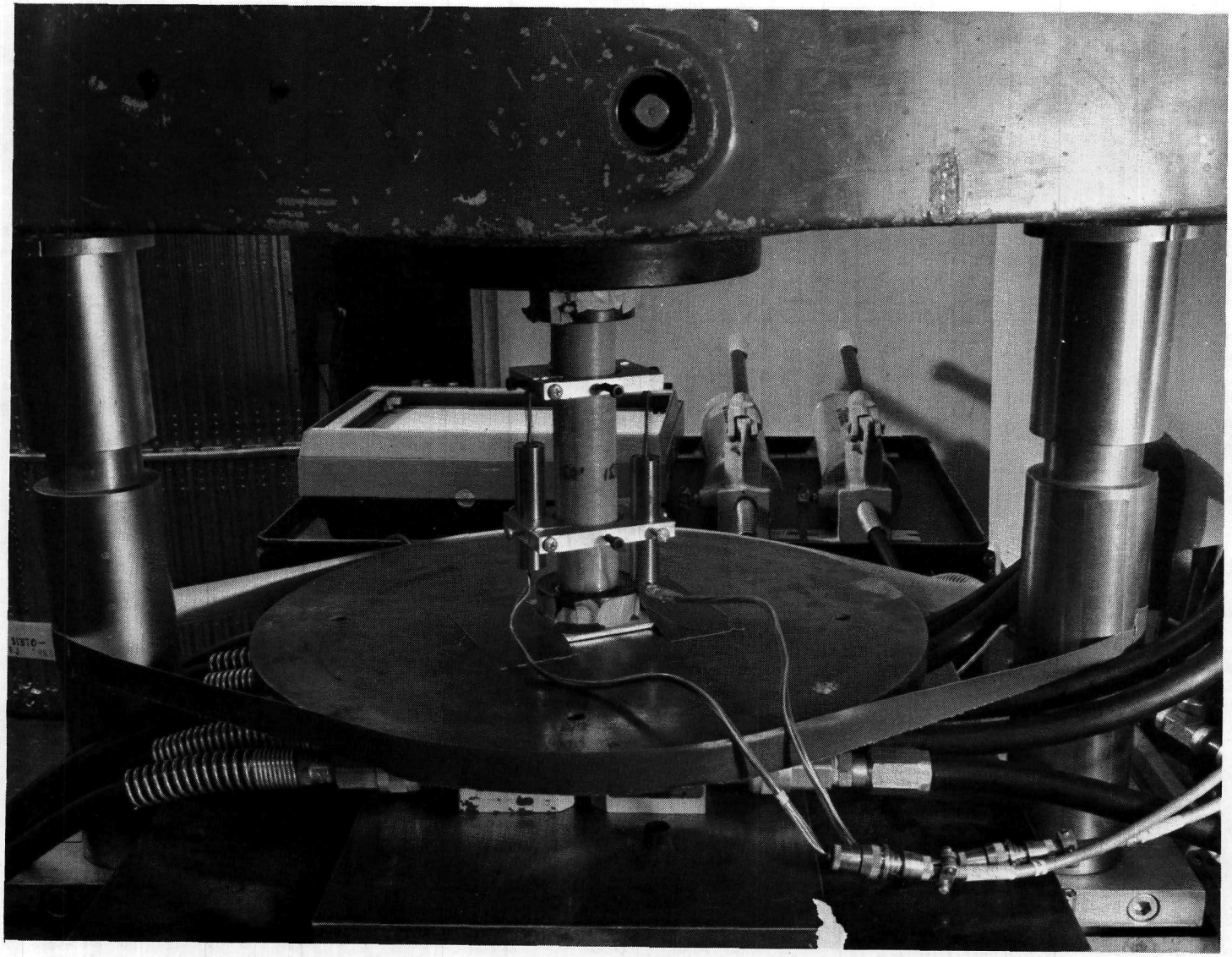

Fig. 4-3 Setup of Short-Column Test Specimens with Single-Axis Bending Control and Strain Measurements

of LVDTs. This setup is shown in Fig. 4-4. An automatic servo-control system was considered but past experience has shown that such a system requires considerable adjustment and tuning, usually accompanied by the loss of several test specimens.

For both the single-axis and the two axis control systems, the LVDTs were attached to the specimens using the special clamps shown in the photographs. Each clamp was attached to the specimen using four screws at 90° intervals. The end of each screw in contact with the specimen was machined to a 90° point, and then ground to provide a spherical contact surface. The clamping screws were torqued finger-tight to minimize stress concentrations and to avoid the introduction of surface flaws.

4.1.3 Test Machine Setup

Task 2 short-column compression tests were performed on a 50,000-lbf (222,400-N) Warner and Swasey universal tension-compression testing machine. The specimens were loaded through a tilting base plate mounted on hydraulic cylinders as discussed in the previous section. Mosley Model 2000A X-Y plotters were used to obtain load-deflection data curves for control of the system, and to show that no significant bending moments were incurred during the testing.

4.2 SHORT-COLUMN SCREENING TESTS

4.2.1 Test Operations and Results

During the Task 2 testing, data were measured and recorded continuously for applied compressive load, average strain over the 3.5-in. (8.89-cm) gage length, and differential strain for each opposed pair of transducers. A total of twelve specimens were tested to failure in compression. A summary of the specimen geometry, failure loads, and number of control axes employed is presented in Table 4-2.

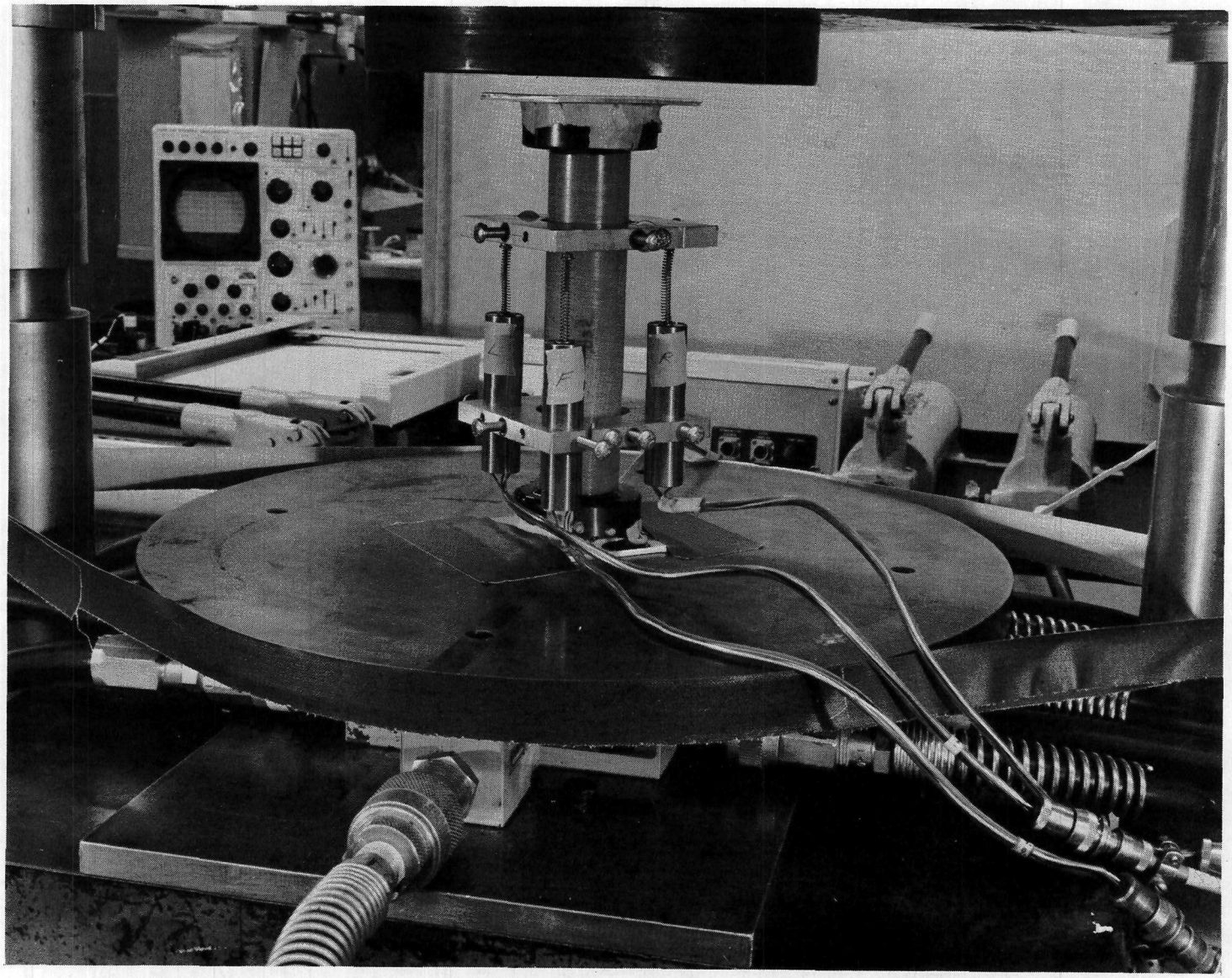

Fig. 4-4 Setup of Short-Column Test Specimens with Two-Axis Bending Control and Strain Measurements

Table 4-2

SUMMARY OF TASK 2 TEST RESULTS

Configuration No.	Specimen No.	Av. Wall Thickness[1] in.	(cm)	Failure Load lbf	(N)	No. of Axes for Moment Control
II-1	X-17-23-1	0.031	(0.079)	6630	(29,490)	1
	-2	0.030	(0.076)	3420	(15,210)	1
	-3	0.0265[2]	(0.0673)	2270	(10,100)	1
II-2	X-14-16-A1	0.032	(0.081)	8630	(38,390)	2
	-A2	0.033	(0.084)	8550	(38,030)	2
	-A3	0.034	(0.086)	8670	(38,560)	2
II-3	X-14-20-B4	0.024	(0.061)	9650	(42,920)	2
	-B5	0.022	(0.056)	6100	(27,130)	2
	X-17-24-1	0.028	(0.071)	7270	(32,340)	2
II-4	X-17-22-1	0.043	(0.109)	16,100	(71,610)	2
	-2	0.043	(0.109)	16,300	(72,500)	2
	-3	0.042	(0.107)	16,450	(73,170)	2

Notes:

(1) Measured at eight locations at 45° intervals around the circumference at midspan.

(2) Specimen damaged due to unraveling of inner circ over approximately one-half the length; reduced wall thickness = 0.0185 in. (0.0470 cm).

Inspection of the data presented shows an average scatter of approximately ±1 percent for the failure loads obtained on specimens of configurations II-2 and II-4. This indicates excellent structural reproducibility for these configurations, and also indicates that the two-axis moment control system was quite satisfactory. However, for the specimens of configuration II-1, the scatter was much greater indicating that single-axis control was inadequate.

Neglecting the results for specimen X-17-23-3, which was known to be defective due to unraveling of approximately half of the inner circ wrap, the average scatter for the other two specimens of this design is approximately ±32 percent. The only possible explanation for this vast discrepancy is that high moments about the uncontrolled axis contributed to the very low failure load of the -2 specimen, and that by coincidence the moments were relatively minor for the -1 specimen.

The data obtained for specimens of the II-3 stiffened cylinder configuration show excessive scatter of approximately ±25 percent, even with two-axis moment control. This result indicates poor structural reproducibility for this design.

Failure in all specimens, except the X-17-23-3 damaged specimen, appears to have resulted from localized compression or crushing failure of the material rather than classic diamond-pattern crippling. Figures 4-5 and 4-6 show typical examples for the II-1 and II-2 configurations, respectively. Failure of the X-17-23-3 damaged specimen is illustrated in Fig. 4-7, and shows classic diamond-pattern buckling of the thin-wall section of the tube. The type of failures observed for specimens of the II-3 stiffened cylinder configuration is shown typically in Fig. 4-8. During these tests, it could not be conclusively determined whether or not failure of the secondary bond between the stiffeners and the strut body wall actually preceded the compressive failure of the wall; however, this appeared to be the case.

4.2.2 Data Reduction and Analysis

The load-deflection data obtained from results of the short-column tests were reduced to determine average compressive stress and strain values for all specimens. Average strain values were computed from the applied load records and the composite cross-sectional area. Average deflection values for the

Fig. 4-5 Specimens of Configuration II-1 After Compressive Failure

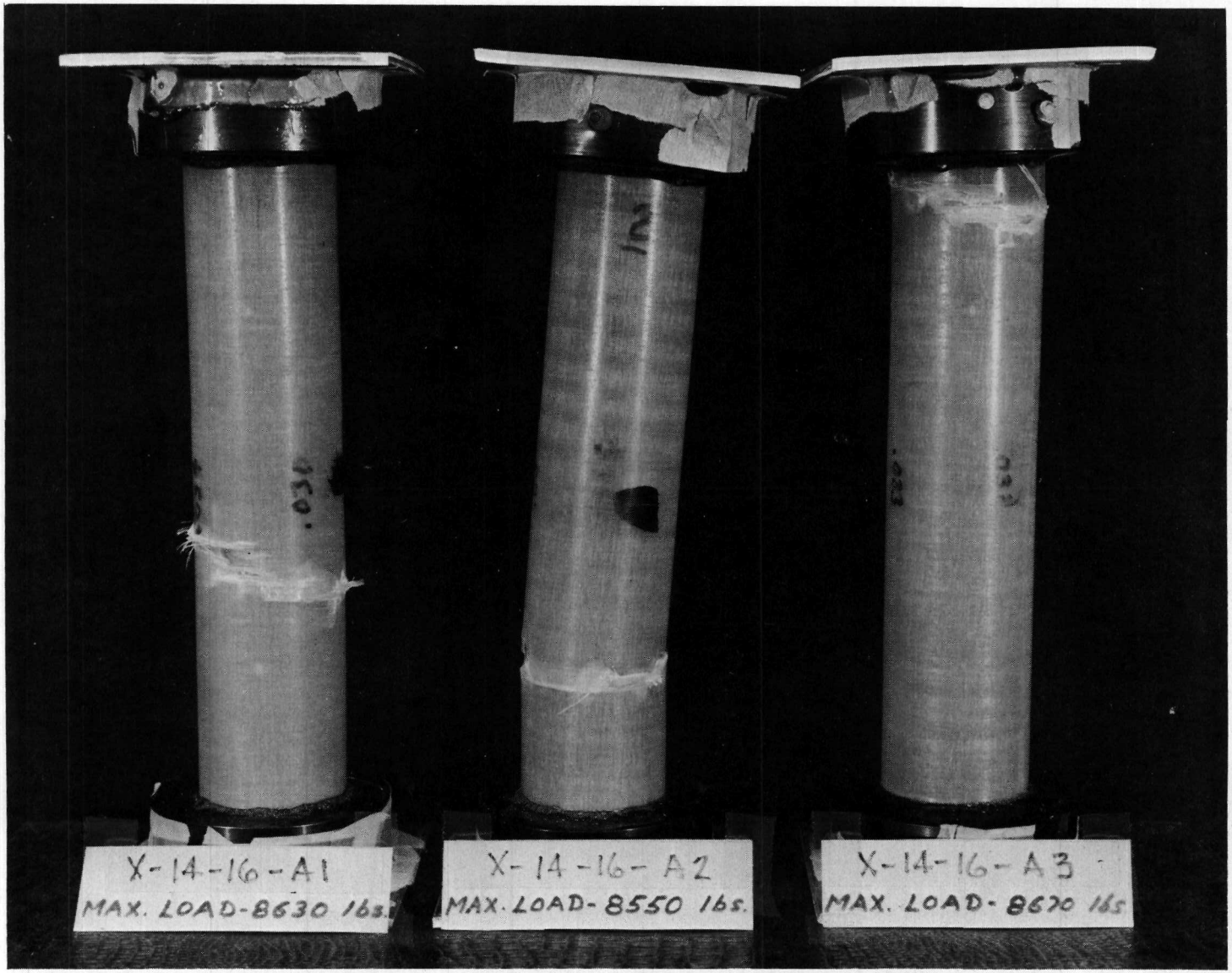

Fig. 4-6 Specimens of Configuration II-2 After Compressive Failure

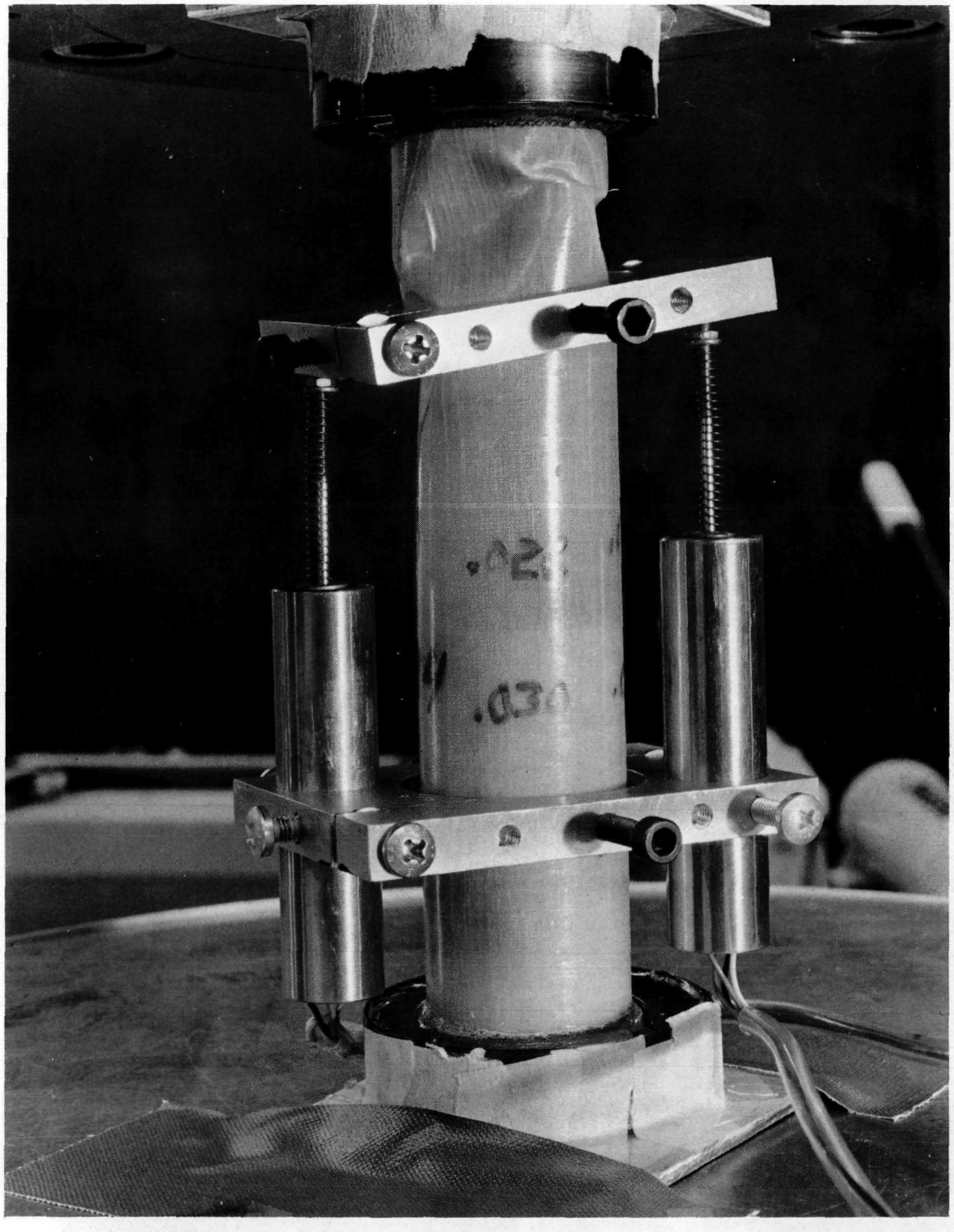

Fig. 4-7 Specimen X-17-23-3 After Failure in Compressive Crippling

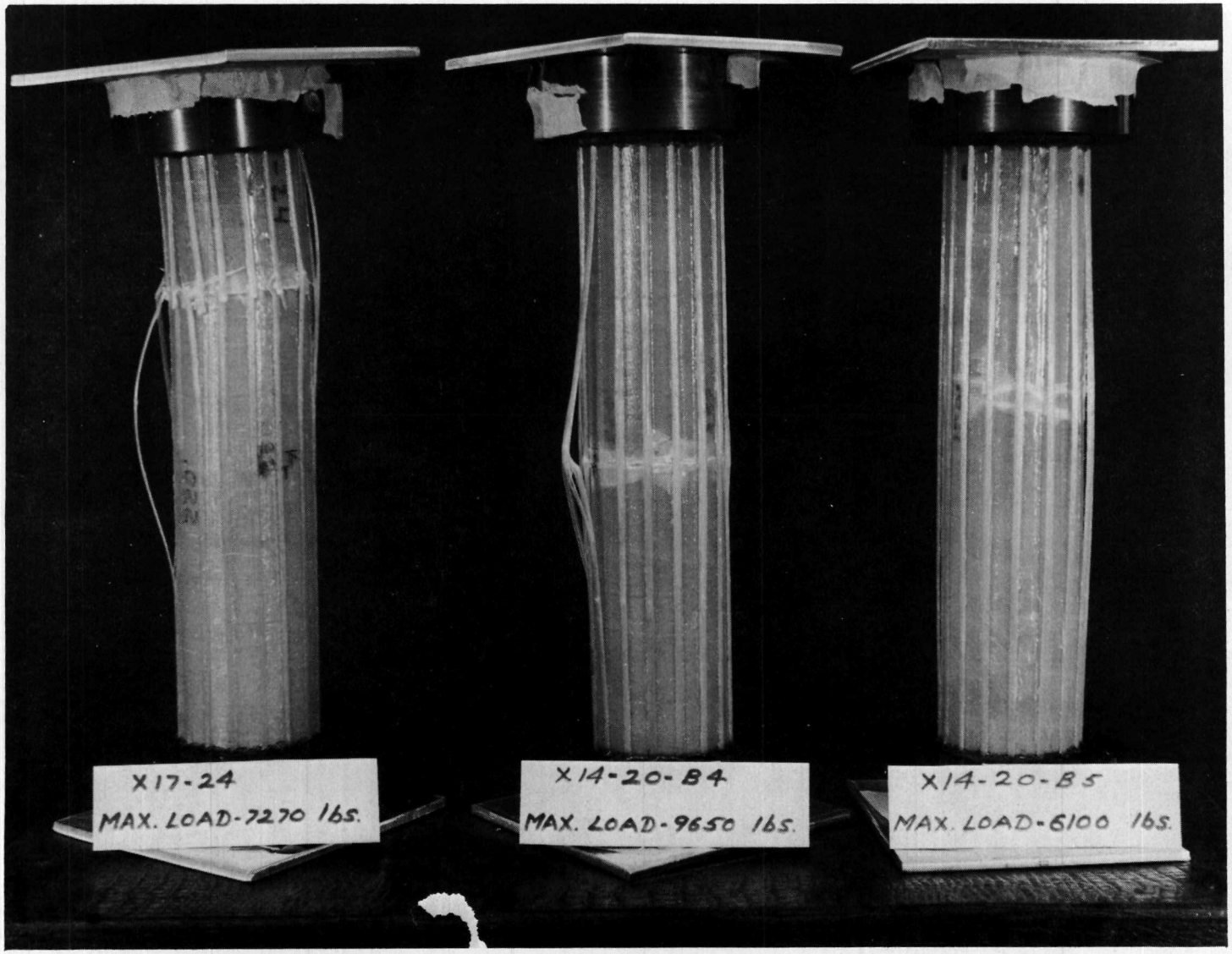

Fig. 4-8 Specimens of Configuration II-3 After Compressive Failure

number of transducers used (i.e., two or four) were divided by the 3.5-in. (8.89-cm) gage length to determine average strain. The resulting stress-strain curves were plotted for each specimen tested. These curves are presented in Figs. 4-9, 4-10, 4-11, and 4-12, respectively for the II-1, II-2, II-3, and II-4 strut configurations.

Values of compressive modulus of elasticity and isotropic crippling coefficient for each specimen were derived from the results of the Task 2 short-column tests. These derivations were performed under Task 5 data correlations and analysis. The results are presented and discussed in Section 7.1.1.

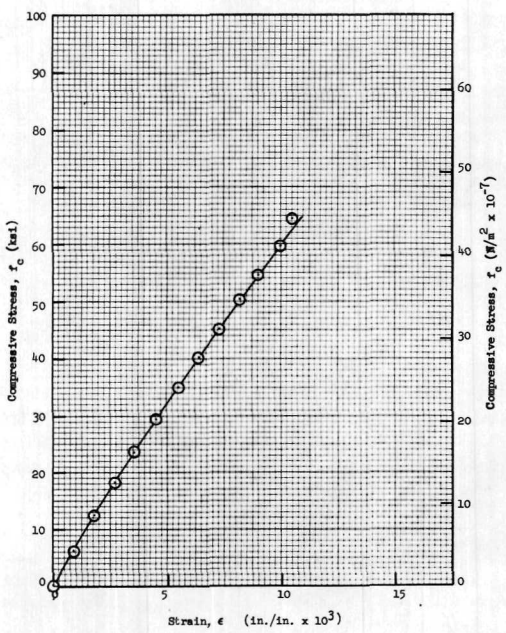

(a) Specimen X-17-23-1

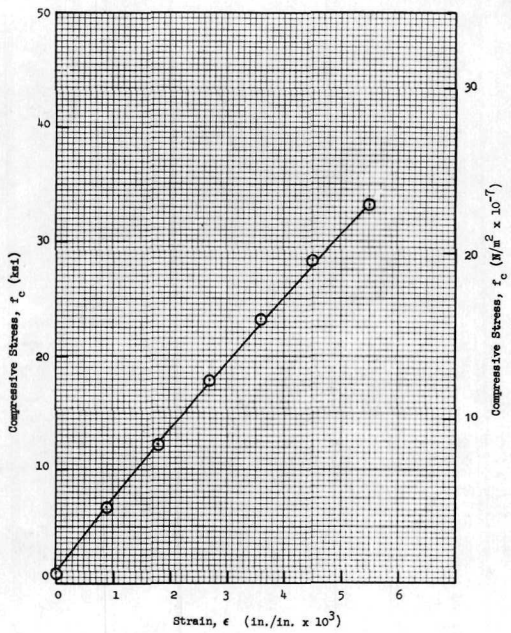

(b) Specimen X-17-23-2

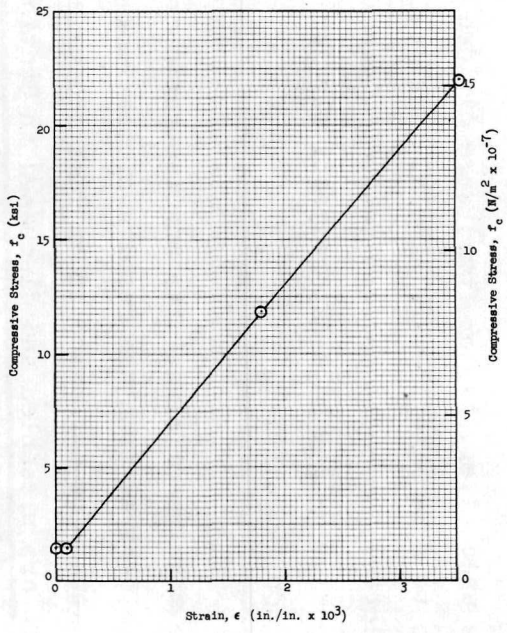

(c) Specimen X-17-23-3

Fig. 4-9 Compressive Stress-Strain Curves for the Configuration II-1 Monocoque Fiberglass Cylinders

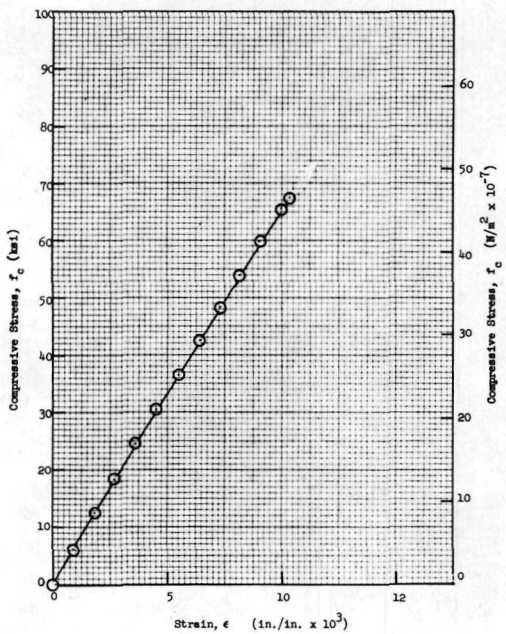

(a) Specimen X-14-16-A1

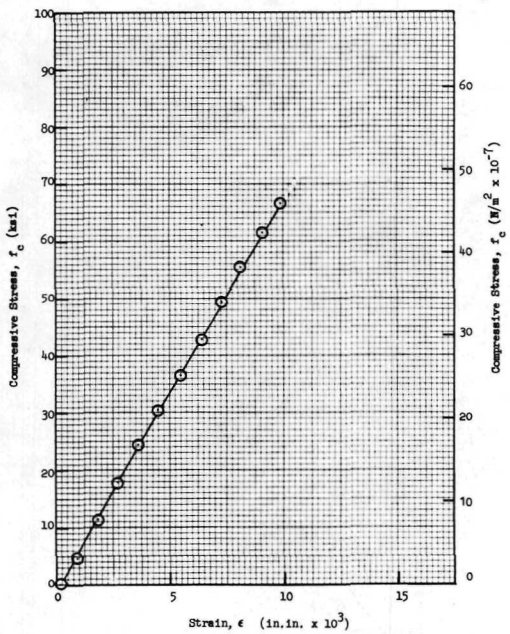

(b) Specimen X-14-16-A2

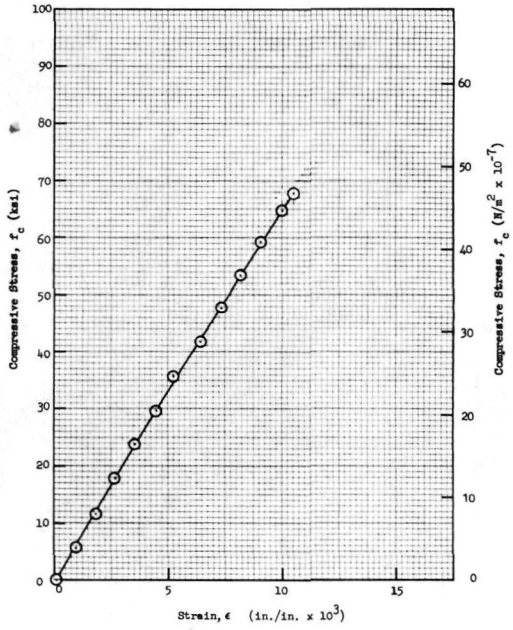

(c) Specimen X-14-16-A3

Fig. 4-10 Compressive Stress-Strain Curves for the Configuration II-2 Monocoque Fiberglass Cylinders

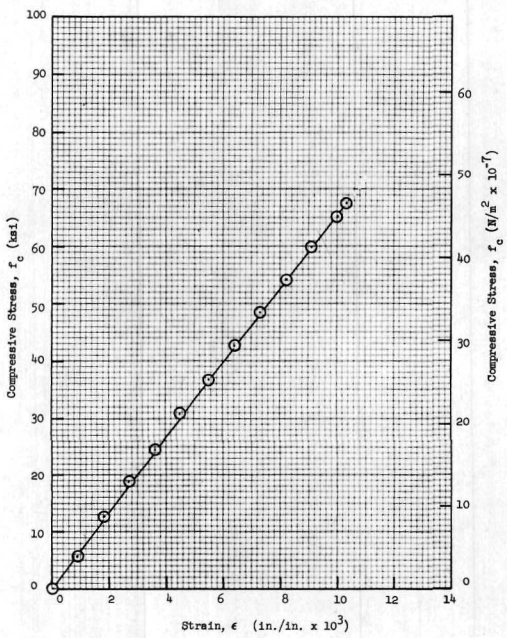

(a) Specimen X-14-20-B4

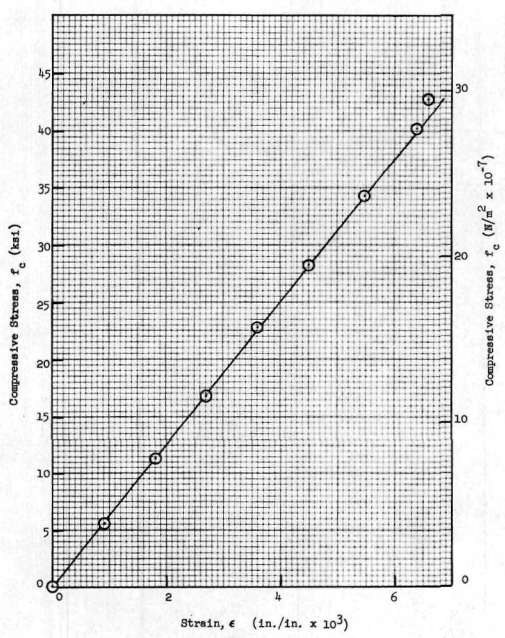

(b) Specimen X-14-20-B5

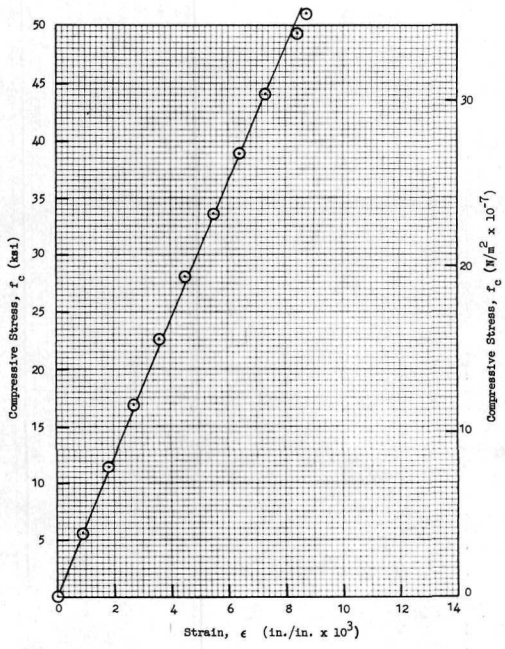

(c) Specimen X-17-24-1

Fig. 4-11 Compressive Stress-Strain Curves for the Configuration II-3 Stiffened Fiberglass Cylinders

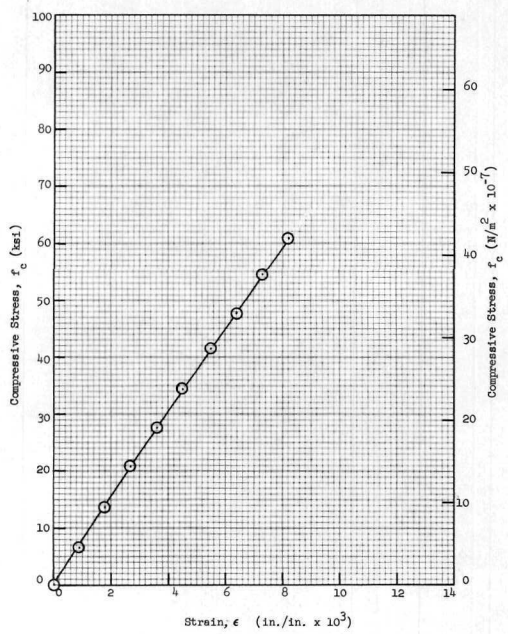

(a) Specimen X-17-22-1

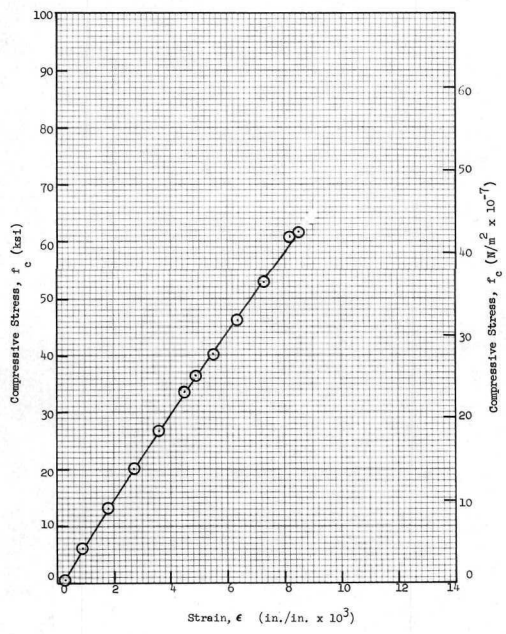

(b) Specimen X-17-22-2

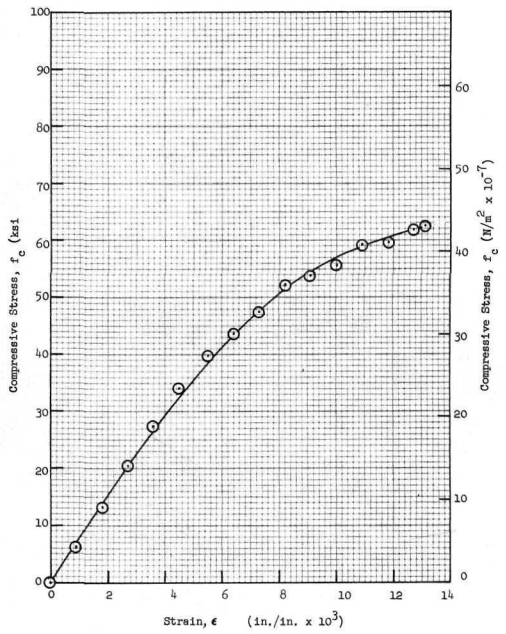

(c) Specimen X-17-22-3

Fig. 4-12 Compressive Stress-Strain Curves for the Configuration II-4 Monocoque Fiberglass Ogives

Section 5

TASK 3 - STRUT FABRICATION

Initially in Task 3, preimpregnated glass fiber-epoxy materials, titanium internal end fittings and caps, and stainless-steel rod-end fittings were procured to produce the strut hardware needed for both the Task 2 and Task 4 test programs. Concurrently, mandrel tooling was developed and winding mandrels were cast to satisfy the requirements of both tasks. Finally, eight struts each of three selected configurations were fabricated to provide the required Task 4 test specimens. These configurations were selected on the basis of the results obtained from the Task 1 analysis and the Task 2 screening tests. Detailed descriptions of these activities, and of the hardware produced in Task 3, are presented in this section.

All of the Task 3 operations, including procurement of materials and fittings, fabrication of tooling and mandrels, and fabrication and assembly of the struts, were performed in accordance with the requirements of Process Specification No. 3060993. This specification, developed during the contract program, is presented in Appendix E.

5.1 MATERIAL AND FITTING PROCUREMENT

5.1.1 Glass Fibers and Resin Prepreg

As specified in the contract (Ref Section 3.1.1), S-901 glass fiber reinforcements and E-787 epoxy resin were used to produce all of the struts required for the program. Initially 3-end, 8-end, and 12-end fiberglass roving sizes were considered. The 8-end roving size was selected based on a tradeoff of its suitability to achieve the required variable wrap thickness and cost.

After delivery of the glass-fiber material by the manufacturer, it was shipped to a separate source for preimpregnation with the E-787 epoxy resin system. The prepregged material was then stored in a refrigerated, B-staged condition until needed for the winding operations. At ambient temperature, the prepreg material was readily removed from the spool and wound into the desired configuration. With the controlled application of heat and pressure, the resin softened, flowed, and formed the desired resin matrix.

5.1.2 Titanium End Fittings and Caps

Selection of titanium as the most suitable material for fabrication of the internal end fittings and compression caps was accomplished in Task 1 (Ref Section 3.2.1). Design of recoverable end fittings and caps which could satisfy the requirements for both the Task 2 and the Task 4 struts was also conducted during the Task 1 studies (Ref Figs. 3-46, 3-47, and 3-48 for applicable drawings).

Eight complete end fitting and cap sets for each of the three selected strut configurations* were machined from Ti-6Al-4V-ELI bar stock. Subsequent to completion of the machining operations, the surface of each fitting was sand-blasted in the area of contact with the composite fiberglass material, external threads were rolled to obtain optimum notch fracture characteristics, and a molybdenum sulfide solid-film lubricant was applied to the threaded section of each fitting.

Throughout the Task 3 program, the titanium fittings and caps were recovered from failed specimens of each strut configuration and reused to fabricate additional struts. A suitable epoxy stripper solvent was selected and used for this purpose.

---

* The end fittings and caps shown in Drawing No. CP3060936 (Fig. 3-47) were used for production of both the II-2 and II-3 strut configurations in Task 2.

5.1.3 Rod-End Fittings

Internally-threaded Monoball* rod-end fittings of the 2BREF series were selected in Task 1 (Ref Section 3.2.1) for use with the Task 4 struts. Two sets each, with left- and right-hand threads, of the -8, -10, and -14 fittings were procured. These fittings were installed in accordance with the requirements specified on the drawings (Ref Figs. 3-46, 3-47, and 3-48), and reused as required to accomplish all of the Task 4 tests.

5.2 TOOLING AND MANDREL FABRICATION

Mandrels are required to provide a smooth, rigid winding surface of the desired shape and size for fabrication of filament-wound fiberglass struts. In addition, the mandrel must maintain dimensional stability during curing operations, and the mandrel material must be readily removable without damage to the fiberglass composite structure once the latter has been cured. Since the strut designs developed and used for this contract program were all of a closed-end configuration, the mandrels had to be removed through relatively small-diameter openings in each of the internal end fittings.

Studies and evaluations conducted under this contract, and under related independent development and manufacturing research investigations, led to the selection of a water-soluble salt-mandrel system which could be cast into hollow cylindrical shapes and could be readily removed by warm water washout of the cured structure. Sand mandrels with water-soluble resin binder materials were also evaluated. It was found that the salt-mandrel system was more cost effective for producing limited numbers of specialized mandrel shapes. In addition, the salt mandrel material is poured into the casting mold in a molten condition and, consequently, is more suitable for achieving the complex mandrel shapes required for some strut configurations.

---

* Southwest Products Co., Inc., Monrovia, California

5.2.1 Metal Masters and Fiberglass Molds

Salt mandrels fabricated in Task 3 were produced using two-piece split fiberglass casting molds. The typical mold shown in Fig. 5-1 was used to fabricate the mandrels for ogive strut configurations II-4 and III-3. Similar molds were fabricated for each of the other selected strut configurations. The molds were layed up, using fiberglass-epoxy materials, over aluminum masters which had been machined to the desired contour and dimensions. All dimensions of the aluminum master were increased by approximately 1.04 percent over the corresponding strut dimensions to allow for shrinkage of the salt material in cooling from the casting temperature to room temperature.

Dimensional studies conducted on the salt mandrels produced in Task 3 showed minor bowing and out-of-roundness imperfections which can be attributed directly to the split casting molds used. Since the dimensional precision of the mandrels is directly proportional to the precision achieved in the mold, these dimensional imperfections could have been reduced by using more precise (and more costly) tooling. However, the imperfections incurred were not significant, and the split casting molds were found to be entirely satisfactory to achieve the goals of this program.

5.2.2 Cast Salt Mandrels

Using the fiberglass split casting molds described in the previous section, salt mandrels were cast and used to wind the Task 2 and Task 3 struts. The salt material selected was compounded specifically for use in wash-away mandrels. Properties of this material, identified as Paraplast 36 by the supplier*, are shown in Table 5-1.

Using this material, salt mandrels were cast by melting the salt at 400°F (204°C), and by then pouring it into the preheated mold. After filling, the mold was rotated and cooled until a solid wall of salt, approximately 0.25-in. (0.635-cm) thick, had been formed. The excess molton material was

* Resolin, Inc., Chatsworth, California

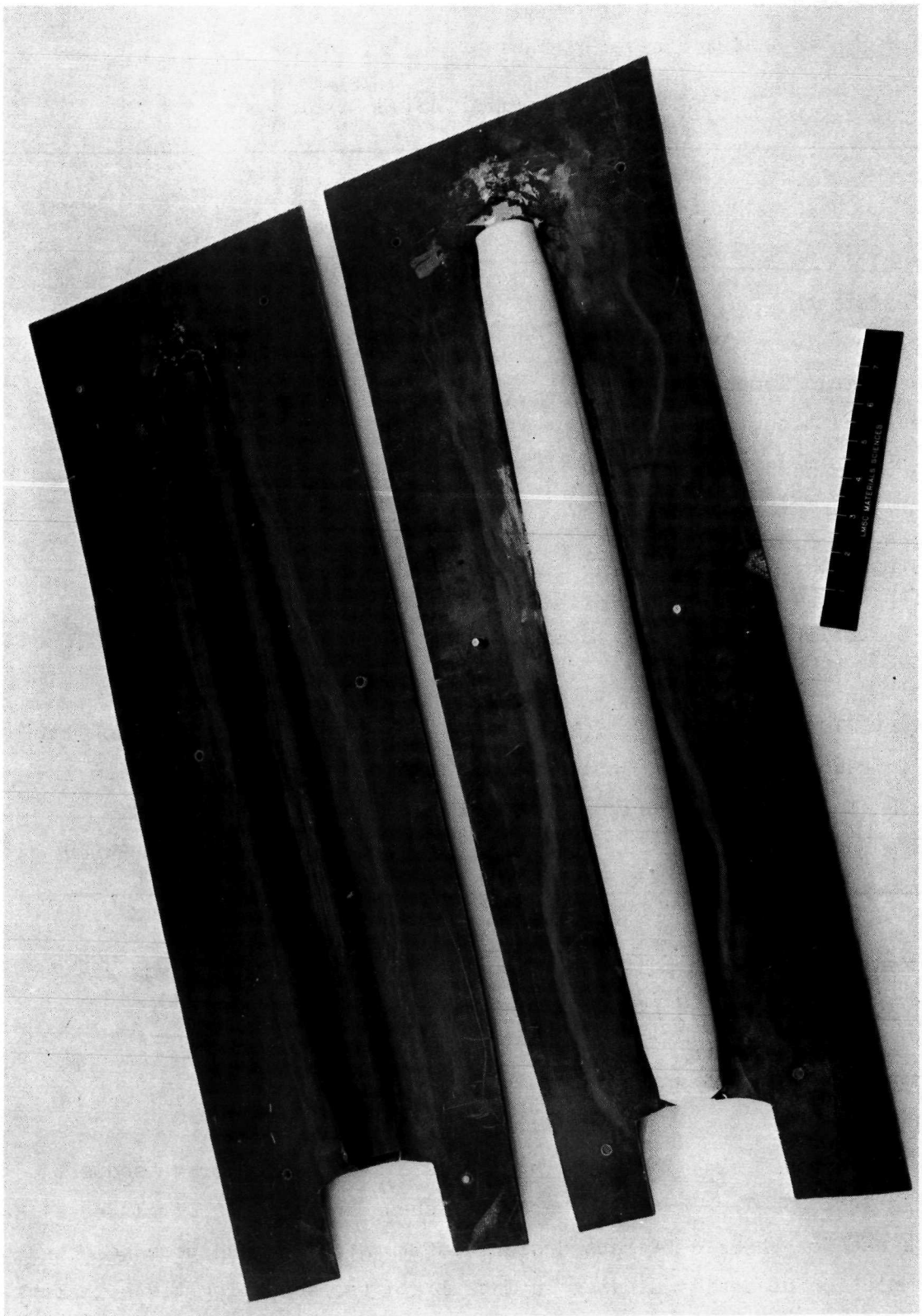

Fig. 5-1 Typical Split Casting Mold Used to Produce Salt Mandrels for Ogive Struts

Table 5-1

PROPERTY DATA FOR PARAPLAST 36 SALT

Form	Powder
Color	Green
Decomposition Temp, °F (°C)	Approx 1200 (649)
Heat Resistance, °F(°C)	350 (177)
Melt or Pour Temp, °F (°C)	400 to 420 (204 to 216)
Preheated Mold Temp, °F (°C)	175 to 225 (79 to 107)
Compressive Strength:	
Av. psi (N/m^2) at 75°F (24°C)	15,000 (1.03×10^8)
Av. psi (N/m^2) at 300°F(149°C)	2,300 (1.59×10^7)
Coefficient of Expansion from 75°F (24°C) to 300°F (149°C), in./in. °F (cm/cm°C)	2.9×10^{-5} (5.2×10^{-5})
Water Solubility Rate in Tap Water at 140°F (60°C), min/lbm (min/kg)	5 to 10 (11 to 22)
Density (Solid Cast), lbm/ft^3 (kg/m^3)	129 to 133 (2067 to 2131)
Specific Heat, Btu/lbm °F (joule/gm °C)	0.33 to 0.37 (1.4 to 1.5)
Latent Heat of Fusion, Btu/lbm (joule/gm)	35 (81)
Heat Conductivity	Approx. Equal to Water

then poured back into the melt pot. After cooling, the mandrel was removed from the mold and finished prior to use in the winding operation.

5.3 STRUT FABRICATION AND ASSEMBLY

In Task 3, a total of 24 fiberglass struts were fabricated for subsequent testing in Task 4. The completed hardware, shown in Fig. 5-2, included eight specimens each of three different design configurations which were selected after completion of design studies in Task 1 and the screening tests in Task 2. Drawings of the selected designs are presented in Section 3(Ref Figs. 3-46, 3-47, and 3-48).

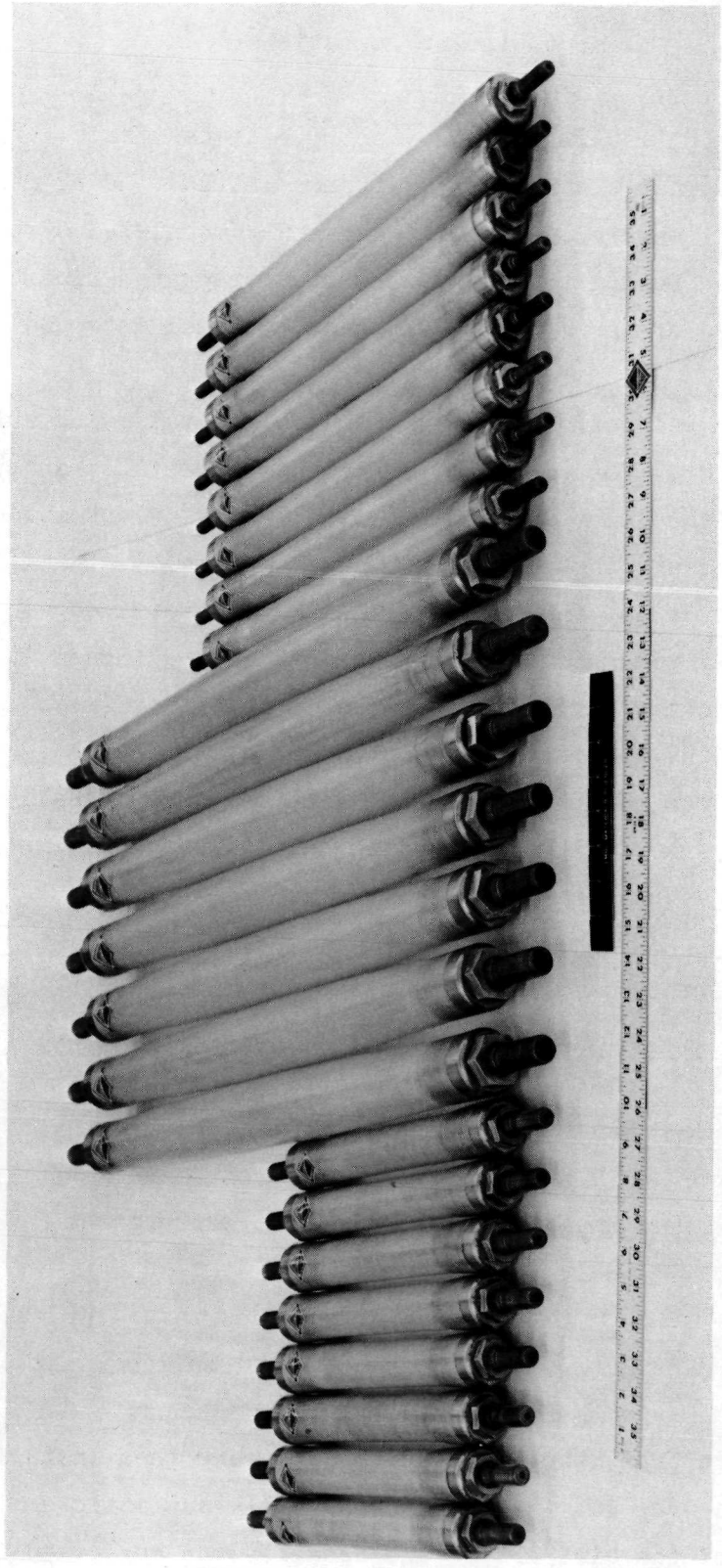

Fig. 5-2 Completed Fiberglass Test Specimens

5.3.1 Setup and Filament Winding Operations

Strut fabrication was initiated by setup of a cast salt mandrel and the corresponding internal titanium end fittings in the winding machine. Fig. 5-3 shows a typical mandrel, end fittings, and a completed strut of the III-1 configuration. During the setup, the preimpregnated fiberglass material was weighed, placed on the machine, and then threaded into the feed mechanism.

The inner circ was wound directly onto the mandrel using automatically-controlled mandrel rotation, horizontal carriage feed, and winding tension. Subsequently, the longo wraps were installed using automatic controls for winding tension and the placement of each roving. Between successive rovings, the polar fixture was indexed manually to predetermined settings. Struts with pure polar windings (zero-degree longos) and those with cross-center windings (approximately 3- to 6-degree longos) were investigated. Those fabricated under the contract were of the cross-center type. During installation of the longo rovings, steel tension rods were installed through the holes in each end fitting and used to help support the cantilevered assembly from the drive chuck.

Manufacturing research studies, conducted outside of the contract effort, indicate that fully-automated winding of polar-wound longo designs, such as those fabricated under the contract, could be accomplished with the development of suitable thread guides peculiar to each design configuration. However, such development was not considered to be cost-effective for the limited number of specimens produced under the contract program.

Subsequent to installation of the longo wraps, heat-shrinkable Mylar tape was applied onto the windings, and initial debulking of the structure was accomplished through application of controlled heat and pressure. **After removal of the tape, the compression caps were then installed and the external circ wrap was installed using fully-automatic controls. During application of the circ wraps, the assembly was supported from both the**

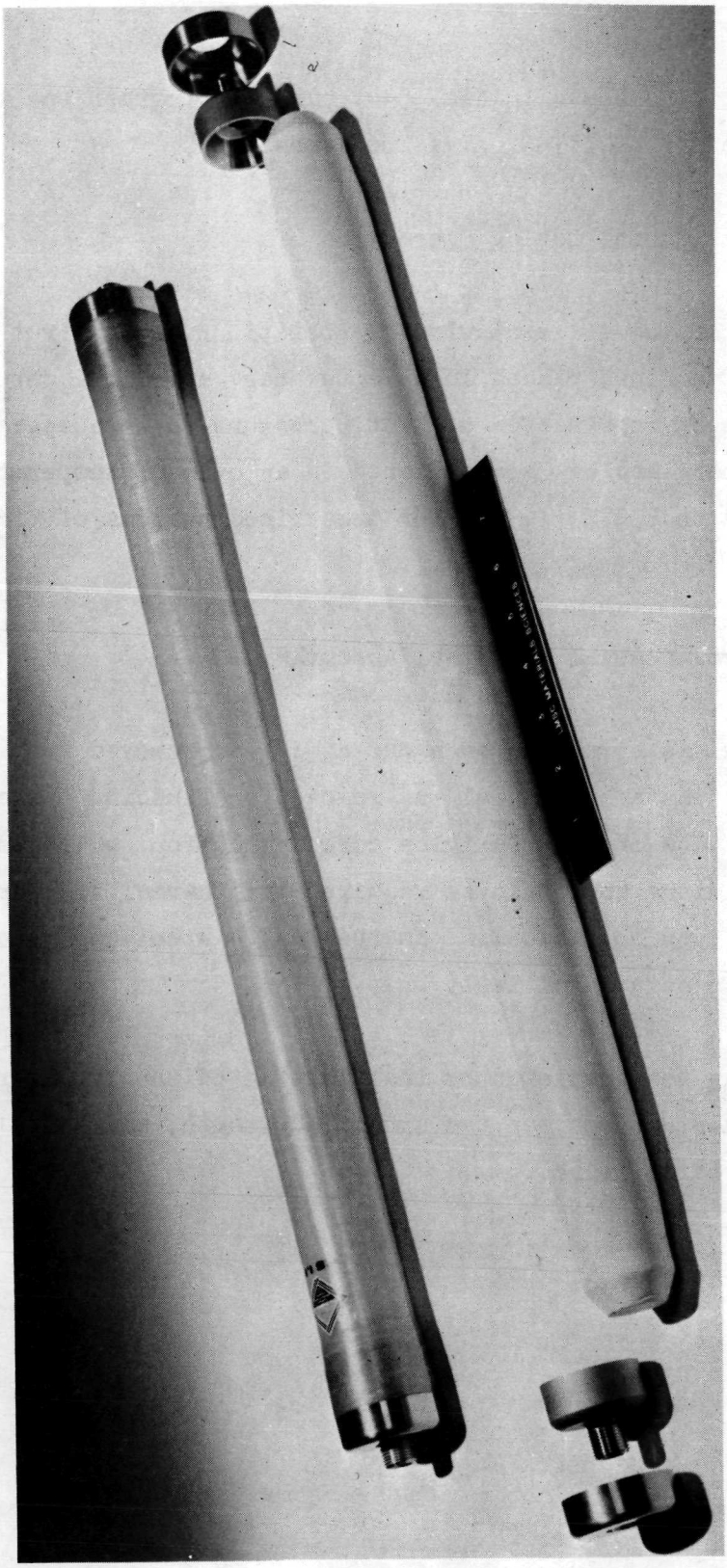

Fig. 5-3 Typical Salt Mandrel, End Fittings, and a Completed III-1 Specimen

head and tail stock as shown in Fig. 5-4. This photograph was taken near completion of one of the III-3 ogive specimens.

5.3.2 Debulking and Curing Operations

After completion of the filament winding operations, each strut was removed from the winding machine, placed in a vacuum bag, and final debulking was accomplished using a combination of heat, pressure, and squeegee techniques. Curing of the fiberglass was accomplished in an oven at temperatures ranging from 200°F (93°C) to 300°F (149°C) for prescribed periods of time (Ref Appendix E).

5.3.3 Mandrel Removal and Final Assembly

After each fiberglass strut had been cured, it was removed from the vacuum bag, cleaned, and the salt mandrel was removed by flushing the core cavity with warm water. The chopped Dexiglas core insulation, which is specified in the design drawings and would be required for thermal test or flight article hardware, was not installed in the Task 4 specimens since they were to be subjected to structural tests only.

The strut assembly was completed by installation of the proper rod-end fittings, adjustment to achieve the specified length, and installation of the locknuts and safety wire.

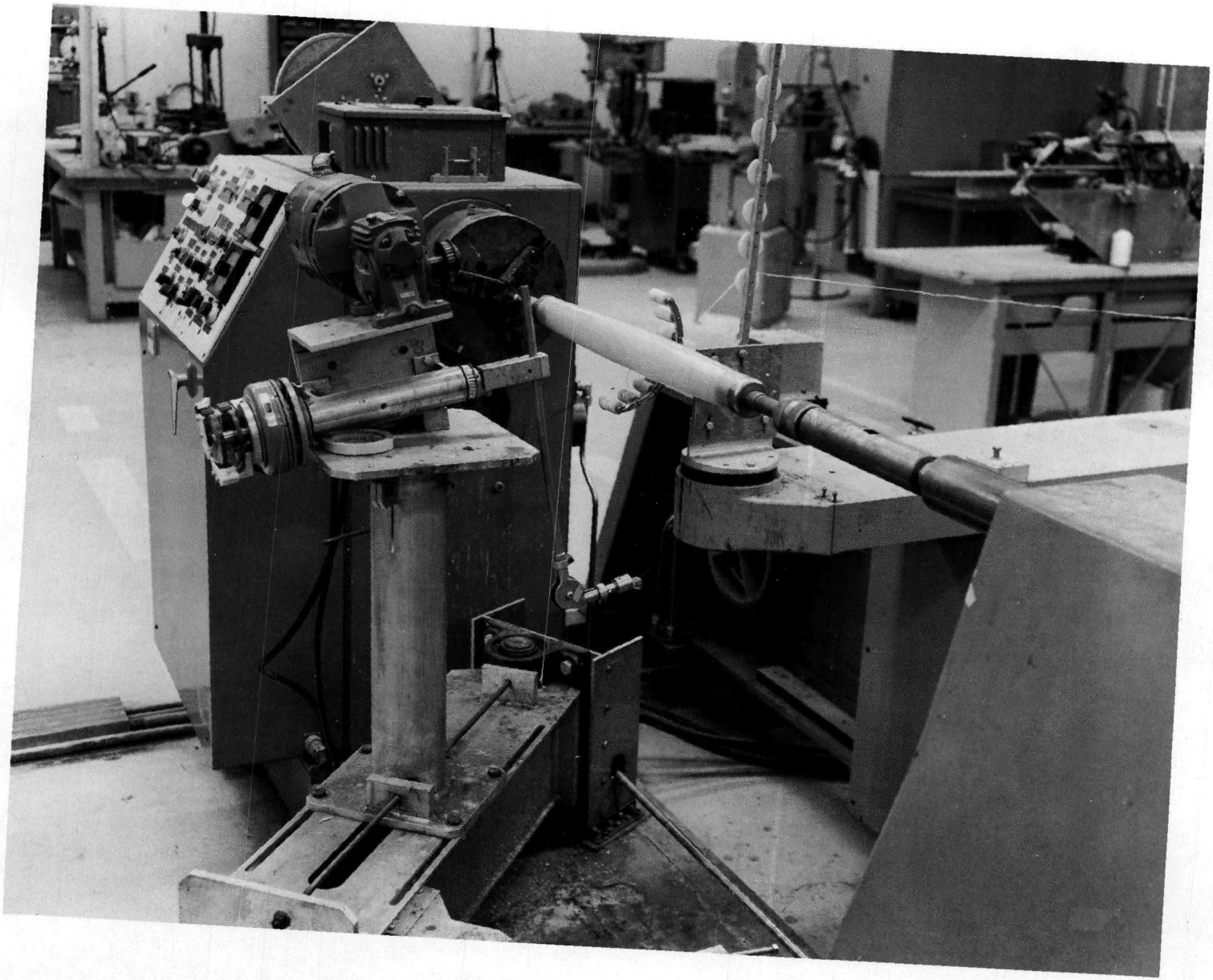

Fig. 5-4 Typical Winding Operation Near Completion

Section 6

TASK 4 - TEST PROGRAM

The fiberglass struts which were fabricated in Task 3 were tested to failure in Task 4. For each of the selected designs (Ref Table 3-12 and Figs. 3-46, 3-47, and 3-48), two or more specimens were tested in compression, two or more in tension, and two or more in cyclic loading modes. Each of the specimens was tested using a 60,000 lbf (266,900 N) dynamic test machine with one end of the strut submerged in liquid nitrogen to simulate design environment temperatures. Compression and tension specimens were tested using the two-axis LVDT instrumentation system described in Section 4.1.2 for the short-column screening test. Cyclic test specimens were subjected to design limit load values (ultimate/1.4) in both tension and compression modes, except that, where the ratio of limit tension to limit compression loads exceeded 2.5, the applied tension loads were reduced to maintain this maximum ratio. Cyclic loads were applied at a 10-cps rate for each of these tests. The facilities, instrumentation, test operations, and results pertaining to the full-scale strut tests are described and discussed in this section.

6.1 FACILITY DESCRIPTION

6.1.1 Dynamic Test Machine

An MTS Corporation shaker system, with a maximum rated capacity of 60,000 lbf (266,900 N) in tension, compression, or cyclic loads was used to perform the Task 4 strut tests. The system is located within the Cryogenic Test Compex at Lockheed's Santa Cruz Test Base. An aerial view of the complex is shown in Fig. 6-1. Specific areas of the complex which are pertinent to the program include (1) the Test Pad area where the MTS shaker system is located, (2) the Control and Instrumentation Building which houses the control and data-acquisition equipment, and (3) the Pressurant and Cryogen Storage Area.

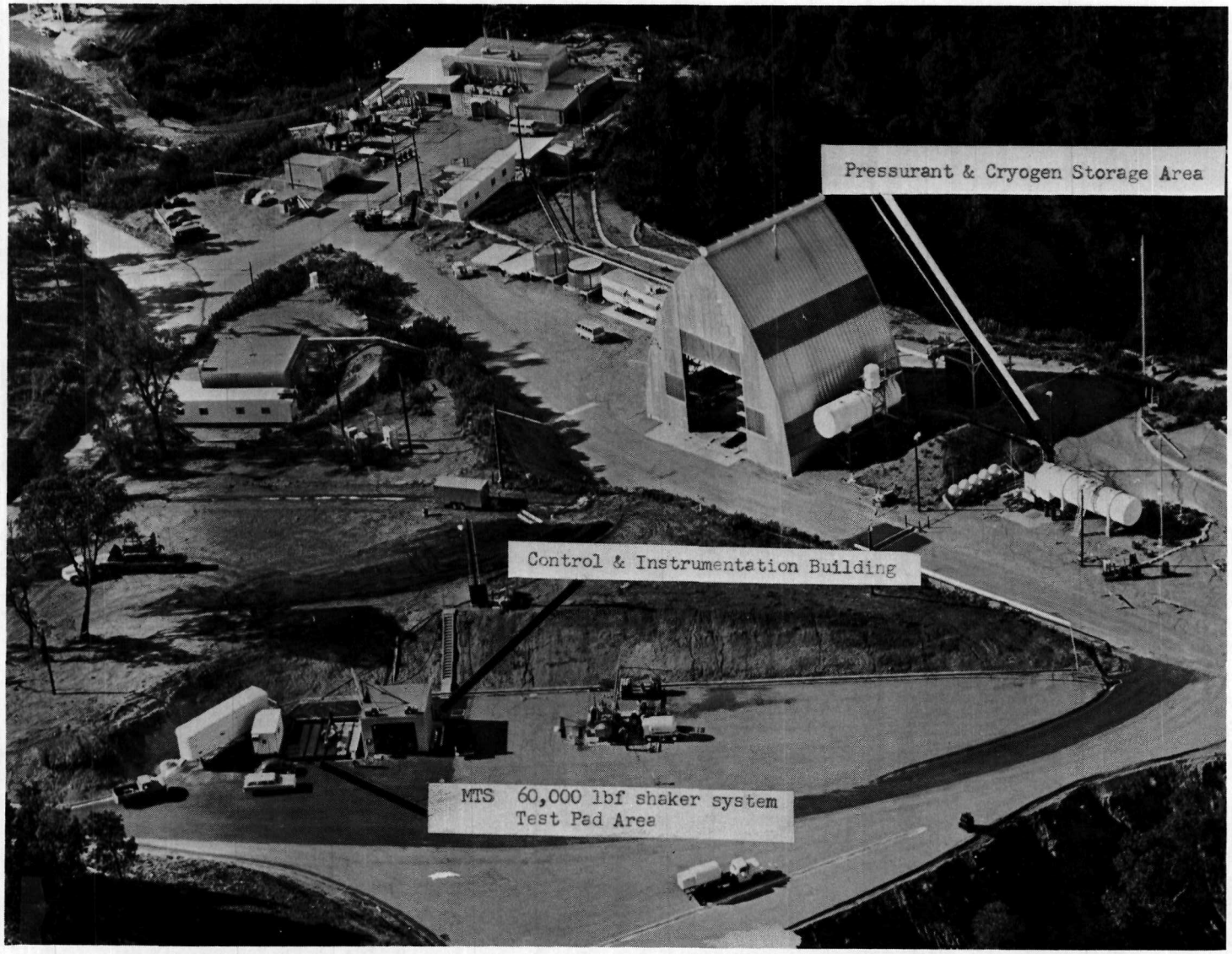

Fig. 6-1 Cryogenic Test Complex

The 60,000-lbf (266,900-N) shaker system consists of a hydraulic power supply and two 30,000-lbf (133,400-N) hydraulic actuator heads. The actuator heads are shown in Fig. 6-2 with a typical strut of the III-3 configuration set up for test. The liquid nitrogen container used to maintain the lower end of the strut at 140°R (78°K) during the test, and the LVDT transducers used to obtain deflection measurements under load, can be seen in this photograph.

A schematic of the MTS dynamic test system is presented in Fig. 6-3. Tension, compression, and cyclic loads were programmed for application at predetermined constant rates using a deflection-feedback control mode. Limits of the system are shown in Fig. 6-4. In this figure, maximum attainable peak-to-peak displacement is plotted as a function of frequency for operation with either one or two of the actuator heads. As shown, the system capability is limited by a maximum peak-to-peak displacement of 2 in. (5.08 cm) and by a maximum crosshead velocity of 30 in./sec (76 cm/sec). The crosshead velocity limit depends on hydraulic pumping capacity and could be increased by increasing the size of the pumping system.

During the Task 4 test program, the MTS system was operated with two actuators, since true axial loading was desired. Inspection of Fig. 6-4 shows that, for this operational mode, the maximum cyclic load frequency that can be achieved with the maximum peak-to-peak displacement of the crosshead is approximately 3 hz. For a typical strut test where the displacement required to achieve the desired load is 0.48 in. (1.22 cm), the maximum attainable frequency is approximately 10.7 hz.

6.1.2 Instrumentation and Data Acquisition Equipment

In the Task 4 tests, the same linear variable differential transformers (LVDTs) which had been used previously in the Task 2 program (Ref Section 4.1.2) were again used to obtain specimen deflections over a 3.5-in. (8.89-cm) gage length centered about the midspan location. These transducers were installed using the same special clamps and attachment techniques which were

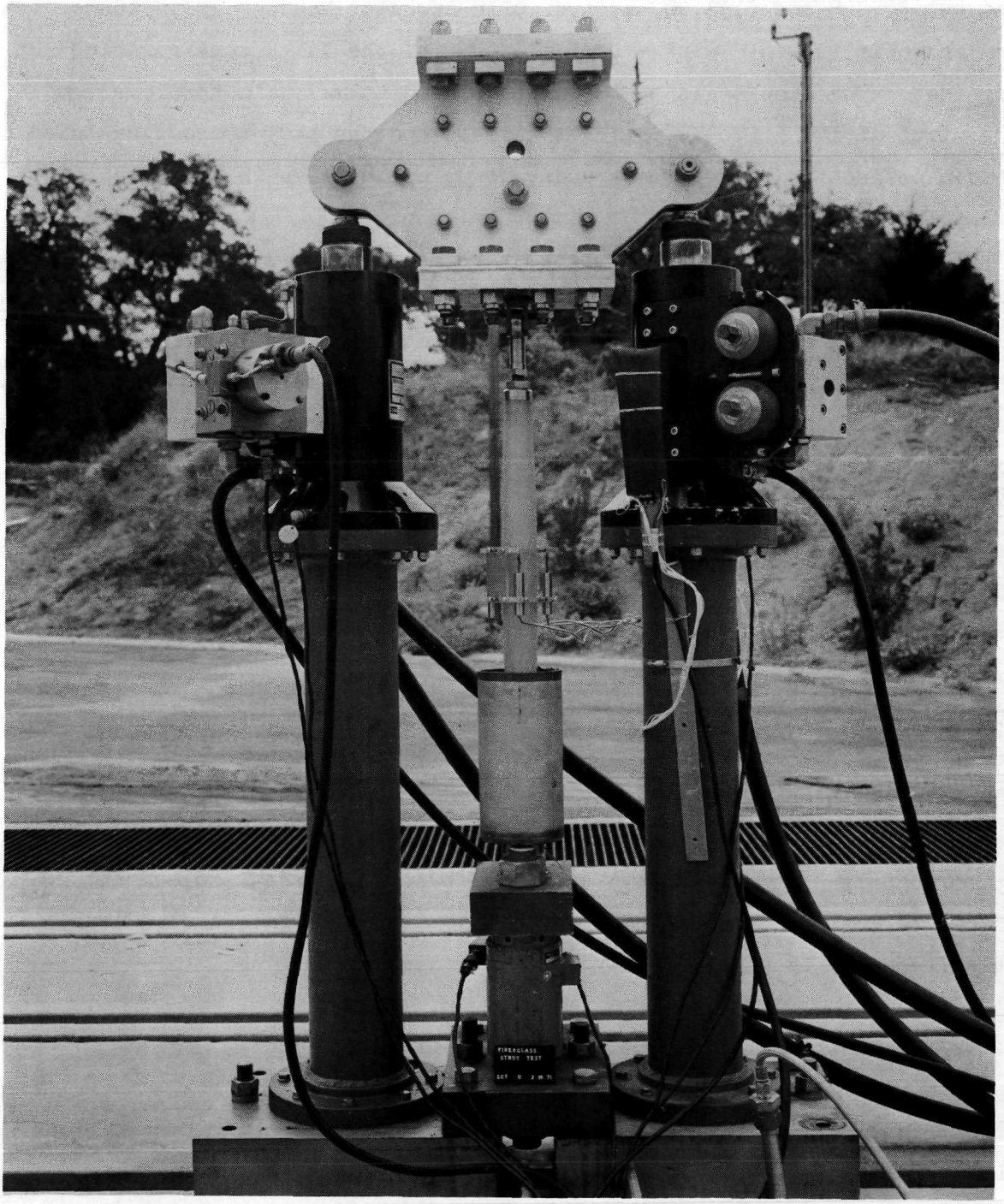

Fig. 6-2 Typical Test Setup

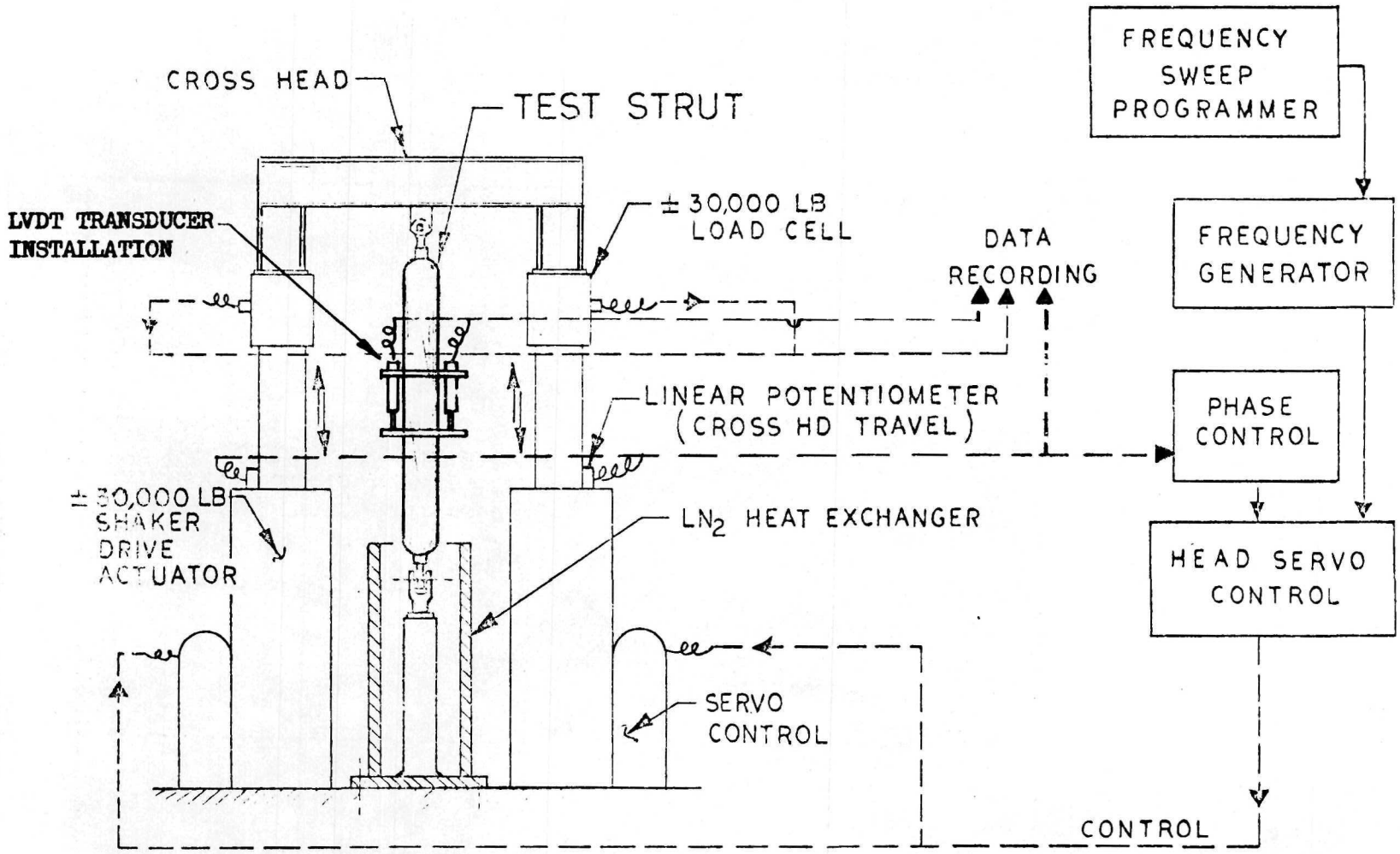

Fig. 6-3 Schematic of the Dynamic Test System

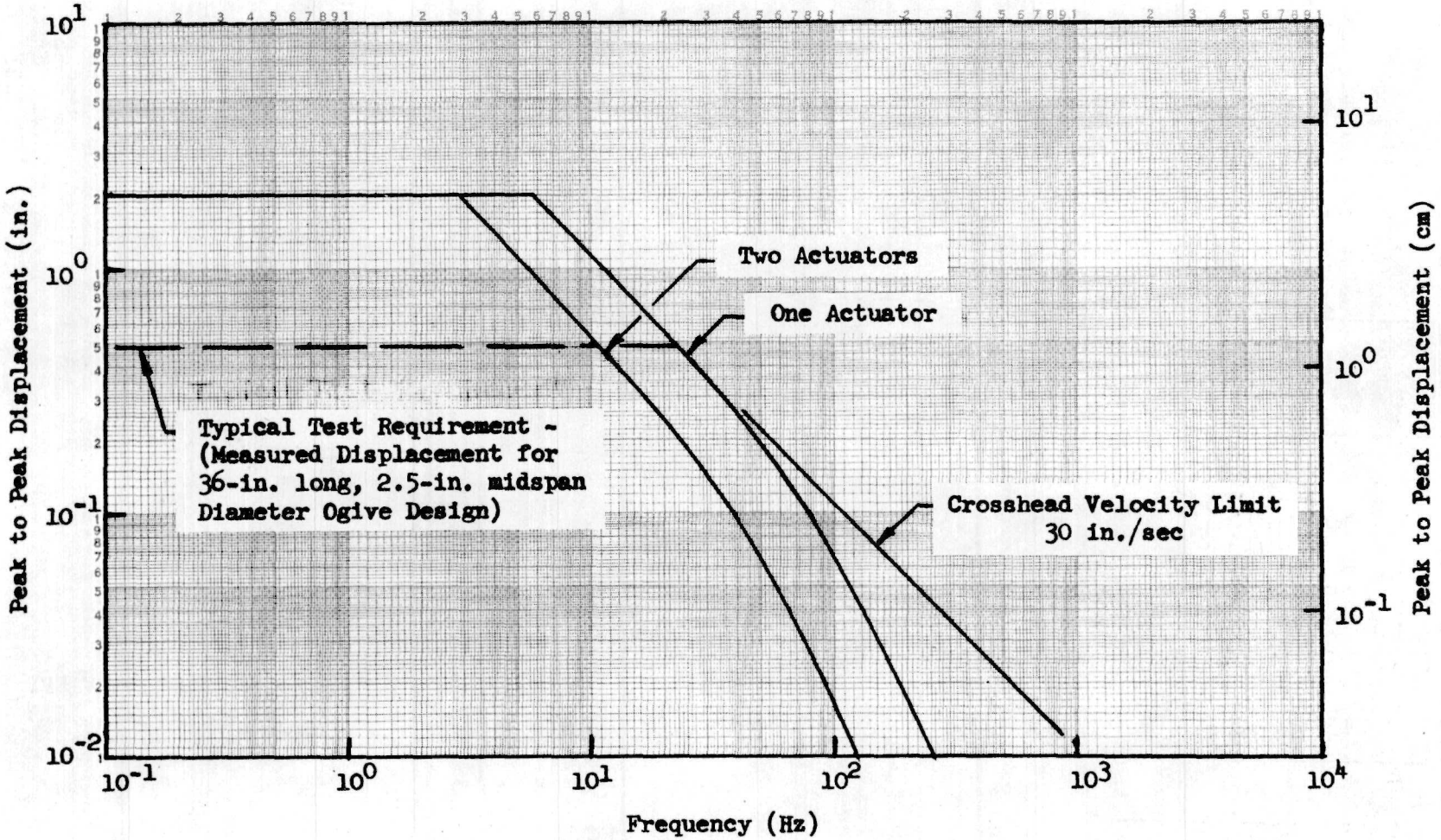

Fig. 6-4 Maximum Displacement-Frequency Characteristics of the MTS Test System

used in Task 2. However, deflection measurements were obtained for the tension and compression test specimens only, since the sensors and the mounting system were not suitable for use under dynamic loading conditions, and since these measurements were not required for the cyclic load specimens.

In addition to specimen deflection measurements, applied load and crosshead travel data were also measured using transducers built into the MTS shaker system (Ref Fig. 6-3).

Output signals from the LVDT, applied load, and crosshead travel instrumentation transducers were fed through signal conditioners and amplifiers to Moseley Model 7100 B strip chart recorders. Continuous data records were obtained on the strip charts for each of these three functions.

6.2 STRUCTURAL TESTING

Prior to initiation of the Task 4 test program, each of the strut specimens was measured to determine the direction and magnitude of any manufacturing eccentricity that existed between the center of the strut cross-section at midspan and the true reference centerline. Initially, cross-section outside diameters were measured at four midspan locations, spaced at 45° intervals, using a micrometer. The strut was then supported on a flat reference table with the end fittings placed in identical V-blocks. The distance between the highest point on the cross-section and the reference table surface, for each 45° of strut rotation, was measured using a height gage. The distance from the cross-section centerline to the reference table was then calculated by subtracting half of the measured outside diameter at that location from the measured height. These data were plotted as a function of interval angle to determine the direction, and magnitude of any existing eccentricity. The locations determined in this manner were then marked on the outer surface of each strut and used to locate and install the LVDT instrumentation.

An analysis was conducted to determine the effect of the measured eccentricities on predicted ultimate column buckling loads. Results of the analysis are summarized in Table 6-1.

Table 6-1

SUMMARY OF MEASURED ECCENTRICITIES AND PREDICTED ULTIMATE COMPRESSION LOADS FOR TASK 4 STRUT SPECIMENS

Configuration No.	III-1	III-2	III-3
Configuration Description	Monocoque Cylinder	Monocoque Cylinder	Monocoque Ogive
Predicted Nominal* Ult Comp Load, lbf (N)	2900 (12900)	6430 (28600)	4600 (20460)
Measured Eccentricity, e, in. (cm) and Predicted Ult Comp Load, P_c, lbf (N):			
Specimen A, e	0.078 (0.198)	0.018 (0.046)	0.038 (0.097)
P_c	2135 (9495)	5375 (23910)	3825 (17010)
Specimen B, e	0.053 (0.135)	0.019 (0.048)	0.034 (0.086)
P_c	2250 (10010)	5350 (23800)	3920 (17440)
Specimen C, e	0.058 (0.147)	0.006 (0.015)	0.032 (0.081)
P_c	2220 (9875)	5874 (26130)	3940 (17530)
Specimen D, e	0.005 (0.013)	0.004 (0.010)	0.019 (0.048)
P_c	2795 (12430)	6005 (26710)	4120 (18330)
Specimen E, e	0.037 (0.094)	0.018 (0.046)	0.024 (0.061)
P_c	2375 (10560)	5375 (23910)	4040 (17970)
Specimen F, e	0.037 (0.094)	0.009 (0.023)	0.065 (0.165)
P_c	2375 (10560)	5710 (25400)	3625 (16120)
Specimen G, e	0.038 (0.097)	0.003 (0.008)	0.062 (0.157)
P_c	2365 (10520)	6080 (27040)	3670 (16320)
Specimen H, e	0.062 (0.157)	0.010 (0.025)	0.009 (0.023)
P_c	2195 (9765)	5655 (25150)	4315 (19190)

* Assuming zero eccentricity

6.2.1 Static Tension-Compression Tests

During the static tension and compression tests conducted in Task 4, data were measured and recorded continuously for applied load, crosshead travel, and average strain over the 3.5-in. (8.89-cm) gage length. The lower end fitting of each specimen tested was immersed in liquid nitrogen throughout the test duration. A linear controlled rate program was used to apply the axial tension or compression load until failure occurred.

Two specimens each of strut configurations III-1, III-2, and III-3 were tested to failure in tension. No data were obtained for two additional tensile-test specimens of the III-2 design when the test machine servo system malfunctioned causing tilting of the crosshead and destruction of the specimens. The two typical types of failure observed for testing in this mode are illustrated in Figs. 6-5 and 6-6, respectively, for specimens III-1A and III-3F. Failure occurred due to fracture of the longo fibers near the upper LVDT mounting point for specimen III-1A. Stress concentrations due to the mounting screws may have initiated this failure; however, the failure load exceeded that predicted by approximately 2 percent (see Section 6.2.3). As shown in Fig. 6-6, the failure of specimen III-3F was typical of those for the III-2 and III-3 designs. In these tests, the initial failure occurred in tensile fracture of the longo fibers where they wrapped around the warm end fitting. Additional damage then occurred at several points along the length of the strut during compressive rebound after the initial tensile fracture had occurred.

In the compression test mode, three specimens each of the III-1 and III-3 configurations and two specimens of the III-2 configuration were tested to failure. Results for one of the III-1 specimens were questionable due to an uncertainty of the load value recorded subsequent to chilldown and prior to initiation of the test (see Section 6.2.3). Compression failures for all of the specimens tested in this mode were similar to that shown in Fig. 6-7 for specimen III-2B where local crushing of the composite material occurred near

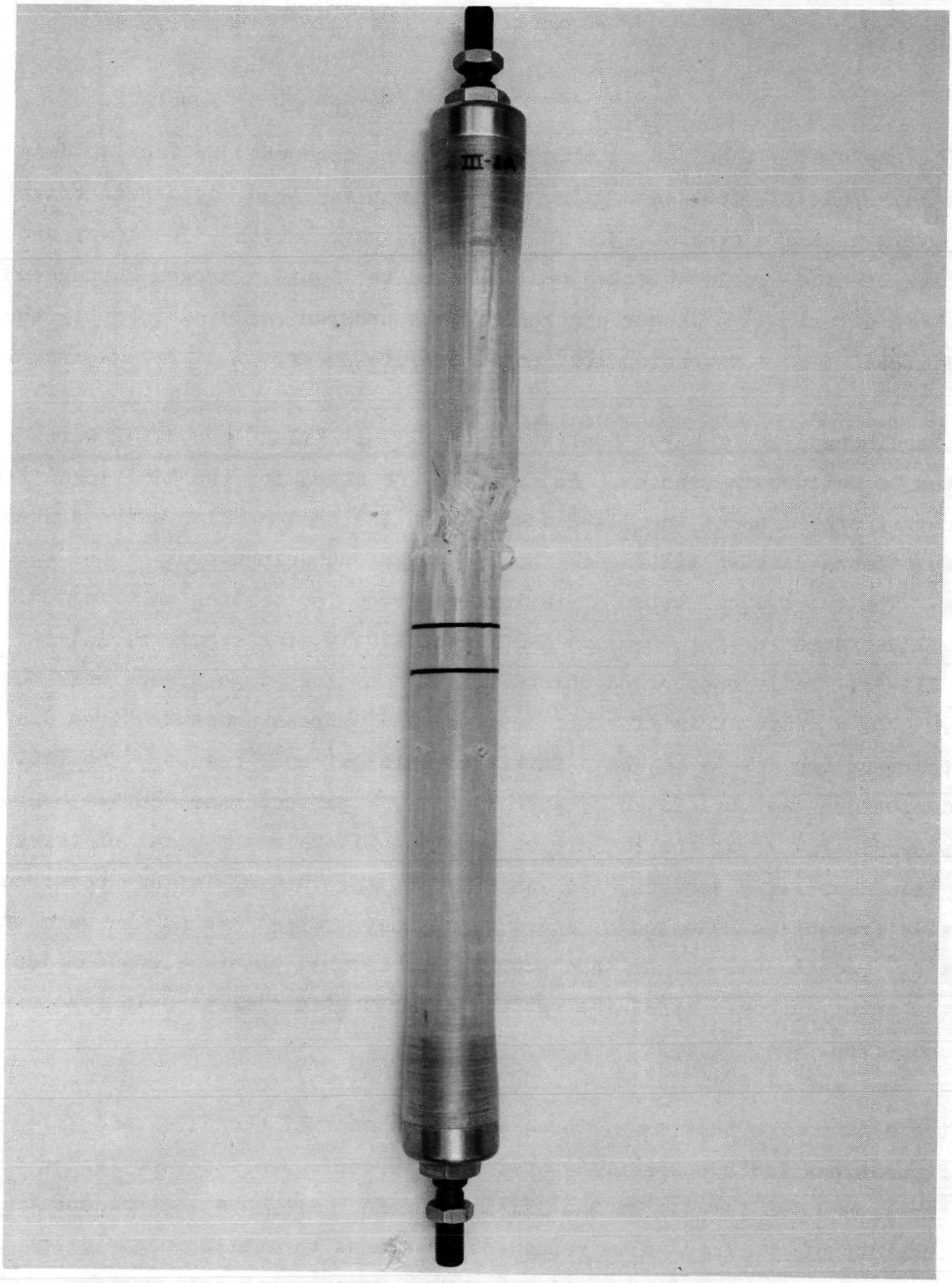

Fig. 6-5 Specimen III-1A After Failure in Tension

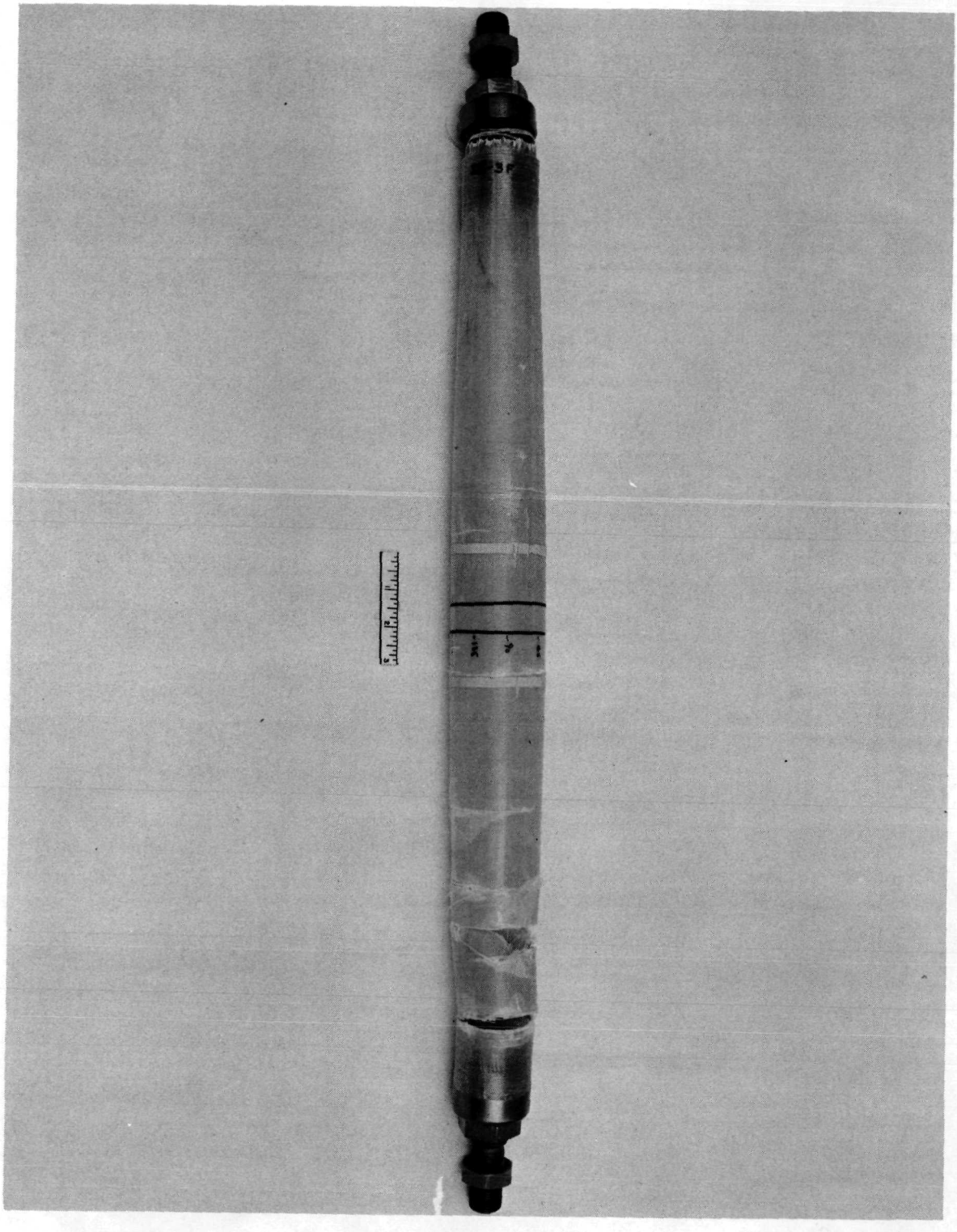

Fig. 6-6 Specimen III-3F After Failure in Tension

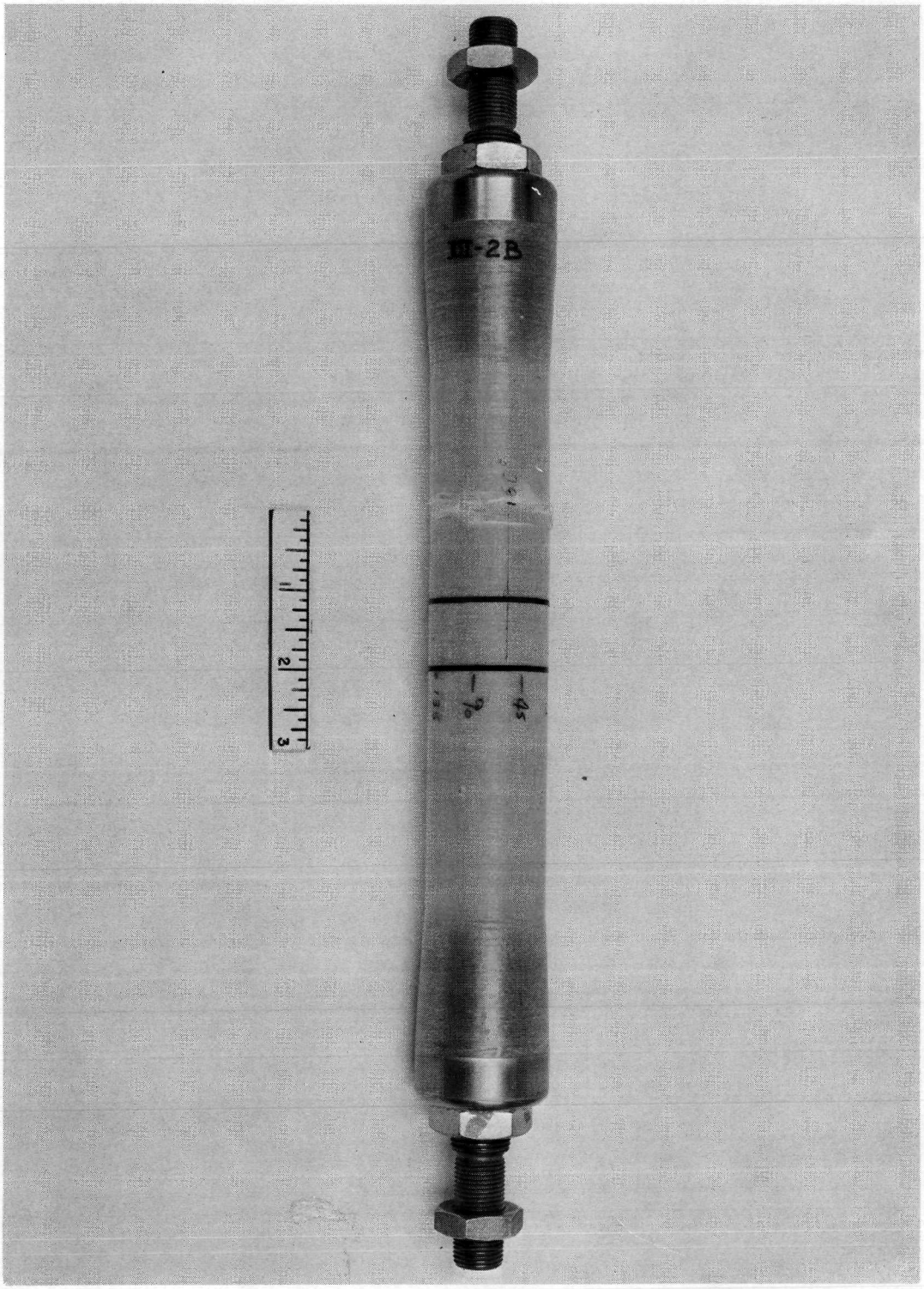

Fig. 6-7 Specimen III-2B After Failure in Compressive Crushing

midspan. Classic diamond-pattern crippling failures were not observed for any of the compressive test specimens.

6.2.2 Cyclic Tests

The specimens to be tested in cyclic loading were installed in the test machine without the LVDT transducers, since strain measurements were not required for these tests. During each of the tests, data on applied load and crosshead travel were measured and recorded continuously. As in the case of the static test specimens, liquid nitrogen was used to immerse the lower end fitting of each strut to simulate the design environment temperature. Loads were applied in a sine-wave pattern at a constant cycle rate of 10 hz until failure occurred.

Two specimens each of the III-1, III-2, and III-3 strut configurations were tested to failure under cyclic loading. Typically, failures in this test mode occurred due to initial tensile fracture of the longo rovings at the warm end fitting, followed by damage at other points along the strut due to compressive rebound or to application of the next compressive load cycle. This is illustrated by the photograph of specimen III-3D shown in Fig. 6-8.

6.2.3 Test Results and Analysis

A summary of the test mode, predicted ultimate load, failure load, failure margin, and the number of load cycles applied prior to failure is presented in Table 6-2 for all of the Task 4 tests. Inspection of these data shows that the failure loads were generally within ± 15 percent of those predicted. In two cases where the failure margin was outside of this scatter band, the actual loads achieved exceeded those predicted by 17.7 percent and 25.4 percent. No failures occurred near the cold end of the strut, and none occurred in either the internal titanium end fittings or in the rod-end fittings.

Photographs showing the specimens of the III-1, III-2, and III-3 strut

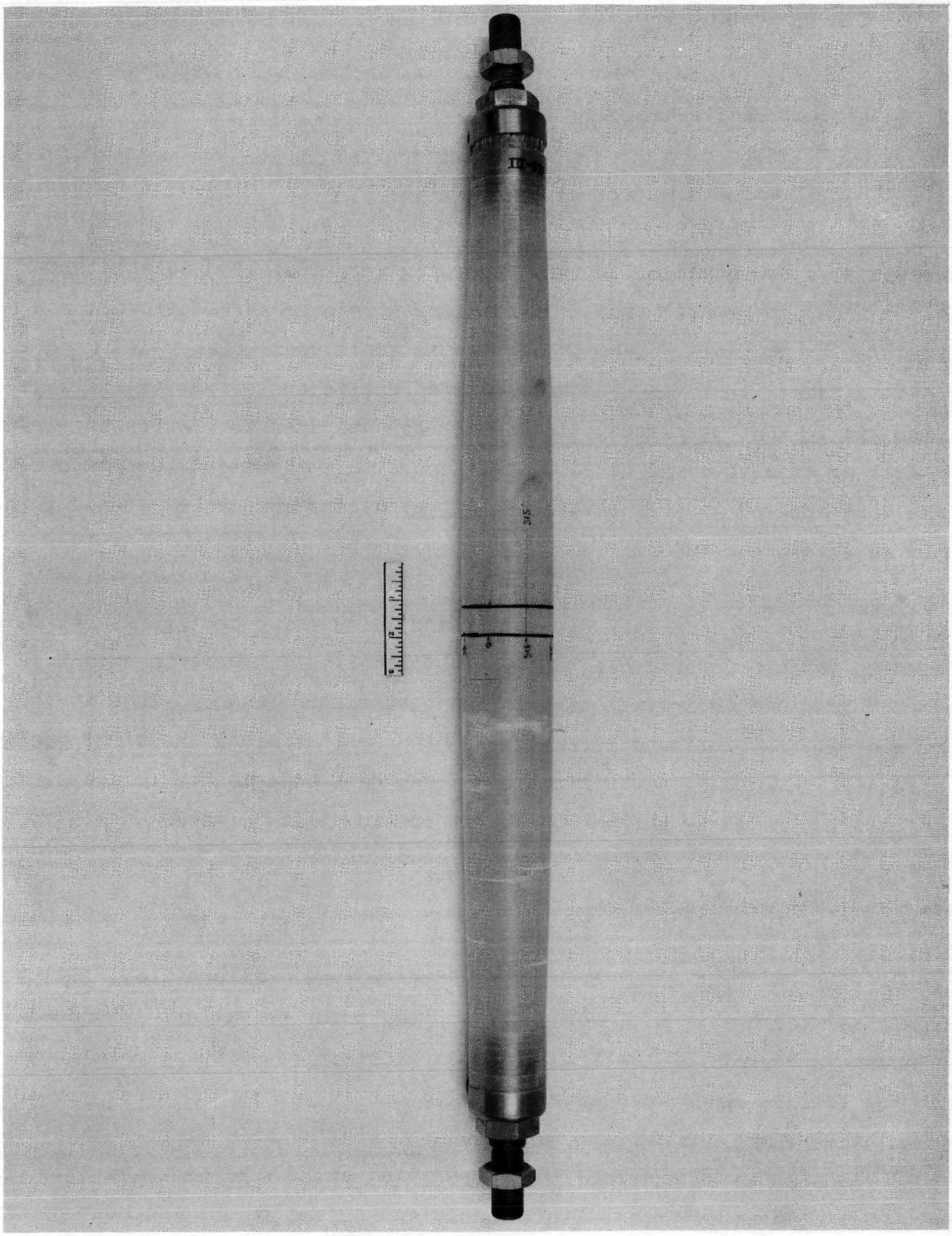

Fig. 6-8 Specimen III-3D After Failure in Cyclic Loading

Table 6-2

SUMMARY OF TASK 4 FIBERGLASS STRUT TEST RESULTS

Specimen No.	Test Mode	Predicted Ult Load, P_P lbf	(N)	Failure Load, P_F lbf	(N)	Margin $100(P_F/P_P-1)$ percent	No. of Cycles at Failure
III-1A	Tension	7660	(34,070)	7780	(34,610)	+1.6	1
III-1H	Tension	7660	(34,070)	8040	(35,760)	+5.0	1
III-1D	Comp	2795	(12,430)	3290	(14,630)	+17.7	1
III-1E	Comp	2375	(10,560)	2680(1)	(11,920)	+12.8(1)	1
III-1G	Comp	2365	(10,520)	2600	(11,560)	+9.9	1
III-1B	Cyclic	2250C/7660T	(10,010C/34,070T)	1910C/3870T	(8495C/17,210T)	(N.A.)	209
III-1C	Cyclic	2220C/7660T	(9875C/34,070T)	1600C/3980T	(7115C/17,700T)	(N.A.)	283
III-2E	Tension	14,320	(63,700)	12,960	(57,650)	-9.5	1
III-2G	Tension	14,320	(63,700)	13,790	(61,340)	-3.7	1
III-2A	Comp	5375	(23,910)	6740	(29,980)	+25.4	1
III-2B	Comp	5350	(23,800)	5950	(26,470)	+11.2	1
III-2C	Cyclic	5875C/14320T	(26,130C/63,700T)	4500C/10,030T	(20,020C/44,610T)	(N.A.)	210
III-2D	Cyclic	6005C/14,320T	(26,710C/63,700T)	4360C/10,080T	19,390C/44,840T)	(N.A.)	207
III-3F	Tension	16,010	(71,210)	15,350	(68,280)	-4.1	1
III-3G	Tension	16,010	(71,210)	15,625	(69,500)	-2.4	1
III-3A	Comp	3825	(17,010)	3950	(17,570)	+3.3	1
III-3B	Comp	3920	(17,440)	4450	(19,790)	+13.5	1
III-3C	Comp	3940	(17,530)	3720	(16,550)	-5.6	1
III-3D	Cyclic	4120C/16,010T	(18,330C/71,210T)	3020C/7545T	(13,430C/33560T)	(N.A.)	2509
III-3E	Cyclic	4040C/16,010T	(17,970C/71,210T)	2940C/7150T	(13,080C/31,800T)	(N.A.)	5761

(1) Data shown is uncertain due to poor strip chart record

configurations, respectively, after the tests were completed are presented in Figs. 6-9, 6-10, and 6-11. Specimens III-2E and III-2F are not shown, since they were unavailable at the time this photograph was taken. Also, specimens III-1D, III-2G, and III-3H had not been tested at this time.

Data on average stress and strain were determined by analysis of the load-deflection data records for typical Task 4 tension and compression specimens. These data were plotted and are presented in Figs. 6-12, 6-13, and 6-14, respectively, for struts of configurations III-1, III-2, and III-3. The stress values shown were determined using the total nominal cross-sectional composite area for each specimen. Average strain values were determined over the gage length used by dividing total deflection by 3.5 in. (8.89 cm).

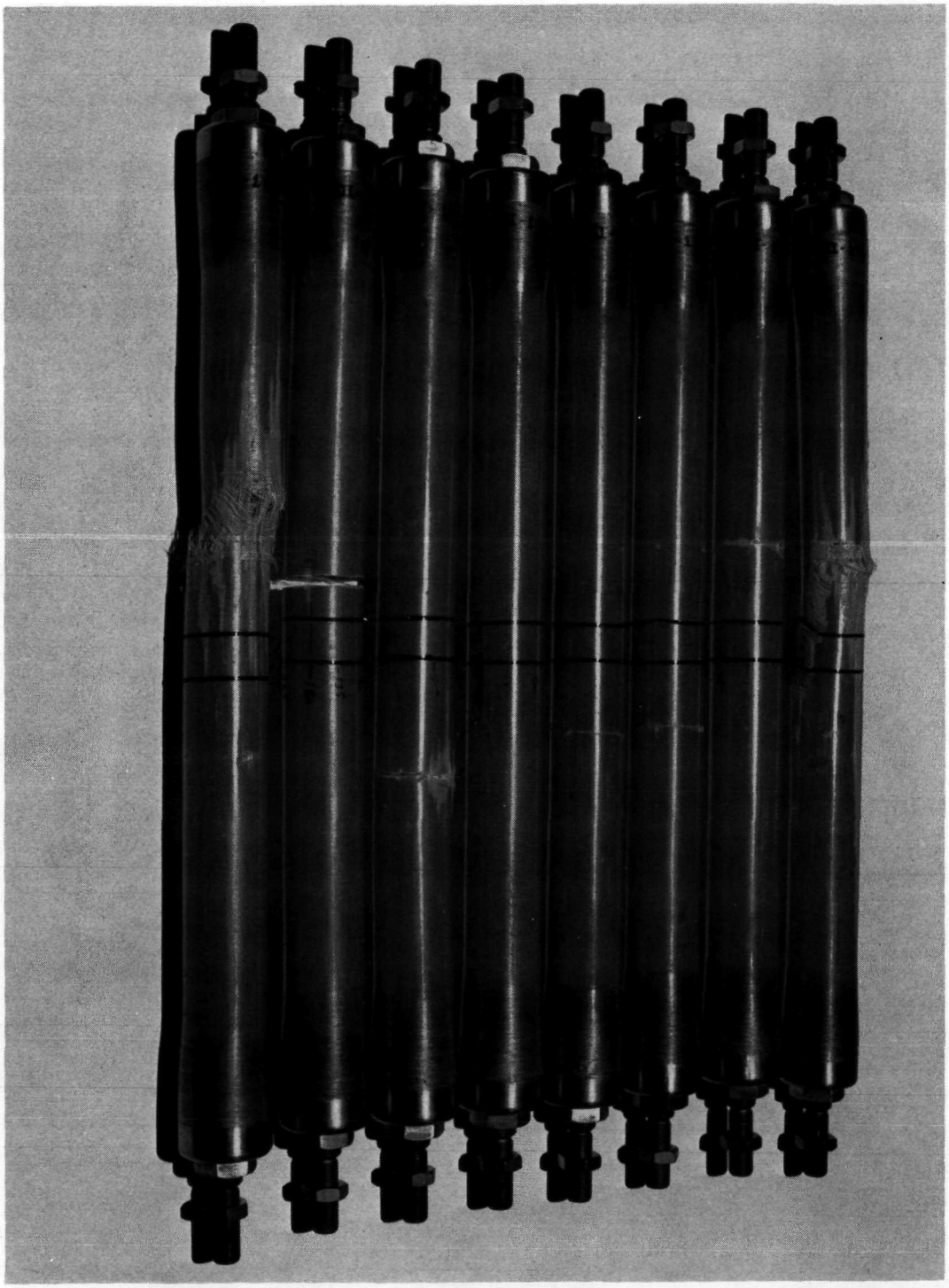

Fig. 6-9 Specimens of Configuration III-1 After Testing to Failure

Fig. 6-10 Specimens of Configuration III-2 After Testing to Failure

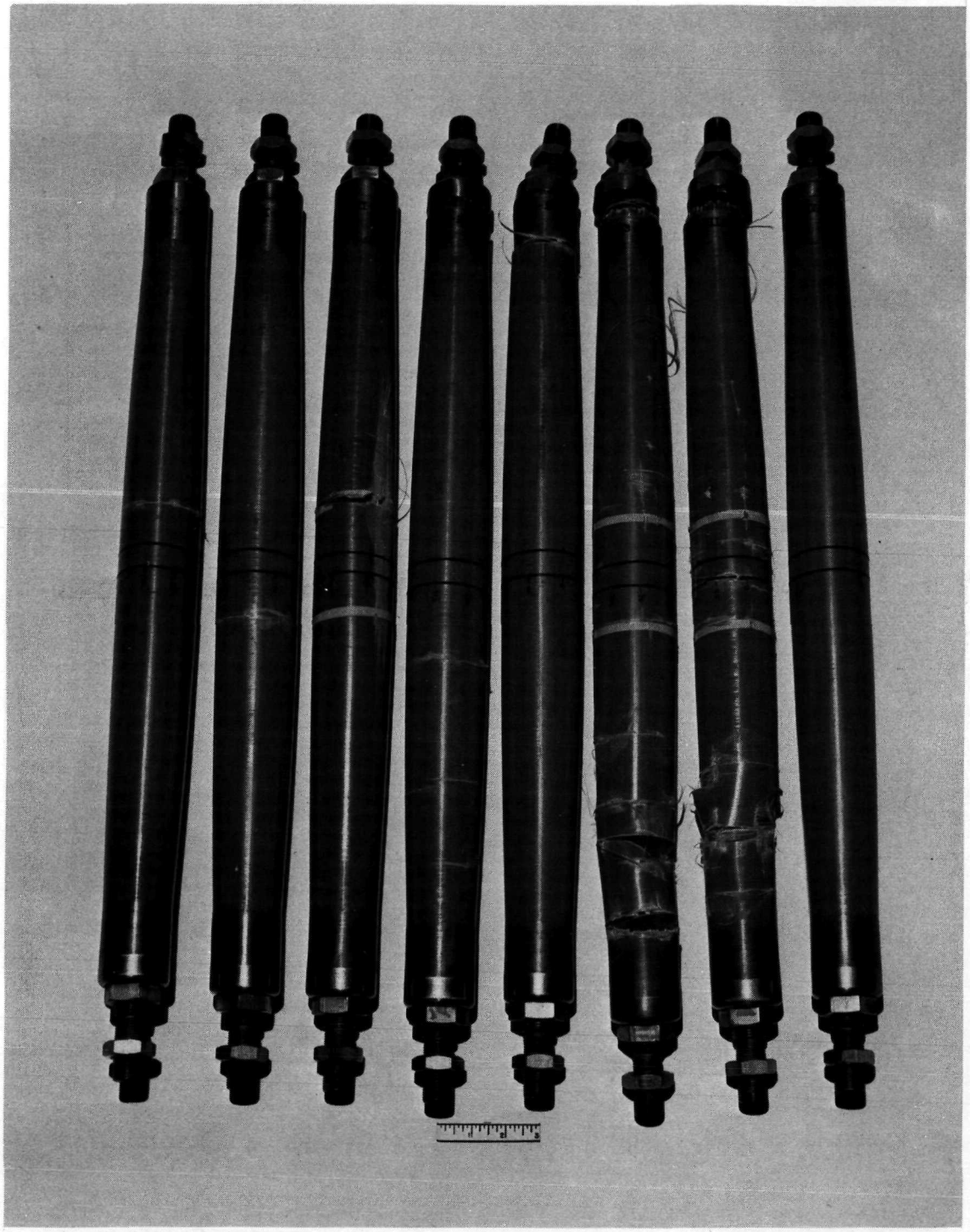

Fig. 6-11 Specimens of Configuration III-3 After Testing to Failure

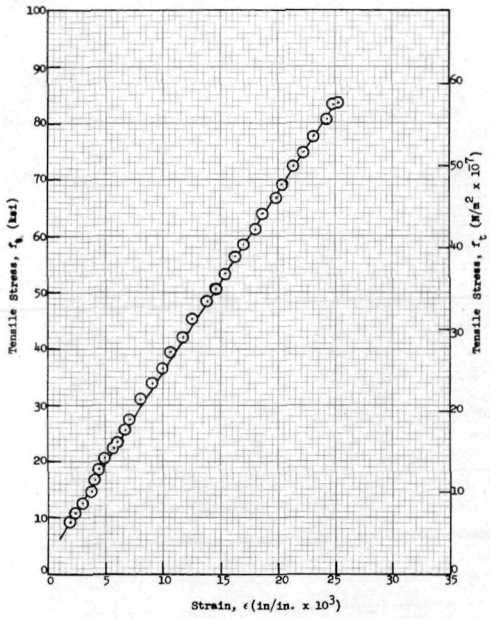

(a) Tension Specimen III-1A

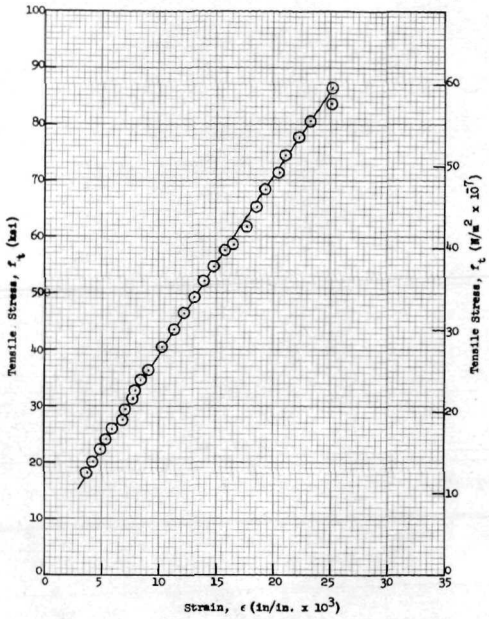

(b) Tension Specimen III-1H

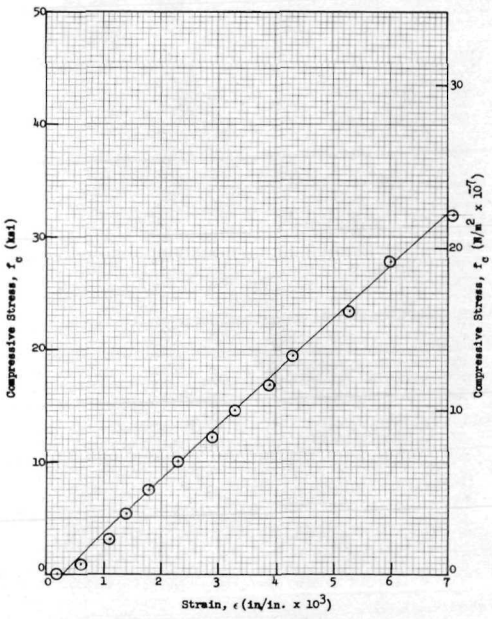

(c) Compression Specimen III-1D

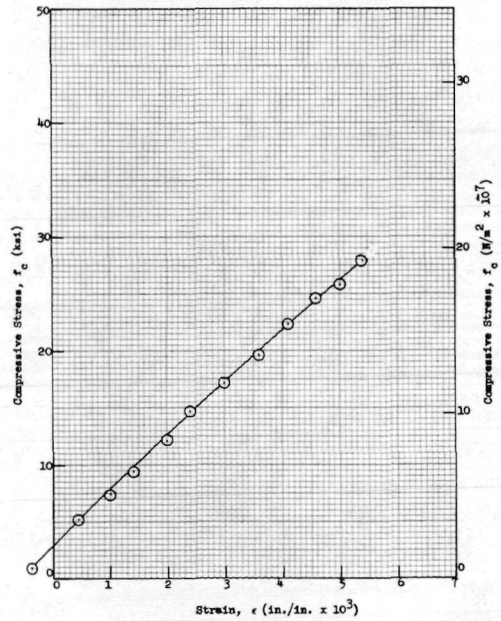

(d) Compression Specimen III-1G

Fig. 6-12 Stress-Strain Curves for Typical Specimens of Strut Configuration III-1

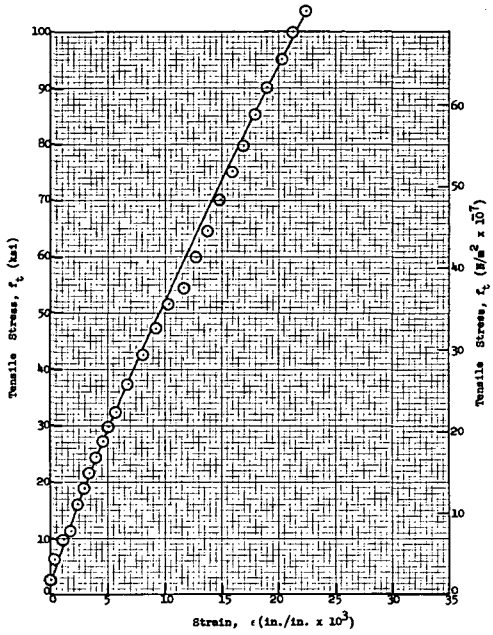

(a) Tension Specimen III-2E

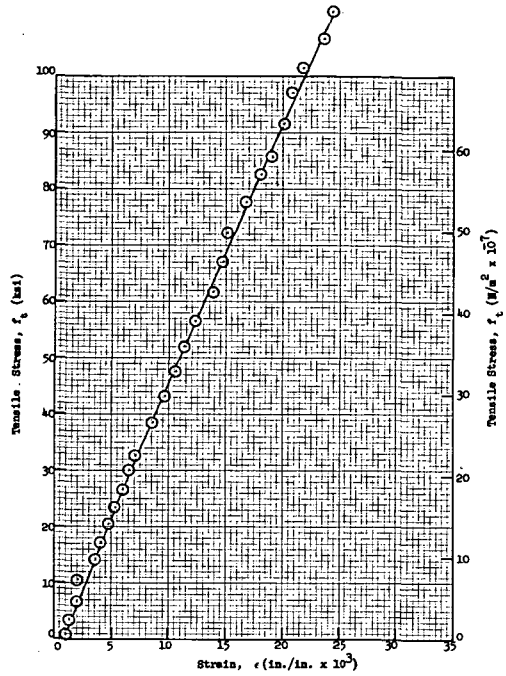

(b) Tension Specimen III-2G

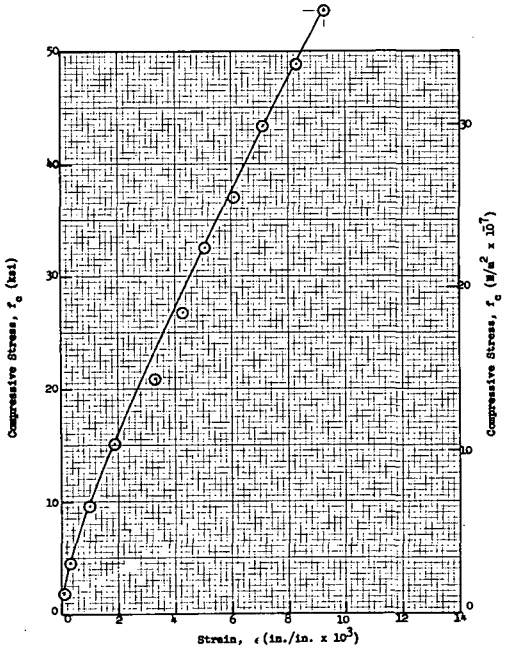

(c) Compression Specimen III-2A

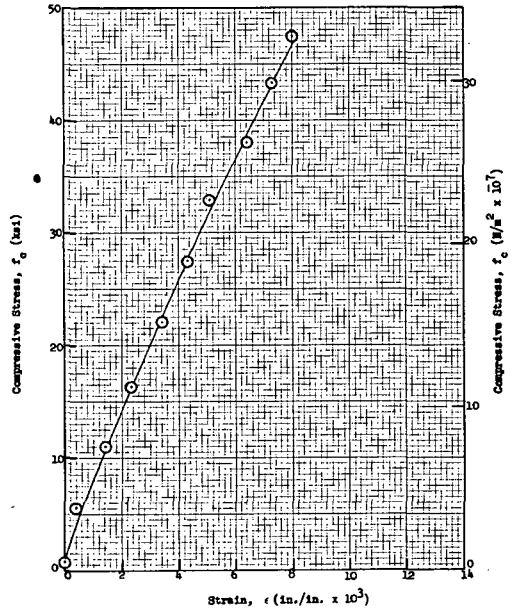

(d) Compression Specimen III-2B

Fig. 6-13 Stress-Strain Curves for Typical Specimens of Strut Configuration III-2

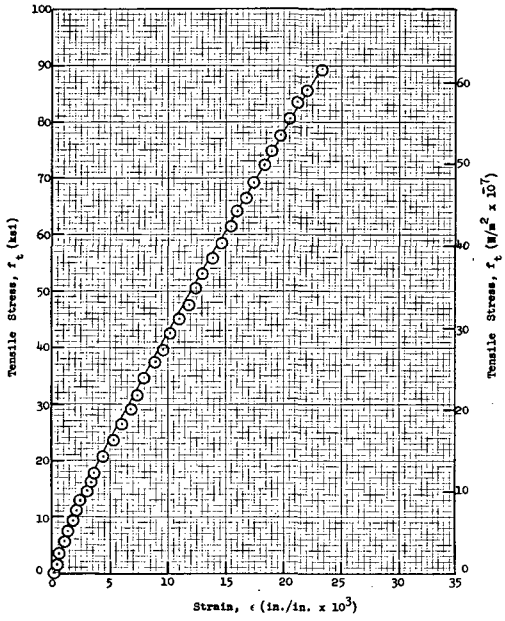

(a) Tension Specimen III-3F

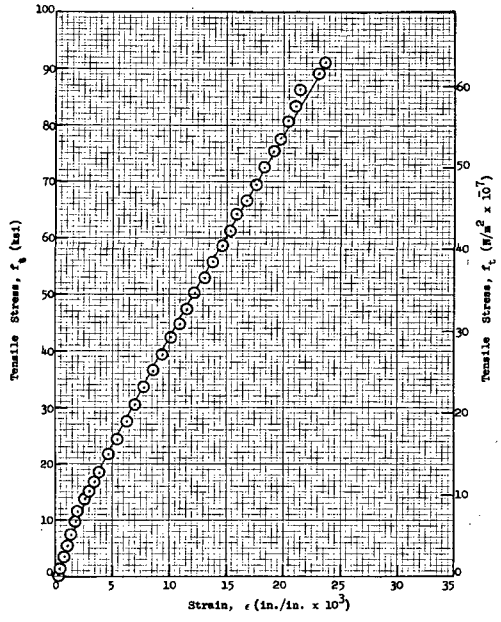

(b) Tension Specimen III-3G

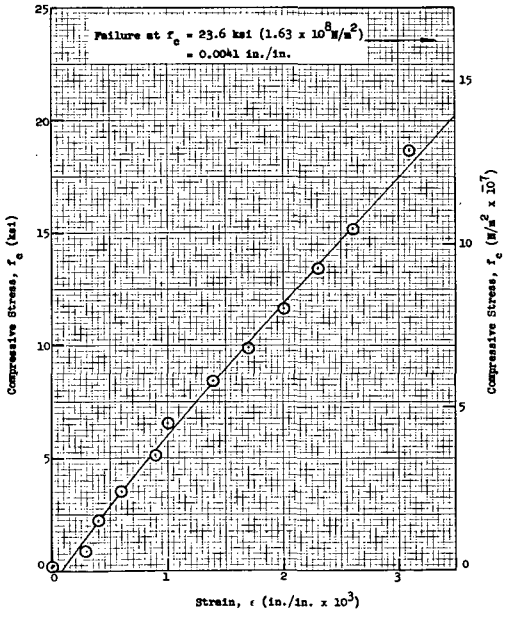

(c) Compression Specimen III-3A

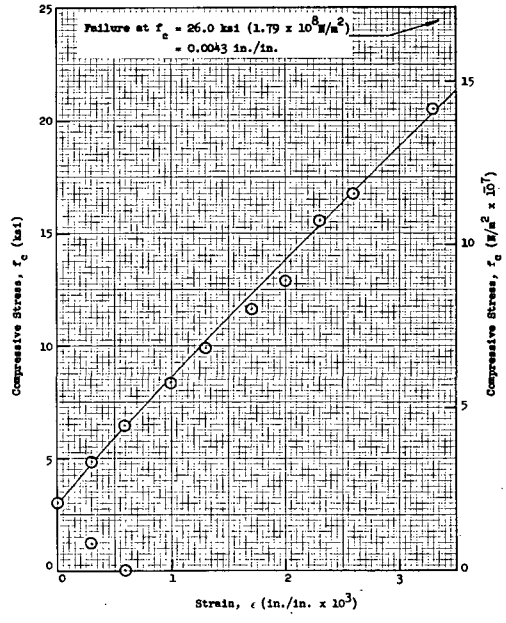

(d) Compression Specimen III-3B

Fig. 6-14 Stress-Strain Curves for Typical Specimens of Strut Configuration III-3

Section 7

TASK 5 - POST-TEST INSPECTION AND DATA CORRELATION

Strut specimens fabricated under Tasks 2 and 3 of the program were subjected to extensive pre-test and post-test laboratory analyses in Task 5. In these analyses, weight data, dimensional measurements, composite density, weight and volume fractions of the glass and resin, and void volume fractions were determined. In addition, values of elastic modulus and isotropic crippling coefficient were computed from results of the Task 2 short-column tests. The elastic modulus values were then used to revise and update the parametric column buckling design curves developed during the Task 1 structural analysis (Ref Figs. 3-37 through 3-42). Values of isotropic crippling coefficient were summarized for use in future preliminary design studies or for comparison with those obtained from other sources. However, the crippling cutoff curves obtained from the orthotropic computer analysis conducted in Task 1 were retained in Figs. 3-37 through 3-42 for use in the final design of Task 4 test specimens and for future detailed design studies since it was shown that better correlations could be obtained in this manner (Ref Section 3.). Finally in the Task 5 laboratory analysis and evaluation, representative photomicrographs of the cross-sections of failed strut specimens were obtained to inspect the distribution of fiber, resin, and voids, and cyclic-load data were analyzed and plotted to determine fatigue-life characteristics for each candidate design.

As a second part of the Task 5 work, a complete review of current fiberglass strut technology was conducted. In this review, thermal and mechanical property data were compiled, a recommended design approach was developed, other system concepts were evaluated, and a comparison was made of system performance for fiberglass struts with that for titanium struts of equal length and load capability.

Details and results of the Task 5 activities are presented and discussed in this section.

7.1 LABORATORY ANALYSIS AND EVALUATION

7.1.1 Task 2 Test Specimens

Early in Task 5, a laboratory analysis was conducted to evaluate critical manufacturing parameters for the Task 2 short column test specimens. Each strut specimen was weighed immediately following completion of the winding operation and again after the fiberglass curing operation. The composite material, internal titanium end fittings, compression caps, lock nuts, and washers for the full-size strut (prior to cut-out of the short column specimen) were included in these weights. Rod-end fitting and core insulation weights were not included. These weight data, in addition to weights of the prepreg supply spool prior to and following completion of the winding, were used to calculate total composite weight and the volatile content of the resin.

In addition to the weight data, measurements of strut body length were also obtained. Subsequently, the short column test specimens were cut from the full-size struts. Measurements of outside diameter for two locations at 90° intervals, and measurements of wall thickness for eight locations at 45° intervals were obtained.

Following completion of the short-column compression tests, a small sample of the composite material was cut from each specimen near the failure point. Each sample was weighed and its volume was determined using a gravimetric technique. Composite density values were computed from the sample weights and volumes. Subsequently, the samples were placed in an oven and maintained at approximately 1000°F (538°C) for 16 hours to completely burn away the resin. The resin weight fraction, resin volume fraction, and total fiber volume fraction were then determined from ignition weight losses and the densities of the resin and fiber components. Longo and circ fiber volume fractions were computed from the weights of each and the fiber density. Finally, void volume fraction of the original composite was determined as

the difference between unity and the sum of the resin and total fiber volume fractions.

Results of the laboratory analysis performed for the Task 2 strut specimens are presented in Tables 7-1 through 7-4. Inspection of these data shows that length and outside diameter values achieved were within ± 1.5 percent of the design nominal values. On the other hand, variations in wall thickness were much greater, ranging from -8 to +29 percent of the design values. Maximum scatter for total assembly weight, composite weight, and composite density was within ±4 percent of the average values obtained. Finally, weight and volume fractions of the resin and fiber components were found to be within ±9 percent of the design nominal values, and the void volume fraction values ranged from 0 to +6 percent for all but one specimen that contained 9.1 percent voids by volume.

An analysis of the short-column test results obtained in Task 2 was conducted in Task 5 to determine compressive stress values at failure, experimental elastic modulus values, and experimental crippling coefficients. The compressive stress values were determined simply by dividing the failure loads by the nominal total composite area. Elastic modulus values were determined graphically by evaluating the slope of the stress-strain curves (Ref Section 4.2.2) at zero load. Experimental values of the isotropic crippling coefficient were then obtained using the relationship given by

$$K_e = P_F/E_{cm} A_{cn} (t_n/R_n) \qquad (7\text{-}1)$$

A summary of the compressive stress, elastic modulus, and isotropic crippling coefficient values calculated in Task 5 is presented in Table 7-5. As shown, compressive failure stress values ranged from 60.9 ksi (4.20×10^8 N/m^2) to 67.5 ksi (4.65×10^8 N/m^2) for monocoque specimens of configurations II-1, II-2, and II-4 (excluding specimens X-17-23-2 and X-17-23-3 which failed prematurely due to inadequate moment control and pretest damage, respectively). The scatter of compressive failure stresses achieved was much greater for

Table 7-1

RESULTS OF LABORATORY ANALYSIS FOR CONFIGURATION II-1 TEST SPECIMENS

Specimen No.	X-17-23-1	X-17-23-2	X-17-23-3	Average
Nom Outside Dia, in.(cm)	1.5 (3.81)	1.5 (3.81)	1.5 (3.81)	1.5 (3.81)
Nom Wall Thickness, mil (mm)	24 (0.61)	24 (0.61)	24 (0.61)	24 (0.61)
Meas Length, in. (cm)	21.52(54.66)	21.44(54.46)	21.53(54.69)	21.50(54.61)
Meas Outside Dia, in.(cm)	1.51(3.84)	1.52(3.86)	1.52(3.86)	1.517(3.85)
Meas Wall Thickness, mil (mm)	31 (0.79)	30 (0.76)	18.5 (0.47)* 26.5 (0.67)	30.5(0.775)
Total Strut Weight, lbm(kg)	0.948(0.430)	0.933(0.423)	0.926(0.420)	0.935(0.424)
Composite Weight, percent	30.0	29.6	31.6	30.4
Composite Density, $lbm/in.^3$ (gm/cm^3)	0.0712(1.97)	0.0683(1.89)	-	0.0697(1.93)
Resin Weight Fraction, percent	19.9	19.2	-	19.55
Resin Vol Fraction,percent	32.4	29.8	-	31.1
Longo Fiber Vol Fraction, percent	26.4	26.9	-	26.65
Circ Fiber Vol Fraction, percent	36.8	34.2	-	35.5
Total Fiber Vol Fraction, percent	63.2	61.1	-	62.15
Void Vol Fraction, percent	4.4	9.1	-	6.75

* Wall thickness with inner circ partially unraveled

Table 7-2

RESULTS OF LABORATORY ANALYSIS FOR CONFIGURATION II-2 TEST SPECIMENS

Specimen No.	X-14-16-A1	X-14-16-A2	X-14-16-A3	Average
Nom Outside Dia, in. (cm)	1.5 (3.81)	1.5 (3.81)	1.5 (3.81)	1.5 (3.81)
Nom Wall Thickness, mil (mm)	30 (0.76)	30 (0.76)	30 (0.76)	30 (0.76)
Meas Length, in. (cm)	15.80(40.13)	15.75(40.01)	15.74(39.98)	15.76(40.03)
Meas Outside Dia, in.(cm)	1.51(3.84)	1.50(3.81)	1.50(3.81)	1.503(3.818)
Meas Wall Thickness, mil (mm)	32 (0.81)	33 (0.84)	34 (0.86)	33.0(0.840)
Total Strut Weight, lbm(kg)	0.871(0.395)	0.860(0.390)	0.860(0.390)	0.864(0.392)
Composite Weight, percent	27.0	25.8	26.2	26.33
Composite Density, $lbm/in.^3$ (kg/cm^3)	0.0705(1.95)	0.0697(1.93)	0.0715(1.98)	0.0706(1.953)
Resin Weight Fraction, percent	24.2	24.4	23.8	24.13
Resin Vol Fraction, percent	39.1	38.8	39.2	39.03
Longo Fiber Vol Fraction, percent	40.4	39.6	36.4	38.8
Circ Fiber Vol Fraction, percent	19.1	18.7	23.9	20.57
Total Fiber Vol Fraction, percent	59.5	58.3	60.3	59.37
Void Vol Fraction, percent	1.4	2.9	0.5	1.6

Table 7-3

RESULTS OF LABORATORY ANALYSIS FOR CONFIGURATION II-3 TEST SPECIMENS

Specimen No.	X-14-20-B4	X-14-20-B5	X-17-24-1	Average
Nom Outside Dia, in.(cm)	1.488(3.78)	1.488(3.78)	1.488(3.78)	1.488(3.78)
Nom Wall Thickness, mil (mm)	24 (0.61)	24 (0.61)	24 (0.61)	24 (0.61)
Meas Length, in. (cm)	15.80(40.13)	15.80(40.13)	15.80(40.13)	15.80(40.13)
Meas Outside Dia, in.(cm)	1.50(3.81)	1.50(3.81)	1.50(3.81)	1.500(3.810)
Meas Wall Thickness, mil (mm)	24 (0.61)	22 (0.56)	28 (0.71)	24.7(0.627)
Total Strut Weight, lbm(kg)	0.864(0.392)	0.860(0.390)	0.860(0.390)	0.862(0.391)
Composite Weight, percent	26.7	26.7	26.7	26.7
Composite Density, $lbm/in.^3$ (gm/cm^3)	0.0719(1.99)	0.0730(2.02)	0.0723(2.00)	0.0724(2.003)
Resin Weight Fraction, percent	19.8	22.6	22.6	21.67
Resin Vol Fraction, percent	30.6	35.9	36.4	34.3
Longo Fiber Vol Fraction, percent	43.7	40.3	32.2	38.73
Circ Fiber Vol Fraction, percent	20.2	18.5	26.1	21.6
Total Fiber Vol Fraction, percent	63.9	58.8	58.3	60.33
Void Vol Fraction, percent	5.5	5.3	5.3	5.37

Table 7-4

RESULTS OF LABORATORY ANALYSIS FOR CONFIGURATION II-4 TEST SPECIMENS

Specimen No.	X-17-22-1	X-17-22-2	X-17-22-3	Average
Nom Midspan Dia, in.(cm)	2.5 (6.35)	2.5 (6.35)	2.5 (6.35)	2.5 (6.35)
Nom Wall Thickness, mil (mm)	36 (0.91)	36 (0.91)	36 (0.91)	36 (0.91)
Meas Length, in. (cm)	31.68(80.47)	31.70(80.52)	31.69(80.49)	31.69(80.49)
Meas Midspan Dia, in. (cm)	2.51(6.38)	2.51(6.38)	2.50(6.35)	2.507(6.368)
Meas Wall Thickness, mil (mm)	43 (1.09)	43 (1.09)	42 (1.07)	42.7(1.08)
Total Strut Weight, lbm(kg)	2.383(1.081)	2.348(1.065)	2.372(1.076)	2.368(1.074)
Composite Weight, percent	31.5	30.6	29.5	30.53
Composite Density, $lbm/in.^3$ (gm/cm^3)	0.0744(2.06)	0.0744(2.06)	0.0726(2.01)	0.0738(2.043)
Resin Weight Fraction, percent	18.7	17.7	19.7	18.7
Resin Vol Fraction, percent	31.8	30.2	32.8	31.6
Longo Fiber Vol Fraction, percent	38.7	39.3	37.5	38.5
Circ Fiber Vol Fraction, percent	28.3	28.8	27.4	28.17
Total Fiber Vol Fraction, percent	67.0	68.1	64.9	66.67
Void Vol Fraction, percent	1.2	1.7	2.3	1.73

Table 7-5

SUMMARY OF COMPRESSIVE STRESS, ELASTIC MODULUS, AND CRIPPLING COEFFICIENT VALUES FROM TASK 2 SHORT-COLUMN TESTS

Configuration and Specimen Numbers	Failure Load, P_F lbf (N)	Failure Stress, f_c ksi ($N/m^2 \times 10^{-8}$)	Elastic Modulus, E_{cm} psi$\times 10^{-6}$ ($N/m^2 \times 10^{-10}$)	Isotropic Crippling Coefficient, K_e
Config II-1:				
X-17-23-1	6630(29,490)	64.5 (4.45)	6.63 (4.57)	0.299
X-17-23-2	3420(15,210)	33.3 (2.29)	6.32 (4.36)	0.162
X-17-23-3	2270(10,100)	28.6 (1.97)	-	-
Average	6630(1) (29,490)	64.5(1) (4.45)	6.47 (4.46)	0.299(1)
Config II-2:				
X-14-16-A1	8630(38,390)	67.2 (4.63)	6.69 (4.61)	0.246
X-14-16-A2	8550(38,030)	66.5 (4.59)	7.01 (4.83)	0.233
X-14-16-A3	8670(38,560)	67.5 (4.65)	6.69 (4.61)	0.247
Average		67.1 (4.62)	6.80 (4.69)	0.242
Config II-3:				
X-14-20-B4	9650(42,920)	67.6 (4.66)	7.05 (4.86)	0.295
X-14-20-B5	6100(27,130)	42.7 (2.95)	6.31 (4.35)	0.208
X-17-24-1	7270(32,340)	50.9 (3.51)	6.26 (4.32)	0.250
Average		53.7 (3.70)	6.54 (4.51)	0.251
Config II-4:				
X-17-22-1	16,100(71,610)	60.9 (4.20)	7.64 (5.27)	0.273
X-17-22-2	16,300(72,500)	61.7 (4.25)	7.64 (5.27)	0.276
X-17-22-3	16,450(73,170)	62.3 (4.29)	7.64 (5.27)	0.279
Average		61.6 (4.25)	7.64 (5.27)	0.276

(1) Based on results for specimen no. X-17-23-1 only

stiffened specimens of configuration II-3, ranging from 42.7 ksi (2.95 x 10^8 N/m^2) to 67.6 ksi (4.66 x 10^8 N/m^2). Average elastic modulus values exhibited by the Task 2 specimens varied from 6.47 x 10^6 psi (4.46 x 10^{10}N/m^2) for an A_{lg}/A_{cg} ratio of 1.0 to 7.64 x 10^6 psi (5.27 x 10^{10} N/m^2) for an A_{lg}/A_{cg} ratio of 2.0. Finally, the average isotropic crippling coefficient values determined for the Task 2 specimens ranged from 0.242 for configuration II-2 specimens to 0.299 for specimens of the II-1 configuration.

7.1.2 Task 4 Test Specimens

The full-scale strut specimens fabricated in Task 3 and tested in Task 4 were also analyzed under Task 5 to evaluate weight, volume, and dimensional data. Measurements of total weight and dimensions for each specimen were obtained prior to the Task 4 tests, while the remaining measurements were determined from the post-test laboratory analysis. The methods used to obtain these data for all manufacturing parameters were similar to those described in Section 7.1.1 for the analysis of Task 2 specimens.

Results of the laboratory analysis for the Task 4 strut specimens are presented in Tables 7-6 through 7-8. Inspection of these data shows that manufacturing reproducibility was generally the same for the Task 4 specimens as had been observed earlier for the specimens of Task 2. For these full-scale specimens, measurements of strut length were not obtained since it was obvious from the results of the analysis conducted for the Task 2 specimens that the small variations encountered could easily be eliminated by adjustment of the rod-end fittings. Values of outside diameter were measured and were found to fall consistently below the nominal design values within the range of -0.1 to -1.6 percent. Wall thickness values for all Task 4 specimens also were found to be lower than the nominal design values, ranging from -20 to -5 percent less than the nominals. The scatter observed for particular values of total strut weight, composite weight, and composite density, compared to average values of these parameters for all eight specimens of a given design, was generally within ±3 percent, although the composite density for three of the

Table 7-6

RESULTS OF LABORATORY ANALYSIS FOR CONFIGURATION III-1 TEST SPECIMENS

Specimen No.	III-1A	III-1B	III-1C	III-1D	III-1E	III-1F	III-1G	III-1H	Average
Nom Outside Dia, in. (cm)	1.5 (3.81)	1.5 (3.81)	1.5 (3.81)	1.5 (3.81)	1.5 (3.81)	1.5 (3.81)	1.5 (3.81)	1.5 (3.81)	1.5 (3.81)
Nom Length, in. (cm)	24.0 (61.0)	24.0 (61.0)	24.0 (61.0)	24.0 (61.0)	24.0 (61.0)	24.0 (61.0)	24.0 (61.0)	24.0 (61.0)	24.0 (61.0)
No. of Longo Rovings	146	146	146	146	146	146	146	146	146
Nom Wall Thickness, mil (mm)	20 (0.51)	20 (0.51)	20 (0.51)	20 (0.51)	20 (0.51)	20 (0.51)	20 (0.51)	20 (0.51)	20 (0.51)
Nom Longo Thickness, mil (mm)	8 (0.20)	8 (0.20)	8 (0.20)	8 (0.20)	8 (0.20)	8 (0.20)	8 (0.20)	8 (0.20)	8 (0.20)
Nom Circ Thickness (Ea Wrap), mil (mm)	6 (0.15)	6 (0.15)	6 (0.15)	6 (0.15)	6 (0.15)	6 (0.15)	6 (0.15)	6 (0.15)	6 (0.15)
Meas Outside Dia, in. (cm) (1)	1.488 (3.780)	1.488 (3.780)	1.488 (3.780)	1.484 (3.769)	1.484 (3.769)	1.482 (3.764)	1.488 (3.780)	1.488 (3.780)	1.486 (3.774)
Meas Wall Thickness, mil (mm) (2)	19 (0.48)	18 (0.46)	17 (0.43)	17 (0.43)	16 (0.41)	17 (0.43)	16 (0.41)	16 (0.41)	17.0 (0.432)
Total Strut Weight, lbm (kg) (3)	0.886 (0.402)	0.886 (0.402)	0.886 (0.402)	0.884 (0.401)	0.877 (0.398)	0.886 (0.402)	0.884 (0.401)	0.873 (0.396)	0.883 (0.401)
Composite Weight, percent (4)	27.2	27.1	26.9	27.0	26.4	27.0	26.7	26.1	26.8
Composite Density, lbm/in.^{3} (gm/cm^3)	0.0733 (2.03)	0.0723 (2.00)	0.0723 (2.00)	0.0733 (2.03)	0.0665 (1.84)	0.0748 (2.07)	0.0737 (2.04)	0.0658 (1.82)	0.0715 (1.98)
Resin Weight Fraction, percent (5)	19.5	19.4	18.4	18.8	17.5	18.5	17.6	18.0	18.5
Resin Volume Fraction, percent (5)	33.4	33.4	29.0	31.0	25.8	32.1	28.6	27.3	30.1
Longo Fiber Vol Fraction, percent (6)	27.3	25.6	24.8	27.6	26.5	28.3	29.0	26.1	26.9
Circ Fiber Vol Fraction, percent (6)	39.3	37.7	39.7	37.9	34.8	39.6	38.9	34.5	37.8
Total Fiber Vol Fraction, percent (6)	66.6	63.3	64.5	65.5	61.3	67.9	67.9	60.6	64.7
Void Vol Fraction, percent (7)	Negl	3.3	6.5	3.5	12.9	Negl	3.5	12.1	5.2

Notes:
(1) Av of 4 measurements at 45° intervals
(2) Av of 8 measurements at 45° intervals
(3) Includes encapsulated fittings, compression caps, lock nuts, and washers (excludes rod-end hardware)
(4) Excludes all metal parts
(5) Values calculated from ignition loss determination
(6) Values calculated from weights of longo and circ glass after ignition loss evaluation
(7) Values calculated as 100 percent less the sum of the resin and total fiber volume fractions

Table 7-7

RESULTS OF LABORATORY ANALYSIS FOR CONFIGURATION III-2 TEST SPECIMENS

Specimen No.	III-2A	III-2B	III-2C	III-2D	III-2E	III-2F	III-2G	III-2H	Average
Nom Outside Dia, in. (cm)	1.5 (3.81)	1.5 (3.81)	1.5 (3.81)	1.5 (3.81)	1.5 (3.81)	1.5 (3.81)	1.5 (3.81)	1.5 (3.81)	1.5 (3.81)
Nom Length, in. (cm)	19.0 (48.3)	19.0 (48.3)	19.0 (48.3)	19.0 (48.3)	19.0 (48.3)	19.0 (48.3)	19.0 (48.3)	19.0 (48.3)	19.0 (48.3)
No. of Longo Rovings	274	274	274	274	274	274	274	274	274
Nom Wall Thickness, mil (mm)	27 (0.69)	27 (0.69)	27 (0.69)	27 (0.69)	27 (0.69)	27 (0.69)	27 (0.69)	27 (0.69)	27 (0.69)
Nom Longo Thickness, mil (mm)	15 (0.38)	15 (0.38)	15 (0.38)	15 (0.38)	15 (0.38)	15 (0.38)	15 (0.38)	15 (0.38)	15 (0.38)
Nom Circ Thickness (Ea Wrap) mil (mm)	6 (0.15)	6 (0.15)	6 (0.15)	6 (0.15)	6 (0.15)	6 (0.15)	6 (0.15)	6 (0.15)	6 (0.15)
Meas Outside Dia, in. (cm) (1)	1.490 (3.785)	1.493 (3.792)	1.493 (3.792)	1.492 (3.790)	1.494 (3.795)	1.498 (3.805)	1.490 (3.785)	1.494 (3.795)	1.493 (3.792)
Meas Wall Thickness, mil (mm) (2)	22 (0.56)	22 (0.56)	23 (0.58)	23 (0.58)	24 (0.61)	25 (0.64)	25 (0.64)	23 (0.58)	23.4 (0.594)
Total Strut Weight, lbm (kg) (3)	0.990 (0.449)	0.990 (0.449)	0.988 (0.448)	0.988 (0.448)	0.992 (0.450)	0.996 (0.452)	0.992 (0.450)	0.996 (0.452)	0.992 (0.450)
Composite Weight, percent (4)	22.2	22.0	21.8	21.9	22.2	22.3	22.5	22.6	22.2
Composite Density lbm/in.^{3} (gm/cm^3)	0.0723 (2.00)	0.0733 (2.03)	0.0733 (2.03)	0.0723 (2.00)	0.0744 (2.06)	0.0730 (2.02)	0.0708 (1.96)	0.0715 (1.98)	0.0726 (2.01)
Resin Weight Fraction, percent (5)	17.3	18.0	16.2	18.2	18.7	19.2	18.7	17.9	18.0
Resin Volume Fraction, percent (5)	27.8	30.0	27.5	29.6	30.3	31.3	31.3	28.6	29.6
Longo Fiber Vol Fraction, percent (6)	37.5	37.0	36.7	36.3	37.7	35.7	35.7	35.2	36.5
Circ Fiber Vol Fraction, percent (6)	28.3	30.5	30.8	30.4	30.7	29.4	29.3	29.1	29.8
Total Fiber Vol Fraction, percent (6)	65.8	67.5	67.5	66.7	68.4	65.1	65.0	64.3	66.3
Void Vol Fraction, percent (7)	6.4	2.5	5.0	3.7	1.3	3.6	3.7	7.1	4.1

Notes:
(1) Av of 4 measurements at 45° intervals
(2) Av of 8 measurements at 45° intervals
(3) Includes encapsulated fittings, compression caps, lock nuts, and washers (excludes rod-end hardware)
(4) Excludes all metal parts
(5) Values calculated from ignition loss determination
(6) Values calculated from weights of longo and circ glass after ignition loss evaluation
(7) Values calculated as 100 percent less the sum of the resin and total fiber volume fractions

Table 7-8

RESULTS OF LABORATORY ANALYSIS FOR CONFIGURATION III-3 TEST SPECIMENS

Specimen No.	III-3A	III-3B	III-3C	III-3D	III-3E	III-3F	III-3G	III-3H	Average
Nom Outside Dia, in. (cm)	2.5 (6.35)	2.5 (6.35)	2.5 (6.35)	2.5 (6.35)	2.5 (6.35)	2.5 (6.35)	2.5 (6.35)	2.5 (6.35)	2.5 (6.35)
Nom Length, in. (cm)	36.0 (91.4)	36.0 (91.4)	36.0 (91.4)	36.0 (91.4)	36.0 (91.4)	36.0 (91.4)	36.0 (91.4)	36.0 (91.4)	36.0 (91.4)
No. of Longo Rovings	306	306	306	306	306	306	306	306	306
Nom Wall Thickness, mil (mm)	22 (0.56)	22 (0.56)	22 (0.56)	22 (0.56)	22 (0.56)	22 (0.56)	22 (0.56)	22 (0.56)	22 (0.56)
Nom Longo Thickness, mil (mm)	10 (0.25)	10 (0.25)	10 (0.25)	10 (0.25)	10 (0.25)	10 (0.25)	10 (0.25)	10 (0.25)	10 (0.25)
Nom Circ Thickness (Ea Wrap) mil (mm)	6 (0.15)	6 (0.15)	6 (0.15)	6 (0.15)	6 (0.15)	6 (0.15)	6 (0.15)	6 (0.15)	6 (0.15)
Meas Outside Dia, in. (cm) (1)	2.466 (6.264)	2.465 (6.261)	2.466 (6.264)	2.466 (6.264)	2.469 (6.271)	2.474 (6.284)	2.467 (6.266)	2.461 (6.251)	2.467 (6.266)
Meas Wall Thickness, mil (mm) (2)	20 (0.51)	19 (0.48)	20 (0.51)	19 (0.48)	18 (0.46)	19 (0.48)	19 (0.48)	Not Tested	19.1 (0.485)
Total Strut Weight, lbm (kg) (3)	2.114 (0.959)	2.114 (0.959)	2.116 (0.960)	2.099 (0.952)	2.105 (0.955)	2.090 (0.948)	2.103 (0.954)		2.105 (0.955)
Composite Weight, percent (4)	23.1	22.9	23.2	22.5	22.5	22.2	22.5		22.7
Composite Density, $lbm/in.^3$ (gm/cm^3)	0.0730 (2.02)	0.0748 (2.07)	0.0715 (1.98)	0.0737 (2.04)	0.0730 (2.02)	0.0733 (2.03)	0.0712 (1.97)		0.0730 (2.02)
Resin Weight Fraction, percent (5)	17.9	17.2	18.0	17.9	18.4	20.0	18.6		18.3
Resin Volume Fraction, percent (5)	30.0	30.6	29.3	30.8	30.4	32.2	29.3		30.4
Longo Fiber Vol Fraction, percent (6)	27.4	28.9	26.5	27.4	29.1	27.6	26.2		27.6
Circ Fiber Vol Fraction, percent (6)	39.3	39.6	38.5	39.3	37.0	38.5	37.6		38.5
Total Fiber Vol Fraction, percent (6)	66.7	68.5	65.0	66.7	66.1	66.1	63.8		66.1
Void Vol Fraction, percent (7)	3.7	0.9	5.7	2.5	3.5	1.7	6.9		3.5

Notes:
(1) Av of 4 measurements at 45° intervals
(2) Av of 8 measurements at 45° intervals
(3) Includes encapsulated fittings, compression caps, lock nuts, and washers (excludes rod-end hardware)
(4) Excludes all metal parts
(5) Values calculated from ignition loss determination
(6) Values calculated from weights of longo and circ glass after ignition loss evaluation
(7) Values calculated as 100 percent less the sum of the resin and total fiber volume fractions

III-1 configurations varied from -8 to +4.6 percent compared to the average values. Resin weight fractions and volume fractions of resin, longo fibers, and circ fibers were assessed and again were found to be within ±9 percent of the nominal design targets. Finally, the void volume fractions determined from the analysis ranged from 0 to 7.1 percent, except that excessive values of 12.1 and 12.9 were determined for two of the configuration III-1 specimens where it was subsequently found that the prepreg material used to wind the struts had been stored for more than the specified maximum shelf life.

During the post-test analysis of the failed Task 4 strut specimens, photomicrographs were obtained of the material immediately adjacent to the failure areas. Typical cross-sectional views of one of the configuration III-1 specimens are presented in Fig. 7-1. It can be seen from these enlarged views that excellent fiber distribution within the resin matrix was achieved with minimum void volume.

Near the conclusion of the Task 5 post-test analysis, results obtained from the cyclic load tests in Task 4 were analyzed and compared to similar results taken from the literature. Fig. 7-2 shows typical fatigue data obtained from this analysis. In this figure, the number of cycles accumulated prior to failure are plotted as a function of the tension stress ratio imposed, F_t/F_{t_U}, and the ratio of minimum-to-maximum load peaks applied, R. Negative values of R indicate that the minimum-load peaks applied were in compression. The curves shown for 181/S-901 cloth and S-994 roving were obtained from the literature, whereas the data points shown were derived from the results of the full-scale Task 4 tests. Test specimen numbers are indicated for each data point. Based on the limited number of tests conducted, these strut designs exhibited excellent fatigue-life capabilities. However, additional cyclic load testing is needed to completely investigate the fatigue-life characteristics of these structures over a wide range of design stress ratios.

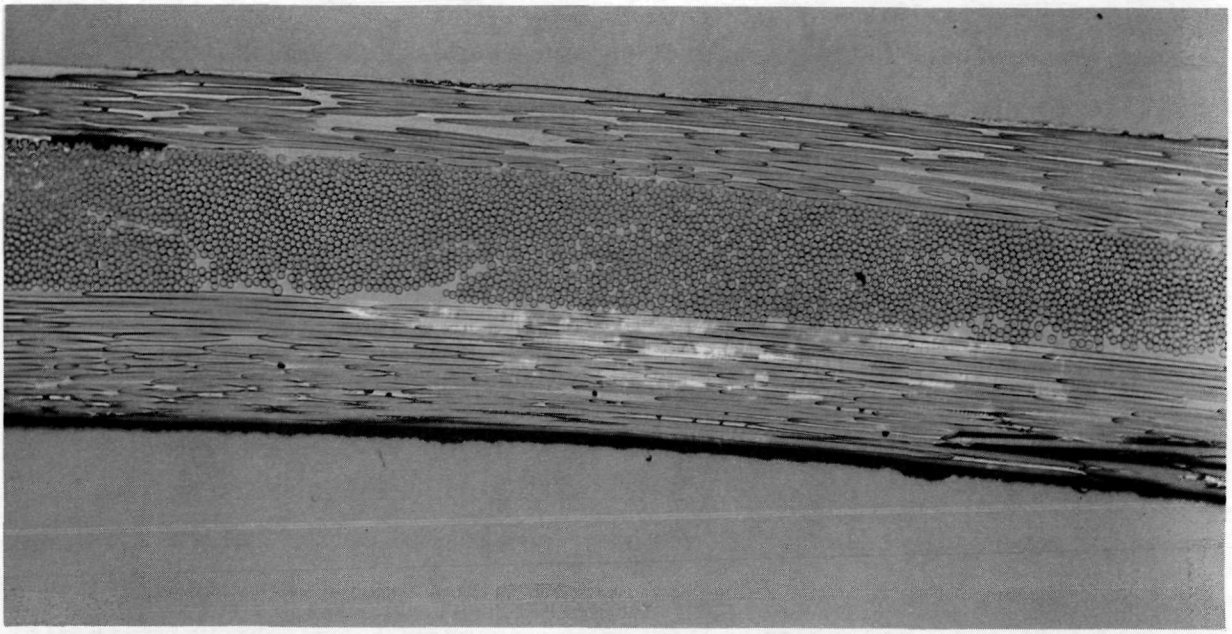

(a) Cross-Section (Enlarged 100 times)

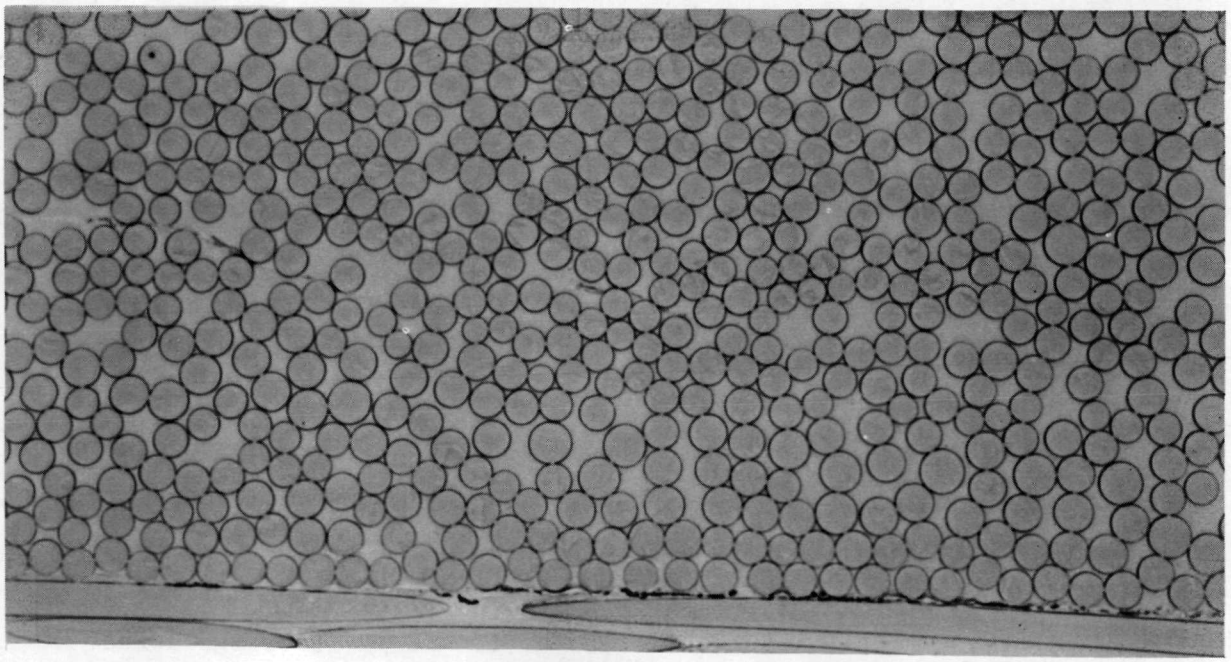

(b) Longo Wraps (Enlarged 500 times)

Fig. 7-1 Photomicrograph of a Typical Specimen

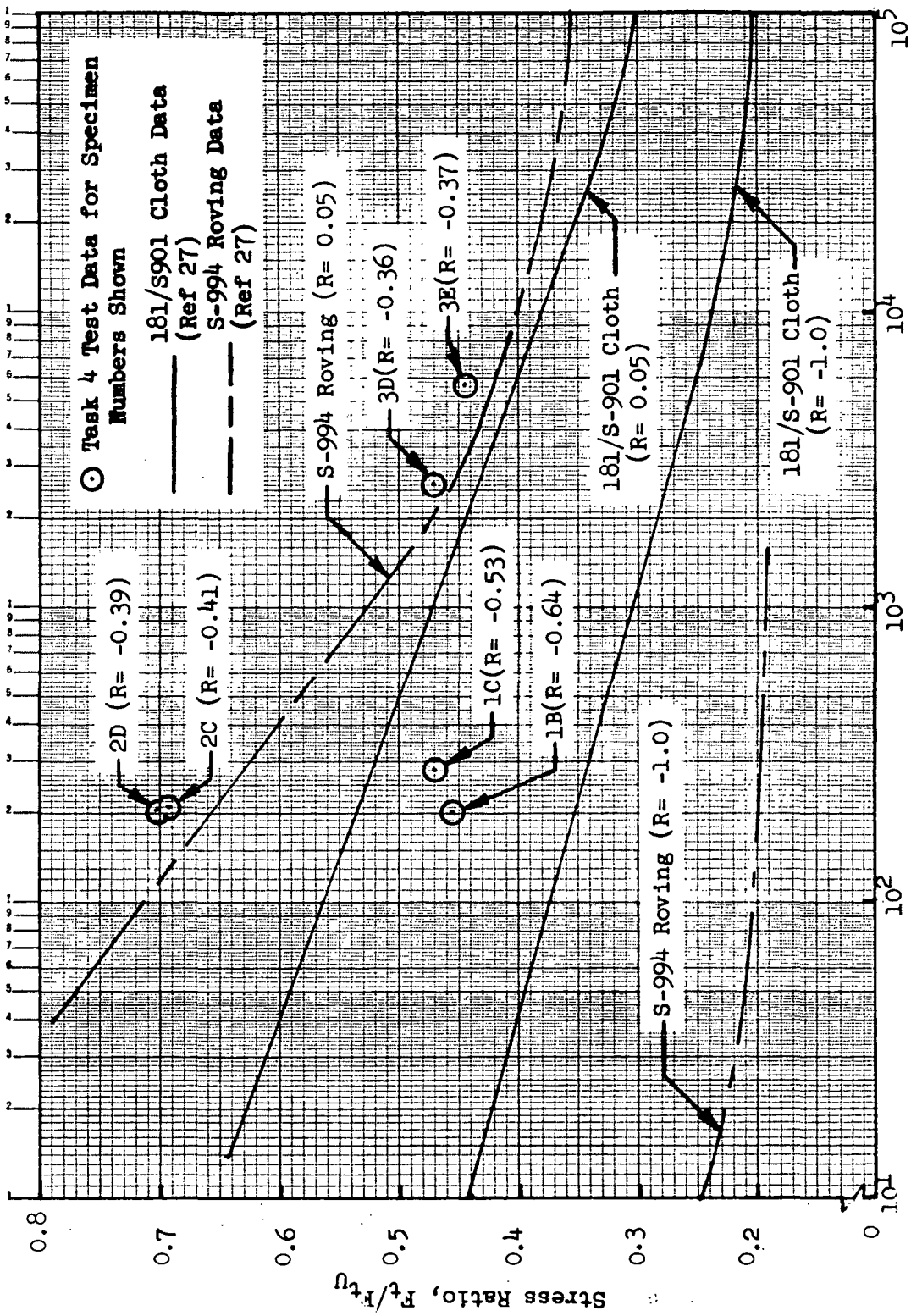

Fig. 7-2 Typical S-N Fatigue Data for Composite Fiberglass Materials

7.2 REVIEW OF FIBERGLASS STRUT TECHNOLOGY

7.2.1 Thermal and Mechanical Properties

Based on a review of the results obtained during this program and of those published in the literature, thermal and mechanical property data were compiled for use in the design and analysis of tubular fiberglass support structures. A summary of these data, indicating the source of each property, is presented in Table 7-9.

As shown in the table, values of thermal conductivity vary with the $A_{\ell g}/A_{cg}$ ratio and should be computed for any particular design using Equation (3-8). The thermal expansion coefficient given represents the integrated average value for a change in temperature from 535°R (297°K) to 37°R (20°K). Values for other temperature ranges can be obtained from Ref. 5 as noted. Density values shown agree well with those from the literature. The variation of density with temperature is not shown since only room temperature data were obtained. The average allowable tensile stress value given in the table can be multiplied directly by the longo composite cross-sectional area in order to obtain the total ultimate tension load capability. Similarly, ultimate compressive crushing load capability can be determined as the product of the allowable crushing stress shown and the longo composite area. Values of crippling or column buckling capability, on the other hand, depend on total cross-section geometry and elastic properties and must be computed for each particular design using the equations noted in the table. The compressive modulus of elasticity value used in these computations should be selected for the proper $A_{\ell g}/A_{cg}$ ratio as shown.

7.2.2 Recommended Design Approach

For the range of loads and lengths investigated during this program, monocoque fiberglass strut designs are recommended. In general, monocoque cylinders will be optimum and are recommended for applications where relatively short,

Table 7-9

THERMAL AND MECHANICAL PROPERTIES OF TUBULAR FIBERGLASS SUPPORT STRUCTURES(1)

Property	Source and Range of Available Test Data	Recommended Design Data
Thermal Conductivity, Btu/hr ft°R at 278.5°R (W/cm°K at 154.7°K), for $A_{\ell g}/A_{cg}$ = 0	Interpolated from Lockheed, Goodyear, and GDC test data (Ref 2, Fig. 23; Ref 10, Table C 1 and Ref 11, Figs. 50 and 51): 0.124 to 0.156 (0.00215 to 0.00270)	Calculate from analytical model, Equation (3-8) (Ref Fig. 3-20): 0.175 (0.00303)
1.0	N/A	0.238 (0.00412)
2.67	0.206 to 0.257 (0.00357 to 0.00445)	0.268 (0.00464)
∞	0.100 to 0.118 (0.00173 to 0.00204)	0.302 (0.00523)
Thermal Expansion from 535°R(297°K)to 37°R(20°K), percent	N/A	Handbook value (Ref 5, Fig. 3-1): -0.138
Density at 535°R(297°K), lbm/in.^{3} (gm/cm^3)	Task 2 test data (Ref Tables 7-1 to 7-4): 0.0683 to 0.0744 (1.89 to 2.06)	Av value for 11 specimens (Ref Tables 7-1 to 7-4): 0.0718 (1.987)
Ult Tensile Strength Parallel to Longos(2), psi x 10^{-3} (N/m^{2}x10^{-8})	Task 4 test data for 2 spec ea of all config (Ref Table 6-2): 187 to 217 (12.9 to 15.0)	Av value for 6 specimens (Ref Table 6-2): 202 (13.9)
Ult Crushing Strength Parallel to Longos(2), psi x 10^{-3} (N/m^{2}x10^{-8})	Task 2 test data for 4 spec of config II-1 and II-2 (Ref Table 7-5): 104 to 119 (7.2 to 8.2)	Handbook value (Ref 26, Table 4.30): 100 (6.9)
Ult Crippling Strength Parallel to Longos(3)(4), psi x 10^{-3} (N/m^{2}x10^{-8})	Task 2 test data for 3 spec of config II-4 (Ref Table 7-5): 86.7 to 88.6 (6.0 to 6.1)	Calculate from classic crippling model:(6) Equation (3-2)(isotropic) Equation (3-3)(orthotropic)
Ult Column Buckling Strength(5), psi x 10^{-3} (N/m^{2}x 10^{-8}) for L'/ρc =	Task 4 test data for 2 or 3 spec ea of all config (Ref Table 6-2):	Calculate from classic Euler buckling model:
45.8 (Config III-1)	28.0 to 35.4 (1.9 to 2.4)	Equation (3-1)
36.4 (Config III-2)	47.6 to 53.9 (3.3 to 3.7)	
41.0 (Config III-3)	21.7 to 26.0 (1.5 to 1.8)	
Compressive Modulus of Elasticity, psi x 10^{-6} (N/m^{2}x10^{-10}) for $A_{\ell g}/A_{cg}$ = 1.0	Task 2 test data for 2 or 3 spec ea of configs II-1, II-2, and II-4 (Ref Table 7-5): 6.3 to 6.6 (4.4 to 4.6)	Av value for 2 or 3 spec of ea $A_{\ell g}/A_{cg}$ ratio (Ref Table 7-5 and Fig. 3-36): 6.47 (4.46)
1.5	6.7 to 7.0 (4.6 to 4.8)	6.80 (4.69)
2.0	7.64 (5.27)	7.64 (5.27)

NOTES:
(1) All data shown are for monocoque struts with a resin content of 20.8 percent by weight (35.0 percent by volume).
(2) Applied over longo composite cross-sectional area only.
(3) Applied over total composite cross-sectional area.
(4) Values vary with cross-section modulus, geometry, and crippling co-efficient (Ref Table 7-5 for typical values).
(5) Values vary with cross-section modulus, geometry, and column eccentricity (Ref Table 6-1 for typical values).
(6) Use isotropic analysis for preliminary design or for comparison of results with those from other studies. Use orthotropic analysis for final design studies. Orthotropic values computed for monocoque cylinders and ogives are given in Figs. 3-37 through 3-42.

lightly-loaded struts are required. For relatively long, heavily loaded struts, monocoque ogive designs are recommended. For intermediate load-length applications, both cylindrical and ogive designs should be investigated to determine which is optimum.

For any given application (i.e., either cylinder or ogive) for a particular load-length design point, the data presented in Figs. 3-37 through 3-42 should be cross-plotted as a function of nominal longo thickness to determine the optimum thickness value for compressive loading. Based on these data, a suitable design can be selected (Ref Figs. 3-42 through 3-45). The longo composite area should then be checked for the design tension load. Finally, winding requirements should be determined using the method presented in Appendix F.

Titanium end fittings and compression caps similar to those shown in Figs. 3-46 through 3-48 are recommended. Also, rod-end fittings of the 2BREF series are recommended and should be selected based on static and cyclic load requirements and the capabilities shown in Table 3-8. Other general design and manufacturing requirements should be specified in accordance with the design drawings (Ref Figs. 3-46 through 3-48) and the process specification (Ref Appendix E) which were developed during this program.

7.2.3 Evaluation of Other System Concepts

During Task 5, an analytical study was conducted to compare design details and system performance for fiberglass strut and fiberglass tension strap support systems where each was applied to a typical flight cryogen tank. The fiberglass tension strap concept was selected for this comparison since it theoretically offers the lowest weight and heat leak for any given application.

In this study, strut and tension strap systems were each designed to support a liquid helium cryostat within the spacecraft structure for an orbiting

cosmic ray spectrometer experiment. The cryostat was designed to provide a liquid helium temperature environment for a one-year operational life. Design gross weight at liftoff was approximately 2750 lbm (1250 kg), and the total system was to fit within a 78.0-in.- (198-cm-) diameter by 93.5-in.- (237-cm-) long cylindrical envelope. The integrated thermal protection system developed in the study consisted of approximately 3.0 in. (7.6 cm) of multilayer insulation installed within a vacuum-jacketed annulus, two vapor-cooled shields positioned within the multilayers, and either the fiberglass strut or the tension strap support system. Nominal design steady-state heat flux for the system in orbit was approximately 0.32 Btu/hr (0.095 W). Nominal design limit load factors of 7-g longitudinal acceleration and 3-g longitudinal rebound were combined independently with a maximum lateral limit load factor of 4.4 g to determine critical design loads for individual strut or tension strap members. In addition, the natural frequency of each support system was determined to ensure that application of critical flight dynamic loads would not cause resonance with subsequent load amplification beyond the nominal design values. It was found from this analysis that for the most critical case a support system natural frequency in the longitudinal direction in excess of 25 hz was required to preclude resonance of the system due to booster engine thrust perturbations in the 16 to 25 hz range during shutdown.

The fiberglass strut support system designed during the study consisted of six 2.25-in.- (5.72-cm-) diameter ogive struts, each 29.0 in. (72.7 cm) in length with a 30-mil (0.76-mm) nominal wall thickness at midspan. The critical ultimate design load was found to be 8570 lbf (38,120 N) in compression. Total inert weight for the system was approximately 10 lbm (4.5 kg). Each strut was thermally shorted to each vapor-cooled shield with a resultant total heat leak through the supports of approximately 0.055 Btu/hr (0.016 W). The natural frequency of the system in the longitudinal direction was found to be approximately 29 hz, well above the critical value range.

Similarly, the fiberglass tension strap system designed during the study was

composed of twelve 0.75-in. (1.91-cm) by 0.10-in. (0.25-cm) rectangular members. Each member was 23.5 in. (59.7 cm) in length, and was designed for an ultimate tension load of approximately 15,200 lbf (66,720 N). Total inert weight of the system was approximately 6 lbm (2.7 kg). Again, each strap was assumed to be thermally shorted to each of the vapor-cooled shields, with a net total system heat leak of approximately 0.031 Btu/hr (0.009 W). In this case, the dynamics analysis showed that longitudinal natural frequency of the system was approximately 16 hz. Since this is significantly below the desired frequency of 25 hz or more, a second calculation was made assuming that the cross-sectional area of each strap was doubled. This modification resulted in a natural frequency of approximately 23 hz, still well below the critical value, but also approximately doubled the system weight and heat leak values noted earlier. Based on this study, it becomes evident that the fiberglass strut system is, in fact, superior to the fiberglass tension strap system for applications where a severe dynamic load environment must be accommodated.

7.2.4 *Comparison of System Performance for Fiberglass and Metallic Strut Supports*

When selecting the support system for a specific application, the vehicle designer must consider the total weight penalty imposed by the system, as well as cost and reliability factors. This total weight is comprised of both inert weight and boiloff due to the heat leak contribution from the support system.

A comparative evaluation was made between fiberglass and titanium strut support systems, each composed of six identical struts, to provide some insight into the relative merits as related to vehicle size (characterized by loads) and the mission duration. Titanium (6AL-4V) was chosen for the comparison because of its high strength-to-weight ratio, and its relatively low thermal conductivity.

Figure 7-3 shows the inert weight comparison as a function of the compression

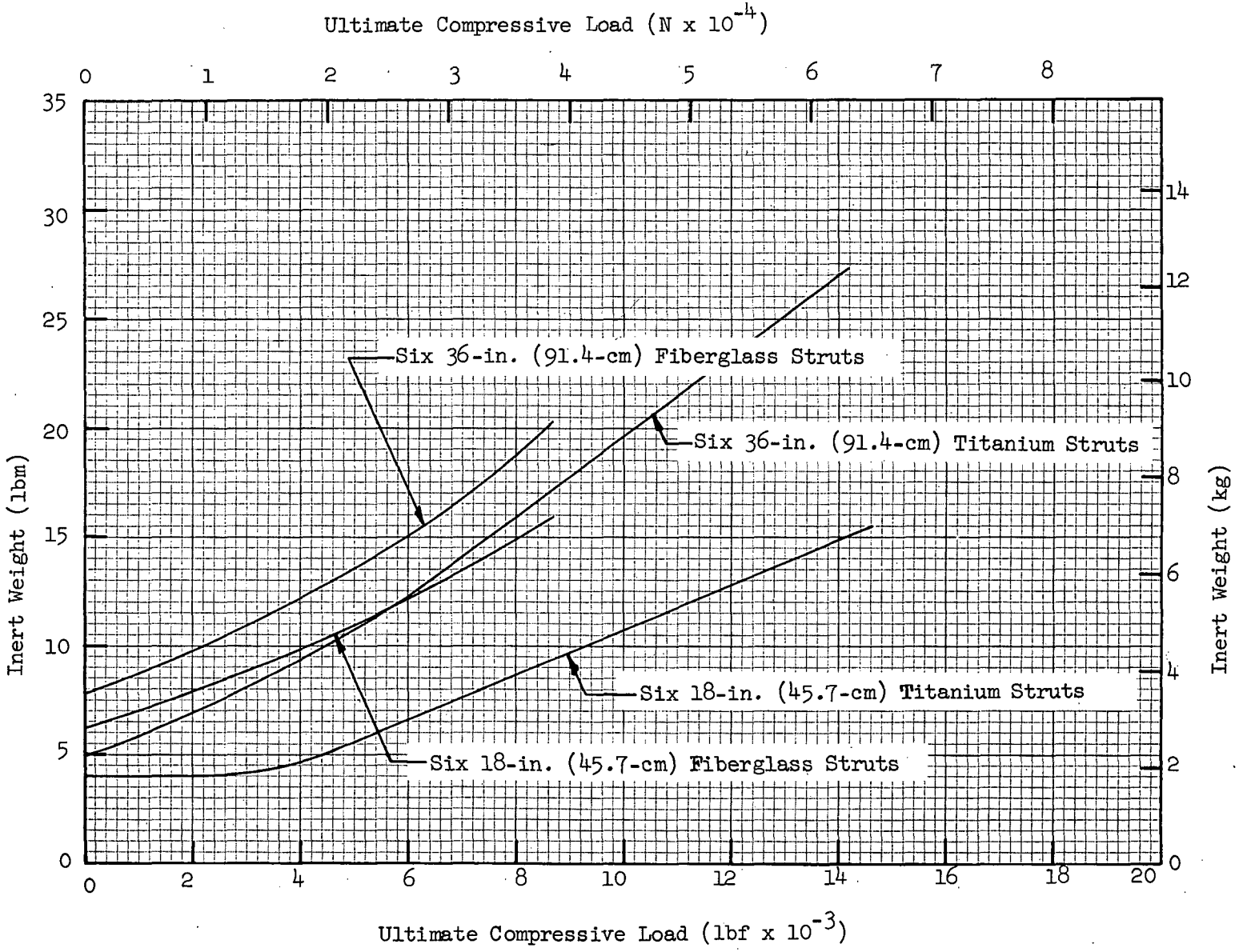

Fig. 7- 3 Comparison of Monocoque Fiberglass and Titanium Strut Inert Weights

load, for both 18-in. (45.7-cm) and 36-in. (101.6-cm) struts (pin-to-pin). These weights include the tube, internal end fittings, rod ends, and the core insulation (chopped Dexiglas). As one would expect, the metal struts are lightest because of higher mechanical properties for the tube wall. However, since the tube wall is the only contributing element for which the different properties apply (i.e., both designs use the same rod ends and end fitting material), the weight differential is minimized. This does illustrate, though, that for a mission duration of a few hours, one might prefer the metal struts. The tension load capability is approximately 2.5 times that for compressive loads for the locus of designs represented in the figure.

The relative thermal performance of the titanium and fiberglass struts is illustrated in Fig. 7-4. These are the basic conduction heat rates between 520°R (289°K) and liquid hydrogen temperature, assuming the external surfaces to be perfectly insulated. The much steeper slope shown for the metal struts is a consequence of the higher conductivity, although the heat rates for both designs increase with increasing load and cross-sectional area.

The heat rates from Fig. 7-4 were used to calculate the hydrogen boiloff weights for a system of six struts for a 220-day mission. These were then added to the inert weights from Fig. 7-3 to derive a system weight penalty. The results are shown in Table 7-10 for three different design loads. This table illustrates a marked advantage for fiberglass, particularly for high load conditions. The differences would be less for shorter mission durations. Also, only monocoque cylinder designs were compared in this task. In view of the fact that the ogive fiberglass strut is more optimum at high loads than the cylinder, any comparison between ogive and metal struts would merely add to the already obvious advantage of fiberglass.

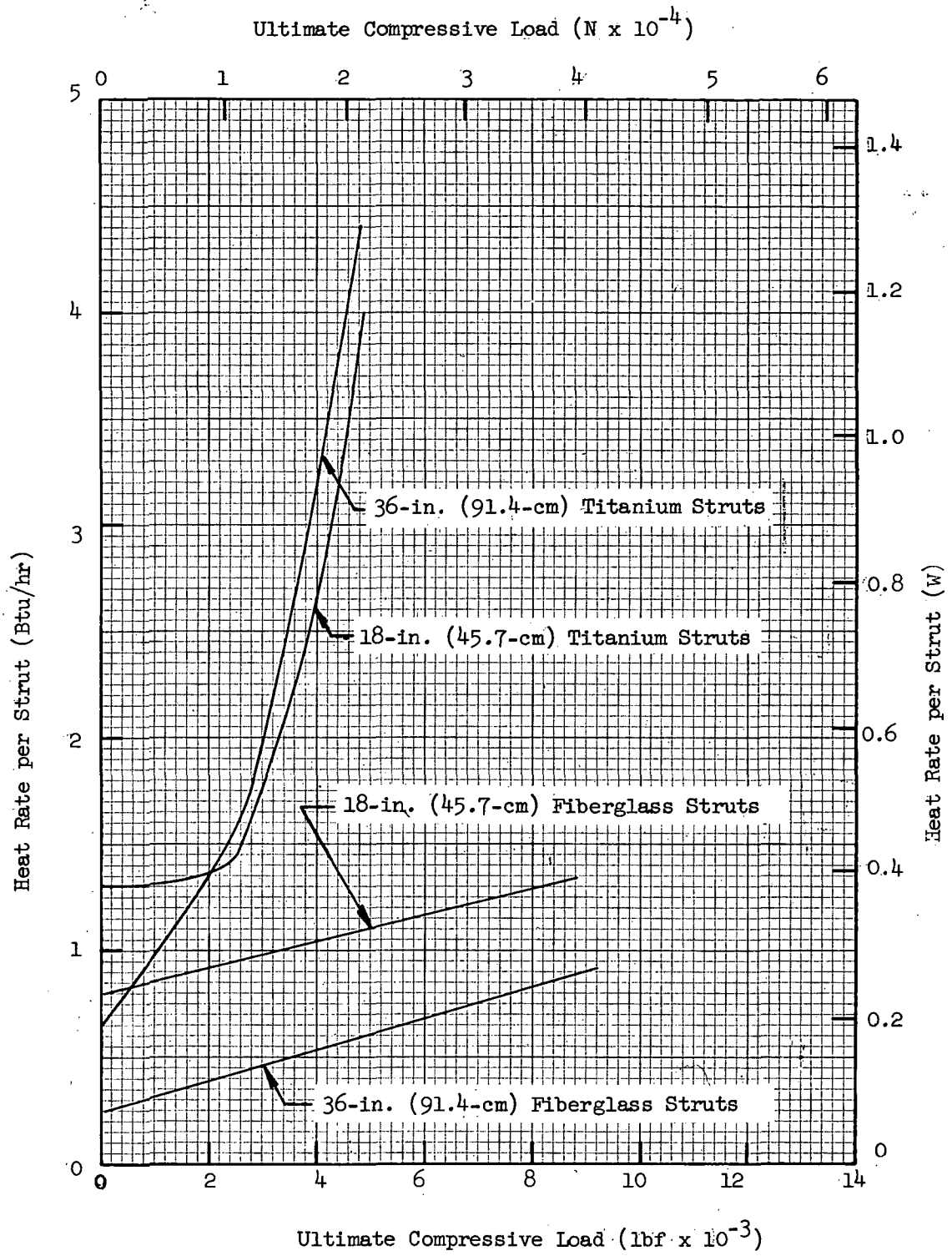

Fig. 7-4 Comparison of Heat Rates for Fiberglass and Titanium Strut Supports

Table 7-10

COMPARISON OF EFFECTIVE SYSTEM WEIGHTS FOR FIBERGLASS AND TITANIUM STRUT SUPPORTS

Material	L_s, in. (cm)	Ultimate Compressive Load, lbf (N)		
		980 (4360)	4690 (20,860)	8400 (37,360)
		Effective Weights*, lbm (kg)		
Titanium 6AL4V	18 (45.7)	26 (11.8)	76.6 (34.6)	123 (55.5)
	36 (91.4)	22.1 (10)	75.5 (34.2)	120 (54.2)
Fiberglass S-901/E-787	18 (45.7)	21.2 (9.6)	28.8 (12.8)	37.5 (17)
	36 (91.4)	14 (6.4)	23.2 (10.6)	33.9 (15.4)

* Based on mission duration of 220 days for a system composed of six identical struts

Section 8

DISCUSSION OF RESULTS

During this contract program, a low heat leak, filament-wound fiberglass strut was developed that has a strength-to-weight ratio in tension and compression exceeding that for any metallic strut of equal length and load capability. Thus the primary goal of the program was achieved in addition to many secondary goals.

The basic design concept of providing axial load transfer between the composite strut body and the metallic end fittings without relying on glass-to-metal bond strength or on mechanical fasteners was verified conclusively by test. With this concept, longo rovings are wound continuously over the internal end fittings, and compression caps are then installed over the resulting closed-end composite structure. Axial tension loads are reacted directly in bearing of the longo material on the internal fittings. Similarly, axial compression loads are reacted in bearing of this material on the compression caps which, in turn, are attached to the internal fittings.

In Task I, sixteen selected strut design configurations were analyzed to determine their relative merit for application to a wide range of design loads and lengths (Ref Tables 3-I and 3-2). Candidates with either cylindrical or ogive shells of revolution and with either monocoque or longeron-stiffened walls were included in the analysis. For monocoque shell designs, both polyurethane foam and non-structural core insulations were analyzed. For stiffened shell designs, both glass-fiber and boron-fiber longerons, as well as an additional boron-fiber longo layer, were investigated.

It was found from the parametric analysis conducted in Task I that the total inert weight does not vary significantly for short, lightly-loaded struts of the configurations studied. For example, the inert weight per strut varied less than 0.06 lbm (0.027 kg), or approximately 6 percent of the average total weight value of

1.13 lbm (0.51 kg), for four 18-in.-(45.7-cm-) long strut candidates designed for an ultimate compressive load of 980 lbf (4360 N) (Ref Section 3.1.8, Figs. 3-25 and 3-26). However, for seven candidate strut configurations, 40 in. (101.6 cm) in length and designed for an ultimate compressive load of 8400 lbf (37,360 N), a somewhat greater difference in inert weight was observed of 0.34 lbm (0.15 kg) per strut, or approximately 10 percent of the average total weight value of 3.36 lbm (1.52 kg) (Ref Figs. 3-29 and 3-30).

Where propellant boiloff weight, resulting from the longitudinal heat leak, was added to the strut inert weight to obtain total system weight, a more significant variation was found for selected candidate designs. The greatest variation was observed for fluorine tank supports with boundary temperatures of 400°R (222°K) and 140°R (78°K), compared to that for hydrogen tank supports with boundary temperatures of 520°R (289°K) and 37°R (20°K). Also, a much greater variation in total system weight was found for short, lightly-loaded struts where the cross-sectional area for some of the candidates was dependent on minimum diameter and minimum wall thickness (fabrication) constraints rather than on load capability. For example, the total system weight for four selected fluorine tank support configurations, each 18 in. (45.7 cm) long and designed for an ultimate compressive load of 980 lbf (4360 N), ranged from 4.38 lbm (1.99 kg) to 8.00 lbm (3.63 kg) per strut based on a mission duration (storage time) of 200 days (Ref Fig. 3-26). This is a maximum variation of 3.62 lbm (1.64 kg), or approximately 60 percent of the average total system weight of 6.07 lbm (2.75 kg). For seven candidate fluorine tank strut configurations, each 40 in. (101.6 cm) long and designed for an ultimate compressive load of 8400 lbf (37,360 N), the difference in total system weight was 0.66 lbm (0.30 kg) per strut, or approximately 10 percent of the average total weight value of 6.75 lbm (3.06 kg) (Ref Fig. 3-30).

Based on the parametric structural and thermal analyses described above, monocoque cylinders of configuration 1 (Ref Table 3-2) were found to provide the lightest total system weight for short, lightly-loaded struts (Ref Figs. 3-25 and 3-26). For struts of medium length and load capability, stiffened cylinders of configurations 8 and 13 were found to be the lightest (Ref Table 3-2 and Figs. 3-27 and 3-28). Finally, for long, heavily-loaded struts, stiffened cylinders of configuration 10

and monocoque ogives of configuration 6 offered the lightest total system weight (Ref Table 3-2 and Figs. 3-29 and 3-30). These results also show, however, that the system weight penalties incurred are insignificant where monocoque cylinder or ogive designs are used in lieu of the optimum stiffened cylinder designs for struts of medium length and load capability or for long, highly-loaded struts. For example, total system weights of 5.66 lbm (2.57 kg) and 5.58 lbm (2.53 kg) per strut were computed for a configuration 6 monocoque ogive and a configuration 10 stiffened cylinder, respectively. In this example, each candidate was designed as a hydrogen tank support 40 in. (101.6 cm) long with an ultimate compressive load capability of 8400 lbf (37,360 N) for a mission duration of 200 days (Ref Fig. 3-29). If the monocoque ogive design is selected rather than the stiffened cylinder, it can be seen that the resulting weight penalty is only 0.08 lbm (0.04 kg), or approximately 1.4 percent of the optimum system weight.

In the detailed design and analysis of selected strut candidates, it was found that titanium is the most suitable metallic material from which to fabricate the internal end fittings and compression caps. The selection was based on a comparison of thermal coefficient of expansion, density, and thermal conductivity of aluminum, stainless steel, and titanium with those same properties for fiberglass (Ref Section 3.2.1, Table 3-5). Titanium was selected primarily because its thermal coefficient of expansion most nearly approaches that for the fiberglass. The analysis showed that titanium shrinks approximately 20 percent more than the fiberglass in chilling from room temperature to liquid hydrogen temperature, whereas stainless steel and aluminum shrink 100 percent more and 200 percent more, respectively. In addition, titanium offers the lowest thermal conductivity of the three metallic candidates, and is approximately 56 percent less dense than stainless steel (although approximately 58 percent more dense than aluminum).

Off-the-shelf stainless steel Monoball* rod-end fittings were selected for all candidate strut designs since they provide self-alignment capability during installation and chilldown, provide good fatigue life capability, and are readily available in a variety of types, sizes, and load ratings. Rod-ends of the 2 BREF series were

---

* Southwest Products Company

selected from several different types considered in the analysis (Ref Section 3.2.1). Since these rod-ends are internally threaded, the mating internal titanium fittings (i.e., those integrally wrapped into the strut) are externally threaded. This enhances the longo winding characteristics by providing an increased outside diameter to threaded section diameter ratio. In addition, the external threads of the titanium fittings are rolled to significantly improve their fatigue-life capabilities. Another reason why the 2 BREF series fittings were selected is that they are suitable for both the warm-end and cold-end environments. This simplifies the design and procurement since left- and right-hand variations of the same fitting can be used on a given strut. Finally, the 2 BREF series fittings provide the longest fatigue life ratings at high loads for any of the rod-ends considered.

An evaluation of strut core insulations was conducted to complete the detailed design and analysis in Task I. Closed-cell polyurethane foam, chopped Dexiglas, and spaced metallized Mylar radiation shield candidates were analyzed. Geometry, heat rates, and total system weights were computed for a typical 24-in.- (61-cm-) long liquid hydrogen tank support with each of the candidate core insulations installed. A mission duration of 220 days was assumed in the analysis. The resulting total system weight for each case was then compared to that for a reference case where no core insulation was provided. It was found that the lowest total system weight resulted from use of spaced metallized Mylar radiation shields (Ref Table 3-10). However, the system weight penalty was only approximately 4 percent of the optimum value where the strut core was insulated with chopped Dexiglas rather than metallized Mylar shields. Where polyurethane foam was used, the system weight penalty increased by 66 percent over the value for metallized Mylar shields, and where no core insulation at all was provided, the system weight increased by 800 percent over the optimum value.

Based on these results, chopped Dexiglas was selected as the best core insulation overall. The system weight penalty incurred with its use is insignificant, especially considering that the system weight computed for spaced metallized Mylar shields does not include an allowance for installation and maintenance of the shields at the required spacing. Also, the surface emittance of the spaced metallized Mylar shields is subject to degradation which would significantly increase

heat transfer for this system, whereas surface emittance is not significant to the thermal performance of chopped Dexiglas.

Results of the short column compression tests conducted in Task 2 show conclusively that the design techniques and fabrication procedures developed in Tasks I and 2 are valid. For strut configurations II-2 and II-4, the scatter of the failure loads obtained for three specimens of each design was approximately ± I percent of the average value (Ref Section 4.2.I). For two specimens of configuration II-I which were tested with only single-axis control of spurious bending moments, the scatter of failure loads obtained was approximately ± 32 percent. It was concluded that the single-axis moment control mode was inadequate, and all later tests were conducted with control about both principal axes. An excessive scatter of approximately ± 25 percent of the average value was also observed for three specimens of the stiffened cylinder design, configuration II-3, even though the two-axis moment control mode was used. It was concluded that the relatively high scatter of the data obtained for this configuration resulted from unpredictable strength properties for the secondary resin bond between the cylinder wall and the external longeron stiffeners. It appears that the design could be improved significantly by integrally-winding internal longeron sitffeners into grooves premachined into the salt mandrels in order to obtain a primary bond between the stiffeners and the cylinder wall. However, the additional complexity and cost of fabrication associated with this design change do not appear to be justified by the potential weight savings for stiffened struts compared to those with monocoque walls. Consequently, the stiffened design was not investigated further during the program.

Stress-strain data obtained from analysis of the Task 2 short column tests show near-linear slopes from zero load through the failure load achieved (Ref Figs. 4-9, 4-I0, and 4-II). Values of compressive modulus of elasticity obtained from these tests were used to update the Task I parametric data prior to design of the Task 4 test specimens (Ref Figs. 3-37 through 3-42). These values are presented and discussed later in this section with results of Task 5 activities.

In Task 3, materials were procured, mandrel tooling and water-soluble mandrels were fabricated, and eight specimens each of three selected final strut designs were fabricated (Ref Section 5). During this effort, a comprehensive process specification was developed (Ref Appendix E) that defines requirements for material procurement and fabrication of fiberglass struts of each design.

Results of the tension, compression, and cyclic-load tests conducted in Task 4 verified conclusively the design data, the analysis procedures, and the fabrication processes developed in Tasks I, 2, and 3. For all specimens tested, efficient axial load transfer was achieved through the integrally-wrapped end fitting joints. All failures occurred within the composite fiberglass structure as predicted. No failures of internal end fittings, compression caps, or rod-end fittings were encountered. In addition, no failures occurred within the composite fiberglass material near the cold end fittings which were completely immersed in liquid nitrogen to simulate the design environment temperature for all Task 4 test specimens.

Typically, static tension test specimens failed in fracture of the longo rovings near midspan for strut configuration III-I, and in the center section of the closed-end composite structure where it was wrapped over the warm-end fitting for configurations III-2 and III-3. Significant damage of configuration III-2 and III-3 specimens was also sustained due to compressive rebound after the initial tensile failure (Ref Section 6.2.1 and Fig. 6-6).

Local crushing failures were observed in the strut body wall near midspan for all Task 4 static compression test specimens (Ref Fig. 6-7). It was not determined conclusively whether or not these failures were induced initially by general instability (Euler column buckling). However, it was concluded that this is most likely since all Task 4 strut designs were biased to fail in this mode (Ref Figs. 3-43, 3-44, and 3-45).

In the cyclic test mode, typical failures occurred initially due to tensile fracture of the longo rovings at the warm end fitting, followed by damage at other points along the strut body due to compressive rebound or to application of the next compressive load cycle (Ref Fig. 6-8).

Analysis of the Task 4 test data showed that the failure loads were generally within ± 15 percent of those predicted for all static tension and compression test specimens (Ref Table 6-2). For two cases where the failure margin was greater, the actual loads exceeded those predicted by 17.7 and 25.4 percent. Also, it was found that each of the designs offered good fatigue-life capabilities for near design limit cyclic loads in tension and compression. Specimens of configurations III-1 and III-2 achieved from 207 to 283 cycles prior to failure, while those of configuration III-3 achieved from 2509 to 5761 cycles (Ref Table 6-2).

In Task 5, strut fabrication reproducibility was determined from extensive pre-test and post-test laboratory analyses of the Task 2 and Task 4 test specimens. In general, critical dimensions, strut assembly weight, composite weight and density, resin weight and volume fractions, and fiber weight and volume fractions were found to be reproducible within approximately ± 10 percent (Ref Tables 7-1 through 7-4 and Tables 7-6 through 7-8). Average void volume fractions determined for specimens of any particular design ranged from 1.6 to 6.8 percent. For two specimens of configuration III-1 where excessive void volume fractions of 12.1 and 12.9 percent were observed, it was found that the prepreg fiberglass material had been stored somewhat longer than the specified maximum shelf life prior to winding. However, this had no apparent effect on strength properties, since failure loads for these specimens exceeded those predicted by 5.0 and 12.8 percent, respectively (Ref Tables 6-2 and 7-6).

Evaluation of the data obtained in Task 2 for short-column compression test specimens shows that average compressive modulus of elasticity values range from 6.47×10^6 to 7.64×10^6 psi (4.46×10^{10} to 5.27×10^{10} N/m^2) for the selected Task 2 strut designs (Ref Table 7-5). These modulus values correspond to $A_{\ell g}/A_{cg}$ ratios of 1.0 and 2.0, respectively (Ref Table 3-11). The scatter of the data obtained was within ± 3 percent of the average values for monocoque designs (configurations II-1, II-2, and II-4), and within ± 8 percent of the average for the stiffened cylinder design (configuration II-3). Average values of the isotropic crippling coefficient determined from these data ranged from 0.242 for configuration II-2 struts to 0.299 for configurations II-1 struts. For this parameter, the scatter of the data was within ± 4 percent of the average for the monocoque designs, but

increased to ± 18 percent of the average for the stiffened cylinder design (Ref Table 7-5).

A complete review of current fiberglass strut technology was also conducted in Task 5. Thermal and mechanical design properties were selected from results of this program and from other sources in the literature and tabulated for the designer's use (Ref Table 7-9). Based on a comparison of thermal conductivity values computed using the analytical model given by Equation (3-8) with test data from the literature, the analytical model values are recommended for design. In calculating thermal expansion or contraction, handbook values of the thermal coefficient of expansion as a function of temperature should be used. In addition, the room temperature density value recommended for design use is 0.0718 lbm/in.^{3} (1.987 gm/cm^3) based on the measured average for eleven Task 2 test specimens.

With regard to structural design properties, a combination of analytical and test data values are recommended. An average ultimate tensile strength of 202,000 psi (13.9 x 10^8 N/m^2) should be used based on Task 4 test results for six full-size strut specimens. This design value reflects typical stress magnification factors which result from wrapping the longo rovings around the internal end fittings. It is applicable to the longo cross-sectional area only.

For compressive load design, the MIL-HDBK-17A crushing strength value of 100,000 psi (6.9 x 10^8 N/m^2), also applied to the longo cross-sectional area only, is recommended. In addition, the column buckling strength and the local crippling strength values should be determined from the classic Euler column and either the isotropic or orthotropic crippling models, Equations (3-1) and (3-2) or (3-3), respectively. Column buckling and crippling strength design values are applicable to the total composite cross-sectional area of the strut. These values vary with cross-sectional compressive modulus of elasticity and geometry. Column eccentricity also affects the buckling strength, and a suitable crippling coefficient must be selected in order to compute the crippling strength value. Average test values of compressive modulus and crippling coefficient which are recommended for design use can be found in Table 7-5. The decrease in allowable compressive load with

column eccentricity can be determined by equating the maximum fiber compressive stress (i.e., that due to compression plus bending) to the allowable stress from the Euler column buckling equation. In computing the bending moment, the increase in eccentricity due to elastic deformation of the strut under load must be taken into account.

A recommended design approach based on all of the analysis and test results obtained during the program was also developed in Task 5 (Ref Section 7.2.2). Monocoque cylinders should be used for relatively short, lightly-loaded struts. For relatively long, heavily-loaded struts, monocoque ogives were found to be most desirable and should be used. Where applications to intermediate loads and/or lengths are required, both monocoque cylinders and monocoque ogives should be compared to determine the optimum configuration. For all designs, the optimum longo wrap thickness should be determined by cross-plotting column load capability in compression as a function of thickness for column buckling, crippling, and crushing modes of failure. The resulting longo cross-sectional area should then be checked to ensure adequate tensile strength for the intended loading. Other design and manufacturing requirements should be based on the data and procedures given in Appendices E and F.

Finally in Task 5, system weights were evaluated and compared for integrally-wrapped fiberglass struts, fiberglass tension straps, and tubular titanium strut supports. It was found that fiberglass tension straps,designed for given loads and geometry, each required only approximately one-third the cross-sectional area required for integrally-wrapped fiberglass struts of the same length and load capability. However, the number of tension straps required was double the number of struts required to achieve adequate load paths in each direction. This can have a significant detrimental effect on insulation performance due to the additional penetrations, although this effect was not evaluated. In addition, it was found that the total cross-sectional area of the tension strap system had to be increased significantly to achieve adequate structural stiffness for anticipated dynamic loading conditions during launch. The resulting total system weights were approximately the same for the fiberglass tension strap and the fiberglass strut support designs.

When fiberglass struts were compared to titanium struts for equal length and design load cases, it was found that the titanium struts were somewhat lighter based on inert weights only. For example, the inert weight of six 36-in. (91.4-cm) titanium struts designed for an ultimate compressive load of 8400 lbf (37,360 N) was computed to be approximately 16.6 lbm (7.5 kg), compared to approximately 19.6 lbm (8.9 kg) for six fiberglass struts of the same length and load capability (Ref Fig. 7-3). However, when the corresponding propellant boiloff weights for 220 days of storage were added to these inert weights, the resulting total system weights for six struts were 120 lbm (54.2 kg) and 33.9 lbm (15.4 kg) for titanium and fiberglass struts, respectively. It can be seen from this example that significant system weight savings can be achieved where the fiberglass struts are used.

Section 9

CONCLUSIONS

The conclusions which were derived from results of the analysis and testing performed during this contract program are as follows:

- Monocoque cylinders and/or ogives are either optimum or can be used with negligible system weight penalties for the entire range of lengths and loads investigated.

- Inert plus boiloff weights for filament-wound fiberglass struts are significantly lower than for any metallic struts of equal length and load capability.

- Ultimate axial load capabilities of filament-wound fiberglass struts can be predicted analytically within approximately $\pm$ 15 percent.

- Manufacturing reproducibility within approximately $\pm$ 10 percent can be achieved with current equipment and procedures.

- The concept of integrally wrapping metallic end fittings with the longo fibers to achieve axial load transfer without dependence on bond strength or mechanical fasteners has been verified.

- Titanium end fittings with rolled external threads provide significantly longer fatigue-life capabilities than do those with internal threads.

- Additional cyclic-load testing is needed to complete development of filament-wound fiberglass struts for flight hardware applications.

These conclusions show that the goals of this contract program have been achieved. Successful verification of the integral end-fitting design concept, and demonstration of design predictability within ± 15 percent and manufacturing reproducibility within ± 10 percent are significant improvements to the state-of-the-art. With additional cyclic-load testing to complete characterization of the fatigue-life capabilities of these structures, this technology can readily be applied to future designs where exceptionally high strength, low heat leak struts are required.

Appendix A

DESCRIPTION OF COMPUTER PROGRAMS FOR STRUCTURAL ANALYSIS

In Task 1, three different computer programs were used to facilitate the structural analysis. A brief description of each is presented below.

BARSIN

In general, this computer program is used to predict classic elastic buckling loads for simply-supported cylinders with various wall constructions subject to internal or external pressure and axial load. For the cases analyzed during this program, the applied lateral pressure load was zero.

The program determines bifurcation buckling of cylindrical shells based on Donnell equations and on a linear membrane analysis for establishing prebuckling equilibrium. Critical combinations of axial load and lateral pressure are determined for cases where combined loading is applied. Any simply-supported orthotropic shell wall can be analyzed, but special adaptations are provided for commonly-used structures such as:

- Shells with ring and stringer stiffening
- Shells with skew stiffeners
- Fiber reinforced shells
- Layered shells (isotropic or orthotropic)
- Corrugated ring-stiffened shells
- Shells with one corrugated and one smooth skin (with rings)

The analysis is based on the solution presented by Baruch and Singer (Ref 27), although it has been generalized somewhat with respect to constitutive equations and loading. Also, the effect of a soft elastic core has been

included, and load can be introduced through a flexible external cushion. Critical axial loads can be printed out as a function of the number of waves (diamond buckles), or the minimum load capability can be established and printed out. The program is currently run on a Univac 1108 machine, and a user's manual is available (LMSC 681206). Case run time is on the order of a few seconds.

BOSOR 2

This computer program was devised to predict prebuckling stress and buckling loads for segmented shells of revolution with various wall constructions subject to various loads. In Task 1, it was used to obtain an exact solution for selected ogive strut configurations loaded in axial compression.

In its general application, the BOSOR 2 program calculates collapse loads, bifurcation buckling loads, and vibration frequencies of ring-stiffened, segmented shells of revolution with various types of wall construction and submitted to various types of axisymmetric loads. Use of the program is facilitated by provision of special branches with regard to geometry, wall construction, boundary conditions, and type of loading. Its general capability includes:

- Vibration analysis of prestressed shells
- Analysis of segmented shells such as cylinder-core combinations
- Analysis of shells with discrete rings at a number of stations along the meridian, rather than at the boundaries only
- Variable mesh spacing
- Use of the more general Novoshilov-type shell equations rather than Donnell-type equations
- General axisymmetric loading such as variable pressure, line loads, and moments applied at any station along the meridian

- Analysis of shells with wall properties which vary along the meridian
- A routine for plotting stresses, displacements, and modal characteristics

The BOSOR 2 computer program is based on an energy formulation in which the finite difference method is used. The number of mesh points cannot exceed 100. It is currently used with a Univac 1108 computer, and a user's manual is available (LMSC N-26-68-1). Run times are significantly longer than those required for the BARSIN program.

COLUMN

A new computer program was developed specifically to predict the general instability (Euler column buckling) capabilities of ogive struts for the Task 1 analysis. Currently, it provides only for simply-supported columns subject to axial compression loads.

Initially, each ogive strut configuration to be analyzed is divided into 20 end-to-end segments of equal length. The analysis is actually performed for 10 segments over the half-length of the strut, since ogive struts are symmetrical about the midspan station. Each segment is treated as a truncated cone, with cross-sectional geometry and material properties matched at the boundaries of adjacent segments. In the analysis, geometry and material properties of each segment are input with the program. General instability buckling loads are then computed and summed for the combined structure. The program was formulated for solution using the Univac 1108 computer. A user's manual has not been compiled. Run times are short compared to the other programs used in Task 1.

Appendix B

COMPRESSIVE LOAD CAPABILITY FOR LONGERON-STIFFENED FIBERGLASS STRUTS

Results of the analysis conducted in Task 1 to predict compressive load capability for longeron-stiffened fiberglass cylinders (Ref Section 3.1.5) are presented in Figs. B-1 through B-18. In each of these figures, compressive load capabilities for general instability (column buckling) and local instability (crippling) failure modes are plotted as a function of the number of waves (local diamond buckles), n, which form around the circumference at crippling. When longeron stiffeners are added at each point of inflection of each wave (sine wave form), the compressive load capabilities in both column buckling and crippling of the wall panels between longerons increase as shown. The total number of stiffeners required is 2n, and the least weight design (indicated in each figure) is achieved when the capability of the wall (neglecting stiffeners) is the same for each of the primary failure modes. Where the crippling capability is always greater than the column buckling capability (i.e., the curves do not cross), monocoque designs are optimum. Total compressive load capability for the least weight design (also shown in each figure) is then obtained by adding the capability of the stiffeners, assuming equal strain rates in the wall and stiffeners.

Capabilities are shown in Figs. B-1 through B-5 for 18-in.-(45.7-cm-) long cylinders with a 12-mil (0.30-mm) longo wrap thickness stiffened with glass-fiber longerons. Those for 29-in.-(73.7-cm-) long cylinders with the same longo wrap thickness are presented in Figs. B-6 through B-9. The capabilities for 40-in.-(101.6-cm-) long cylinders with a 12-mil (0.30-mm) longo wrap thickness are presented in Figs. B-10 through B-14 for both glass-fiber and boron-fiber longerons. Finally, capabilities are shown in Figs. B-15 through B-18 for 40-in.-(101.6-cm) long cylinders with an 18-mil (0.46-mm) longo wrap thickness stiffened with glass-fiber longerons.

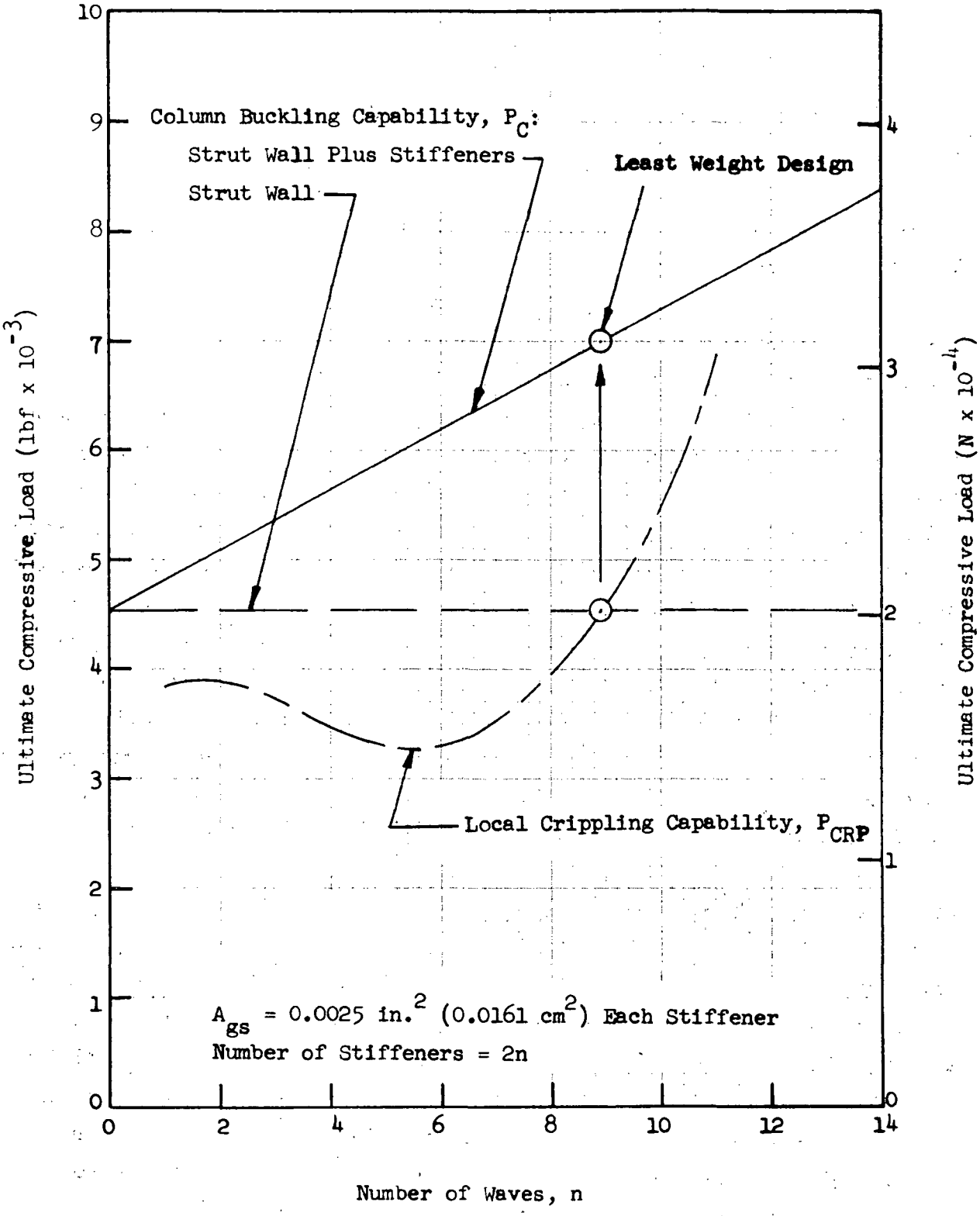

Fig. B-1 Predicted Ultimate Compressive Loads for 18-in.-(45.7-cm-) Long, 1.5-in.-(3.81-cm-) Diameter Stiffened Fiberglass Cylinders with a 12-mil (0.30-mm) Longo Wrap Thickness

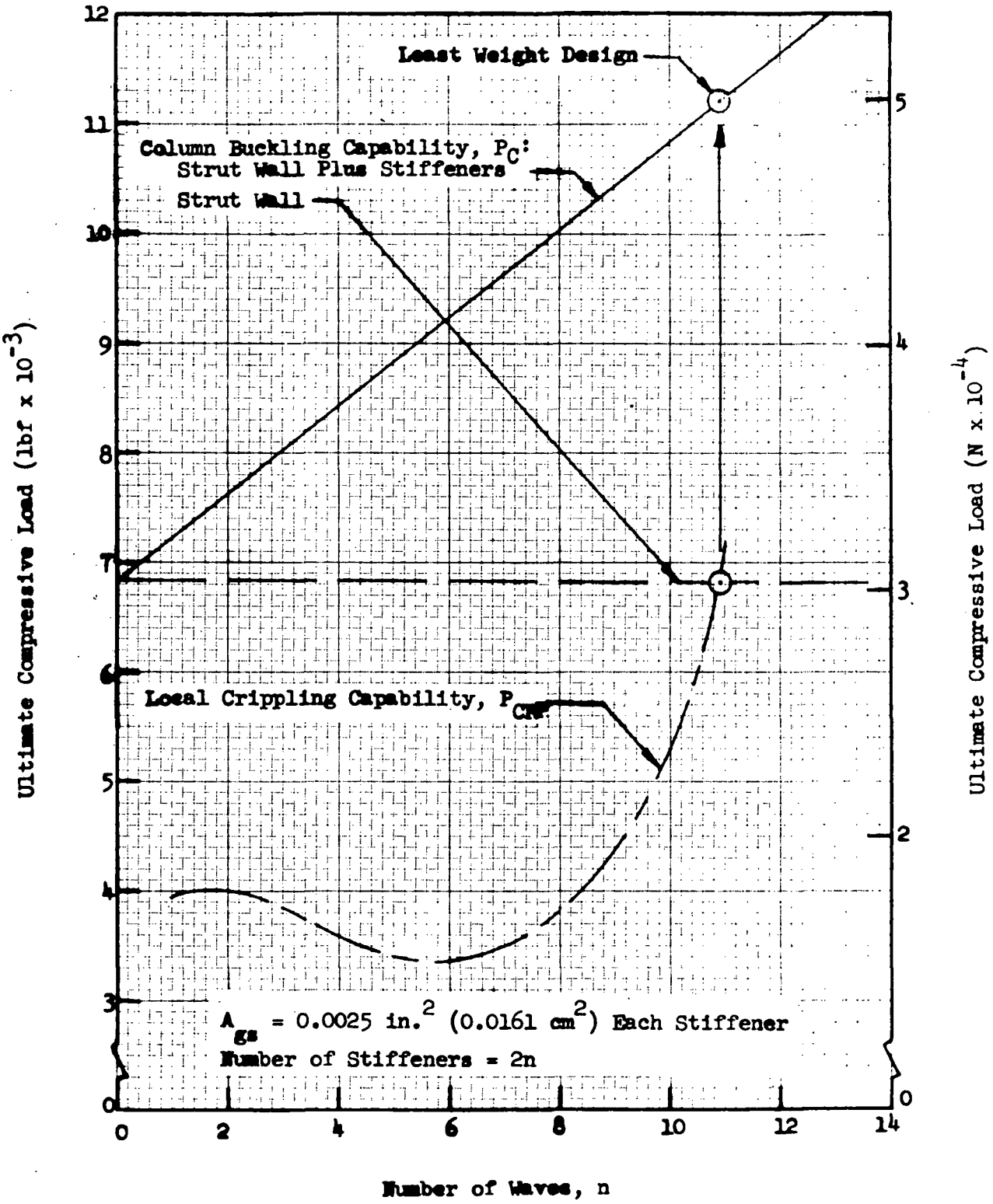

Fig. B-2 Predicted Ultimate Compressive Loads for 18-in.-(45.7-cm-) Long, 1.75-in.-(4.45-cm-) Diameter Stiffened Fiberglass Cylinders with a 12-mil (0.30-mm) Longo Wrap Thickness

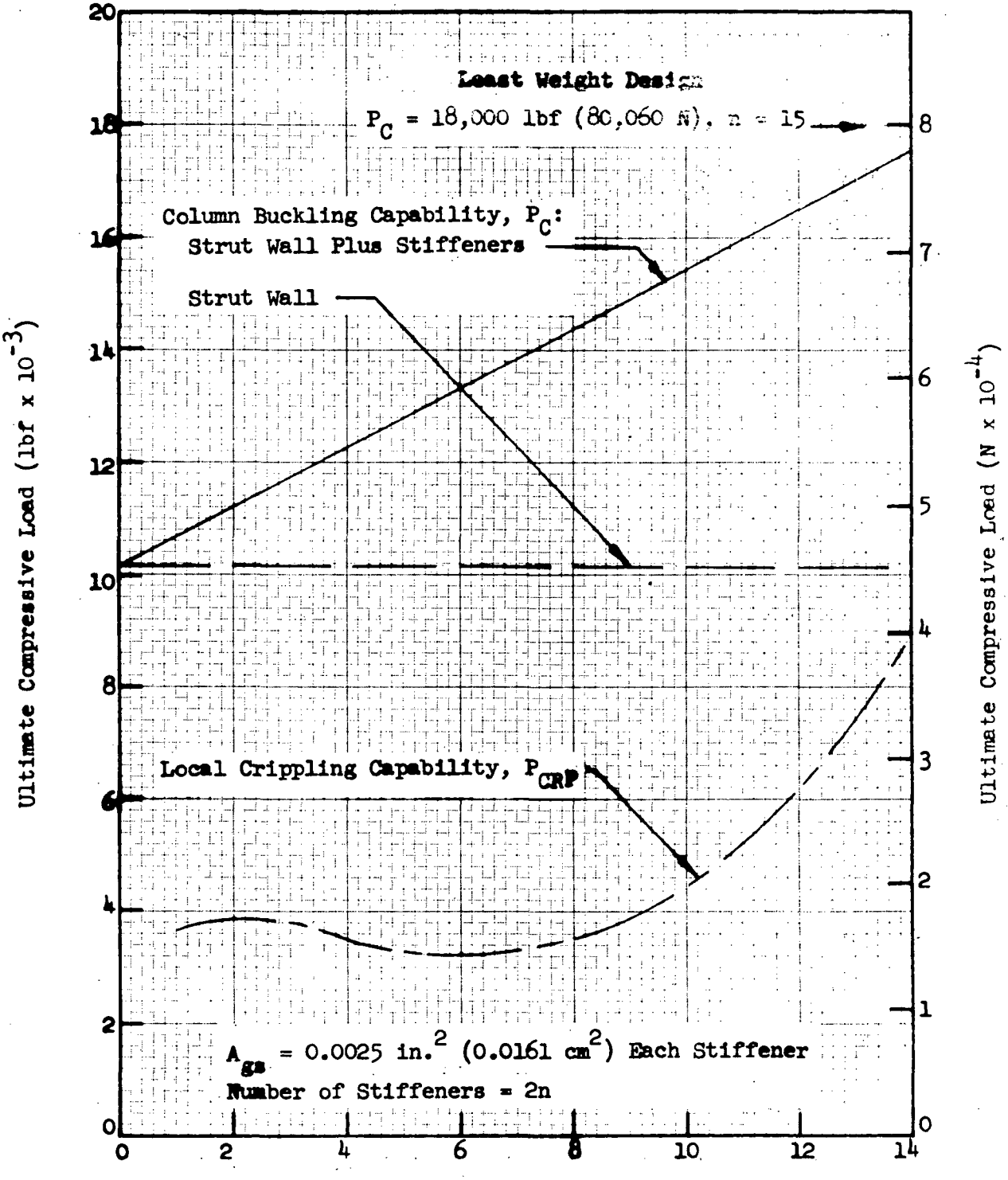

Fig. B-3 Predicted Ultimate Compressive Loads for 18-in.-(45.7-cm-) Long, 2.0-in.-(5.08-cm-) Diameter Stiffened Fiberglass Cylinders with a 12-mil (0.30-mm) Longo Wrap Thickness

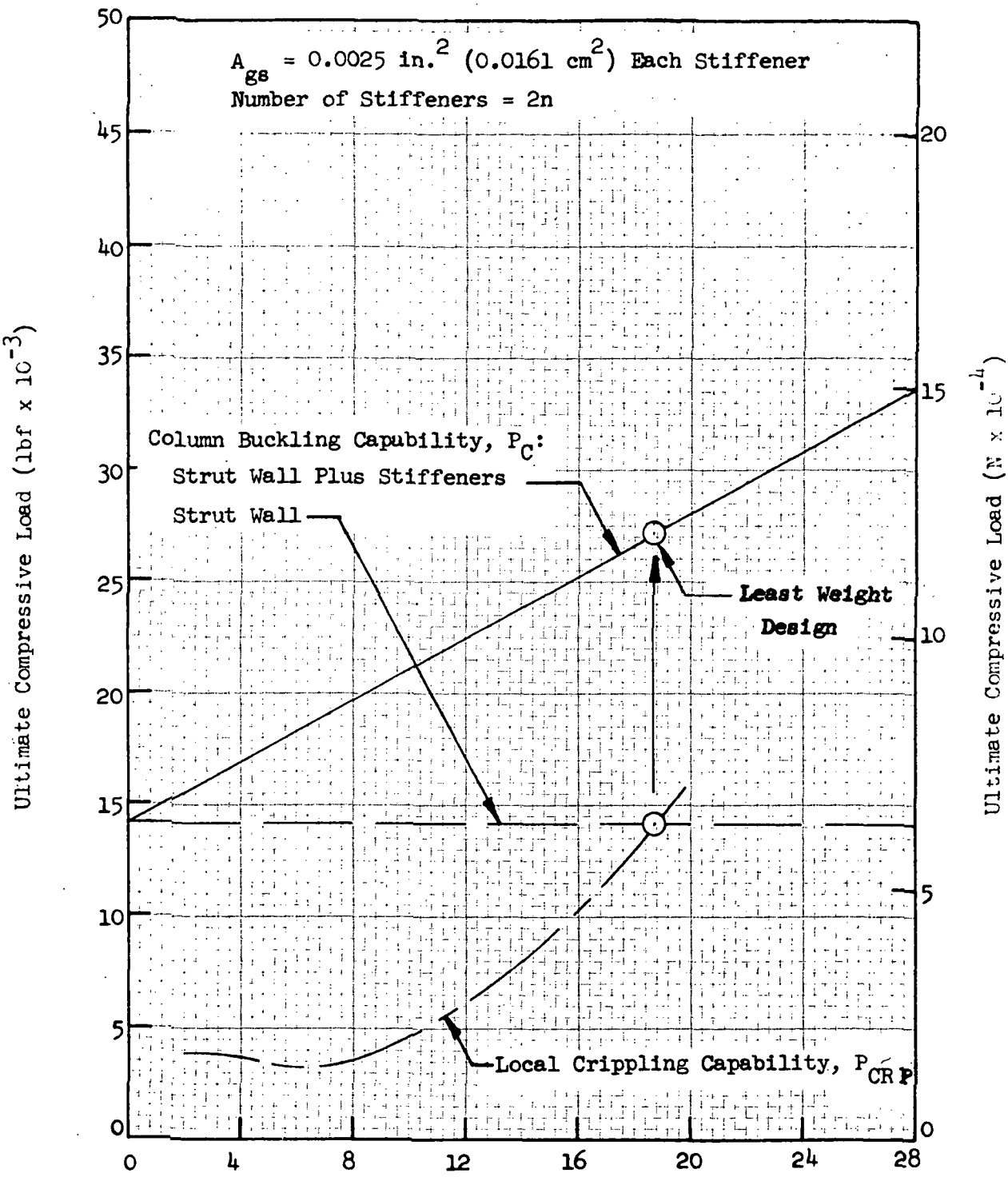

Fig. B-4 Predicted Ultimate Compressive Loads for 18-in.-(45.7-cm-) Long, 2.25-in.-(5.72-cm-) Diameter Stiffened Fiberglass Cylinders with a 12-mil (0.30-mm) Longo Wrap Thickness

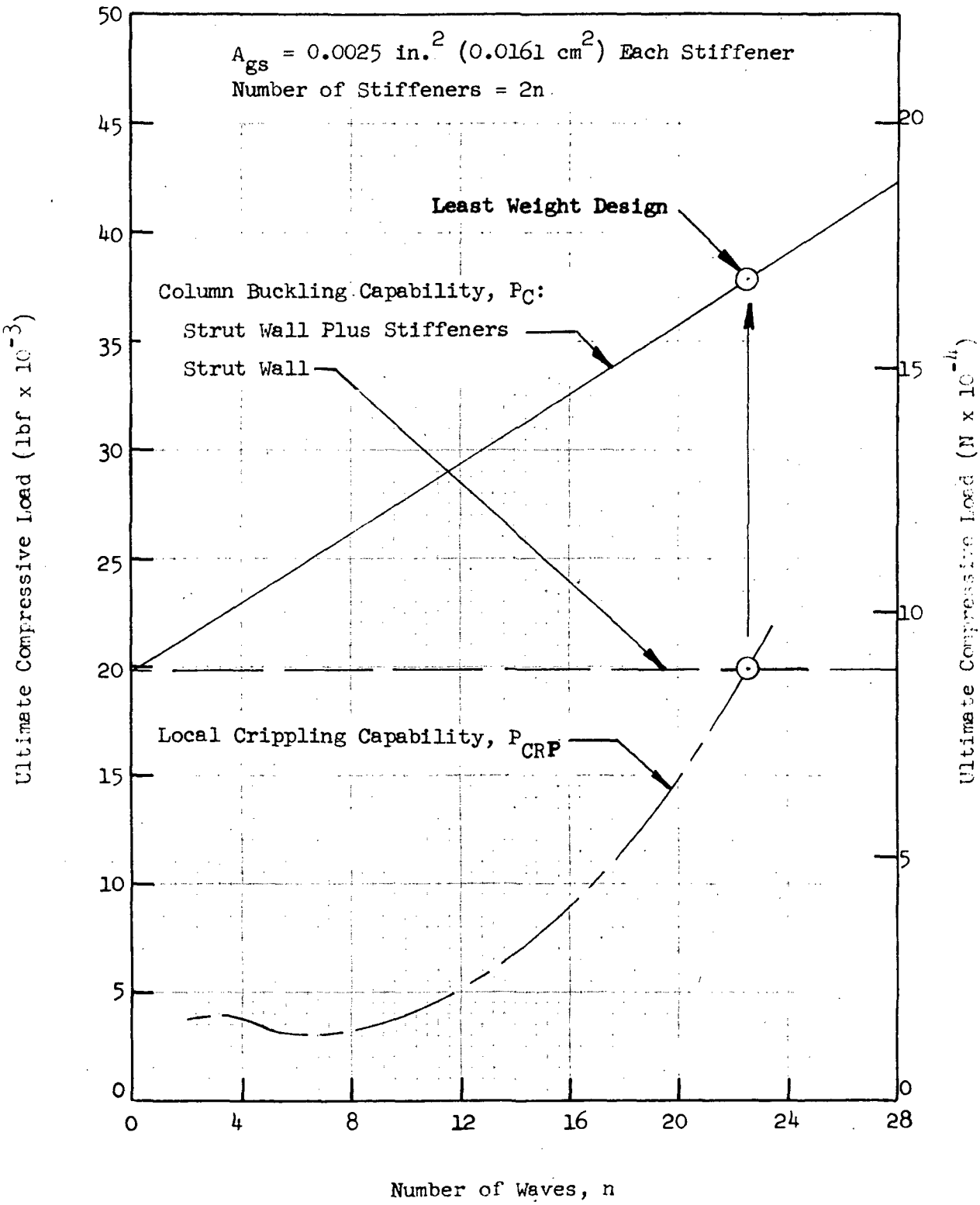

Fig. B-5 Predicted Ultimate Compressive Loads for 18-in.-(45.7-cm-) Long, 2.5-in.-(6.35-cm-) Diameter Stiffened Fiberglass Cylinders with a 12-mil (0.30-mm) Longo Wrap Thickness

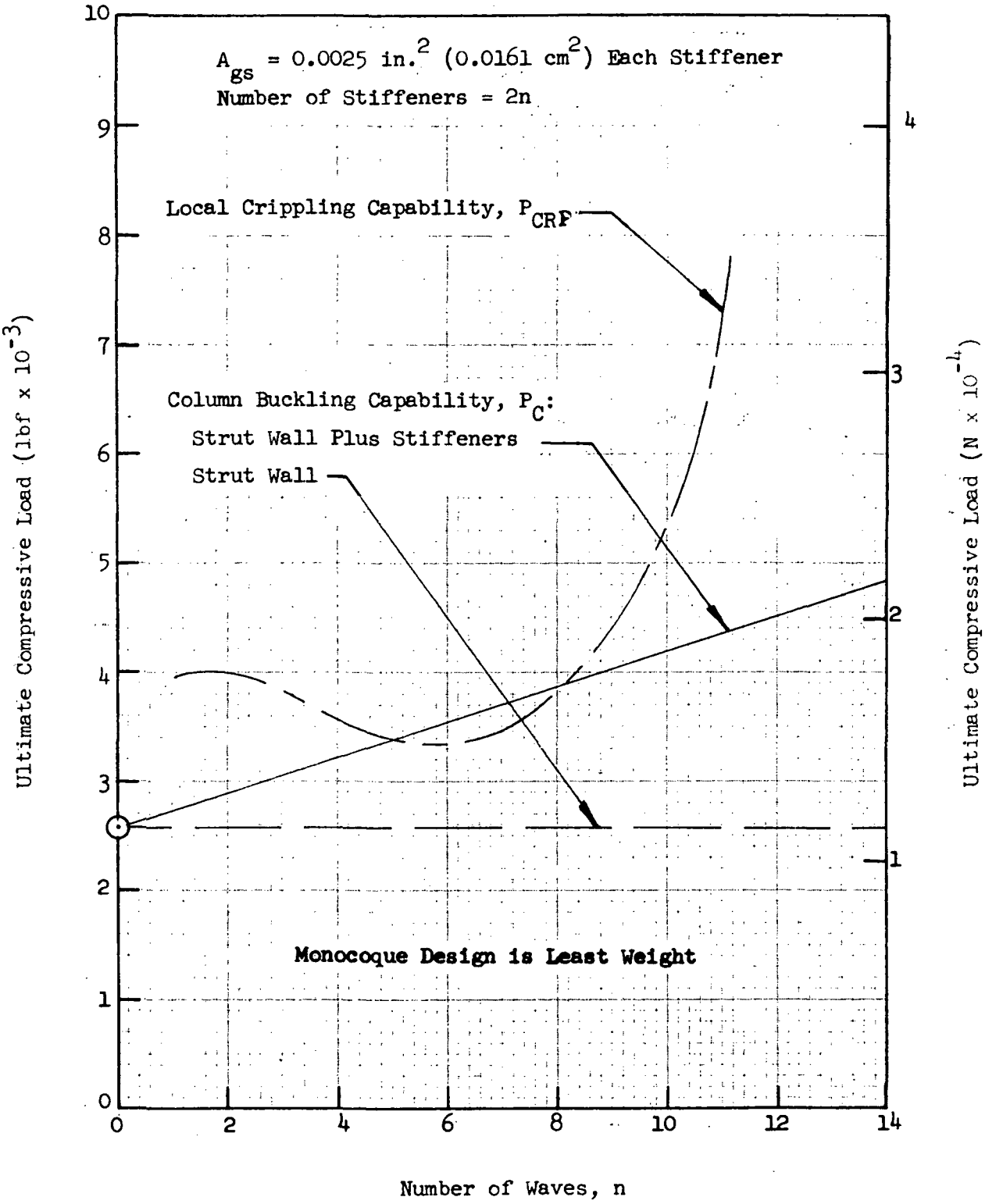

Fig. B-6 Predicted Ultimate Compressive Loads for 29-in.-(73.7-cm-) Long, 1.75-in.-(4.45-cm-) Diameter Stiffened Fiberglass Cylinders with a 12-mil (0.30-mm) Longo Wrap Thickness

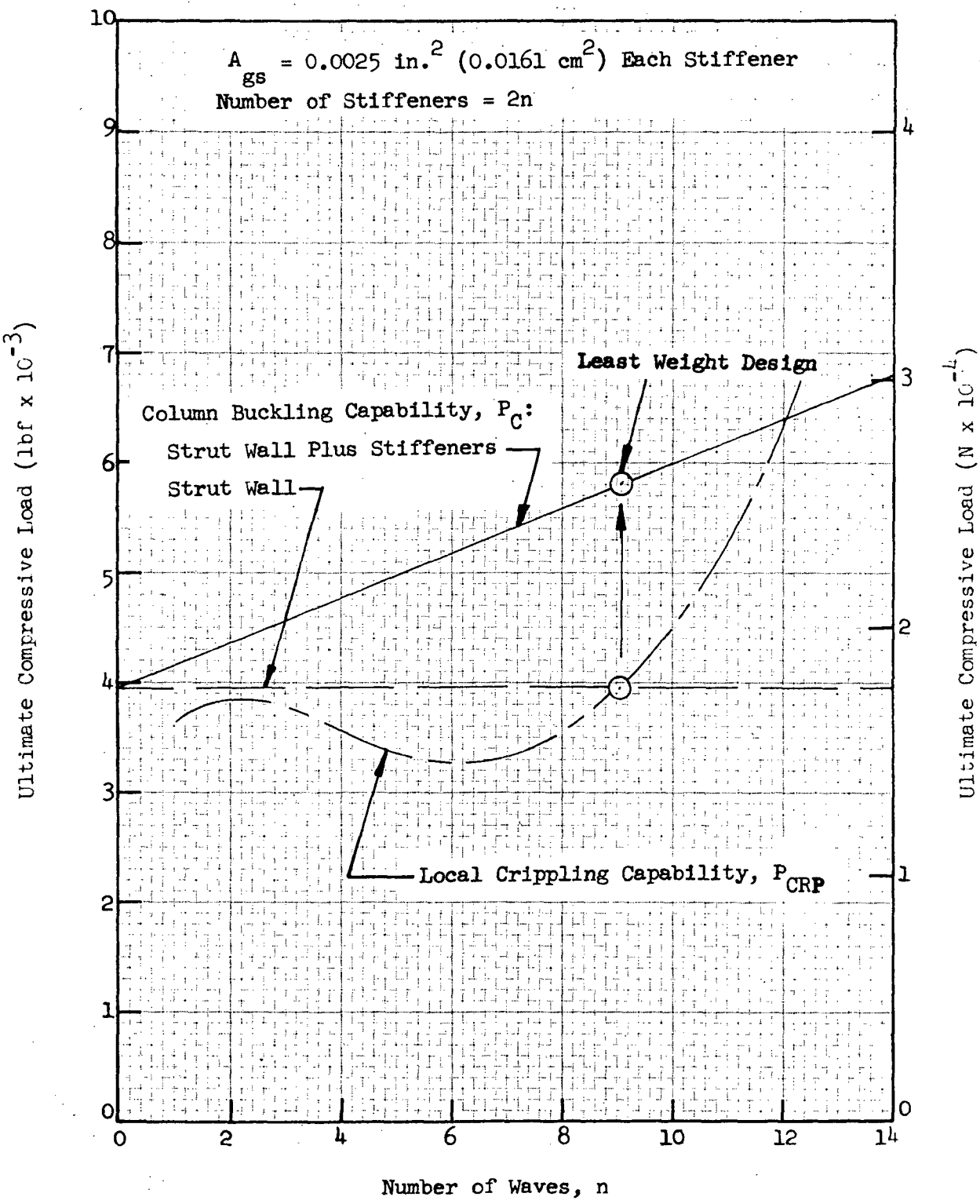

Fig. B-7 Predicted Ultimate Compressive Loads for 29-in.-(73.7-cm-) Long, 2.0-in.-(5.08-cm-) Diameter Stiffened Fiberglass Cylinders with a 12-mil (0.30-mm) Longo Wrap Thickness

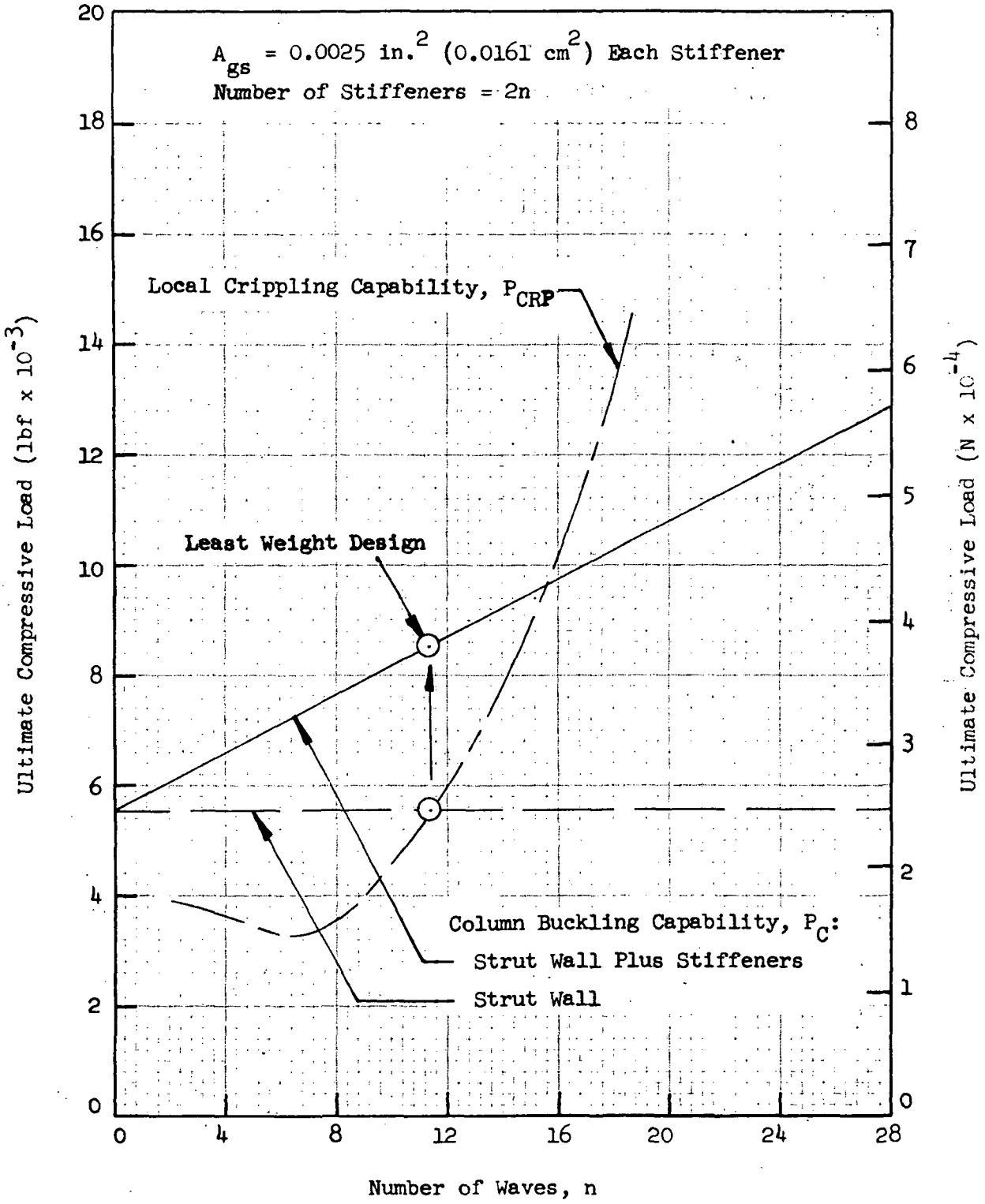

Fig. B-8 Predicted Ultimate Compressive Loads for 29-in.- (73.7-cm-) Long, 2.25-in.-(5.72-cm-) Diameter Stiffened Fiberglass Cylinders with a 12-mil (0.30-mm) Longo Wrap Thickness

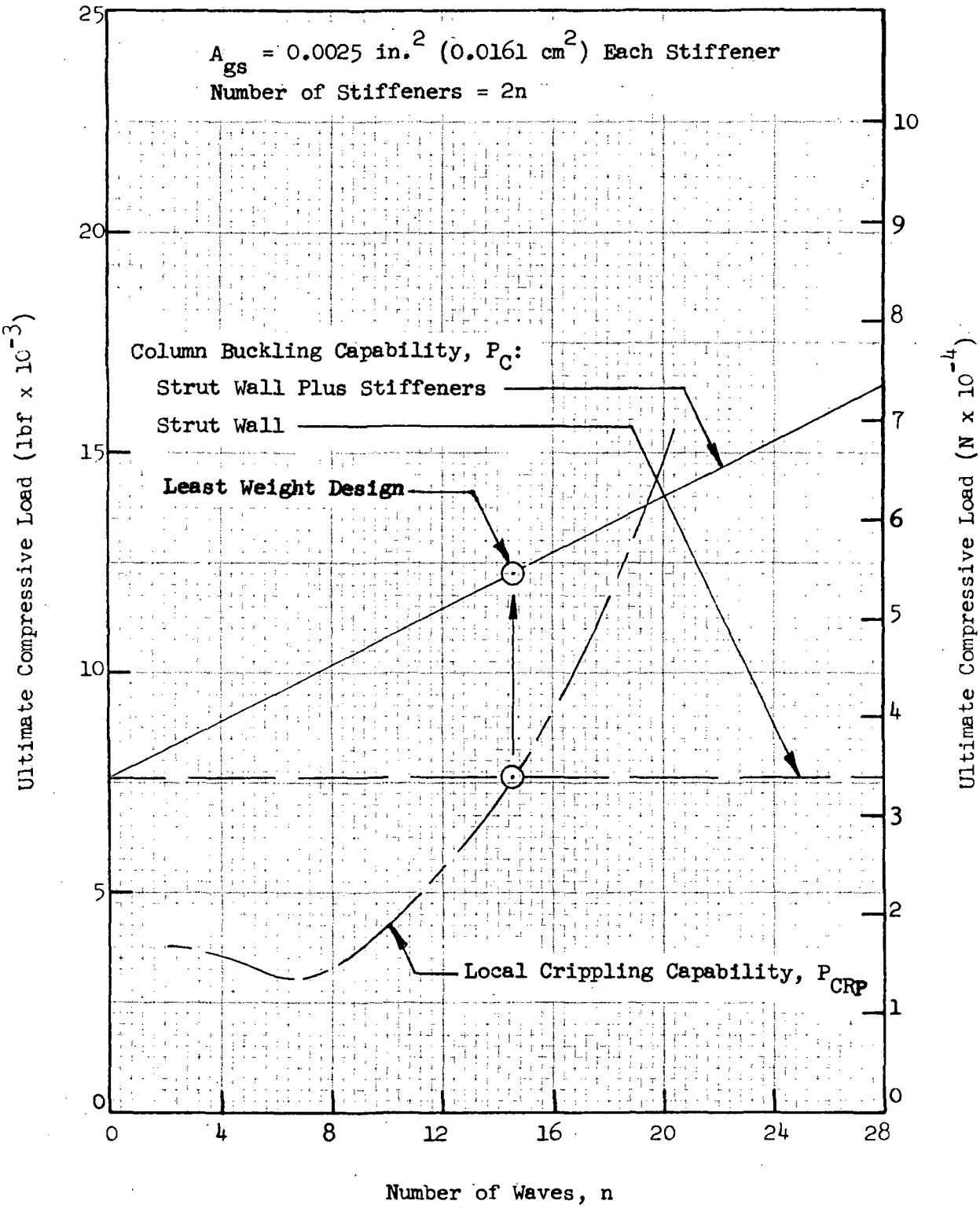

Fig. B-9 Predicted Ultimate Compressive Loads for 29-in.-(73.7-cm-) Long, 2.5-in.-(6.35-cm-) Diameter Stiffened Fiberglass Cylinders with a 12-mil (0.30-mm) Longo Wrap Thickness

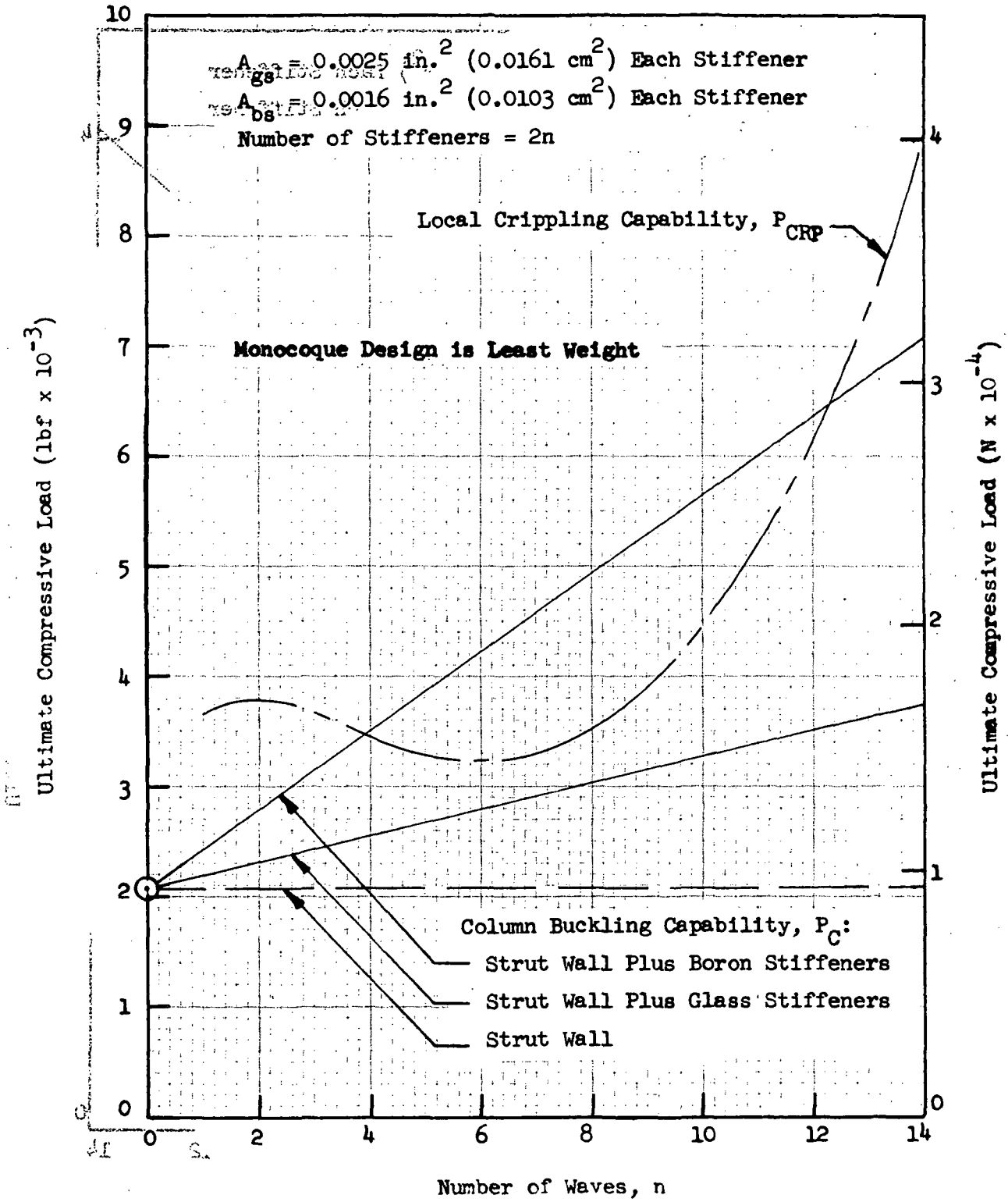

Fig. B-10 Predicted Ultimate Compressive Loads for 40-in.-(101.6-cm-) Long, 2.0-in.-(5.08-cm-) Diameter Stiffened Fiberglass Cylinders with a 12-mil (0.30-mm) Longo Wrap Thickness

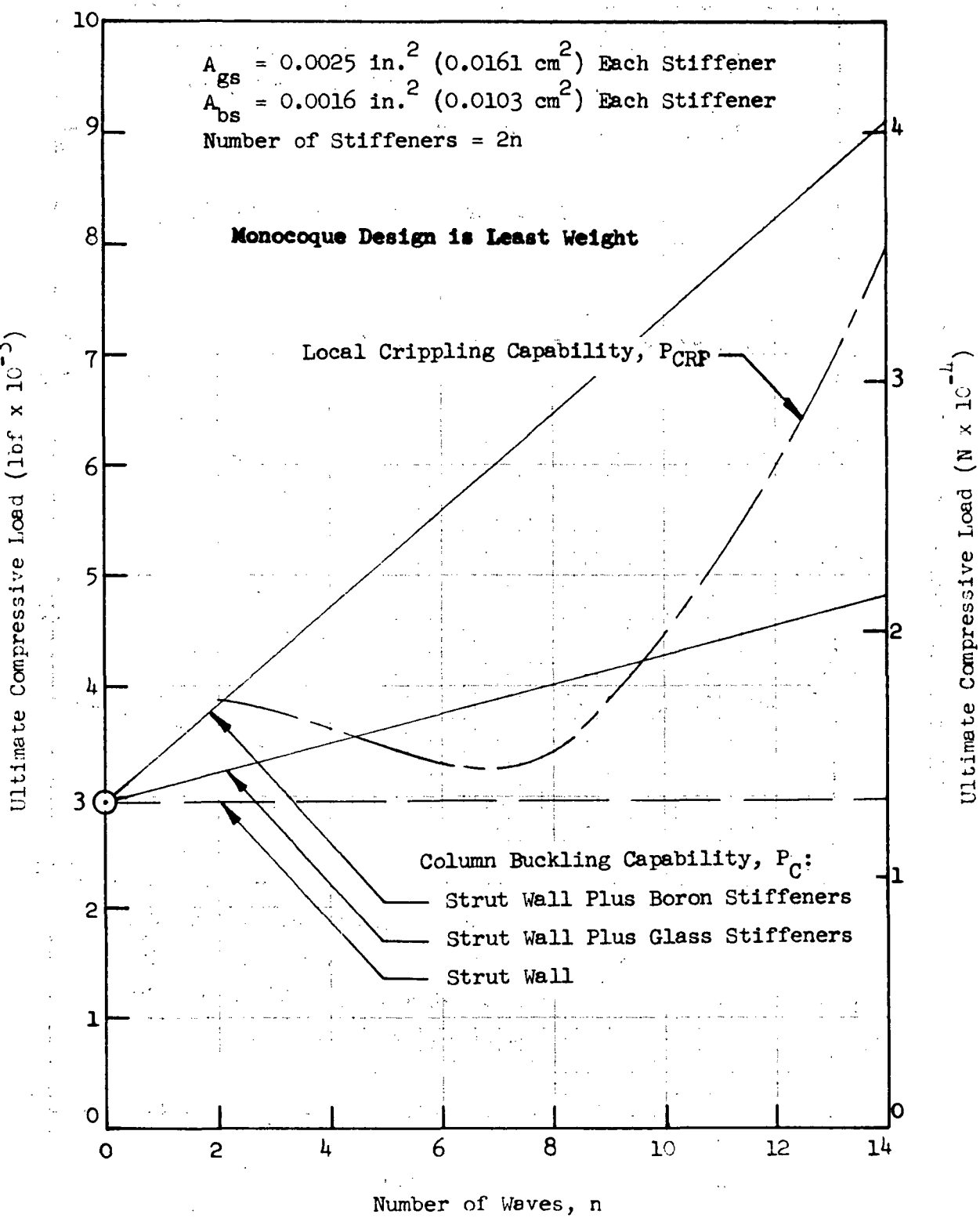

Fig. B-11 Predicted Ultimate Compressive Loads for 40-in.-(101.6-cm-) Long, 2.25-in.-(5.72-cm-) Diameter Stiffened Fiberglass Cylinders with a 12-mil (0.30-mm) Longo Wrap Thickness

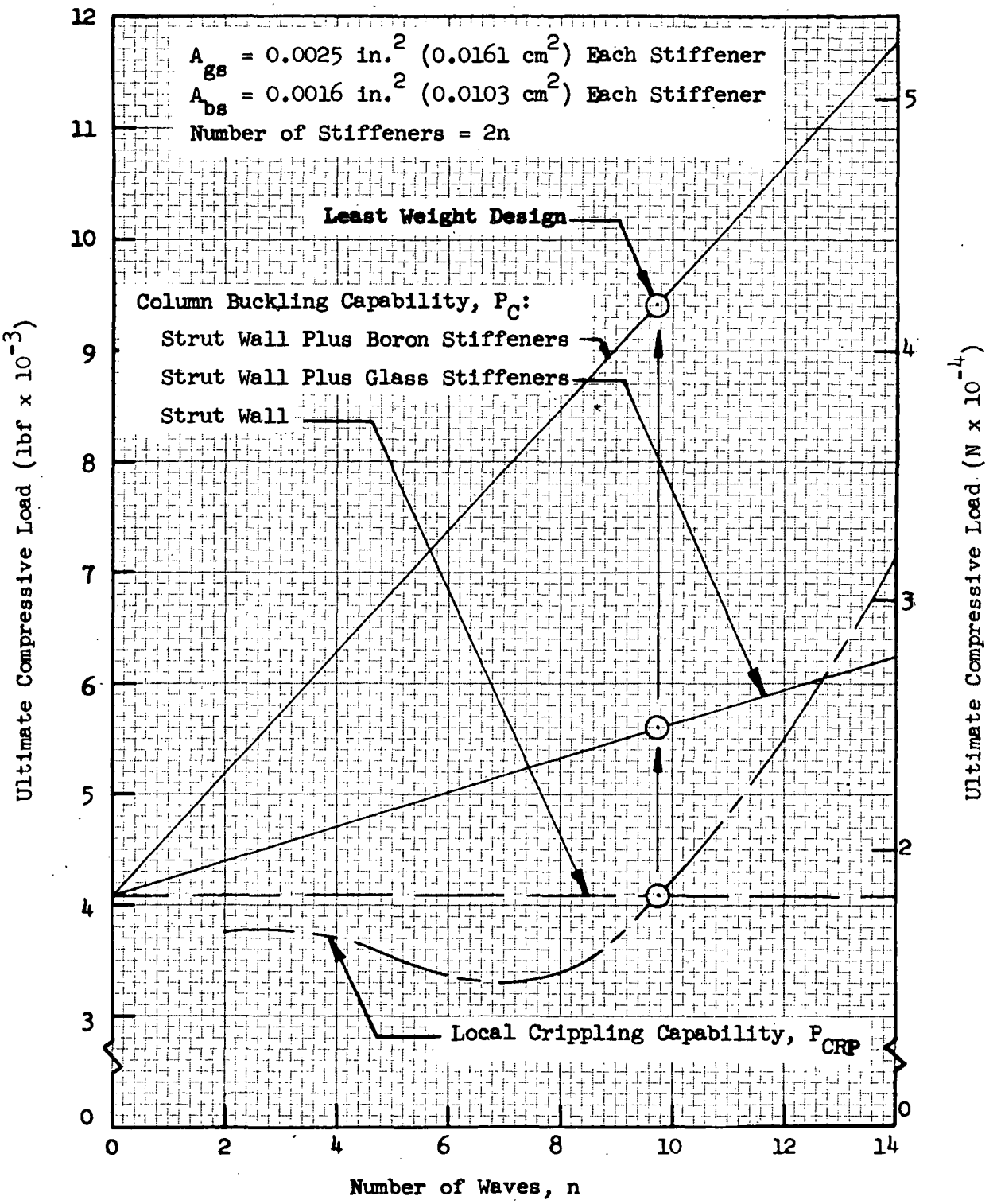

Fig. B-12 Predicted Ultimate Compressive Loads for 40-in.-(101.6-cm-) Long, 2.5-in.-(6.35-cm-) Diameter Stiffened Fiberglass Cylinders with a 12-mil (0.30-mm) Longo Wrap Thickness

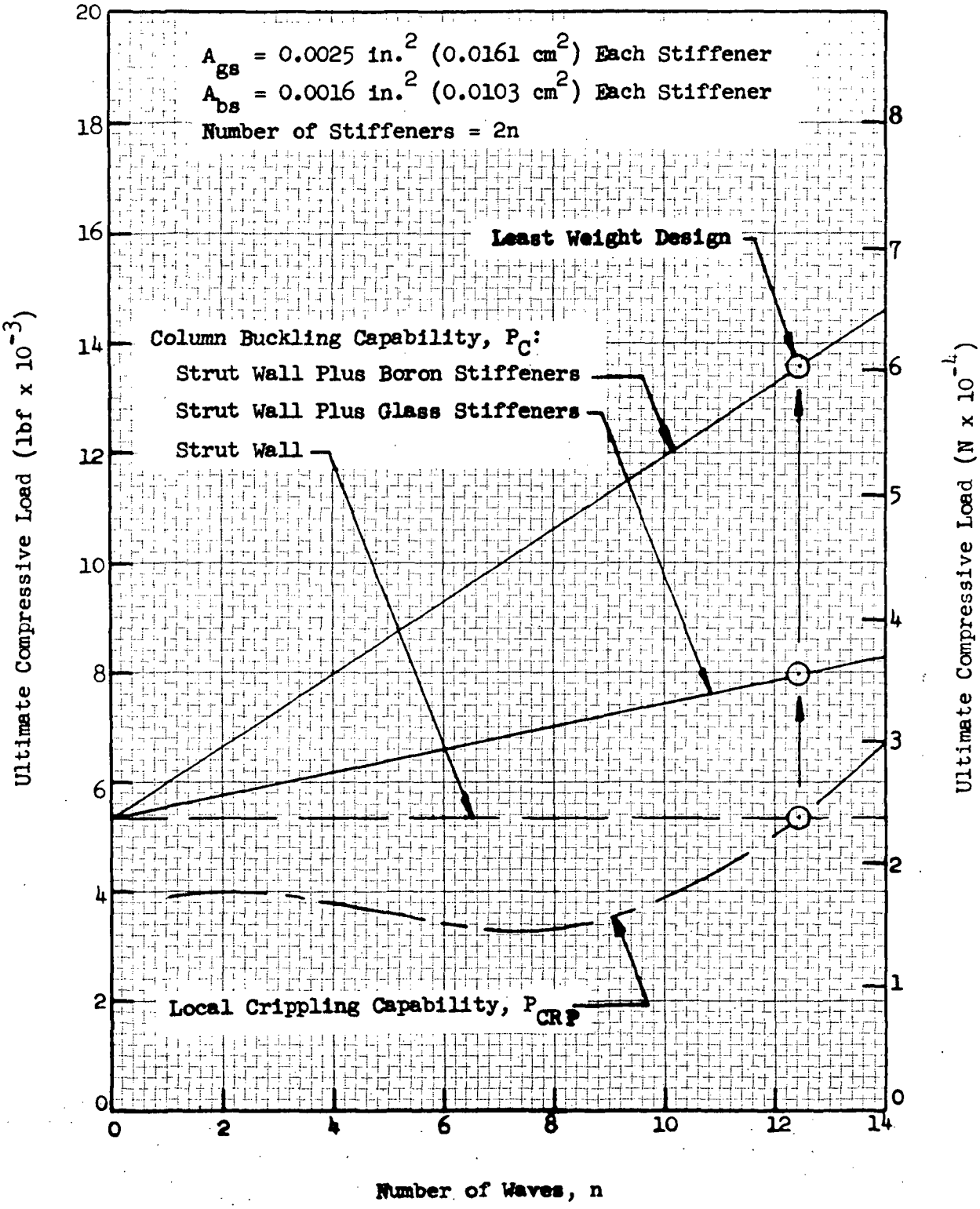

Fig. B-13 Predicted Ultimate Compressive Loads for 40-in.-(101.6-cm-) Long, 2.75-in.-(6.99-cm-) Diameter Stiffened Fiberglass Cylinders witha 12-mil (0.30-mm) Longo Wrap Thickness

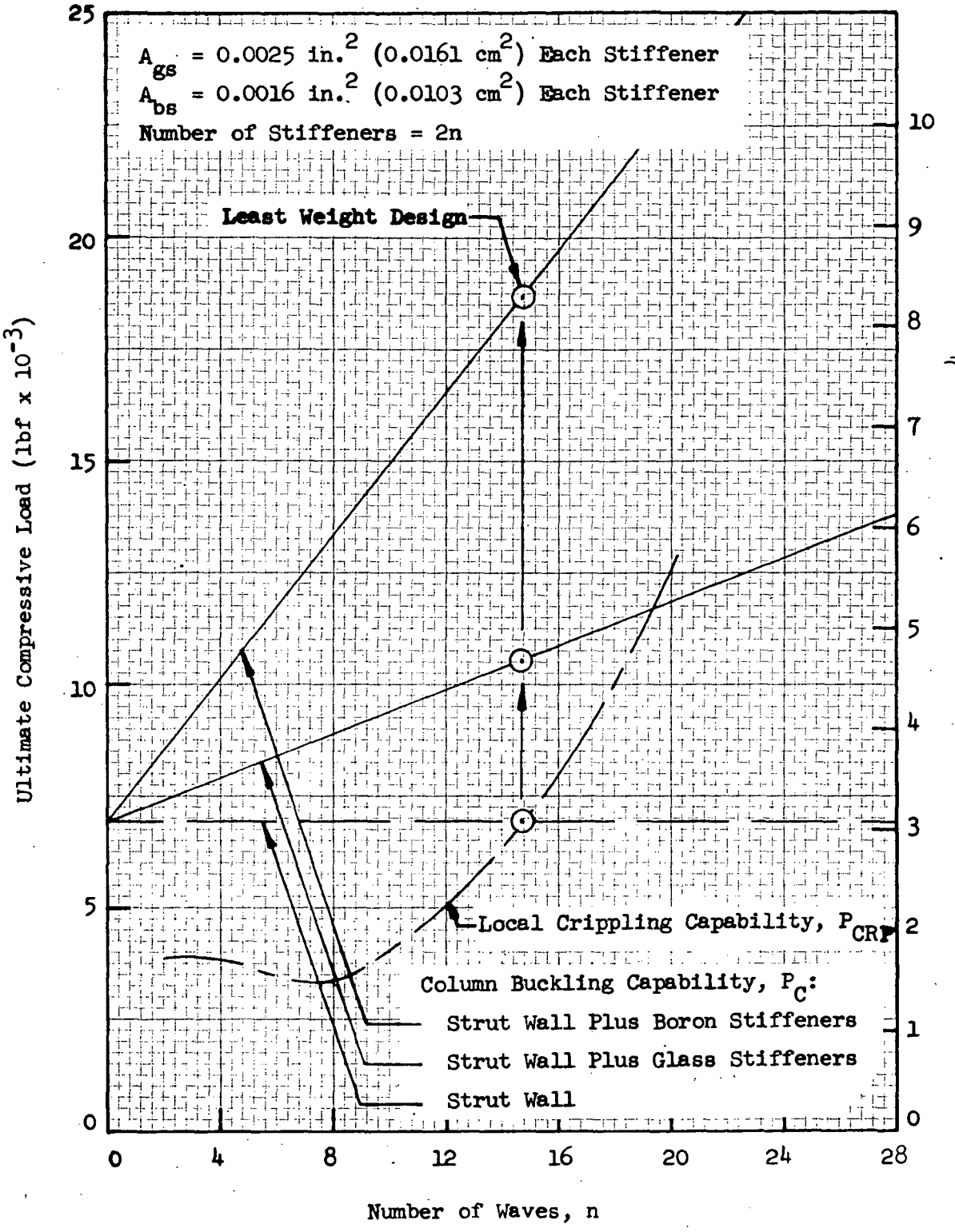

Fig. B-14 Predicted Ultimate Compressive Loads for 40-in.-(101.6-cm-) Long, 3.0-in.-(7.62-cm-) Diameter Stiffened Fiberglass Cylinders with a 12-mil (0.30-mm) Longo Wrap Thickness

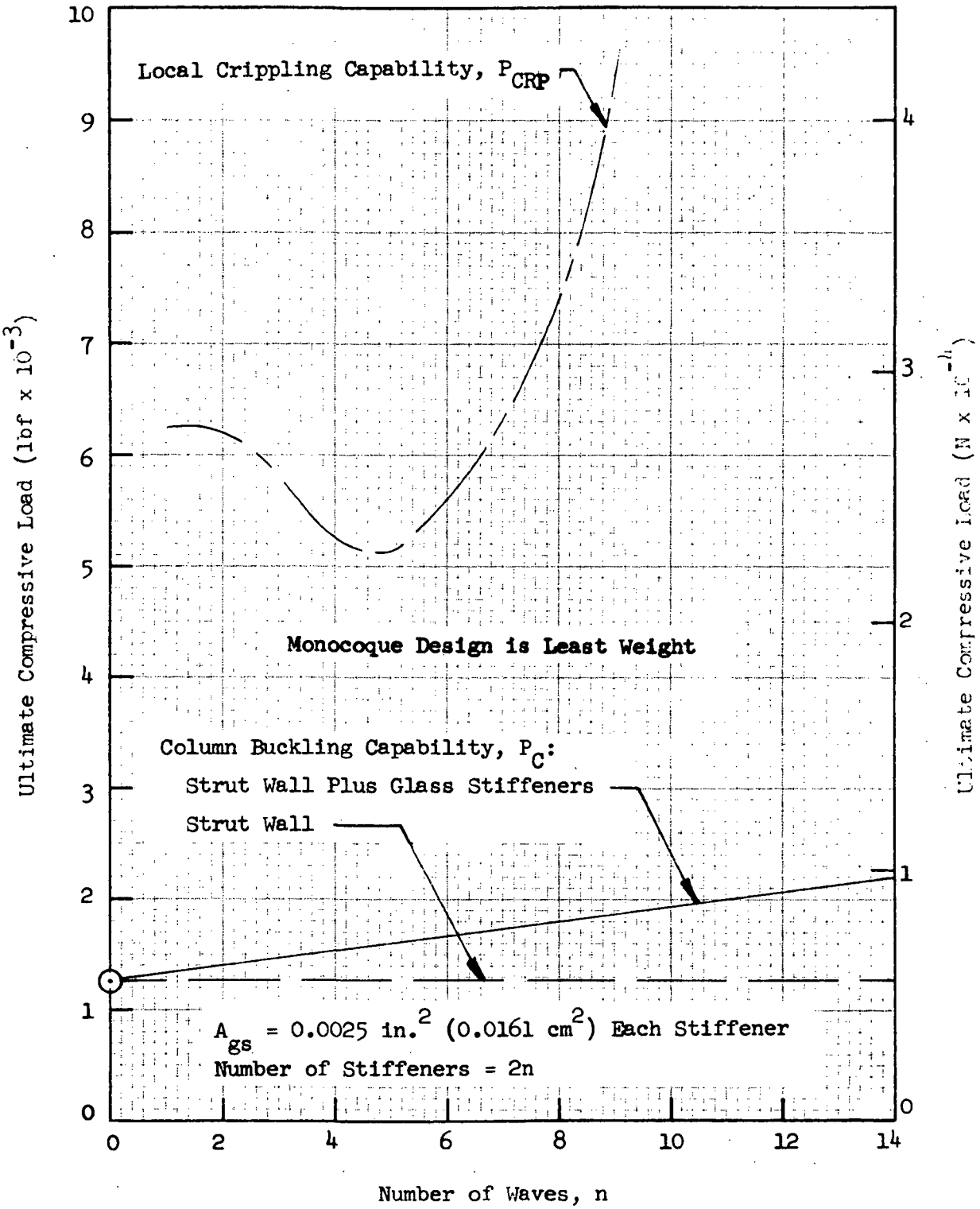

Fig. B-15 Predicted Ultimate Compressive Loads for 40-in.-(101.6-cm-) Long, 1.5-in.-(3.81-cm-) Diameter Stiffened Fiberglass Cylinders with an 18-mil (0.46-mm) Longo Wrap Thickness

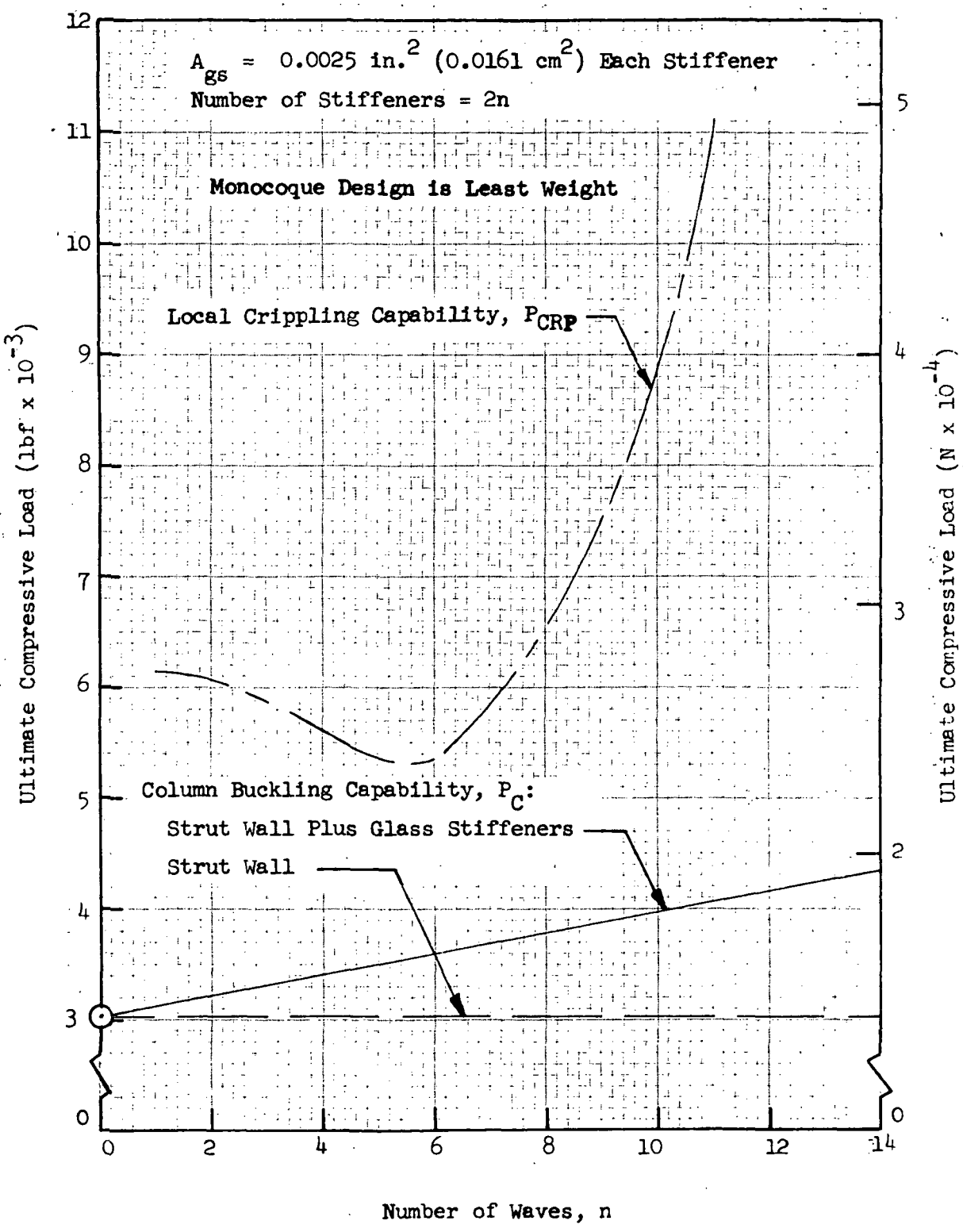

Fig. B-16 Predicted Ultimate Compressive Loads for 40-in.-(101.6-cm-) Long, 2.0-in.-(5.08-cm-) Diameter Stiffened Fiberglass Cylinders with an 18-mil (0.46-mm) Longo Wrap Thickness

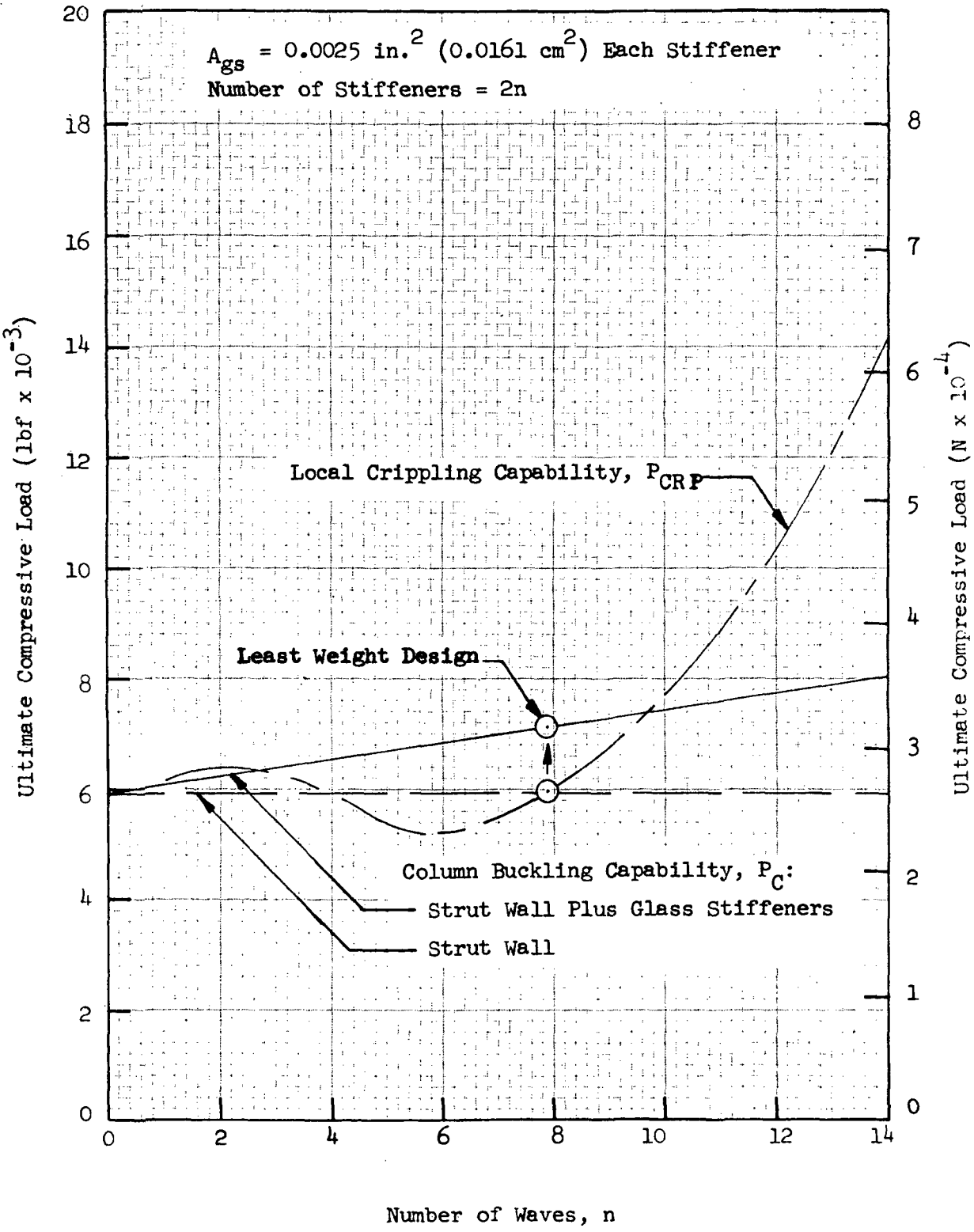

Fig. B-17 Predicted Ultimate Compressive Loads for 40-in.-(101.6-cm-) Long, 2.5-in.-(6.35-cm-) Diameter Stiffened Fiberglass Cylinders with an 18-mil (0.46-mm)Longo Wrap Thickness

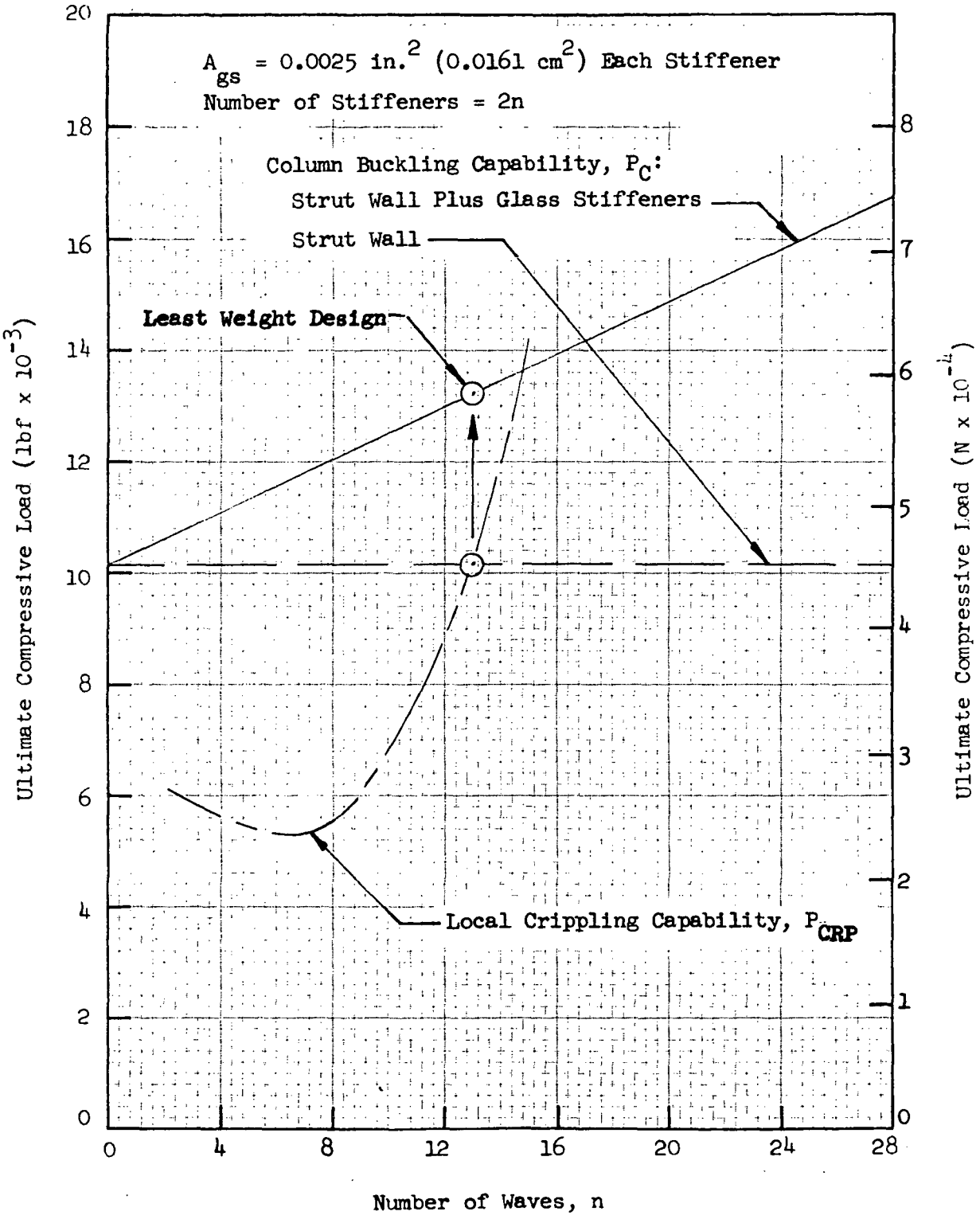

Fig. B-18 Predicted Ultimate Compressive Loads for 40-in.-(101.6-cm-) Long, 3.0-in.-(7.62-cm-) Diameter Stiffened Fiberglass Cylinders with an 18-mil-(0.46-mm) Longo Wrap Thickness

Appendix C

CALCULATION OF ONE-DIMENSIONAL HEAT LEAKS

Values of one-dimensional heat leak for two boundary temperature combinations were computed in Task 1 (Ref Section 3.1.7) for 15 of the 16 analysis cases selected for study (Ref Table 3-2). Results are presented in Tables C-1 through C-10.

For analysis case numbers 1 through 6, the heat leak values were computed directly using equation (3-5). Values of the composite thermal conductivity, k_c, were taken from Fig. 3-20 for the appropriate ratio of longo-to-circ fiber distribution, A_ℓ/A_{cr}. Composite cross-sectional area values, A_c, were obtained from Fig. 3-1, and values of T_H and T_C were those specified in the contract. The composite length, L_c, was taken as the total strut length, L_s, less 6 in. (15.2 cm). For the ogive struts (analysis case numbers 4, 5, and 6), values of k_{c1}, k_{c2}, and A_c at midspan and at the ends were averaged and used to compute the composite heat leaks.

Values of total composite heat leak for analysis case number 7 were obtained by computing the incremental heat leaks for the single boron-fiber longo wrap, and by then adding these increments to the corresponding fiberglass strut body heat leaks computed for analysis case number 1. Total composite heat leaks for analysis case numbers 8 through 10 and 12 through 16 were obtained in a similar manner. Heat leaks were not computed for analysis case number 11, since this case was eliminated in the structural analysis (Ref Section 3.1.5).

Table C-1

SUMMARY OF HEAT LEAKS FOR MONOCOQUE FIBERGLASS CYLINDERS WITH A 12-MIL (0.30-MM) LONGO WRAP THICKNESS

Analysis Case No. 1 (Ref Table 3-2); $A_{\ell}/A_{cr} = 1.0$

T_{H1} = 520°R (289°K); T_{C1} = 37°R (20°K); T_{H2} = 400°R (222°K); T_{C2} = 140°R (78°K)

k_{c1} = 0.238 Btu/hr ft°R (4.12×10^{-3} W/cm°K) for $T_{H1} - T_{C1}$ = 483°R (268.3°K)

k_{c2} = 0.233 Btu/hr ft°R (4.03×10^{-3} W/cm°K) for $T_{H2} - T_{C2}$ = 260°R (144.4°K)

Strut Length, L_s		Composite Length, L_c		Outside Diameter, D_c		Composite Area, A_c		Composite Heat Leaks			
								Q_{c1}		Q_{c2}	
in.	(cm)	ft.	(cm)	in.	(cm)	$ft^2 \times 10^3$	(cm^2)	Btu/hr x 10^2	(W x 10^2)	Btu/hr x 10^2	(W x 10^2)
18	(45.7)	1.0	(30.5)	1.5	(3.81)	0.785	(0.729)	9.02	(2.64)	4.76	(1.39)
				1.75	(4.45)	0.917	(0.852)	10.5	(3.07)	5.55	(1.63)
				2.0	(5.08)	1.05	(0.975)	12.1	(3.54)	6.36	(1.86)
				2.25	(5.72)	1.18	(1.10)	13.6	(3.98)	7.16	(2.10)
				2.5	(6.35)	1.31	(1.22)	15.1	(4.42)	7.94	(2.32)
				2.75	(6.99)	1.44	(1.34)	16.6	(4.86)	8.73	(2.56)
				3.0	(7.62)	1.56	(1.45)	17.9	(5.24)	9.45	(2.77)
				3.25	(8.26)	1.70	(1.58)	19.6	(5.74)	10.3	(3.02)
29	(73.7)	1.917	(58.4)	1.5	(3.81)	0.785	(0.729)	4.69	(1.37)	2.47	(0.723)
				1.75	(4.45)	0.917	(0.852)	5.44	(1.59)	2.90	(0.849)
				2.0	(5.08)	1.05	(0.975)	6.29	(1.84)	3.31	(0.969)
				2.25	(5.72)	1.18	(1.10)	7.07	(2.07)	3.73	(1.09)
				2.5	(6.35)	1.31	(1.22)	7.84	(2.30)	4.13	(1.21)
				2.75	(6.99)	1.44	(1.34)	8.64	(2.53)	4.55	(1.33)
				3.0	(7.62)	1.56	(1.45)	9.36	(2.74)	4.93	(1.44)
				3.25	(8.26)	1.70	(1.58)	10.2	(2.99)	5.37	(1.57)
40	(101.6)	2.833	(86.4)	1.5	(3.81)	0.785	(0.729)	3.09	(0.905)	1.63	(0.477)
				1.75	(4.45)	0.917	(0.852)	3.61	(1.06)	1.91	(0.559)
				2.0	(5.08)	1.05	(0.975)	4.14	(1.21)	2.18	(0.638)
				2.25	(5.72)	1.18	(1.10)	4.65	(1.36)	2.45	(0.717)
				2.5	(6.35)	1.31	(1.22)	5.17	(1.51)	2.73	(0.799)
				2.75	(6.99)	1.44	(1.34)	5.85	(1.71)	3.08	(0.902)
				3.0	(7.62)	1.56	(1.45)	6.33	(1.85)	3.34	(0.978)
				3.25	(8.26)	1.70	(1.58)	6.90	(2.02)	3.64	(1.07)

Table C-2

SUMMARY OF HEAT LEAKS FOR MONOCOQUE FIBERGLASS CYLINDERS WITH AN 18-MIL (0.46-MM) LONGO WRAP THICKNESS

Analysis Case No. 2 (Ref Table 3-2); $A\ell/A_{cr} = 1.5$

$T_{H1} = 520°R$ (289°K); $T_{C1} = 37°R$ (20°K); $T_{H2} = 400°R$ (222°K); $T_{C2} = 140°R$ (78°K)

$k_{c1} = 0.248$ Btu/hr ft°R (4.29×10^{-3} W/cm°K) for $T_{H1} - T_{C1} = 483°R$ (268.3°K)

$k_{c2} = 0.243$ Btu/hr ft°R (4.21×10^{-3} W/cm°K) for $T_{H2} - T_{C2} = 260°R$ (144.4°K)

Strut Length, L_s		Composite Length, L_c		Outside Diameter, D_o		Composite Area, A_c		Composite Heat Leaks			
								Q_{c1}		Q_{c2}	
in.	(cm)	ft.	(cm)	in.	(cm)	$ft^2 x10^3$	(cm^2)	Btu/ $hr x10^2$	($Wx10^2$)	Btu/ $hr x10^2$	($Wx10^2$)
18	(45.7)	1.0	(30.5)	1.5	(3.81)	0.981	(0.911)	11.8	(3.46)	6.21	(1.82)
				1.75	(4.45)	1.15	(1.07)	13.8	(4.04)	7.26	(2.13)
				2.0	(5.08)	1.31	(1.22)	15.7	(4.60)	8.29	(2.43)
				2.25	(5.72)	1.48	(1.37)	17.7	(5.18)	9.35	(2.74)
				2.5	(6.35)	1.63	(1.51)	19.5	(5.71)	10.3	(3.02)
				2.75	(6.99)	1.78	(1.65)	21.4	(6.27)	11.2	(3.28)
29	(73.7)	1.917	(58.4)	1.5	(3.81)	0.981	(0.911)	6.11	(1.79)	3.23	(0.946)
				1.75	(4.45)	1.15	(1.07)	7.17	(2.10)	3.78	(1.11)
				2.0	(5.08)	1.31	(1.22)	8.16	(2.39)	4.31	(1.26)
				2.25	(5.72)	1.48	(1.37)	9.24	(2.71)	4.88	(1.43)
				2.5	(6.35)	1.63	(1.51)	10.2	(2.99)	5.37	(1.57)
				2.75	(6.99)	1.78	(1.65)	11.1	(3.25)	5.87	(1.72)
40	(101.6)	2.833	(86.4)	1.5	(3.81)	0.981	(0.911)	4.02	(1.18)	2.13	(0.624)
				1.75	(4.45)	1.15	(1.07)	4.71	(1.38)	2.49	(0.729)
				2.0	(5.08)	1.31	(1.22)	5.38	(1.58)	2.85	(0.834)
				2.25	(5.72)	1.48	(1.37)	6.07	(1.78)	3.20	(0.937)
				2.5	(6.35)	1.63	(1.51)	6.69	(1.96)	3.54	(1.04)
				2.75	(6.99)	1.78	(1.65)	7.53	(2.20)	3.97	(1.16)

Table C-3

SUMMARY OF HEAT LEAKS FOR MONOCOQUE FIBERGLASS CYLINDERS WITH A 24-MIL (0.61-MM) LONGO WRAP THICKNESS

Analysis Case No. 3 (Ref Table 3-2); $A\ell/A_{cr} = 2.0$

T_{H1} = 520°R (289°K); T_{C1} = 37°R (20°K; T_{H2} = 400°R (222°K); T_{C2} = 140°R (78°K)

k_{c1} = 0.256 Btu/hr ft°R (4.43×10^{-3} W/cm°K) for $T_{H1} - T_{C1}$ = 483°R (268.3°K)

k_{c2} = 0.250 Btu/hr ft°R (4.33×10^{-3} W/cm°K) for $T_{H2} - T_{C2}$ = 260°R (144.4°K)

Strut Length, L_s		Composite Length, L_c		Outside Diameter, D_o		Composite Area, A_c		Composite Heat Leaks			
								Q_{c1}		Q_{c2}	
in	(cm)	ft.	(cm)	in.	(cm)	$ft^2 x10^3 (cm^2)$		Btu/ $hr x10^2$	$(W x10^2)$	Btu/ $hr x10^2$	$(W x10^2)$
18	(45.7)	1.0	(30.5)	1.5	(3.81)	1.17	(1.09)	14.5	(4.25)	7.61	(2.23)
				1.75	(4.45)	1.38	(1.28)	17.1	(5.01)	8.97	(2.63)
				2.0	(5.08)	1.57	(1.46)	19.4	(5.68)	10.2	(2.99)
				2.25	(5.72)	1.77	(1.64)	21.9	(6.41)	11.5	(3.37)
				2.5	(6.35)	1.96	(1.82)	24.2	(7.09)	12.8	(3.75)
				2.75	(6.99)	2.16	(2.01)	26.7	(7.82)	14.0	(4.10)
29	(73.7)	1.917	(58.4)	1.5	(3.81)	1.17	(1.09)	7.52	(2.20)	3.96	(1.16)
				1.75	(4.45)	1.38	(1.28)	8.87	(2.60)	4.67	(1.37)
				2.0	(5.08)	1.57	(1.46)	10.1	(2.96)	5.32	(1.56)
				2.25	(5.72)	1.77	(1.64)	11.4	(3.34)	5.99	(1.75)
				2.50	(6.35)	1.96	(1.82)	12.6	(3.69)	6.64	(1.94)
				2.75	(6.99)	2.16	(2.01)	13.9	(4.07)	7.31	(2.14)
40	(101.6)	2.833	(86.4)	1.5	(3.81)	1.17	(1.09)	4.96	(1.45)	2.61	(0.764)
				1.75	(4.45)	1.38	(1.28)	5.85	(1.71)	3.07	(0.899)
				2.0	(5.08)	1.57	(1.46)	6.64	(1.94)	3.49	(1.02)
				2.25	(5.72)	1.77	(1.64)	7.52	(2.20)	3.95	(1.16)
				2.5	(6.35)	1.96	(1.82)	8.32	(2.44)	4.38	(1.28)
				2.75	(6.99)	2.16	(2.01)	9.17	(2.68)	4.81	(1.41)

Table C-4

SUMMARY OF HEAT LEAKS FOR MONOCOQUE FIBERGLASS
OGIVES WITH A 12-MIL (0.30-MM) LONGO WRAP THICKNESS AT MIDSPAN

Analysis Case No. 4 (Ref Table 3-2); T_{H1} = 520°R (289°K); T_{C1} = 37°R (20°K); T_{H2} = 400°R (222°K); T_{C2} = 140°R (78°K)

See Table C-1 for Values of A_ℓ/A_{cr}, k_{c1}, k_{c2}, and A_c at Midspan; D_{oe} = 1.5 in. (3.81 cm)

Strut Length, L_s		Composite Length, L_c		Outside Dia at Midspan, D_{om}		A_ℓ/A_{cr} at Ends	Average of Values at Midspan and at Ends						Average Composite Heat Leaks			
							k_{c1}		k_{c2}		Area, A_c		Q_{c1}		Q_{c2}	
in.	(cm)	ft.	(cm)	in.	(cm)		Btu/ hr ft°R x 10^3	(W/cm°K)	Btu/ hr ft°R x 10^3	(W/cm°K)	$ft^2 x10^3$	(cm^2)	Btu/ $hr x10^2$	($Wx10^2$)	Btu/ $hr x10^2$	($Wx10^2$)
18	(45.7)	1.0	(30.5)	1.5	(3.81)	1.0	0.238	(4.12)	0.233	(4.03)	0.785	(0.729)	9.02	(2.64)	4.76	(1.39)
				1.75	(4.45)	1.17	0.240	(4.15)	0.235	(4.07)	0.885	(0.822)	10.3	(3.02)	5.41	(1.58)
				2.0	(5.08)	1.33	0.242	(4.19)	0.237	(4.10)	0.985	(0.915)	11.5	(3.37)	6.07	(1.78)
				2.25	(5.72)	1.5	0.243	(4.21)	0.238	(4.12)	1.08	(1.00)	12.7	(3.72)	6.68	(1.96)
				2.5	(6.35)	1.67	0.245	(4.24)	0.239	(4.14)	1.18	(1.10)	14.0	(4.10)	7.33	(2.15)
				2.75	(6.99)	1.83	0.246	(4.26)	0.241	(4.17)	1.28	(1.19)	15.2	(4.45)	8.02	(2.35)
				3.0	(7.62)	2.0	0.247	(4.28)	0.242	(4.19)	1.37	(1.27)	16.3	(4.77)	8.62	(2.52)
				3.25	(8.26)	2.16	0.248	(4.29)	0.243	(4.21)	1.47	(1.37)	17.6	(5.15)	9.29	(2.72)
				3.5	(8.89)	2.33	0.249	(4.31)	0.244	(4.22)	1.61	(1.50)	19.4	(5.68)	10.2	(2.99)
29	(73.7)	1.917	(58.4)	1.5	(3.81)	1.0	0.238	(4.12)	0.233	(4.03)	0.785	(0.729)	4.71	(1.38)	2.49	(0.729)
				1.75	(4.45)	1.17	0.240	(4.15)	0.235	(4.07)	0.885	(0.822)	5.35	(1.57)	2.83	(0.829)
				2.0	(5.08)	1.33	0.242	(4.19)	0.237	(4.10)	0.985	(0.915)	6.01	(1.76)	3.17	(0.928)
				2.25	(5.72)	1.5	0.243	(4.21)	0.238	(4.12)	1.08	(1.00)	6.61	(1.94)	3.50	(1.02)
				2.5	(6.35)	1.67	0.245	(4.24)	0.239	(4.14)	1.18	(1.10)	7.29	(2.13)	3.84	(1.12)
				2.75	(6.99)	1.83	0.246	(4.26)	0.241	(4.17)	1.28	(1.19)	7.93	(2.32)	4.20	(1.23)
				3.0	(7.62)	2.0	0.247	(4.28)	0.242	(4.19)	1.37	(1.27)	8.53	(2.50)	4.51	(1.32)
				3.25	(8.26)	2.16	0.248	(4.29)	0.243	(4.21)	1.47	(1.37)	9.19	(2.69)	4.86	(1.42)
				3.5	(8.89)	2.33	0.249	(4.31)	0.244	(4.22)	1.61	(1.50)	10.1	(2.96)	5.34	(1.56)
40	(101.6)	2.833	(86.4)	1.5	(3.81)	1.0	0.238	(4.12)	0.233	(4.03)	0.785	(0.729)	3.19	(0.934)	1.68	(0.492)
				1.75	(4.45)	1.17	0.240	(4.15)	0.235	(4.07)	0.885	(0.822)	3.63	(1.06)	1.91	(0.559)
				2.0	(5.08)	1.33	0.242	(4.19)	0.237	(4.10)	0.985	(0.915)	4.08	(1.19)	2.14	(0.627)
				2.25	(5.72)	1.5	0.243	(4.21)	0.238	(4.12)	1.08	(1.00)	4.49	(1.31)	2.36	(0.691)
				2.5	(6.35)	1.67	0.245	(4.24)	0.239	(4.14)	1.18	(1.10)	4.94	(1.45)	2.59	(0.758)
				2.75	(6.99)	1.83	0.246	(4.26)	0.241	(4.17)	1.28	(1.19)	5.38	(1.58)	2.83	(0.829)
				3.0	(7.62)	2.0	0.247	(4.28)	0.242	(4.19)	1.37	(1.27)	5.79	(1.70)	3.04	(0.890)
				3.25	(8.26)	2.16	0.248	(4.29)	0.243	(4.21)	1.47	(1.37)	6.23	(1.82)	3.28	(0.960)
				3.5	(8.89)	2.33	0.249	(4.31)	0.244	(4.22)	1.61	(1.50)	6.86	(2.01)	3.61	(1.06)

Table C-5

SUMMARY OF HEAT LEAKS FOR MONOCOQUE FIBERGLASS
OGIVES WITH AN 18-MIL (0.46-MM) LONGO WRAP THICKNESS AT MIDSPAN

Analysis Case No. 5 (Ref Table 3-2); T_{H1} = 520°R (289°K); T_{C1} = 37°R (20°K);
T_{H2} = 400°R (222°K); T_{C2} = 140°R (78°K)

See Table C-2 for Values of $A\ell/A_{cr}$, k_{c1}, k_{c2}, and A_c at Midspan; D_{oe} = 1.5 in. (3.81 cm)

Strut Length, L_s		Composite Length, L_c		Outside Dia at Midspan, D_{om}		$A\ell/A_{cr}$ at Ends	Average of Values at Midspan and at Ends				Average Composite Heat Leaks			
							k_{c1}		k_{c2}		Area, A_c		Q_{c1}		Q_{c2}	
in.	(cm)	ft.	(cm)	in.	(cm)		Btu/hr ft°R	(W/cm°K x 10^3)	Btu/hr ft°R	(W/cm°K x 10^3)	$ft^2 x 10^3$	(cm^2)	Btu/hr x 10^2	(W x 10^2)	Btu/hr x 10^2	(W x 10^2)
18	(45.7)	1.0	(30.5)	1.5	(3.81)	1.5	0.248	(4.29)	0.243	(4.21)	0.981	(0.911)	11.8	(3.46)	6.20	(1.82)
				1.75	(4.45)	1.75	0.250	(4.33)	0.245	(4.24)	1.12	(1.04)	13.5	(3.95)	7.13	(2.09)
				2.0	(5.08)	2.0	0.252	(4.36)	0.247	(4.28)	1.24	(1.15)	15.1	(4.42)	7.96	(2.33)
				2.25	(5.72)	2.25	0.253	(4.38)	0.248	(4.29)	1.38	(1.28)	16.9	(4.95)	8.90	(2.61)
				2.50	(6.35)	2.5	0.255	(4.41)	0.249	(4.31)	1.50	(1.39)	18.5	(5.42)	9.71	(2.84)
				2.75	(6.99)	2.75	0.256	(4.43)	0.251	(4.34)	1.62	(1.50)	20.0	(5.86)	10.6	(3.10)
				3.0	(7.62)	3.0	0.257	(4.45)	0.252	(4.36)	1.74	(1.62)	21.6	(6.32)	11.4	(3.34)
29	(73.7)	1.917	(58.4)	1.5	(3.81)	1.5	0.248	(4.29)	0.243	(4.21)	0.981	(0.911)	6.13	(1.79)	3.24	(0.949)
				1.75	(4.45)	1.75	0.250	(4.33)	0.245	(4.24)	1.12	(1.04)	7.06	(2.07)	3.73	(1.09)
				2.0	(5.08)	2.0	0.252	(4.36)	0.247	(4.28)	1.24	(1.15)	7.87	(2.30)	4.17	(1.22)
				2.25	(5.72)	2.25	0.253	(4.38)	0.248	(4.29)	1.38	(1.28)	8.80	(2.58)	4.65	(1.36)
				2.5	(6.35)	2.5	0.255	(4.41)	0.249	(4.31)	1.50	(1.39)	9.64	(2.82)	5.08	(1.49)
				2.75	(6.99)	2.75	0.256	(4.43)	0.251	(4.34)	1.62	(1.50)	10.5	(3.07)	5.53	(1.62)
				3.0	(7.62)	3.0	0.257	(4.45)	0.252	(4.36)	1.74	(1.62)	11.3	(3.31)	5.96	(1.75)
40	(101.6)	2.833	(86.4)	1.5	(3.81)	1.5	0.248	(4.29)	0.243	(4.21)	0.981	(0.911)	4.16	(1.22)	2.20	(0.644)
				1.75	(4.45)	1.75	0.250	(4.33)	0.245	(4.24)	1.12	(1.04)	4.79	(1.40)	2.52	(0.738)
				2.0	(5.08)	2.0	0.252	(4.36)	0.247	(4.28)	1.24	(1.15)	5.34	(1.56)	2.81	(0.823)
				2.25	(5.72)	2.25	0.253	(4.38)	0.248	(4.29)	1.38	(1.28)	5.97	(1.75)	3.14	(0.919)
				2.5	(6.35)	2.5	0.255	(4.41)	0.249	(4.31)	1.50	(1.39)	6.54	(1.91)	3.43	(1.00)
				2.75	(6.99)	2.75	0.256	(4.43)	0.251	(4.34)	1.62	(1.50)	7.09	(2.08)	3.73	(1.09)
				3.0	(7.62)	3.0	0.257	(4.45)	0.252	(4.36)	1.74	(1.62)	7.65	(2.24)	4.03	(1.18)

Table C-6

SUMMARY OF HEAT LEAKS FOR MONOCOQUE FIBERGLASS
OGIVES WITH A 24-MIL (0.61-MM) LONGO WRAP THICKNESS AT MIDSPAN

Analysis Case No. 6 (Ref Table 3-2); T_{H1} = 520°R (289°K); T_{C1} = 37°R (20°K);
T_{H2} = 400°R (222°K); T_{C2} = 140°R (78°K)

See Table C-3 for Values of A_ℓ/A_{cr}, k_{c1}, k_{c2}, and A_c at Midspan; D_{oe} = 1.5 in. (3.81 cm)

Strut Length, L_s		Composite Length, L_c		Outside Dia at Midspan, D_{cm}		A_ℓ/A_{cr} at Ends	Average of Values at Midspan and at Ends						Average Composite Heat Leaks			
							k_{c1}		k_{c2}		Area, A_c		Q_{c1}		Q_{c2}	
in.	(cm)	ft.	(cm)	in.	(cm)		Btu/ hr ft°R	(W/cm°K x 10^3)	Btu/ hr ft°R	(W/cm°K x 10^3)	$ft^2 x 10^3$	(cm^2)	Btu/ $hr x 10^2$	($W x 10^2$)	Btu/ $hr x 10^2$	($W x 10^2$)
18	(45.7)	1.0	(30.5)	1.5	(3.81)	2.0	0.256	(4.43)	0.250	(4.33)	1.17	(1.09)	14.5	(4.25)	7.61	(2.23)
				1.75	(4.45)	2.33	0.258	(4.47)	0.252	(4.36)	1.35	(1.25)	16.8	(4.92)	8.85	(2.59)
				2.0	(5.08)	2.67	0.260	(4.50)	0.254	(4.40)	1.51	(1.40)	19.0	(5.56)	9.97	(2.92)
				2.25	(5.72)	3.0	0.261	(4.52)	0.255	(4.41)	1.67	(1.55)	21.1	(6.18)	11.1	(3.25)
				2.5	(6.35)	3.33	0.262	(4.54)	0.256	(4.43)	1.83	(1.70)	23.2	(6.79)	12.2	(3.57)
				2.75	(6.99)	3.67	0.264	(4.57)	0.258	(4.47)	2.0	(1.86)	25.5	(7.47)	13.4	(3.92)
29	(73.7)	1.917	(58.4)	1.5	(3.81)	2.0	0.256	(4.43)	0.250	(4.33)	1.17	(1.09)	7.55	(2.21)	3.98	(1.17)
				1.75	(4.45)	2.33	0.258	(4.47)	0.252	(4.36)	1.35	(1.25)	8.78	(2.57)	4.63	(1.36)
				2.0	(5.08)	2.67	0.260	(4.50)	0.254	(4.40)	1.51	(1.40)	9.89	(2.90)	5.22	(1.53)
				2.25	(5.72)	3.0	0.261	(4.52)	0.255	(4.41)	1.67	(1.55)	11.0	(3.22)	5.79	(1.70)
				2.5	(6.35)	3.33	0.262	(4.54)	0.256	(4.43)	1.83	(1.70)	12.1	(3.54)	6.37	(1.87)
				2.75	(6.99)	3.67	0.264	(4.57)	0.258	(4.47)	2.0	(1.86)	13.3	(3.89)	7.02	(2.06)
40	(101.6)	2.833	(86.4)	1.5	(3.81)	2.0	0.256	(4.43)	0.250	(4.33)	1.17	(1.09)	5.12	(1.50)	2.69	(0.788)
				1.75	(4.45)	2.33	0.258	(4.47)	0.252	(4.36)	1.35	(1.25)	5.96	(1.75)	3.12	(0.914)
				2.0	(5.08)	2.67	0.260	(4.50)	0.254	(4.40)	1.51	(1.40)	6.71	(1.96)	3.52	(1.03)
				2.25	(5.72)	3.0	0.261	(4.52)	0.255	(4.41)	1.67	(1.55)	7.45	(2.18)	3.91	(1.14)
				2.5	(6.35)	3.33	0.262	(4.54)	0.256	(4.43)	1.83	(1.70)	8.20	(2.40)	4.30	(1.26)
				2.75	(6.99)	3.67	0.264	(4.57)	0.258	(4.47)	2.0	(1.86)	9.03	(2.64)	4.74	(1.39)

Table C-7

SUMMARY OF HEAT LEAKS FOR MONOCOQUE FIBERGLASS-BORON CYLINDERS

Analysis Case No. 7 (Ref Table 3-2)

T_{H1} = 520°R (289°K); T_{C1} = 37°R (20°K); T_{H2} = 400°R (222°K); T_{C2} = 140°R (78°K)

k_{cb1} = 1.264 Btu/hr ft°R (2.188 x 10^{-2} W/cm°K) for $T_{H1} - T_{C1}$ = 483°R (268.3°K)

k_{cb2} = 1.262 Btu/hr ft°R (2.185 x 10^{-2} W/cm°K) for $T_{H2} - T_{C2}$ = 260°R (144.4°K)

See Table C-1 for Values of k_{c1}, k_{c2}, A_c, Q_{c1}, and Q_{c2}

Strut Length, L_s	Composite Length, L_c	Outside Diameter, D_o	Composite Boron Area, A_{cb}	Total Composite Heat Leaks	
				$Q_{c1} + Q_{cb1}$	$Q_{c2} + Q_{cb2}$
in. (cm)	ft. (cm)	in. (cm)	$ft^2 x10^3 (cm^2)$	Btu/hr x10^2 (W x10^2)	Btu/hr x10^2 (W x10^2)
18 (45.7)	1.0 (30.5)	1.5 (3.81)	0.156 (0.145)	18.5 (5.42)	9.88 (2.89)
		1.75 (4.45)	0.181 (0.168)	21.6 (6.32)	11.5 (3.37)
		2.0 (5.08)	0.208 (0.193)	24.8 (7.26)	13.2 (3.86)
		2.25 (5.72)	0.233 (0.216)	27.8 (8.14)	14.8 (4.33)
29 (73.7)	1.917 (58.4)	1.5 (3.81)	0.156 (0.145)	9.64 (2.82)	5.13 (1.50)
		1.75 (4.45)	0.181 (0.168)	11.2 (3.28)	5.98 (1.75)
		2.0 (5.08)	0.208 (0.193)	12.9 (3.78)	6.88 (2.01)
		2.25 (5.72)	0.233 (0.216)	14.5 (4.25)	7.73 (2.26)
40 (101.6)	2.833 (86.4)	1.5 (3.81)	0.156 (0.145)	6.45 (1.89)	3.43 (1.00)
		1.75 (4.45)	0.181 (0.168)	7.52 (2.20)	4.01 (1.17)
		2.0 (5.08)	0.208 (0.193)	8.60 (2.52)	4.58 (1.34)
		2.25 (5.72)	0.233 (0.216)	9.66 (2.83)	5.14 (1.50)

Table C-8

SUMMARY OF HEAT LEAKS FOR GLASS-STIFFENED FIBERGLASS CYLINDERS

Analysis Case Numbers 8, 9, and 10 (Ref Table 3-2); A_{gs} = 0.0025 in.^{2} (0.0161 cm^2)

T_{H1} = 520°R (289°K); T_{C1} = 37°R (20°K); T_{H2} = 400°R (222°K); T_{C2} = 140°R (78°K)

k_{gs1} = 0.288 Btu/hr ft°R (4.99 x 10^{-3} W/cm°K) for $T_{H1} - T_{C1}$ = 483°R (268.3°K)

k_{gs2} = 0.283 Btu/hr ft°R (4.90 x 10^{-3} W/cm°K) for $T_{H2} - T_{C2}$ = 260°R (144.4°K)

See Tables C-1 and C-2 for Values of k_{c1}, k_{c2}, A_c, Q_{c1}, and Q_{c2}

Strut Length, L_s in. (cm)	Composite Length, L_c ft. (cm)	Outside Diameter, D_o in. (cm)	Optimum Number of Longerons, N_o	Glass Longeron Area, A_{gs} ft^{2}x10^3(cm^2)	Total Composite Heat Leaks $Q_{c1} + Q_{gs1}$ Btu/hrx10^2 (Wx10^2)	$Q_{c2} + Q_{gs2}$ Btu/hrx10^2 (Wx10^2)
(1) 18 (45.7)	1.0 (30.5)	1.5 (3.81)	17	0.296 (0.275)	13.1 (3.84)	6.94 (2.03)
		1.75 (4.45)	23	0.400 (0.372)	16.1 (4.71)	8.49 (2.49)
		2.0 (5.08)	30	0.522 (0.485)	19.4 (5.68)	10.2 (2.99)
		2.25 (5.72)	37	0.644 (0.598)	22.6 (6.62)	11.9 (3.48)
(1) 29 (73.7)	1.917(58.4)	2.0 (5.08)	18	0.313 (0.291)	8.56 (2.51)	4.51 (1.32)
		2.25 (5.72)	23	0.400 (0.372)	9.98 (2.92)	5.27 (1.54)
		2.5 (6.35)	29	0.505 (0.469)	11.5 (3.37)	6.07 (1.78)
(1) 40 (101.6)	2.833(86.4)	2.5 (6.35)	20	0.348 (0.323)	6.88 (2.01)	3.64 (1.07)
		3.0 (7.62)	30	0.522 (0.485)	8.89 (2.60)	4.69 (1.37)
(2) 40 (101.6)	2.833(86.4)	2.5 (6.35)	16	0.278 (0.258)	8.05 (2.36)	4.26 (1.25)
		3.0 (7.62)	26	0.452 (0.420)	10.4 (3.05)	5.51 (1.61)

Notes: (1) Cylinders with a 12-mil (0.30-mm) longo wrap thickness.
(2) Cylinders with an 18-mil (0.46-mm) longo wrap thickness.

Table C-9

SUMMARY OF HEAT LEAKS FOR BORON-STIFFENED FIBERGLASS CYLINDERS

Analysis Case Numbers 12, 13, and 14 (Ref Table 3-2); A_{bs} = 0.0016 in.^{2}(0.0103 cm^2)
T_{H1} = 520°R (289°K); T_{C1} = 37°R (20°K); T_{H2} = 400°R (222°K); T_{C2} = 140°R (78°K)
k_{bs1} = 1.264 Btu/hr ft°R (2.188 x 10^{-2} W/cm°K) for $T_{H1} - T_{C1}$ = 483°R (268.3°K)
k_{bs2} = 1.262 Btu/hr ft°R (2.185 x 10^{-2} W/cm°K) for $T_{H2} - T_{C2}$ = 260°R (144.4°K)
See Table C-1 for Values of k_{c1}, k_{c2}, A_c, Q_{c1}, and Q_{c2}

Strut Length, L_s	Composite Length, L_c	Outside Diameter, D_o	Number of Longerons, N	Boron Longeron Area, A_{bs}	Total Composite Heat Leaks	
					$Q_{c1} + Q_{bs1}$	$Q_{c2} + Q_{bs2}$
in. (cm)	ft. (cm)	in. (cm)		$ft^2 x10^3 (cm^2)$	Btu/hr$x10^2$ (W$x10^2$)	Btu/hr$x10^2$ (W$x10^2$)
18 (45.7)	1.0 (30.5)	1.5 (3.81)	4	0.044 (0.041)	11.7 (3.43)	6.20 (1.82)
			8	0.089 (0.083	14.5 (4.25)	7.68 (2.25)
			12	0.133 (0.124)	17.1 (5.01)	9.12 (2.67)
			16	0.178 (0.165)	19.9 (5.83)	10.6 (3.10)
29 (73.7)	1.917(58.4)	1.94 (4.93)	4	0.044 (0.041)	7.45 (2.18)	3.95 (1.16)
			8	9.089 (0.083)	8.86 (2.59)	4.71 (1.38)
			12	0.133 (0.124)	10.3 (3.02)	5.46 (1.60)
			16	0.178 (0.165)	11.7 (3.43)	6.25 (1.83)
40 (101.6)	2.833(86.4)	2.40 (6.10)	4	0.044 (0.041)	6.00 (1.76)	3.18 (0.931)
			8	0.089 (0.083)	6.91 (2.02)	3.68 (1.08)
			12	0.133 (0.124)	7.89 (2.31)	4.20 (1.23)
			16	0.178 (0.165)	8.87 (2.60)	4.73 (1.38)

Table C-10

SUMMARY OF HEAT LEAKS FOR BORON-STIFFENED FIBERGLASS OGIVES

Analysis Case Numbers 15 and 16 (Ref Table 3-2); A_{bs} = 0.0016 in.^{2} (0.0103 cm^2)

T_{H1} = 520°R (289°K); T_{C1} = 37°R (20°K); T_{H2} = 400°R (222°K); T_{C2} = 140°R (78°K)

k_{bs1} = 1.264 Btu/hr ft°R (2.188 x 10^{-2} W/cm°K) for $T_{H1} - T_{C1}$ = 483°R (268.3°K)

k_{bs2} = 1.262 Btu/hr ft°R (2.185 x 10^{-2} W/cm°K) for $T_{H2} - T_{C2}$ = 260°K (144.4°K)

See Table C-4 for Values of k_{c1}, k_{c2}, A_c, Q_{c1}, and Q_{c2}

Strut Length, L_s	Composite Length, L_c	Outside Diameter, D_o	Number of Longerons, N	Boron Longeron Area, A_{bs}	Total Composite Heat Leaks	
					$Q_{c1} + Q_{bs1}$	$Q_{c2} + Q_{bs2}$
in. (cm)	ft. (cm)	in. (cm)		$ft^2 x 10^3 (cm^2)$	Btu/hr x 10^2 (W x 10^2)	Btu/hr x 10^2 (W x 10^2)
29 (73.7)	1.917(58.4)	1.96 (4.98)	4	0.044 (0.041)	7.25 (2.12)	3.87 (1.13)
			8	0.089 (0.083)	8.66 (2.54)	4.63 (1.36)
			12	0.133 (0.124)	10.1 (2.96)	5.38 (1.58)
			16	0.178 (0.165)	11.5 (3.37)	6.17 (1.81)
40 (101.6)	2.833(86.4)	2.46 (6.25)	4	0.044 (0.041)	5.81 (1.70)	3.05 (0.893)
			8	0.089 (0.083)	6.72 (1.97)	3.55 (1.04)
			12	0.133 (0.124)	7.70 (2.25)	4.07 (1.19)
			16	0.178 (0.165)	8.68 (2.54)	4.60 (1.35)

Appendix D

CALCULATION OF COMPARATIVE SYSTEM WEIGHTS

Comparative system weights for fifteen strut configuration analysis cases (Ref Table 3-2), each applied where appropriate to nine load-length design points, were computed in Task 1. Summaries of these weights are presented in Tables D-1 and D-2. In addition to the total system weights, component weights are also shown for the strut body and stiffeners, end fittings, core insulation, external insulation, and boiloff. A storage time of 200 days was assumed in computing boiloff weights for both liquid hydrogen and liquid fluorine propellants, which correspond to boundary temperature cases 1 and 2, respectively.

Strut body and stiffener weights were computed as the product of the average cross-sectional composite area, total strut length less 3 in. (7.6 cm), and the composite densities given in Section 3.1.8. End fitting weights used in the analysis were those presented in Table 3-3. Core insulation volume was obtained by multiplying the average cross-sectional area of the core cavity by total strut length less 3 in. (7.6 cm). The core insulation density was assumed to be 2.0 lbm/ft^3 (32.0 kg/m^3) (Ref Section 3.1.8). External insulation weight was determined using the strut circumference at midspan, total strut length, an assumed thickness of 0.5 in. (1.27 cm), and a density of 1.2 lbm/ft^3 (19.2 kg/m^3) (Ref Section 3.1.8). Finally, boiloff weights were computed as the product of heat leak (Ref Section 3.1.7 and Appendix C) and storage time divided by the latent heat of vaporization given for the stored cryogen in Section 3.1.8.

Table D-1

SUMMARY OF COMPARATIVE SYSTEM WEIGHTS FOR ANALYSIS CASES 1 THROUGH 6

Analysis Case No. (Ref Table 3-2)	1			2					
Strut Length, L_s, in. (cm)	18.0 (45.7)	29.0 (73.7)	40.0 (101.6)	18.0 (45.7)		29.0 (73.7)		40.0 (101.6)	
Ult Compressive Load, P_c, lbf (N)	980 (4360)	980 (4360)	980 (4360)	980 (4360)	4690 (20,860)	980 (4360)	4690 (20,860)	980 (4360)	4690 (20,860)
L_{sb}, in. (cm)	15 (38.1)	26 (66.0)	37 (94.0)	15 (38.1)	15 (38.1)	26 (66.0)	26 (66.0)	37 (94.0)	37 (94.0)
D_o, in. (cm)	1.5 (3.81)	1.5 (3.81)	1.58 (4.01)	1.5 (3.81)	1.5 (3.81)	1.5 (3.81)	1.90 (4.83)	1.5 (3.81)	2.32 (5.89)
W_{sb}, lbm (kg)	0.125 (0.057)	0.217 (0.098)	0.322 (0.146)	0.157 (0.071)	0.157 (0.071)	0.272 (0.123)	0.333 (0.151)	0.386 (0.175)	0.596 (0.270)
W_f, lbm (kg)	0.920 (0.417)	0.920 (0.417)	0.920 (0.417)	0.920 (0.417)	1.500 (0.680)	0.920 (0.417)	1.500 (0.680)	0.920 (0.417)	1.500 (0.680)
W_{ci}, lbm (kg)	0.030 (0.014)	0.053 (0.024)	0.081 (0.037)	0.030 (0.014)	0.030 (0.014)	0.053 (0.024)	0.079 (0.036)	0.075 (0.034)	0.178 (0.081)
W_{ei}, lbm (kg)	0.029 (0.013)	0.047 (0.021)	0.068 (0.031)	0.029 (0.013)	0.029 (0.013)	0.047 (0.021)	0.058 (0.026)	0.065 (0.029)	0.101 (0.046)
W_{ti}, lbm (kg)	1.104 (0.501)	1.237 (0.561)	1.391 (0.631)	1.136 (0.515)	1.716 (0.778)	1.292 (0.586)	1.970 (0.894)	1.446 (0.6559)	2.375 (1.077)
W_{bo1}, lbm (kg)	2.323 (1.054)	1.210 (0.549)	0.826 (0.375)	3.033 (1.376)	3.033 (1.376)	1.559 (0.707)	1.959 (0.889)	1.040 (0.472)	1.613 (0.732)
W_{bo2}, lbm (kg)	3.280 (1.486)	1.714 (0.777)	1.180 (0.535)	4.315 (1.957)	4.315 (1.957)	2.236 (1.014)	2.770 (1.256)	1.466 (0.665)	2.278 (1.033)
W_{ts1}, lbm (kg)	3.427 (1.552)	2.447 (1.110)	2.217 (1.006)	4.169 (1.891)	4.749 (2.154)	2.851 (1.293)	3.929 (1.782)	2.486 (1.128)	3.988 (1.809)
W_{ts2}, lbm (kg)	4.384 (1.986)	2.951 (1.339)	2.571 (1.166)	5.451 (2.473)	6.031 (2.736)	3.528 (1.600)	4.740 (2.150)	2.912 (1.321)	4.653 (2.111)

Analysis Case No. (Ref Table 3-2)	3								
Strut Length, L_s, in. (cm)	18.0 (45.7)			29.0 (73.7)			40.0 (101.6)		
Ult Compressive Load, P_c, lbf (N)	980 (4360)	4690 (20,860)	8400 (37,360)	980 (4360)	4690 (20,860)	8400 (37,360)	980 (4360)	4690 (20,860)	8400 (37,360)
L_{sb}, in. (cm)	15 (38.1)	15 (38.1)	15 (38.1)	26 (66.0)	26 (66.0)	26 (66.0)	37 (94.0)	37 (94.0)	37 (94.0)
D_o, in. (cm)	1.5 (3.81)	1.5 (3.81)	1.5 (3.81)	1.5 (3.81)	1.74 (4.42)	2.11 (5.36)	1.5 (3.81)	2.14 (5.44)	2.58 (6.55)
W_{sb}, lbm (kg)	0.188 (0.085)	0.188 (0.085)	0.188 (0.085)	0.326 (0.148)	0.372 (0.169)	0.448 (0.203)	0.464 (0.210)	0.647 (0.293)	0.799 (0.362)
W_f, lbm (kg)	0.920 (0.417)	1.500 (0.680)	2.340 (1.061)	0.920 (0.417)	1.500 (0.680)	2.340 (1.061)	0.920 (0.417)	1.500 (0.680)	2.340 (1.061)
W_{ci}, lbm (kg)	0.030 (0.014)	0.030 (0.014)	0.030 (0.014)	0.053 (0.024)	0.068 (0.031)	0.099 (0.045)	0.075 (0.034)	0.145 (0.066)	0.222 (0.101)
W_{ei}, lbm (kg)	0.029 (0.013)	0.029 (0.013)	0.029 (0.013)	0.047 (0.021)	0.055 (0.025)	0.066 (0.030)	0.065 (0.029)	0.093 (0.042)	0.111 (0.050)
W_{ti}, lbm (kg)	1.167 (0.529)	1.747 (0.792)	2.587 (1.173)	1.346 (0.611)	1.995 (0.905)	2.953 (1.339)	1.524 (0.691)	2.385 (1.082)	3.472 (1.575)
W_{bo1}, lbm (kg)	3.670 (1.665)	3.670 (1.665)	3.670 (1.665)	1.936 (0.878)	2.220 (1.007)	2.671 (1.212)	1.280 (0.581)	1.809 (0.821)	2.220 (1.007)
W_{bo2}, lbm (kg)	5.290 (2.400)	5.290 (2.400)	5.290 (2.400)	2.696 (1.223)	3.140 (1.424)	3.775 (1.712)	1.812 (0.822)	3.220 (1.461)	3.132 (1.421)
W_{ts1}, lbm (kg)	4.837 (2.194)	5.417 (2.457)	6.257 (2.838)	3.282 (1.489)	4.215 (1.912)	5.624 (2.551)	2.804 (1.272)	4.194 (1.902)	5.692 (2.582)
W_{ts2}, lbm (kg)	6.457 (2.929)	7.037 (3.192)	7.877 (3.573)	4.042 (1.833)	5.135 (2.329)	6.728 (3.052)	3.336 (1.513)	5.605 (2.542)	6.604 (2.996)

Analysis Case No. (Ref Table 3-2)	4	5		6					
Strut Length, L_s, in. (cm)	40.0 (101.6)	29.0 (73.7)	40.0 (101.6)	18.0 (45.7)	29.0 (73.7)		40.0 (101.6)		
Ult Compressive Load, P_c, lbf (N)	980 (4360)	4690 (20,860)	4690 (20,860)	8400 (37,360)	4690 (20,860)	8400 (37,360)	4690 (20,860)	8400 (37,360)	
L_{sb}, in. (cm)	37 (94.0)	26 (66.0)	37 (94.0)	15 (38.1)	26 (66.0)	26 (66.0)	37 (94.0)	37 (94.0)	
D_{om}, in. (cm)	1.56 (3.96)	1.91 (4.85)	2.38 (6.05)	1.54 (3.91)	1.73 (4.39)	2.14 (5.44)	2.17 (5.51)	2.67 (6.78)	
W_{sb}, lbm (kg)	0.311 (0.141)	0.309 (0.140)	0.499 (0.226)	0.190 (0.086)	0.369 (0.167)	0.442 (0.200)	0.650 (0.295)	0.767 (0.348)	
W_f, lbm (kg)	0.920 (0.417)	1.500 (0.680)	1.500 (0.680)	2.340 (1.061)	1.500 (0.680)	2.340 (1.061)	1.500 (0.680)	2.340 (1.061)	
W_{ci}, lbm (kg)	0.175 (0.079)	0.060 (0.027)	0.097 (0.044)	0.030 (0.014)	0.136 (0.062)	0.171 (0.078)	0.255 (0.116)	0.320 (0.145)	
W_{ei}, lbm (kg)	0.068 (0.031)	0.060 (0.027)	0.104 (0.047)	0.030 (0.014)	0.054 (0.024)	0.067 (0.030)	0.094 (0.043)	0.115 (0.052)	
W_{ti}, lbm (kg)	1.474 (0.669)	1.929 (0.875)	2.200 (0.998)	2.590 (1.175)	2.059 (0.934)	3.020 (1.370)	2.499 (1.134)	3.542 (1.607)	
W_{bo1}, lbm (kg)	0.826 (0.375)	1.969 (0.893)	1.626 (0.738)	3.871 (1.756)	2.220 (1.007)	2.633 (1.194)	1.871 (0.849)	2.119 (0.961)	
W_{bo2}, lbm (kg)	1.188 (0.539)	2.772 (1.266)	2.313 (1.049)	5.488 (2.489)	3.140 (1.424)	3.620 (1.642)	2.667 (1.210)	3.012 (1.366)	
W_{ts1}, lbm (kg)	2.300 (1.043)	3.898 (1.768)	3.826 (1.735)	6.461 (2.931)	4.279 (1.941)	5.653 (2.564)	4.370 (1.982)	5.661 (2.568)	
W_{ts2}, lbm (kg)	2.662 (1.207)	4.721 (2.141)	4.513 (2.047)	8.078 (3.664)	5.199 (2.358)	6.640 (3.012)	5.166 (2.343)	6.554 (2.973)	

Table D-2

SUMMARY OF COMPARATIVE SYSTEM WEIGHTS FOR ANALYSIS CASES 7 THROUGH 10 AND 12 THROUGH 16

Analysis Case No. (Ref Table 3-2)	7								
Strut Length, L_s, in. (cm)	180.0 (45.7)			29.0 (73.7)			40.0 (101.6)		
Ult Compressive Load, P_C, lbf (N)	980 (4360)	4690 (20,860)	8400 (37,360)	980 (4360)	4690 (20,860)	8400 (37,360)	980 (4360)	4690 (20,860)	8400 (37,360)
L_{sb}, in. (cm)	15 (38.1)	15 (38.1)	15 (38.1)	26 (66.0)	26 (66.0)	26 (66.0)	37 (94.0)	37 (94.0)	37 (94.0)
D_o, in. (cm)	1.5 (3.81)	1.5 (3.81)	1.5 (3.81)	1.5 (3.81)	1.62 (4.11)	1.96 (4.98)	1.5 (3.81)	2.01 (5.11)	2.42 (6.15)
W_{sb}, lbm (kg)	0.149 (0.068)	0.149 (0.068)	0.149 (0.068)	0.257 (0.117)	0.278 (0.126)	0.335 (0.152)	0.366 (0.166)	0.491 (0.223)	0.591 (0.268)
W_f, lbm (kg)	0.920 (0.417)	1.500 (0.680)	2.340 (1.061)	0.920 (0.417)	1.500 (0.680)	2.340 (1.061)	0.920 (0.417)	1.500 (0.680)	2.340 (1.061)
W_{ci}, lbm (kg)	0.030 (0.014)	0.030 (0.014)	0.030 (0.014)	0.053 (0.024)	0.057 (0.026)	0.083 (0.038)	0.075 (0.034)	0.124 (0.056)	0.180 (0.082)
W_{ei}, lbm (kg)	0.029 (0.013)	0.029 (0.013)	0.029 (0.013)	0.047 (0.021)	0.051 (0.023)	0.062 (0.028)	0.065 (0.029)	0.087 (0.039)	0.105 (0.048)
W_{ti}, lbm (kg)	1.128 (0.512)	1.708 (0.775)	2.548 (1.156)	1.277 (0.579)	1.886 (0.855)	2.820 (1.279)	1.426 (0.647)	2.202 (0.999)	3.216 (1.459)
W_{bol}, lbm (kg)	4.745 (2.152)	4.745 (2.152)	4.745 (2.152)	2.450 (1.111)	2.646 (1.200)	2.760 (1.252)	1.677 (0.761)	2.248 (1.020)	2.704 (1.227)
W_{bo2}, lbm (kg)	6.875 (3.119)	6.875 (3.119)	6.875 (3.119)	3.654 (1.657)	3.946 (1.790)	4.721 (2.141)	2.430 (1.102)	3.273 (1.485)	3.974 (1.803)
W_{ts1}, lbm (kg)	5.873 (2.664)	6.453 (2.927)	7.293 (3.308)	3.727 (1.691)	4.532 (2.052)	5.580 (2.531)	3.103 (1.408)	4.450 (2.019)	5.920 (2.685)
W_{ts2}, lbm (kg)	8.003 (3.630)	8.583 (3.893)	9.423 (4.274)	4.931 (2.237)	5.832 (2.645)	7.541 (3.421)	3.856 (1.749)	5.475 (2.483)	7.190 (3.261)

Analysis Case No. (Ref Table 3-2)	8				9		10	12	
Strut Length, L_s, in. (cm)	18.0 (45.7)		29.0 (73.7)		40.0 (101.6)		40.0 (101.6)	18.0 (45.7)	
Ult Compressive Load, P_C, lbf (N)	4690 (20,860)	8400 (37,360)	4690 (20,860)	8400 (37,360)	4690 (20,860)	8400 (37,360)	8400 (37,360)	4690 (20,860)	8400 (37,360)
	(N=16)	(N=19)	(N=17)	(N=22)	(N=18)	(N=25)	(N=20)	(N=4)	(N=13)
L_s, in. (cm)	15 (38.1)	15 (38.1)	26 (66.0)	26 (66.0)	37 (94.0)	37 (94.0)	37 (94.0)	15 (38.1)	15 (38.1)
D_o, in. (cm)	1.5 (3.81)	1.58 (3.81)	1.96 (4.98)	2.20 (5.59)	2.40 (6.10)	2.76 (7.01)	2.62 (6.65)	1.5 (3.81)	1.5 (3.81)
W_{sb}, lbm (kg)	0.153 (0.069)	0.177 (0.080)	0.363 (0.165)	0.429 (0.195)	0.624 (0.283)	0.741 (0.336)	0.673 (0.305)	0.132 (0.060)	0.146 (0.066)
W_f, lbm (kg)	1.500 (0.680)	2.340 (1.061)	1.500 (0.680)	2.340 (1.061)	1.500 (0.680)	2.340 (1.061)	2.340 (1.061)	1.500 (0.680)	2.340 (1.061)
W_{ci}, lbm (kg)	0.030 (0.014)	0.035 (0.016)	0.087 (0.039)	0.115 (0.052)	0.189 (0.086)	0.256 (0.116)	0.225 (0.102)	0.030 (0.014)	0.030 (0.014)
W_{ei}, lbm (kg)	0.029 (0.013)	0.031 (0.014)	0.062 (0.028)	0.069 (0.031)	0.104 (0.047)	0.119 (0.054)	0.113 (0.051)	0.029 (0.013)	0.029 (0.013)
W_{ti}, lbm (kg)	1.712 (0.777)	2.583 (1.172)	2.012 (0.913)	2.953 (1.331)	2.417 (1.096)	3.456 (1.568)	3.351 (1.520)	1.691 (0.767)	2.545 (1.154)
W_{bol}, lbm (kg)	3.136 (1.422)	3.243 (1.471)	1.814 (0.823)	2.130 (0.966)	1.504 (0.682)	2.282 (1.035)	2.230 (1.012)	3.019 (1.369)	4.465 (2.025)
W_{bo2}, lbm (kg)	4.515 (2.048)	4.615 (2.093)	2.824 (1.281)	3.335 (1.513)	2.278 (1.033)	3.213 (1.457)	3.175 (1.440)	4.307 (1.954)	6.560 (2.976)
W_{ts1}, lbm (kg)	4.848 (2.199)	5.826 (2.643)	3.826 (1.735)	5.083 (2.306)	3.921 (1.779)	5.738 (2.603)	5.581 (2.532)	4.710 (2.136)	7.010 (3.180)
W_{ts2}, lbm (kg)	6.227 (2.825)	7.198 (3.265)	4.836 (2.194)	6.288 (2.852)	4.695 (2.130)	6.669 (3.025)	6.526 (2.960)	5.998 (2.721)	9.105 (4.130)

Analysis Case No. (Ref Table 3-2)	13		14		15		16		
Strut Length, L_s, in. (cm)	29.0 (73.7)		40.0 (101.6)		29.0 (73.7)		40.0 (101.6)		
Ult Compressive Load, P_C, lbf (N)	4690 (20,860)	8400 (37,360)	4690 (20,860)	8400 (37,360)	4690 (20,860)	8400 (37,360)	4690 (20,860)	8400 (37,360)	
	(N=4)	(N=16)	(N=5)	(N=20)	(N=4)	(N=16)	(N=5)	(N=20)	
L_s, in. (cm)	26 (66.0)	26 (66.0)	37 (94.0)	37 (94.0)	26 (66.0)	26 (66.0)	37 (94.0)	37 (94.0)	
D_o, in. (cm)	1.94 (4.93)	1.94 (4.93)	2.40 (6.10)	2.40 (6.10)	1.96 (4.98)	1.96 (4.98)	2.46 (6.25)	2.46 (6.25)	
W_{sb}, lbm (kg)	0.290 (0.013)	0.324 (0.147)	0.513 (0.233)	0.572 (0.259)	0.280 (0.127)	0.314 (0.142)	0.481 (0.218)	0.540 (0.245)	
W_f, lbm (kg)	1.500 (0.680)	2.340 (1.061)	1.500 (0.680)	2.340 (1.061)	1.500 (0.680)	2.340 (1.061)	1.500 (0.680)	2.340 (1.061)	
W_{ci}, lbm (kg)	0.087 (0.039)	0.087 (0.039)	0.189 (0.086)	0.189 (0.086)	0.156 (0.071)	0.156 (0.071)	0.293 (0.133)	0.293 (0.133)	
W_{ei}, lbm (kg)	0.061 (0.028)	0.061 (0.028)	0.104 (0.047)	0.104 (0.047)	0.061 (0.028)	0.061 (0.028)	0.106 (0.048)	0.106 (0.048)	
W_{ti}, lbm (kg)	1.938 (0.879)	2.812 (1.276)	2.306 (1.046)	3.205 (1.454)	1.997 (0.906)	2.871 (1.302)	2.380 (1.080)	3.279 (1.487)	
W_{bol}, lbm (kg)	1.923 (0.872)	3.019 (1.369)	1.605 (0.728)	2.550 (1.157)	1.871 (0.849)	2.968 (1.346)	1.559 (0.707)	2.506 (1.137)	
W_{bo2}, lbm (kg)	2.744 (1.245)	4.342 (1.970)	2.292 (1.040)	3.668 (1.664)	2.688 (1.219)	4.286 (1.944)	2.202 (0.999)	3.577 (1.623	
W_{ts1}, lbm (kg)	3.861 (1.751)	5.831 (2.645)	3.911 (1.774)	5.755 (2.610)	3.868 (1.755)	5.839 (2.649)	3.939 (1.787)	5.785 (2.624)	
W_{ts2}, lbm (kg)	4.682 (2.124)	7.154 (3.245)	4.598 (2.086)	6.873 (3.118)	4.685 (2.125)	7.157 (3.246)	4.582 (2.078)	6.856 (3.110)	

Appendix E

PROCESS SPECIFICATION NO. 3060993
FIBERGLASS SUPPORTS FOR CRYOGENIC TANKS

1.0 SCOPE

1.1 Contract Requirement

This specification meets the specific requirements of Task III, Contract NAS 3-12037, which states: "The Contractor shall provide a process specification to the NASA-LeRC Project Manager that provides in complete detail the manufacturing process for each strut design."

1.2 Application

This specification establishes the materials, equipment, and procedures necessary for fabrication, assembly, and cure of filament wound fiberglass supports for cryogenic tanks.

2.0 APPLICABLE DOCUMENTS

The following documents form a part of this specification to the extent specified herein. Unless otherwise indicated in the listing, the latest issue in effect shall apply.

2.1 Specifications

2.1.1 Military

° MIL-S-5059	Steel, Corrosion-Resistant (18-8) Plate, Sheet and Strip

° MIL-S-8879 — Screw Threads, Controlled Radius Root with Increased Minor Diameter, General Specification for

° MIL-T-9047 — Titanium and Titanium Alloy Bars and Forging Stock

2.1.2 Lockheed

° LAC 0170 — General Cleaning of Parts and Surfaces

° LAC 3552 — Lubricant Solid-Film; Impingement Application

° LAC 3900 — Limited-Calendar-Life Materials, Control of

2.2 Standards

2.2.1 Military

° MS 33540 — Safety Wire

3.0 GENERAL INFORMATION

3.1 Process Flow Diagram

Process Flow Diagram

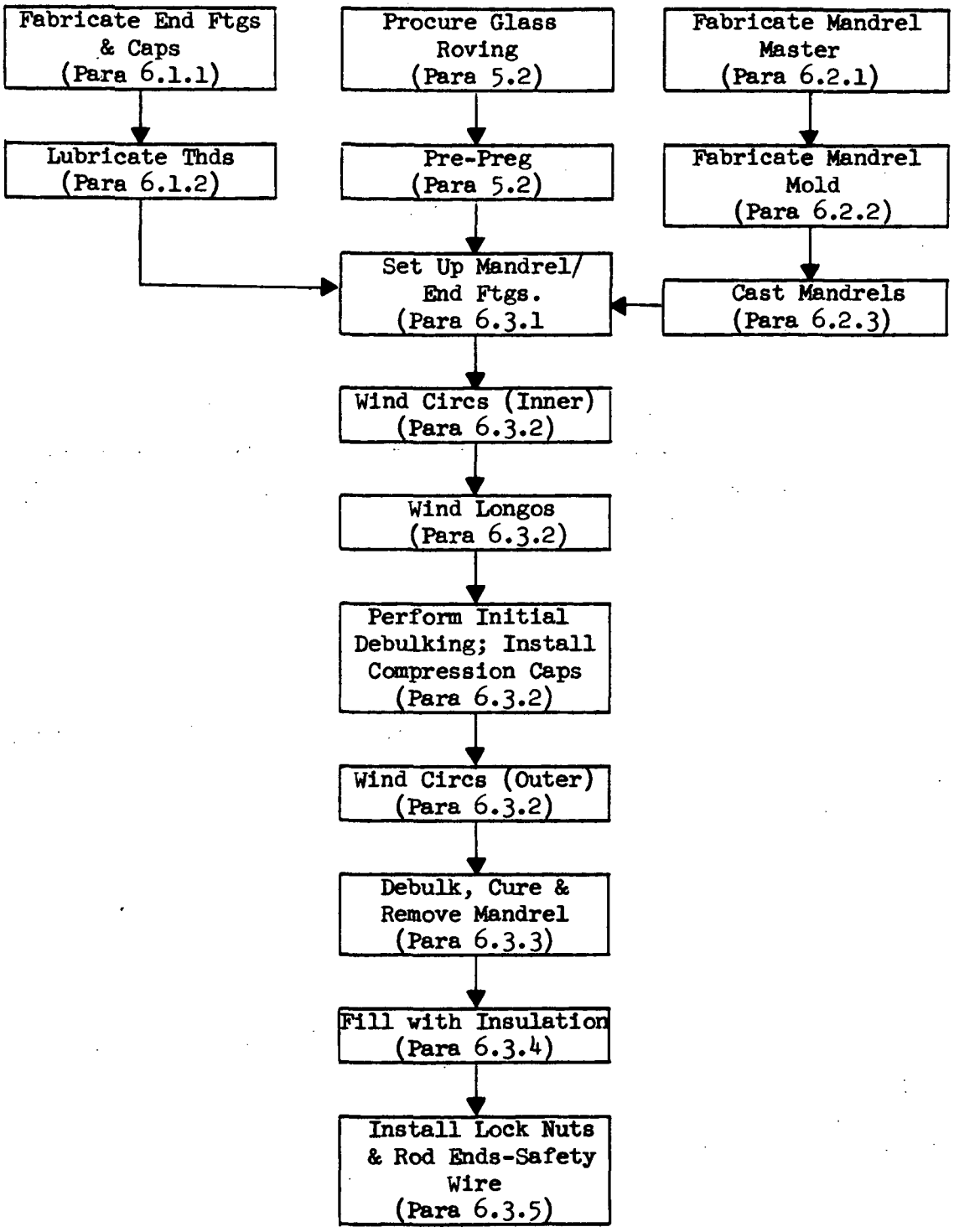

4.0 GENERAL REQUIREMENTS

4.1 Materials

All materials used shall be in accordance with applicable documents as referenced in this specification or as specified on the engineering drawing.

4.2 Workmanship

Workmanship shall be of sufficient quality to insure proper operation and service function of the assemblies during the operational life of these assemblies and the associated equipment, and shall comply with the applicable Lockheed standards.

4.3 Equipment

The equipment used shall be capable of producing hardware in accordance with the requirements of this specification and the engineering drawings.

4.4 Calibration

All instruments shall be maintained in current calibration.

4.5 Process Areas

Good housekeeping, neatness, and orderliness shall be maintained in all process areas.

4.6 Overage Materials

Materials which have exceeded their shelf-life limitations shall not be used.

4.7 Surveillance

Surveillance shall be exercised to insure compliance with all of the requirements of this specification.

5.0 MATERIALS

5.1 Manufacturing Materials

- Aluminum bar stock
- Glass fabric/epoxy resin
- Paraplast 36 soluble salt procured from Resolin Inc., Chatsworth, California
- Heat-Shrinkable Mylar

5.2 Productive Materials

- S-901, 8-end roving glass filament, preimpregnated with E-787 epoxy resin.
- Glass filament shall be procured from Owens-Corning Fiberglas Corp., San Francisco, California.
- Prepreg resin content shall be 23 percent ± 3 percent by weight and shall have a maximum volatile content of 3 percent by weight.
- Resin preimpregnation of the glass filament shall be accomplished by U.S. Polymeric Corp., Santa Ana, California.
- The epoxy resin system used for cap installation shall consist of the following formulation:

Epon 828	50 parts
Epon 1031	50 parts
BDMA Curing Agent	0.5 parts
NMA Curing Agent	90 parts

  It shall be procured from the Shell Chemical Co., Pastics & Resins Div., San Francisco, California.
- Titanium, alloy 6Al-4V-ELl per MIL-T-9047 Type III, Comp. A.
- Spherical rod ends procured from Southwest Products Co., Monrovia, California.
- Dexiglas core insulation procured from C. H. Dexter and Sons Paper Company, Windsor Locks, Connecticut.

6.0 PROCESS

6.1 End Fitting Preparation

6.1.1 Fabricate End Fittings and Caps

- Machine end fittings and caps from titanium alloy 6Al-4V-ELI bar stock, or from titanium alloy 5Al-2.5Sn-ELI.
- Dry abrasive blast the surface of each end fitting in the area of contact with the glass fibers with aluminum oxide sand.
- All external threads must be rolled to obtain the optimum notch fracture characteristics.
- Provide each end fitting with a through-hole for flushing out the mandrel salt, filling the core cavity with insulation, and evacuation of the initial gas and outgas components.

6.1.2 Lubricate Threads

- Apply by impingement application to all external threads a molybdenum sulfide solid-film lubricant.

6.2 Mandrel Preparation

6.2.1 Fabricate Mandrel Master

- The mandrel master should be fabricated from aluminum for ease of machining.
- The mandrel master shall have a male configuration conforming to the inside contour of the desired strut.
- When machining the mandrel master, increase all specified dimensions by approximately 1.04 percent or 0.125 in./ft (1.04 cm/m) in order to compensate for subsequent shrinkage in the fabrication of the mandrel mold and in the casting of the individual salt mandrels.

6.2.2 Fabricate Mandrel Mold

° Set up mandrel master with plaster, and layup glass cloth/resin winding-mandrel mold in two halves.

° Vacuum-bag and oven-cure the two mold halves, and clean for use.

6.2.3 Prepare Salt Mandrels

° Cast the winding-mandrels of soluble Paraplast 36 salt, or equivalent.

° Melt the salt at 400°F (204°C), assemble the split casting mold and preheat to 200°F (93.3°C), pour melted salt into the mold, rotate and cool sufficiently to form approximately a 0.25-in.-(0.635-cm-) thick wall of solid salt, and pour the remaining melted salt out of the mold.

° Remove the salt mandrel from the mold when cool.

° Clean flash material from the mandrel and apply a parting agent such as Fluorocarbon S122.

6.3 Filament-Winding Procedure

6.3.1 Setup Winding Machine

° Assemble salt mandrel with internal end-fittings and place in winding machine.

° Program winding equipment for the specific strut design requirements (Ref Table E-1).

° Prepare glass fiber-epoxy resin prepreg material, weigh prepreg material, record weight, and thread prepreg material into the winding and tension-control equipment.

6.3.2 Wind Strut and Install Compression Caps
(Ref Table E-1 for specific design requirements)

° Wind the interior end-fillet and interior circ wrap rovings in a side-by-side pattern. Use programmed mandrel fixture rotation and horizontal carriage feed rates to achieve the desired yarn placement and spacing. Yarn tension during inner circ winding should be approximately 3.5 lbf (15.6 N).

- Wind the specified number of longo rovings for each specified wrap in a side-by-side polar pattern so that each roving crosses the longitudinal centerline of the strut (i.e., 180° spacing over the opposite-end fitting). Use programmed horizontal carriage feed in combination with either programmed or predetermined manual mandrel fixture rotation to achieve the desired yarn placement and spacing. Yarn tension during longo winding should be approximately 1.5 lbf (6.7 N).
- Apply heat-shrinkable Mylar tape over the longo windings, and apply minimum heat for initial smoothing and debulking of the composite structure. When complete, remove the tape.
- Install metallic end caps over the polar windings at each end. Apply sufficient E-787 epoxy resin between each cap and the longo windings to provide a smooth faying surface with minimum voids. Secure each cap in place with the specified washer and check nut.
- Wind the exterior circ wrap and end-fillet rovings in a side-by-side pattern. Use programmed mandrel fixture rotation and horizontal carriage feed rates to achieve the desired yarn placement and spacing. Yarn tension during external circ winding should be approximately 3.5 lbf (15.6 N).

6.3.3 Debulk, Cure, and Perform Post-Winding Operations

- Remove winding from machine and prepare for vacuum bagging.
- Remove prepreg material from the winding equipment, weigh prepreg material, and record weight.
- Place completed strut structure into vacuum bag, apply vacuum and heat, and force entrapped air from composite structure by squeegee techniques.
- Place vacuum bag assembly in oven for curing.
- Cure as follows:

  1 hr. at 200°F (93.3°C)
  2 hrs. at 250°F (121°C)
  2 hrs. at 300°F (149°C)

- After curing, remove from vacuum bag and clean-up. Remove salt mandrel by the use of continuous-flow warm water.
- Weigh, measure, and calculate the dimensional and constituent properties of the finished strut. (Ref Table E-2 for maximum allowable tolerances.)

6.3.4 Insulate Strut Core Cavity

° Fill strut with chopped Dexiglas particles to 4-6 lbm/ft^3 density. Particle size should be approximately 1/4-inch square.

6.3.5 Complete Final Assembly

° Install locknuts and rod ends. Safety wire, Double Twist Method per MS 33540.

Table E-1

SUMMARY OF DIMENSIONS AND WINDING REQUIREMENTS

Configuration No. Drawing No.	III-1 CP3060932	III-2 CP3060936	III-3 CP3060934
Length, Center-to-Center of Rod-End Fittings, in. (cm)	24.0 (61.0)	19.0 (48.3)	36.0 (91.4)
Midspan O.D., in. (cm)	1.5 (3.8)	1.5 (3.8)	2.5 (6.35)
No. of 8-End Longo Rovings	146	374	306
No. of 8-End Longo Revolutions	73	137	153
No. of Longo Wraps	2	2	2
Nominal Longo Thickness, in. (cm)	0.008 (0.020)	0.015 (0.038)	0.010 (0.025)
Nominal Longo Cross-Section Area, in.^{2} (cm^2)	0.0371 (0.2394)	0.0694 (0.4478)	0.0776 (0.5007)
Av. Longo Spacing, Ea. Wrap, in. (cm)	0.0637 (0.1618)	0.0339 (0.0861)	0.0509 (0.1292)
No. of 8-End Circ Rovings (Ea. Circ Wrap Excluding End Transition Areas)	385	241	579
Nominal Circ Thickness, Ea. Wrap, in. (cm)	0.006 (0.015)	0.006 (0.015)	0.006 (0.015)
Av. Circ Spacing, Ea. Wrap, in. (cm)	0.0424 (0.1077)	0.0424 (0.1077)	0.0424 (0.1077)
Nominal Total Wall Thickness, in. (cm)	0.020 (0.051)	0.027 (0.069)	0.022 (0.056)
Nominal Total Wall Cross-Section Area, in.^{2} (cm^2)	0.0930 (0.6000)	0.1250 (0.8065)	0.1713 (1.105)

Table E-2

SUMMARY OF MAXIMUM ALLOWABLE MANUFACTURING TOLERANCES

Configuration No. Drawing No.	III-1 CP3060932	III-2 CP3060936	III-3 CP3060934
Length, Strut Body and Final Assembly, in. (cm)	±0.03 (±0.08)	±0.03 (±0.08)	±0.03 (±0.08)
Outside Diameter, in. (cm)	±0.010 (±0.025)	±0.010 (±0.025)	±0.010 (±0.025)
Diameter, Out-of-Roundness, in. (cm)	±0.025 (±0.064)	±0.025 (±0.064)	±0.040 (±0.102)
Column Eccentricity at Midspan, in. (cm)	0.080 (0.203)	0.060 (0.152)	0.120 (0.305)
Longitudinal Centerline Misalignment, Strut Body to End Fittings, Degrees	±2	±2	±2
Prepreg Resin Content by Weight, Percent of Nominal	±3	±3	±3
Composite Weight, Percent of Nominal	±1.5	±1.5	±1.5
Total Assembly Weight, Percent of Nominal	±1.8	±1.8	±1.8
Glass/Resin Weight Fraction, Percent of Nominal	±10	±10	±10
Glass/Resin Volume Fraction, Percent of Nominal	±15	±15	±15
Void Volume Fraction, Percent	8	8	8

Appendix F

ANALYTICAL METHOD TO DETERMINE WINDING REQUIREMENTS

In Task 1 it was shown that optimum values of total longo wrap thickness for monocoque struts can be determined by cross-plotting data on ultimate compressive load capability for failure in each of the primary modes (i.e., column buckling, crippling, and crushing) as a function of nominal longo thickness. Plots of this type were presented in Figs. 3-43, 3-44, and 3-45 (Ref Section 3.2.3) for selected configurations III-1, III-2, and III-3, respectively. However, spacing of the rovings, rather than thickness, is the parameter used to control the winding of both longo and circ wraps during fabrication of a strut. Consequently, it was necessary to develop an analytical method to determine the spacings required to achieve the thicknesses specified in the design.

Initially, to develop such a method, the cross-sectional glass area of a single 8-end roving of fibers (without the resin matrix) was determined from values of dry roving weight per unit length and glass-fiber density. The nominal unit weight value used in the analysis was 0.2420 gm/yard (Ref 28) which is equivalent to 1.482×10^{-5} lbm/in. (2.647×10^{-3} gm/cm). The glass-fiber density value used was 0.0897 lbm/in.^{3} (2.483 gm/cm^3) (Ref 1, page 157). Dividing the weight per unit length by the density yields a nominal glass area of 1.653×10^{-4} in.^{2} (1.067×10^{-3} cm^2) for each 8-end roving.

The total composite cross-sectional area of glass plus resin for a single 8-end roving was then obtained by dividing the cross-sectional area of the glass by the design fiber volume fraction of 0.65 (Ref Section 3.1.1). Void volume, nominally 2 to 6 percent (Ref Sections 7.1.1 and 7.1.2), was neglected in this calculation. A nominal composite cross-sectional area value of 2.543×10^{-4} in.^{2} (1.641×10^{-3} cm^2) for a single 8-end roving was obtained in this manner.

The effect of roving unit weight tolerance and fiber volume fraction tolerance

on the total composite cross-section area of a single 8-end roving was also investigated in the analysis. Maximum and minimum values of roving unit weight were combined, respectively, with minimum and maximum values of fiber volume fraction to determine the worst-case tolerance effects. The maximum and minimum values of roving unit weight used were 0.2592 and 0.2240 gm/yard, respectively, (1.588×10^{-5} lbm/in. or 2.836×10^{-3} gm/cm and 1.372×10^{-5} lbm/in. or 2.450×10^{-3} gm/cm, respectively) (Ref 28). A minimum fiber volume fraction value of 0.61 was used, corresponding to the maximum design resin content of 20.8 + 3.0 percent by weight (Ref Section 3.1.1 and Ref 1, Fig. 6-83). Similarly, the maximum fiber volume fraction value used was 0.69, based on the minimum design resin content of 20.8 - 3.0 percent by weight. The worst-case single-roving total composite cross-sectional areas which resulted from the combination of these unit weight and volume fraction tolerances are 2.902×10^{-4} $in.^2$ (1.872×10^{-3} cm^2) and 2.219×10^{-4} $in.^2$ (1.432×10^{-3} cm^2), respectively, which are +14.1 and -12.7 percent deviations from the nominal composite cross-sectional area value.

During the Task 1 design and analysis, a constant nominal thickness value of 6 mil (0.15 mm) was selected for each of the inner and outer circ wraps. Assuming that the composite material is perfectly distributed to achieve a rectangular cross-section of this constant thickness, the required nominal circ roving spacing then becomes 0.0424 in. (0.1077 cm). This is equivalent to 23.6 rovings/in. (9.3 rovings/cm). If the circ rovings are wound at this nominal spacing, the worst-case tolerances on single-roving composite cross-sectional area (due to unit weight and volume fraction tolerances) will result in maximum and minimum average circ wrap thickness values of 6.8 mil (0.17 mm) and 5.2 mil (0.13 mm), respectively.

The number of longo rovings and the average longo roving spacing required to achieve the selected design longo wrap thickness depends on cross-section geometry. Fig. F-1 shows the idealized cross-section geometry for the general case.

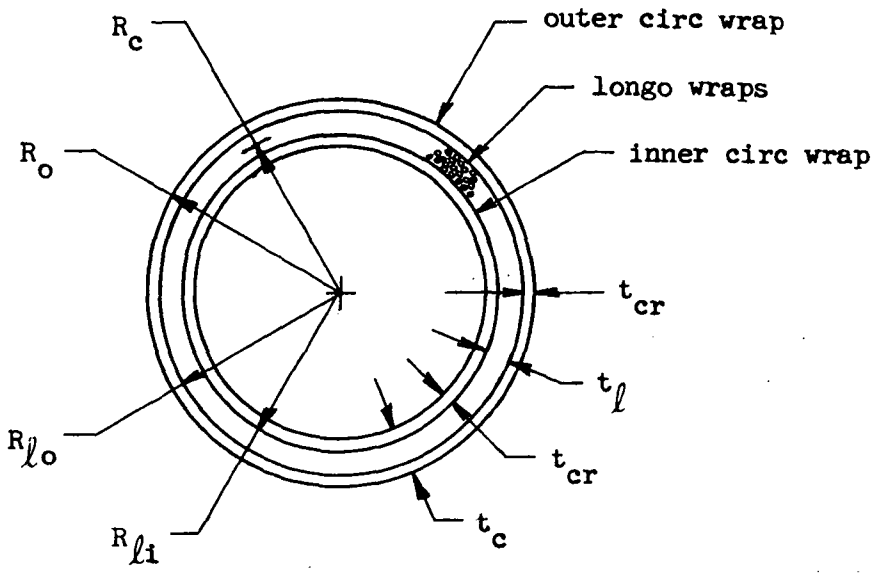

Fig. F-1 Idealized Strut Cross-Section Geometry

Referring to the figure, the outer radius of the strut, R_o, the circ wrap thickness, t_{cr}, and the total longo wrap thickness, t_ℓ, are specified in the design. The outer and inner radii of the total required longo wraps, $R_{\ell o}$ and $R_{\ell i}$, respectively, can then be determined from the expressions

$$R_{\ell o} = R_o - t_{cr} \tag{F-1}$$

and

$$R_{\ell i} = R_{\ell o} - t_\ell \tag{F-2}$$

Using these values, the total required cross-sectional area of the longitudinal wraps can be calculated using the equation

$$A_\ell = \pi(R_{\ell o}^2 - R_{\ell i}^2) \tag{F-3}$$

Once the required longo wrap area has been determined, the total number of

8-end longo rovings required to achieve it can be computed as

$$N_{\ell} = \frac{A_{\ell}}{A_{sr}} \qquad \text{(F-4)}$$

Also, the required average longo roving spacing can be determined from

$$w_{\ell} = \frac{2\pi R_c N_{\ell w}}{N_{\ell}} \qquad \text{(F-5)}$$

In this expression, the average longo wrap radius, R_c, (which is also equal to the average radius for the total wall thickness) is simply $(R_{\ell o} + R_{\ell i})/2$. The number of longo wraps required, $N_{\ell w}$, is specified in the design based on the total required longo wrap thickness, t_{ℓ}. For t_{ℓ} values of 8 to 24 mil (0.20 to 0.61 mm), two longo wraps are required (Ref Section 3.1.1). Total longo wrap thicknesses of less than 8 mil (0.20 mm) are not practical using 8-end roving yarn, and those greater than 24 mil (0.61 mm) require two additional longo wraps for each additional 24 mil (0.61 mm) (or fraction thereof) of thickness. The number of longo rovings per unit of circumference is simply the reciprocal of the spacing (i.e., $1/w_{\ell}$).

Strut cross-section geometry and optimum winding requirements for the selected Task 2 and Task 3 designs were determined using the method presented in this appendix. Results are shown in Table 4-1 for the Task 2 struts, and in Figs. 3-46, 3-47, and 3-48 as well as in Table E-1 for the Task 3 struts.

Appendix G

NOMENCLATURE

SYMBOLS:

A	cross-sectional area, $in.^2$ (cm^2)
A_{bs}	cross-sectional area of longeron stiffeners reinforced with boron fibers, $in.^2$(cm^2) or ft^2 (cm^2)
A_c	cross-sectional area of the total composite strut wall, $in.^2$(cm^2) or ft^2(cm^2)
A_{cg}	cross-sectional area of the circumferential glass fibers, $in.^2$(cm^2)
A_{cn}	nominal cross-sectional area of the total composite strut wall based on the product of the number of rovings and the nominal roving area, $in.^2$(cm^2)
A_{cr}	cross-sectional area of the circumferential wraps, $in.^2$(cm^2)
A_{gs}	cross-sectional area of longeron stiffeners reinforced with glass fibers, $in.^2$(cm^2) or ft^2(cm^2)
A_ℓ	cross-sectional area of the longitudinal wraps, $in.^2$(cm^2)
$A_{\ell g}$	cross-sectional area of the longitudinal glass fibers, $in.^2$(cm^2)
A_R	cross-sectional area of the strut core cavity for radiation heat transfer, ft^2(m^2)
A_r	cross-sectional area of the resin matrix, $in.^2$(cm^2)

A_{sr} cross-sectional area (glass plus resin) of a single 8-end roving of fiberglass material. Nominal value is 2.543×10^{-4} $in.^2$ (1.641×10^{-3} cm^2) (Ref Appendix F)

D_o outside diameter of the composite strut body, in. (cm)

D_{oe} outside diameter of a composite ogive strut body at each end, in. (cm)

D_{om} outside diameter of a composite ogive strut body at midspan, in. (cm)

E modulus of elasticity, psi (N/m^2)

E_c longitudinal modulus of elasticity of the total composite strut wall, psi (N/m^2)

E_{cm} longitudinal modulus of elasticity of the total composite strut wall based on test results (i.e., the slope of the stress-strain curve at zero load), psi (N/m^2)

E_g modulus of elasticity of glass fibers in the parallel direction, psi (N/m^2)

E_r modulus of elasticity of the resin matrix, psi (N/m^2)

G shear modulus, psi (N/m^2)

I area moment of inertia of the total composite strut wall, $in.^4$ (cm^4)

J torsion constant, $in.^4$ (cm^4)

K	isotropic crippling coefficient for the total composite strut wall, dimensionless
K_e	isotropic crippling coefficient for the total composite strut wall based on test results, dimensionless
L	length, in. (cm)
L'	effective strut length for predicting column buckling allowables (equals total length for a pin-ended colum), in. (cm)
L_c	effective composite strut body length for computing longitudinal heat leak, in. (cm) or ft (m)
L_s	total strut length (pin-to-pin), in. (cm)
L_{sb}	effective composite strut body length for computing weight, in. (cm)
N	number of longeron stiffeners, dimensionless
N_ℓ	total number of 8-end longo rovings, dimensionless
$N_{\ell w}$	number of longo wraps, dimensionless
N_o	optimum number of longeron stiffeners, dimensionless
P_C	ultimate compressive load capability for failure in Euler column buckling, lbf (N). Also, design ultimate compressive load, lbf (N)

P_{CR} ultimate compressive load capability for failure in any critical mode, lbf (N)

P_{CRP} ultimate compressive load capability for failure in local crippling, lbf (N)

P_{CRS} ultimate compressive load capability for failure in crushing, lbf (N)

P_F failure load achieved in tension or compression, lbf (N)

P_P predicted ultimate load capability in tension or compression, lbf (N)

Q_C component of longitudinal one-dimensional heat leak due to conduction through the wall of a composite strut, Btu/hr (W)

Q_c longitudinal one-dimensional heat leak through a composite strut (equal to Q_C where radiation component is neglected), Btu/hr (W)

Q_{c1} longitudinal one-dimensional heat leak through a composite strut for boundary temperatures of 520°R (289°K) and 37°R (20°K), Btu/hr (W)

Q_{c2} longitudinal one-dimensional heat leak through a composite strut for boundary temperatures of 400°R (222°K) and 140°R (78°K), Btu/hr (W)

Q_R component of longitudinal one-dimensional heat leak due to radiation through the core cavity of a composite strut, Btu/hr (W)

R_c radius to the center of the thickness of the total composite strut wall, in. (cm)

$R_{\ell i}$ radius to the inside surface of the longo wraps, in. (cm)

$R_{\ell o}$ radius to the outside surface of the longo wraps, in. (cm)

R_n nominal radius to the center of the thickness of the total composite strut wall based on nominal diameter and wall thickness values, in. (cm)

R_o radius to the outside surface of the total composite strut wall, in. (cm)

T_C absolute temperature of the cold end boundary, °R (°K)

T_H absolute temperature of the hot end boundary, °R (°K)

T_m absolute mean temperature of the composite wall material (i.e., the average of the T_C and T_H values for a particular case), °R (°K)

V volume of a particular strut component, ft^3 (m^3)

W_{bol} total hydrogen boiloff weight per strut for a specified storage time with boundary temperatures of 520°R (289°K) and 37°R (20°K), lbm (kg)

W_{bo2} total fluorine boiloff weight per strut for a specified storage time with boundary temperatures of 400°R (222°K) and 140°R (78°K), lbm (kg)

W_{ci}	weight of the core insulation per strut, lbm (kg)
W_{ei}	weight of the external insulation per strut, lbm (kg)
W_f	total weight of the metallic end fittings per strut (includes rod ends, internal fittings, compression caps, and attachment hardware), lbm (kg)
W_{sb}	total weight of the composite strut body and longeron stiffeners (if any) per strut, lbm (kg)
W_{ti}	total inert weight per strut, lbm (kg)
W_{ts}	total system weight per strut (includes component inert weights plus boiloff), lbm (kg)
W_{tsl}	total system weight per strut for LH_2 tank supports, lbm (kg)
W_{ts2}	total system weight per strut for LF_2 tank supports, lbm (kg)
e	eccentricity between the geometric center of the composite cross-section and the longitudinal axis measured at midspan, in. (cm)
f_c	average compressive stress distributed over the total composite wall cross-section due to an applied load, psi (N/m^2)
f_t	average tensile stress distributed over the total composite wall cross-section due to an applied load, psi (N/m^2)
k_b	thermal conductivity in the parallel direction of boron fibers (excluding the tungsten core), Btu/hr ft°R (W/cm°K)

k_c thermal conductivity in the longitudinal direction of the total composite strut wall, Btu/hr ft°R (W/cm°K)

k_{cg} thermal conductivity in the longitudinal direction of the total composite wall of a fiberglass strut, Btu/hr ft°R (W/cm°K)

k_{cr} thermal conductivity of the circ wraps in the longitudinal direction, Btu/hr ft°R (W/cm°K)

k_f thermal conductivity in the parallel direction of the reinforcement fibers, Btu/hr ft°R (W/cm°K)

k_g thermal conductivity in the parallel direction of glass fibers, Btu/hr ft°R (W/cm°K)

k_ℓ thermal conductivity in the longitudinal direction of the longo wraps, Btu/hr ft°R (W/cm°K)

k_r thermal conductivity of the resin matrix, Btu/hr ft°R (W/cm°K)

k_t thermal conductivity in the parallel direction of the tungsten core of boron reinforcing fibers, Btu/hr ft°R (W/cm°K)

n number of waves (i.e., diamond pattern buckles) which form around the circumference of a composite strut wall during compressive crippling, dimensionless. Also, the number of circular radiation shields used to insulate the strut core cavity, dimensionless

t_c thickness of the total composite strut wall, mil (mm)

t_{cm} thickness of the total composite wall of an ogive strut at midspan, mil (mm)

t_{cr}	thickness of each of the inner and outer circ wraps, mil (mm)
t_{ℓ}	total thickness of the longo wraps, mil (mm)
$t_{\ell m}$	total thickness of the longo wraps of an ogive strut at midspan, mil (mm)
t_m	measured thickness of the total composite strut wall, in. (cm) or mil (mm)
t_n	nominal thickness of the total composite strut wall based on nominal values of outside diameter and cross-sectional area, in. (cm) or mil (mm)
v_b	volume fraction of boron reinforcement fibers (excluding the tungsten core), dimensionless
v_f	volume fraction of the reinforcement fibers, dimensionless
v_r	volume fraction of the resin matrix, dimensionless
v_t	volume fraction of the tungsten core of boron reinforcement fibers, dimensionless
w_{ℓ}	average longo roving spacing within a particular wrap, in. (cm)
ϵ	average strain measured over a specified gage length due to an applied axial load, in./in. (cm/cm)
ϵ_o	emissivity of a boundary surface, dimensionless

ϵ_{os}	emissivity factor applying between a boundary surface and an adjacent radiation shield, dimensionless
ϵ_s	emissivity of a radiation shield, dimensionless
ϵ_{ss}	emissivity factor applying between adjacent radiation shields, dimensionless
ρ	density of a particular strut component, lbm/ft^3 (kg/m^3)
ρ_c	radius of gyration of the total composite strut wall cross-section, in. (cm)
σ	Stefan-Boltzmann constant, equal to 1.713×10^{-9} Btu/hr ft^2 $°R^4$ (5.669×10^{-8} $W/m^2 °K^4$)
μ	Poisson's ratio, dimensionless

ABBREVIATIONS:

LVDT	linear variable differential transducer
circ	circumferential roving
longo	longitudinal roving

Appendix H

REFERENCES

1. Bartlett, D. H., "Nonmetallic Parts for Launch Vehicles and Spacecraft Structures," NASA CR-95104, Final Report for Contract NAS 8-18037, March 1968, The Boeing Company

2. Bullard, B. R., "Cryogenic Tank Support Evaluation," NASA CR-72546, Final Report for Contract NAS 3-7979, December 1969, Lockheed Missiles and Space Company

3. Lindquist, C. R., and Lies, G. E., "Lightweight Multilayer Insulation System," NASA CR-72363, Final Report for Contract NAS 3-7953, April 1968, Union Carbide Corporation, Linde Division

4. "Structural Design Guide for Advanced Composite Applications," Second Edition, Volume I, January 1971, Prepared Under Contract F33615-69-C-1368, North American Rockwell Corporation, Los Angeles Division

5. Coston, R. M., and Parmley, R. T., "Handbook of Thermal Design Data for Multilayer Insulation Systems," LMSC-A847882, Volume II, Final Report for Contract NAS 8-20353, June 1967, Lockheed Missiles and Space Company

6. Springer, G. S., and Tsai, S. W., "Thermal Conductivities of Unidirectional Materials," Journal of Composite Materials, Volume 1, page 166, (1967)

7. White, G. K., "Measurement of Solid Conductivities at Low Temperatures," Thermal Conductivity, Vol I, R. P. Tye, Editor, Academic Press, New York, 1969

8. Lucks, C. F., and Bing, G. F., "Experimental Measurements of Thermal Conductivity, Specific Heats, and Density of Metallic Transports and Protective Materials," AFTR-6145, Part II, Contract AF 33(038) 20558, 1952

9. Powell, R. L., and Blanpied, W. A., "A Compendium of the Properties of Materials at Low Temperatures (Phase I)," WADD-TR-60-56, Part II, October 1960, Victor J. Johnson, General Editor, National Bureau of Standards, Cryogenic Engineering Laboratory

10. Toth, L. W. et al, "Program for the Evaluation of Structural Reinforced Plastic Materials at Cryogenic Temperatures," NASA CR-80061, Final Report for Contract NAS 8-11070, August 1966, Goodyear Aerospace Corporation

11. Haskins, J. F., et al, "Thermophysical Properties of Plastic Materials and Composites to Liquid Hydrogen Temperature (-423°F)," Part III, ML-TDR-64-33, August 1965, General Dynamics/Convair

12. Haskins, J. F., et al, "Thermophysical Properties of Plastic Materials and Composites to Liquid Hydrogen Temperature (-423°F)," Part I, ML-TDR-64-33, June 1964, General Dynamics/Astronautics

13. Nadler, M. A., "Thermal Conductivity Versus Temperature, S-994 Glass/Epoxy Resin, Parallel Direction," Letter to J. R. Barber, NASA-LeRC, dated 14 May 1969, North American Rockwell Corporation, Space Systems Division

14. Gabron, F., et al, "Design and Fabrication of Shadow Shield Systems for Thermal Protection of Cryogenic Propellants," NASA CR-72595, Final Report for Contract NAS 3-10292, November 1969, Arthur D. Little, Inc.

15. Gille, J. P., "Development of Advanced Materials for Integrated Tank Insulation System for the Long-Term Storage of Cryogens in Space," NASA CR-102570, Final Report for Contract NAS 8-21330, September 1969, Martin Marietta Corporation

16. Nadler, M. A., et al, "Boron/Epoxy Support Strut for Non-Integral Cryogenic Tankage," SD 68-995-1, Paper Presented at the 15th National Symposium of the Society of Materials and Process Engineers, Los Angeles, California, April 1969, North American Rockwell Corporation, Space Systems Division

17. Talley, C. P., et al, "Preparation and Properties of Massive Amorphous Elemental Boron," Paper published in "Boron, Synthesis, Structure, and Properties," J. A. Kohn, W. F. Nye, and G. K. Gaule, Editors, Plenum Press Inc., New York (1960)

18. Self-Aligning Bearings and Rod End Bearings," Catalog No. 551, Revised January, 1969, Southwest Products Company, Inc., Monrovia, California

19. Cunnington, G. R., et al, "Thermal Performance of Multilayer Insulations - Interim Report," NASA CR-72605, Contract NAS 3-12025, April 1971, Lockheed Missiles and Space Company

20. "Liquid Propellant Manual," compiled and edited by the Chemical Propulsion Information Agency, Johns Hopkins University, Applied Physics Laboratory, Contract NOw 62-0604c, 1961

21. Schwartzberg, F. R., et al, "Cryogenic Materials Data Handbook (Revised)," AFML-TDR-64-280, Supplement 4, Volume I, Contract No. F 36615-67-C-1794, August 1968, Martin-Marietta Corporation

22. "Military Standardization Handbook, Metallic Materials and Elements for Aerospace Vehicle Structures," MIL-HDBK-5B, Volume 2, September 1971

23. Brogan, J. J., "Design of High-Performance Insulation Systems," Volume 1, Summary Report for Contract NAS 8-11347, LMSC-A742593-1, August 1965, Lockheed Missiles and Space Company

24. "Low Temperature Insulation Foams and Composites," Cryogenic Engineering, Page 20, May 1969

25. Coston, R. M., "A Study of High-Performance Insulation Thermal Design Criteria," Volume 1, Final Report for Contract NAS 8-20353, LMSC-A847882, June 1967, Lockheed Missiles and Space Company

26 "Plastics for Aerospace Vehicles, Part 1, Reinforced Plastics," MIL-HDBK-17A, January 1971

27 Hofer, K. E., et al, "An Investigation of Fatigue and Creep Properties of Glass-Reinforced Plastics for Primary Aircraft Structures", IIT Research Institute, Chicago, Illinois, April 1967

28 Baruch, M. and Singer, J., "Effects of Eccentricity of Stiffeners on the General Instability of Stiffened Cylindrical Shells Under Hydrostatic Pressure", Journal of the Mechanical Engineering Society, Vol 5, No. 1, 1963

29 Owens-Corning Specification No. TP291, Owens-Corning Fiberglass Corporation

Appendix I

DISTRIBUTION LIST FOR FINAL REPORT, NASA CR-120937,
FIBERGLASS SUPPORTS FOR CRYOGENIC TANKS
NAS 3-12037

Report Copies R	D	Recipient	Designee
		National Aeronautics & Space Administration Lewis Research Center 21000 Brookpark Road Cleveland, Ohio 44135 Attn:	
1		Contracting Officer, MS 500-313	
5		E. A. Bourke, MS 500-203	
1		Technical Report Control Office, MS 5-5	
1		Technology Utilization Office, MS 3-16	
2		AFSC Liaison Office, 501-3	
2		Library	
1		Office of Reliability & Quality Assurance, MS 500-111	
1		J. W. Gregory, Chief, MS 500-203	
3		J. R. Barber, Project Manager, MS 500-203	
1		D. Petrash, MS 500-318	
1		A. V. Zimmerman, MS 500-318	
1		Director, Physics & Astronomy Programs, SG Office of Space Science NASA, Headquarters Washington, D.C. 20546	
1		Director, Planetary Programs, SL Office of Space Science NASA, Headquarters Washington, D.C. 20546	
1		Director, Shuttle Technology Office, RS Office of Aeronautics & Space Technology NASA, Headquarters Washington, D.C. 20546	

Report Copies R	D	Recipient	Designee
2		Director Space Prop. and Power, RP Office of Aeronautics & Space Technology NASA Headquarters Washing, D.C. 20546	
1		Director, Launch Vehicles & Propulsion, SV Office of Space Science NASA Headquarters Washington, D.C. 20546	
1		Director, Materials & Structures Div, RW Office of Aeronautics & Space Technology NASA Headquarters Washington, D.C. 20546	
1		Director, Advanced Manned Missions, MT Office of Manned Space Flight NASA Headquarters Washington, D.C. 20546	
14		National Technical Information Service Springfield, Virginia 22151	
1		National Aeronautics & Space Administration Ames Research Center Moffett Field, California 94035 Attn: Library	C. A. Syvertson
1		National Aeronautics & Space Administration Flight Research Center P. O. Box 273 Edwards, California 93523 Attn: Library	
1		Director, Technology Utilization Division Office of Technology Utilization NASA Headquarters Washington, D.C. 20546	

Report Copies R	D	Recipient	Designee
1		Office of the Director of Defense Research & Engineering Washington, D.C. 20301 Attn: Office of Asst Dir. (Chem Technology)	
1		Office of Aeronautics & Space Technology, R NASA Headquarters Washington, D.C. 20546	
2		NASA Scientific & Technical Information Facility P. O. Box 33 College Park, Maryland 20740 Attn: NASA Representative	
1		National Aeronautics & Space Administration Goddard Space Flight Center Greenbelt, Maryland 20771 Attn: Library	
1		National Aeronautics & Space Administration John F. Kennedy Space Center Cocoa Beach, Florida 32931 Attn: Library	
1		National Aeronautics & Space Administration Langley Research Center Langley Station Hampton, Virginia 23365 Attn: Library	
1	1	National Aeronautics & Space Administration	C. Humphrey
	1	Manned Spacecraft Center	W. Chandler
	1	Houston, Texas 77001	W. Dusenberry
	1	Attn: Library	R. Polifka
	1		C. Yodis

Report Copies R	D	Recipient	Designee
1	1	National Aeronautics & Space Administration	J. M. Stuckey
	1	George C. Marshall Space Flight Center	I. G. Yates
	1	Huntsville, Alabama 35912	E. H. Hyde
	1	Attn: Library	Clyde Nevins
1	1	Jet Propulsion Laboratory	L. Stimson
	1	4800 Oak Grove Drive	J. Kelly
	1	Pasadena, California 91103	R. Breshears
		Attn: Library	
1		Defense Documentation Center Cameron Station Building 5 5010 Duke Street Alexandria, Virginia 22314 Attn: TISIA	
1		RTD (RTNP) Bolling Air Force Base Washington, D.C. 20332	
1		Arnold Engineering Development Center Air Force Systems Command Tullahoma, Tennessee 37389 Attn: Library	
1		Advanced Research Projects Agency Washington, D.C. 20525 Attn: Library	
1		Aeronautical Systems Division Air Force Systems Command Wright-Patterson Air Force Base, Dayton, Ohio	R. E. Headrick (Code MANE)
1		Attn: Library	
1		AFML (MAAE)	
1		AFML (MAAM)	

Report Copies R	D	Recipient	Designee
1		Air Force Rocket Propulsion Laboratory (RPM) Edwards, California 93523 Attn: Library	
1		Air Force FTC (FTAT-2) Edwards Air Force Base, California 93523 Attn: Library	Donald Ross
1		Air Force Office of Scientific Research Washington, D.C. 20333 Attn: Library	SREP, Dr. J. F. Masi
1		Space & Missile Systems Organization Air Force Unit Post Office Los Angeles, California 90045 Attn: Technical Data Center	
1		Office of Research Analyses (OAR) Holloman Air Force Base, New Mexico 88330 Attn: Library RRRD	
1		U. S. Air Force Washington, D.C. Attn: Library	
1		Commanding Officer U. S. Army Research Office (Durham) Box CM, Duke Station Durham, North Carolina 27706 Attn: Library	
1		Bureau of Naval Weapons Department of the Navy Washington, D.C. Attn: Library	J. Kay, Code RTMS-41

Report Copies R	D	Recipient	Designee
1		Director (Code 6180) U. S. Naval Research Laboratory Washington, D.C. 20390 Attn: Library	H. W. Carhart J. M. Krafft
1		Picatinny Arsenal Dover, New Jersey 07801 Attn: Library	I. Forsten
1		Air Force Aero Propulsion Laboratory Research & Technology Division Air Force Systems Command United States Air Force Wright-Patterson AFB, Ohio 45433 Attn: APRP (Library)	R. Quigley C. M. Donaldson
1		Electronics Division Aerojet-General Corporation P. O. Box 296 Azusa, California 91703 Attn: Library	W. L. Rogers
1		Space Division Aerojet-General Corporation 9200 East Flair Drive El Monte, California 91734 Attn: Library	S. Machlawski
1		Aerojet Ordnance and Manufacturing Aerojet-General Corporation 11711 South Woodruff Avenue Fullerton, California 90241 Attn: Library	
1		Aerojet Liquid Rocket Company P. O. Box 15847 Sacramento, California 95813 Attn: Technical Library 2484-2015A	R. Stiff

Report Copies R	D	Recipient	Designee
1		Aeronutronic Division of Philco Ford Corp. Ford Road Newport Beach, California 92663 Attn: Technical Information Department	Dr. L. H. Linder
1		Aerospace Corporation 2400 E. El Segundo Blvd. Los Angeles, California 90045 Attn: Library-Documents	J. G. Wilder
1		Arthur D. Little, Inc. 20 Acorn Park Cambridge, Massachusetts 02140 Attn: Library	A. C. Tobey R. B. Hinckley
1		Astropower Laboratory McDonnell-Douglas Aircraft Company 2121 Paularino Newport Beach, California 92163 Attn: Library	
1		ARO, Incorporated Arnold Engineering Development Center Arnold AF Station, Tennessee 37389 Attn: Library	Dr. B. H. Boethert
1		Susquehanna Corporation Atlantic Research Division Shirley Highway & Edsall Road Alexandria, Virginia 22314 Attn: Library	
1		Beech Aircraft Corporation Boulder Facility Box 631 Boulder, Colorado Attn: Library	J. H. Rodgers

Report Copies R	D	Recipient	Designee
1		Bell Aerosystems, Inc. Box 1 Buffalo, New York 14240 Attn: Library	T. Reinhardt
1		Bendix Corporation Instruments & Life Support Division P. O. Box 4508 Davenport, Iowa 52808 Attn: Library	W. M. Carlson
1	1	Boeing Company Space Division P. O. Box 868 Seattle, Washington 98124 Attn: Library	D. H. Zimmerman
1		Boeing Company 1625 K Street, N.W. Washington, D.C. 20006	
1		Chemical Propulsion Information Agency Applied Physics Laboratory 8621 Georgia Avenue Silver Spring, Maryland 20910	Tom Reedy
1		Chrysler Corporation Missile Division P. O. Box 2628 Detroit, Michigan Attn: Library	John Gates
1		Chrysler Corporation Space Division P. O. Box 29200 New Orleans, Louisiana 70129 Attn: Library	

Report Copies R	D	Recipient	Designee
1		Curtiss-Wright Corporation Wright Aeronautical Division Woodridge, New Jersey Attn: Library	G. Kelley
1		University of Denver Denver Research Institute P. O. Box 10127 Denver, Colorado 80210 Attn: Security Office	
1		Fairchild Stratos Corporation Aircraft Missiles Division Hagerstown, Maryland Attn: Library	
1		Research Center Fairchild Hiller Corporation Germantown, Maryland Attn: Library	Ralph Hall
1		Republic Aviation Fairchild Hiller Corporation Farmington, Long Island New York	
1	1	General Dynamics/Convair P. O. Box 1128 San Diego, California 92112 Attn: Library	R. Tatro
	1		P. Slysh
1		Missiles & Space Systems Center General Electric Company Valley Forge Space Technology Center P. O. Box 8555 Philadelphia, Pa 19101 Attn: Library	

Report Copies R	D	Recipient	Designee
1		General Electric Company Flight Propulsion Lab Department Cincinnati, Ohio Attn: Library	D. Suichu Leroy Smith
1		Grumman Aircraft Engineering Corporation Bethpage, Long Island, New York Attn: Library	
1		Honeywell, Incorporated Aerospace Division 2600 Ridgeway Road Minneapolis, Minnesota Attn: Library	
1		LLT Research Institute Technology Center Chicago, Illinois 60616 Attn: Library	C. K. Hersh
1		Ling-Temco-Vought Corporation P. O. Box 5907 Dallas, Texas 75222 Attn: Library	
1		Linde-Division of Union Carbide P. O. Box 44 Tonawanda, New York 11450 Attn: G. Nies	
1		Marquardt Corporation 16555 Saticoy Street Box 2013 - South Annex Van Nuys, California 91409	L. R. Bell, Jr.
1		Denver Division Martin-Marietta Corporation P. O. Box 179 Denver, Colorado 80201 Attn: Library	Dr. J. McGrew

Report Copies R	D	Recipient	Designee
1		Western Division McDonnell Douglas Astronautics 5301 Bolsa Avenue Huntington Beach, California 92647 Attn: Library	R. W. Hallet G. W. Burge P. Klevatt
1		McDonnell Douglas Aircraft Corporation P. O. Box 516 Lambert Field, Missouri 63166 Attn: Library	R. A. Herzmark I. G. Hughes L. F. Kohrs
1		Rocketdyne Division North American Rockwell, Inc. 6633 Canoga Avenue Canoga Park, California 91304 Attn: Library, Dept. 596-306	Dr. R. J. Thompson S. F. Iacobellis
1		Space & Information Systems Division North American Rockwell 12214 Lakewood Blvd. Downey, California Attn: Library	
1		Northrop Space Laboratories 3401 West Broadway Hawthorne, California Attn: Library	Dr. William Howard
1		Purdue University Lafayette, Indiana 47907 Attn: Library (Technical)	Dr. Bruce Reese
1	1	Goodyear Aerospace Corporation 1210 Massilon Road Akron, Ohio 44306	Clem Shriver
1		Hamilton Standard Corporation Windsor Locks, Connecticut 06096 Attn: Library	

Report Copies R	D	Recipient	Designee
1		Stanford Research Institute 333 Ravenswood Avenue Menlo Park, California 94025 Attn: Library	Dr. Gerald Marksman
1		TRW Systems, Inc. One Space Park Redondo Beach, California 90278 Attn: Tech Library Document Acquisitions	D. H. Lee
1		United Aircraft Corporation Pratt & Whitney Division Florida Research & Development Center P. O. Box 2691 West Palm Beach, Florida 33402 Attn: Library	
1		United Aircraft Corporation United Technology Center P. O. Box 358 Sunnyvale, California 94038 Attn: Library	Dr. David Altman
1		Vickers, Incorporated Box 302 Troy, Michigan	
1		Airesearch Manufacturing Division Garrett Corporation 9851 Sepulveda Blvd Los Angeles, California 90009 Attn: Library	T. C. Coull F. R. Ruder R. K. Fisher R. J. Gambon V. A. ViLona
1		Airesearch Manufacturing Division Garrett Corporation 402 South 36th Street Phoenix, Arizona 85034 Attn: Library	

Report Copies R	D	Recipient	Designee
1		Commanding Officer U.S. Naval Underwater Ordnance Station Newport, Rhode Island 02844 Attn: Library	W. W. Bartlett
1		National Science Foundation, Engineering Division 1800 G Street N.W. Washington, D.C. 20540 Attn: Library	
1		G. T. Schjeldahl Company Northfield, Minnesota Attn: Library	
1		General Dynamics P. O. Box 748 Fort Worth, Texas 76101	D. E. Westerheide
1		Cryonetics Corporation Northwest Industrial Park Burlington, Massachusetts	J. F. Howlett
1		Institute of Aerospace Studies University of Toronto Toronto 5, Ontario Attn: Library	Dr. I. I. Glass
1		FMC Corporation Chemical Research & Development Center P. O. Box 8 Princeton, New Jersey 08540	
1		Westinghouse Research Laboratories Beulah Road, Churchill Boro Pittsburg, Pennsylvania 15235	G. O. Sankey J. H. Bitler

Report Copies R	D	Recipient	Designee
1		Cornell University Dept. of Materials Science & Engineering Ithaca, New York 14850 Attn: Library	H. H. Johnson
1		Narco Research & Development Company Whittaker Corporation 131 N. Ludlow Street Dayton, Ohio 45402	
		General Electric Company Apollo Support Department P. O. Box 2500 Daytona Beach, Florida 32015 Attn: C. Bay	
1		Celanese Corporation Box 1000 Summit, New Jersey 07901 Attn: J. D. Lassiter	
1		E. I. DuPont, DeNemours and Company Eastern Laboratory Gibbstown, New Jersey 08027 Attn: Library	
1		Esso Research and Engineering Company Special Projects Unit P. O. Box 8 Linden, New Jersey 07036 Attn: Library	D. L. Beader
1		Minnesota Mining & Manufacturing Company 900 Bush Avenue St. Paul, Minnesota 55106 Attn: Library	H. C. Zeman